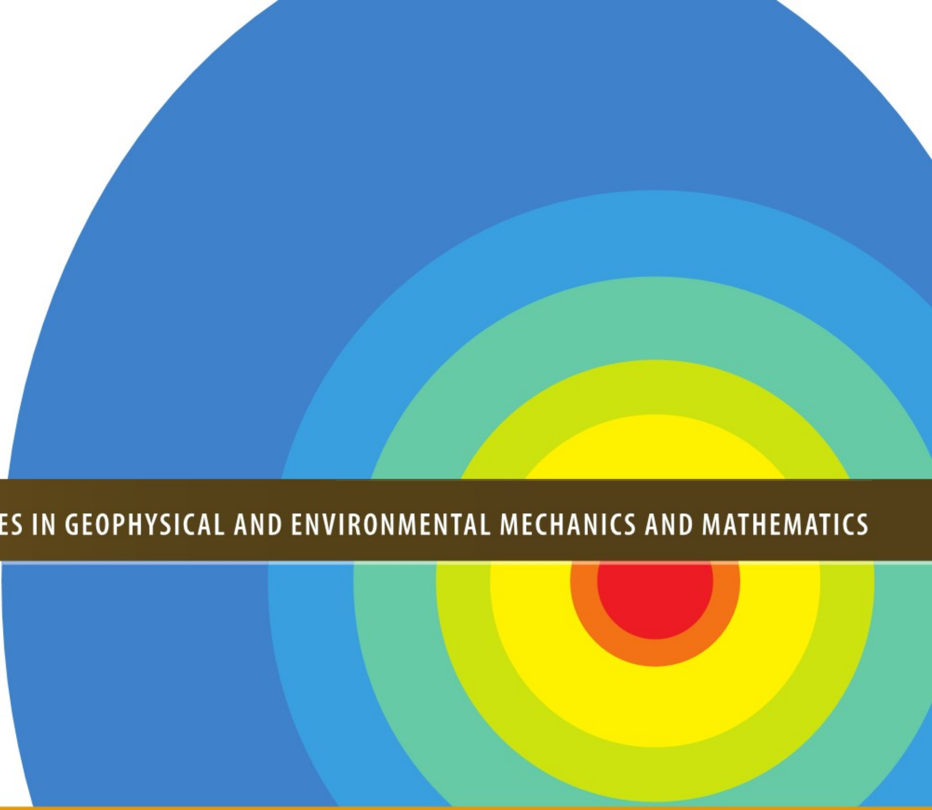

ADVANCES IN GEOPHYSICAL AND ENVIRONMENTAL MECHANICS AND MATHEMATICS

Chongbin Zhao

Dynamic and Transient Infinite Elements

Theory and Geophysical, Geotechnical and Geoenvironmental Applications

Springer

Advances in Geophysical and Environmental Mechanics and Mathematics

---

Series Editor: Professor Kolumban Hutter

Chongbin Zhao

Dynamic and Transient Infinite Elements

Theory and Geophysical, Geotechnical and Geoenvironmental Applications

Springer

Dr. Chongbin Zhao
Computational Geosciences Research Center
Central South University
Changsha, China
Chongbin.zhao@iinet.net.au

ISSN 1866-8348 e-ISSN 1866-8356
ISBN 978-3-642-00845-0 e-ISBN 978-3-642-00846-7
DOI 10.1007/978-3-642-00846-7
Springer Dordrecht Heidelberg London New York

Library of Congress Control Number: 2009926843

Cover design: deblik, Berlin

Printed on acid-free paper

Springer is part of Springer Science+Business Media (www.springer.com)

Preamble

Effective and efficient modelling of infinite media is important to the production of accurate and useful solutions for many scientific and engineering problems involving infinite domains, such as earthquake wave propagation within the upper crust of the Earth in the fields of geophysics and seismology, dynamic structure–foundation interaction in the fields of geotechnical, civil and dam engineering, transient pore-fluid flow, heat transfer and mass transport within the interior of the Earth in the fields of geoscience and geoenvironmental engineering, to name only a few. Such an effective and efficient modelling provides useful analytical and numerical tools for simulating, both accurately and efficiently, the effect of the far field of a system on the near field of the system so that computational resources can be concentrated on the simulation aspects of multiple processes, multiple scales, complicated geological and geometrical conditions for the near field of the system. Towards this end, dynamic and transient infinite elements have been developed during the past few decades.

This monograph aims to provide a state-of-the-art report on the theory and application of dynamic and transient infinite elements for simulating the far fields of infinite domains involved in many scientific and engineering problems, based on the author's own work during the last two decades. For this purpose, while the theoretical aspects of either dynamic infinite elements or transient infinite elements are systematically presented, the related application examples are immediately followed to illustrate the usefulness and applicability of these infinite elements for simulating a wide range of dynamic and transient problems involving infinite domains. To broaden the readership of this monograph, common mathematical notations are used to derive the formulations of both dynamic and transient infinite elements. This enables this monograph to be used either as a useful textbook for postgraduate students or as a valuable reference book for computational geoscientists, geotechnical engineers, civil engineers and applied mathematicians. In addition, each chapter is written independently of the remainder of the monograph so that readers may read the chapters of interest separately.

In this monograph, the coupled computational method of finite elements and dynamic infinite elements is used to solve wave propagation problems in infinite domains. For a given wave propagation problem, the near field of the problem is simulated using finite elements so that complicated geometries and complex material properties can be considered in the coupled computational method. The far field of the problem is simulated using dynamic infinite elements so that waves can be propagated from the near field to the far field without causing spurious reflection and refraction at the interface between finite elements and dynamic infinite elements in the coupled computational model. By taking advantages of both finite elements and dynamic infinite elements, the coupled computational method of finite elements and dynamic infinite elements provides a powerful simulation tool for dealing with a wide range of practical problems, such as the distributions of free-field motion during earthquakes, the seismic responses of dam–reservoir water–sediment–foundation systems and the dynamic analyses of civil structure–foundation interactions. To simulate transient pore-fluid flow, heat transfer and mass transport problems in infinite domains, the coupled computational method of finite elements and transient infinite elements is also presented. As an application example, this coupled method has been used to investigate the effects of several key factors on contaminant transport processes in fractured porous media of infinite domains. The related theoretical developments and application results are briefly described as follows: (1) Owing to the characteristics of propagating waves from the near field to the far field of a system, the wave propagation function of a dynamic infinite element plays a key role in the formulation of the element. Since the wave propagation function is explicitly dependent on frequency, the coupled computational method of finite elements and dynamic infinite elements can be directly used to solve linear wave propagation problems in the frequency domain, while it can be only used to deal with nonlinear wave propagation problems in the hybrid frequency–time domain. (2) For a two-dimensional dynamic infinite element, the corresponding wave propagation function has two independent wavenumbers so that it can be used to simulate explicitly both P-wave and SV-wave propagation in the far field of a system. Similarly, for a three-dimensional dynamic infinite element, the corresponding wave propagation function has three independent wavenumbers so that it is capable of simulating simultaneously P-wave, SV-wave and R-wave propagation in the far field of a system. (3) The coupled computational model of finite elements and dynamic infinite elements can be used to solve both wave scattering and wave radiation problems in infinite domains. When dealing with wave scattering problems, a wave input procedure, which can be easily applied to the coupled computational model of finite elements and dynamic infinite elements, is presented to transform an incident wave into equivalent nodal loads at a wave input boundary located within the coupled computational model. (4) For the application of dynamic infinite elements to dam engineering problems, the coupled computational method of two-dimensional finite elements and dynamic infinite elements has been used to simulate the dynamic responses of both a gravity dam–water–sediment–foundation system and an embankment dam–water–sediment–foundation system. For a gravity dam, the related numerical results have indicated that the reservoir bottom sediment has a remarkable effect on the dynamic response of the dam, while in the case of an embankment dam, the corresponding results have demonstrated that both the type and the location of impervious members within the dam have significant influences on the dynamic response of the embankment dam. (5) As an application example of simulating wave scattering problems in the fields of geophysics and seismology, the coupled computational method of two-dimensional finite elements and dynamic infinite elements has been used to investigate the effects of canyon topographical and geological conditions on the distributions of free-field motion during earthquakes. The related numerical results have demonstrated that both topographical and geological conditions have significant influences on seismic acceleration distributions along the surface of a canyon, implying that structures located on softer soils may be subjected to stronger seismic loads than those located on stiffer rocks. (6) The coupled computational model of three-dimensional finite elements and dynamic infinite elements has been used to solve dynamic framed structure–raft foundation–underlying medium interaction problems in the field of civil engineering. The related numerical results have demonstrated that since the radiation damping of an underlying medium plays a predominant role in determining the total damping of the underlying medium, the dynamic response of a three-dimensional framed structure on a layered medium is much stronger than that on a homogeneous medium, as a result of wave reflection and refraction within the soft layer. (7) To construct transient infinite elements for simulating transient pore-fluid flow and heat transfer problems in fluid-saturated porous media of infinite domains, the hydraulic head distribution and heat transfer functions are used to derive the formulations of the transient infinite elements. Since these functions are explicitly dependent on time, the coupled computational method of finite elements and transient infinite elements can be straightforwardly employed to solve transient pore-fluid flow and heat transfer problems in the time domain. (8) Based on the mass transport function concept, the formulations of transient infinite elements are derived for simulating the far fields of mass transport problems in fractured porous media of infinite domains. With the use of the double porosity continuum approach, the porous block and fissured network in a fractured porous medium can be treated as an equivalent medium consisting of two overlapping continua. This enables the coupled computational method of finite elements and transient infinite elements to be used for investigating the effects of various key factors on contaminant transport processes in fractured porous media of infinite domains. The related numerical results have demonstrated that the leakage between the porous block and the fissure network, the porosity ratio of the fissured network to the porous block, pore-fluid advection and solute dispersion have significant effects on contaminant concentration distributions in fractured porous media of infinite domains.

November 28, 2008 *Chongbin Zhao*

Acknowledgements

I express sincere thanks to my wife, Ms. Peiying Xu, for her persistent support and encouragement, without which it would have been impossible to write this monograph. The monograph was carefully reviewed by Professor K. Hutter, whom I thank for the valuable comments and suggestions that led to a significant improvement over the early version of the monograph. I am very grateful to the Central South University for financial support during writing this monograph. Partial work of this monograph has also financially been supported by the Natural Science Foundation of China (Grant Nos: 10872219 and 10672190). Special thanks are given to my PhD supervisors, Professors Guangdou Zhang and Chuhan Zhang at the Tsinghua University, for their guidance and support during my early academic career. I also express sincere thanks to Professor S. Valliappan for his valuable discussions and comments during my stay at the University of New South Wales.

Contents

Nomenclature

The following symbols are commonly used with the attached definitions, unless otherwise specified in the monograph.

A	area of a finite element
C	contaminant concentration
$\{\mathrm{C}\}$	contaminant concentration vector
C_1	contaminant concentration in the porous block
C_2	contaminant concentration in the fissured network
c_p	specific heat of pore-fluid
D	dispersion coefficient
g	acceleration due to gravity
h	hydraulic head
H	reference length
K	hydraulic conductivity
L	length of a problem domain
M	mapping function
N	shape function
$[\mathrm{N}]$	shape function matrix
p	pressure
P	nodal force
$\{\mathrm{P}\}$	nodal force vector
P_0	concentrated force
P_λ	nodal force on the wave input boundary
S	boundary length of a finite element
T	temperature
$\{\mathrm{T}\}$	temperature vector
t	temporal variable
u	displacement in the x direction
v	displacement in the y direction
V	volume of a finite element
w	displacement in the z direction
x, y, z	spatial coordinates in a global coordinate system

λ	thermal conductivity
λ_{e0}	reference thermal conductivity in the horizontal direction
ϕ	porosity
ψ	vector potential function
ρ	density
ν	Poisson's ratio
β	stress increase factor
σ	normal stress
τ	shear stress
ω	circular frequency
ξ, η, ζ	spatial coordinates in a local coordinate system
θ	wave incident angle
η_d	hysteretic damping coefficient
χ	transmissive coefficient between the porous block and the fissured network in a fractured porous medium

Subscripts

f	pertaining to pore-fluid
0	pertaining to reference quantities
P	pertaining to P-wave
SV	pertaining to SV-wave

Superscripts

e	pertaining to quantities in a finite element level
$*$	pertaining to dimensionless quantities
s	pertaining to solid matrix
T	pertaining to the transpose of a matrix

Chapter 1
Introduction

Effective and efficient modelling of infinite media is important for the production of accurate and useful solutions for many scientific and engineering problems involving infinite domains (Bettess 1977, 1980; Chow and Smith 1981; Medina and Taylor 1983; Zhang and Zhao 1987; Zhao et al. 1989; Zhao and Valliappan 1993a, b, c, d; Astley 1996, 1998; Yang et al. 1996; Yang and Huang 2001; Yun et al. 2000, 2007; Wang et al. 2006). Some typical examples involving infinite domains are as follows: (1) earthquake wave propagation within the upper crust of the Earth in the fields of geophysics and seismology; (2) dynamic structure–foundation interaction in the fields of geotechnical, civil and dam engineering; and (3) transient pore-fluid flow, heat transfer and mass transport within the interior of the Earth in the fields of geoscience and geoenvironmental engineering. Although the solid Earth is viewed as a bounded domain at the terrestrial scale, it can be treated as an unbounded domain at the human scale. For instance, in the case of predicting possible property damages caused by an earthquake, only a limited region around the epicentre is of interest because the earthquake wave energy is significantly reduced as the distance from the epicentre is increased. Compared with the region of interest around an epicentre, which is called *the near field or the interior domain of a system*, the outside region, referred to as *the far field or the exterior domain of the system*, is large enough to be treated as an infinite domain, from the mathematical point of view. Similarly, the sizes of engineering structures such as civil buildings, dams, embankments, retaining walls and nuclear reactors are very small, compared with those of their foundations. Since only the response of a structure and its surrounding foundation is of interest, from the structural design point of view, computational resources should be concentrated on the analysis of the structure and the near field of the foundation.

In terms of simulating the near fields of systems involving infinite domains, the finite element method provides a very powerful tool in the sense that complicated geometries and complex material distributions can be effectively and efficiently considered in a finite element model (Zienkiewicz 1997; Rao 1989). In particular, the numerical adequacy and convergence properties of a finite element model were extensively studied, so that many numerical simulation criteria have been established. For example, when a finite element is used to simulate wave propagation problems, there is a mesh size requirement criterion available, which states that in

C. Zhao, *Dynamic and Transient Infinite Elements*, Advances in Geophysical and Environmental Mechanics and Mathematics, DOI 10.1007/978-3-642-00846-7_1,

order to ensure the numerical adequacy and convergence of a finite element model, the size of a linear finite element should be less than one-eighth of the wavelength to be simulated, whereas the size of a quadratic finite element should be less than one-fourth of the wave length to be simulated in the finite element model. Similarly, when a finite element is used to simulate transient mass transport problems, the size of the element should satisfy the Courant number, so that the numerical adequacy and convergence of a finite element model can be ensured (Zienkiewicz 1977; Zhao et al. 1994). For these reasons, the finite element mesh of the near field can be designed on the basis of the related mesh criteria available, without a need to conduct a mesh refinement study.

Since the finite element method can be used to simulate problems of finite domains, it is necessary to develop useful numerical techniques for simulating the far fields of problems when they are of infinite domains. Towards this end, static, dynamic and transient infinite elements have been developed for simulating the far fields of many scientific and engineering problems involving infinite domains during the past few decades. *Static infinite elements refer to the time-independent infinite elements* suitable for simulating the far fields of static problems. *Dynamic infinite elements refer to the frequency-dependent infinite elements* suitable for simulating the far fields of dynamic and wave propagation problems, while *transient infinite elements refer to the time-dependent infinite elements* suitable for simulating the far fields of transient pore-fluid flow, heat transfer and mass transport problems. On the other hand, for most scientific and engineering problems involving infinite domains, the near field of a problem can be appropriately determined so that the nonlinear behaviour of the problem can be simulated by finite elements. As a result, for the sake of developing dynamic and transient infinite elements, linear dynamic elasticity (in certain cases including linear visco-elasticity) is used to represent the mechanical behaviour of the far field, while linearized ground water flow and diffusive mass transport equations are used to approximately represent the behaviours of the corresponding far fields.

For the numerical simulation of an infinite domain, a primitive and very simple method, in which the infinite domain was approximately truncated as a large-enough finite domain, was widely used at the early stage of the finite element analysis. The major disadvantages in using this primitive method are as follows: (1) the simulation of a large-enough domain leads to a significant increase in computational resources; (2) the boundary conditions of a problem at infinity cannot be rigorously satisfied. For instance, stresses and displacements attenuating zero at infinity for a static problem and the wave radiation condition in the far field for a dynamic problem have to be violated in the numerical analysis; (3) stretching a fixed number of finite elements to model a vast domain can result in a severe loss of solution accuracy for static problems, while it results in spurious solutions for dynamic problems because the element size requirement for appropriately simulating dynamic problems cannot be satisfied in the numerical simulation; (4) for transient heat transfer and mass transport problems, the use of artificially truncated boundaries can cause unexpected numerical reflections back into the near field, where the solutions are usually of great interest to the analyst, of a system.

To overcome the above-mentioned disadvantages, infinite elements have been developed to simulate, both effectively and efficiently, the physical and mechanical effects of the far field of a system on the near field of the system. In this respect, Ungless (1973) presented the static infinite element concept for simulating infinite domains of static problems. This concept attracted considerable research on the development and application of static infinite elements during both the 1970s and the 1980s (Bettess 1977, 1980, 1992; Beer and Meek 1981; Booker and Small 1981; Zhao et al. 1986). In the early 1980s, Chow and Smith (1981) extended the static infinite element concept to the simulation of infinite domains for dynamic problems. Owing to the wave propagation characteristics associated with dynamic problems, a large amount of research has been contributed to the development and application of dynamic infinite elements for simulating the far-field effects of infinite domains since the 1980s (Medina and Taylor 1983; Zhang and Zhao 1987; Zhao et al. 1989; Zhao and Valliappan 1993a, b, c, d; Astley 1996, 1998; Yang et al. 1996; Yang and Huang 2001; Yun et al. 2000, 2007; Wang et al. 2006). As most of the research conducted in the development of dynamic infinite elements is associated with steady-state wave propagation problems in the frequency domain, it remains desirable to directly develop dynamic infinite elements in the time domain for simulating elastic wave propagation problems involving infinite domains in the future. On the other hand, for dealing with the numerical simulation of infinite domains associated with transient pore-fluid flow, heat transfer and mass transport problems, Zhao and Valliappan (1993e, f, 1994a) presented (time-dependent) transient infinite elements in the time domain. Since the proposed transient infinite elements are time dependent, they have been successfully used, with a combination of the conventional finite element method, to solve a wide range of transient pore-fluid flow, heat transfer and mass transport problems in fluid-saturated porous media of infinite domains (Zhao et al. 1994b, c; Khalili et al. 1999a, b; Lai et al. 2002; Zhang et al. 2007).

The prediction of an earthquake and related property damages has been a hot research topic in the fields of geology, geophysics and seismology. Although earthquakes cannot be predicted using the present day's knowledge of geoscientists, modern advances in computational simulation methods provide some useful tools suitable for investigating the detailed dynamic processes and mechanisms associated with an earthquake. From the computational simulation point of view, an earthquake may involve the following two important stages: an inception stage and an occurrence stage. At an inception stage, the deformation rate of crustal materials (i.e. about a few centimetres per year) is so slow that the geological system related to the inception of an earthquake can be treated as a quasi-static system, indicating that the whole geological system can be simulated using the coupled computational method of finite elements and static infinite elements. However, at the occurrence stage of an earthquake, the resulting earthquake wave propagates at a speed of a few thousand kilometres per second within the crust of the Earth, so that the geological system related to the occurrence of an earthquake must be treated as a dynamic system. In this situation, the whole geological system needs to be simulated using the coupled computational method of finite elements and dynamic infinite elements. To demonstrate the potential application of dynamic infinite elements in the fields of geophysics and seismology, the coupled computational method of two-dimensional finite elements and dynamic infinite elements is used to investigate the effects of canyon topographical and geological conditions on the distributions of free-field motion during earthquakes. This is studied in the fourth chapter of this monograph.

As extensive studies on the dynamic response of concrete gravity and embankment dams due to earthquake loadings have demonstrated, the dynamic response of either a concrete gravity dam or an embankment dam is mainly affected by the following factors: (1) the interaction between the dam and the impounded reservoir water (Chopra 1968; Chakarbarti and Chopra 1974; Liam-Finn et al. 1977); (2) the compressibility of the impounded water (Chopra and Gupta 1982); (3) the interaction between the dam and the foundation rock (Liam-Finn et al. 1977; Liam-Finn and Varoglu 1972a, b,1975); (4) the materials at the reservoir bottom (Hall and Copra 1982; Fenves and Chopra 1983, 1984, 1985; Lotfi et al. 1987; Medina et al. 1990. Based on a substructure method, Chopra and his colleagues considered the above factors and made some interesting conclusions on the dynamic response of concrete gravity dams due to earthquake loadings (Chopra 1968; Chakarbarti and Chopra 1974; Hall and Copra 1982; Fenves and Chopra 1983, 1984, 1985). Owing to the limitations of the substructure method, the reservoir bottom material was assumed to have zero thickness. However, in certain circumstances such as concrete gravity and embankment dams built in the Yellow River valley, China, not only materials at a reservoir bottom have considerable thicknesses, but sediments at the reservoir bottom are also comprised of very soft clay materials. Although some basic studies have been carried out to investigate how reservoir bottom sediments affect the dynamic response of concrete gravity dams (Medina et al. 1990; Zhao 1994), further studies are needed to investigate the detailed dynamic mechanisms associated with the effects of reservoir bottom sediments on the dynamic response of concrete gravity and embankments dams. In view of this fact, the coupled computational method of finite and dynamic infinite elements is used for investigating the effects of reservoir bottom sediments on the dynamic response of concrete gravity and embankment dams. Since the coupled computational model keeps all advantages of the conventional finite element method, complicated geometrical, physical and mechanical properties of a dam–water–foundation system, including the reservoir bottom sediment effect, can be straightforwardly considered in the corresponding numerical simulations.

Transient pore-fluid flow, heat transfer and mass transport in fluid-saturated porous media of infinite domains are important phenomena in many scientific and engineering fields. For example, in the field of exploration geoscience, pore-fluid flow, heat transfer and mass transport from the interior of the Earth to the surface of the Earth are three important physical processes to control ore body formation and mineralization within the upper crust of the Earth. Owing to the increasing demand for natural minerals and the possible exhaustion of existing mineral resources in the foreseeable future, there has been an ever-increasing interest in the study of key controlling processes associated with ore body formation and mineralization within the upper crust of the Earth (Phillips 1991; Yeh and Tripathi 1991; Nield and Bejan 1992; Steefel and Lasaga 1994; Raffensperger and Garven 1995; Schafer et al.

1998a, b; Xu et al. 1999; Schaubs and Zhao 2002; Ord et al. 2002; Gow et al. 2002; Zhao et al. 1997–2008). In the field of environmental engineering, carbon dioxide gas sequestration in the deep Earth is becoming a potential way to reduce the greenhouse effect. Even in our daily lives, pore-fluid flow and contaminant transport through fluid-saturated porous soils can be encountered almost everywhere. This means that transient infinite elements can be used to solve a wide range of scientific and engineering problems encountered in nature. To illustrate how transient infinite elements are used to solve contaminant transport problems in the field of geoenvironmental engineering, the coupled computational method of finite elements and transient infinite elements is used for investigating the effects of various key factors on contaminant transport processes in fractured porous media of infinite domains.

The arrangements of the forthcoming parts of this monograph are as follows. In Chap. 2, the formulations of two-dimensional dynamic infinite elements are presented in detail. To use the coupled computational method of two-dimensional finite elements and dynamic infinite elements for wave scattering problems in infinite media, a wave input procedure is also presented in this chapter. In Chap. 3, the coupled computational method of two-dimensional finite elements and dynamic infinite elements is used to solve dynamic dam–water–sediment–foundation interaction problems in the fields of geotechnical and dam engineering. Both a concrete gravity dam and an embankment dam are considered and some interesting results are presented. In Chap. 4, the coupled computational method of two-dimensional finite elements and dynamic infinite elements is used to simulate the spatial distribution of free-field motion during an earthquake, which is a fundamental scientific problem in the fields of geophysics and seismology. The effects of different topographical and geological conditions on the spatial distributions of free-field motion during earthquakes have been investigated. The detailed formulations associated with three-dimensional dynamic infinite elements are presented in Chap. 5. Through a combination of three-dimensional finite elements and dynamic infinite elements, two benchmark problems have been used to verify the correctness and usefulness of the proposed three-dimensional dynamic infinite elements for simulating wave radiation problems in three-dimensional infinite media. Based on the related formulations presented in Chap. 5, the coupled computational method of three-dimensional finite elements and dynamic infinite elements is used in Chap. 6 to simulate dynamic structure–foundation interaction problems in the fields of civil and structural engineering. For the purpose of understanding the dynamic mechanisms of a structure–foundation interaction problem, a fundamental problem, namely the vibration of a rigid plate foundation on a visco-elastic half-space, is considered before the dynamic response of a three-dimensional framed structure–raft foundation–underlying medium system is simulated by the coupled computational method of three-dimensional finite elements and dynamic infinite elements. In Chap. 7, the detailed formulations of transient infinite elements are presented for simulating pore-fluid flow and heat transfer problems in fluid-saturated porous media of infinite domains, because such problems can be found in a broad range of scientific and engineering fields. Two different approaches are employed to derive the property matrices of these transient infinite elements. The detailed formulations associated with transient infinite elements for simulating mass transport problems are presented in Chap. 8, when the coupled computational method of finite elements and transient infinite elements is used to simulate contaminant transport problems in fractured porous media of infinite domains. On the basis of the double porosity concept, a fractured porous medium can be treated as an equivalent medium consisting of two overlapping continua, namely a porous continuum and a fissured continuum. Finally, some conclusions are given at the end of the monograph.

Chapter 2
Theory of Two-Dimensional Dynamic Infinite Elements for Simulating Wave Propagation Problems in Infinite Media

Numerical simulation of wave propagation problems in infinite media has attracted significant attention in many scientific and engineering fields such as geophysics, seismology, civil engineering and earthquake engineering. From a wave motion point of view, structural vibration problems can be divided into two categories. One is a wave radiation problem, or an interior domain problem, in which wave energy is produced within the near field and then propagated into the far field of the problem in various wave forms. Typical examples of this category are foundation vibration problems as a result of trains passing on railways, machine vibration problems on the foundations of buildings, impacting vibration problems on the ground surface of an airport during airplanes landing, to name just a few. The other is a wave scattering problem, or an exterior domain problem, in which wave energy is produced in the far field and propagated into the near field of the problem. An earthquake source or an explosion in the far field is a typical example of this category. Since the formulations of dynamic infinite elements for simulating wave radiation problems are essentially the same as those for simulating wave scattering problems, the focus of this chapter is on the formulation and derivation of dynamic infinite elements for simulating wave scattering problems. In this regard, a wave input method needs to be developed for simulating incoming waves from the far field of an infinite medium.

For the theoretical analysis of wave scattering problems in the fields of seismology and geophysics, extensive work has been carried out over the past years. Aki and Larner (1970) proposed a practical method using both the discrete wavenumber representation for a wave field and the related Rayleigh assumption. In their method, a scattered wave field is expressed as the superposition of plane waves, which have unknown complex amplitudes and propagate in various directions. The total motion of the system is obtained through integration over the horizontal wavenumber. Under the assumption of horizontal periodicity of irregularity, the resulting integral can be replaced by an infinite series. Truncation of this series and application of interface conditions of continuity for both stress and displacement lead to a set of linear equations for the unknown complex amplitudes. This method has found many applications in the fields of geophysics and seismology (Bard 1982; Geli et al. 1988). Trifunac (1973) and Wong and Trifunac (1974) presented analytical solutions for SH-wave scattering problems around semi-circular and semi-elliptical valleys

C. Zhao, *Dynamic and Transient Infinite Elements*, Advances in Geophysical and Environmental Mechanics and Mathematics, DOI 10.1007/978-3-642-00846-7_2,

using a Hankel function expansion. By means of boundary integral equations, Wong (1982) improved the discrete wavenumber method (Aki and Larner 1970) and presented a general inverse method to solve the P-wave, SV-wave and Rayleigh wave scattering problems for alluvial valleys of both semi-circular and semi-elliptical shapes. Lee (1984) and Eshraghi and Dravinski (1989a, b) used a wave function expansion method to solve wave scattering problems around either hemi-spherical valleys or dipping layers, respectively. Sanchez-Sesma (1983) applied the boundary integration method to the scattering of elastic waves around axisymmetric irregularities. Kawase (1988) suggested a discrete wavenumber boundary element method, in which the conventional boundary element method is used with Green's functions of discrete wavenumbers, for dealing with wave scattering problems. Khair et al. (1989) introduced the hybrid method of finite and boundary elements for solving three-dimensional scattering problems of plane P-waves and SV-waves around cylindrical valleys. Obviously, all methods mentioned above are mainly suitable for dealing with linear, isotropic and homogeneous materials as a result of using half-space elastic wave theory to describe earthquake excitations in these methods.

The finite element method (Zienkiewicz 1977) is one of the most powerful numerical methods for solving complex and complicated problems in both scientific and engineering fields (Zhao et al. 1994, 1995, 1997, 1998). However, for the finite element simulation of wave scattering problems in infinite media, the following two issues have to be considered. The first is the infinite extension of a problem domain, while the second is the incidence of an earthquake wave from the far field of a system. To simulate infinite media both effectively and efficiently, Ungless (1973) and Bettess (1977, 1980) presented a static infinite element method for dealing with static problems. Chow and Smith (1981), Medina and Taylor (1983) and Zhao et al. (1989) extended the static infinite element method to the solution of wave radiation problems in infinite media. Using a combination of finite and infinite elements, a whole system can be divided into a near field and a far field. The near field is simulated using finite elements, while the far field is simulated using dynamic infinite elements. For the seismic analysis of a structure, the main concern is usually about the dynamic response of the structure, so that only a small region of the infinite medium needs to be treated as the near field of the system. This can result in a significant reduction in the total number of finite elements that are used to simulate the computational domain of the system. Since dynamic infinite elements are capable of simulating wave propagation within themselves, unwanted wave reflection phenomena at the interface between a finite element and an infinite element can be avoided.

Early work on earthquake input procedures for the finite element method was carried out by Reimer et al. (1974), with particular attention to the finite element analysis of arch dams. Due to the difficulties of this problem, they suggested a massless finite element model, which is called the *massless foundation earthquake input model*. In this model, only a limited massless foundation is simulated using finite elements, and the acceleration of an earthquake is applied to the whole finite element model. This procedure has some obvious discrepancies from physical reality, as it cannot simulate wave propagation effects in the foundation of an arch dam. To overcome these discrepancies, Clough et al. (1985) proposed a sophisticated earthquake input method, called the *free field input method*, for the finite element analysis of arch dams subjected to earthquakes. Although both the spatial amplitude and the spatial phase differences of an earthquake can be considered in the free field input method, it is difficult to apply this method to practical problems in the field of earthquake engineering, because few earthquakes have been recorded along the surfaces of natural canyons. Another wave input method used in the hybrid model of finite and boundary elements is called the *standard wave input method*, which is established on the basis of the half-space elastic wave theory. Furthermore, Zhao (1987) presented a wave propagation input method on the basis of using finite and dynamic infinite element coupled models and considering wave propagation characteristics in elastic solid media. As this method has been successfully used to solve SH-wave scattering problems (Zhang and Zhao 1988), it is worth extending this method to the solution of P-wave and SV-wave scattering problems because of wave mode conversions in these situations.

To take advantage of the coupled computational model of finite and dynamic infinite elements for simulating natural foundations, a numerical model for dealing with wave scattering problems in infinite media is presented in this chapter. With consideration of P-wave and SV-wave reflection characteristics on a fixed boundary, the harmonic P-wave and SV-wave propagating from the far field of a system are transformed into nodal dynamic forces on the wave input boundary, where scattering waves from canyons or structures can be transmitted back into the far field of the system through dynamic infinite elements. The major advantage of using the proposed model is that, by choosing a horizontal boundary in the underlying rock, full-space elastic wave theory can be used to describe earthquake excitations in the coupled computational model of finite and dynamic infinite elements. As a result, the proposed model is capable of simulating wave propagation and scattering mechanisms within the region of interest, which is located above the wave input boundary, under any geometrical and geological conditions. In addition, the proposed numerical model is clear in the physical concept and easy to be included into the existing finite element computer code. The related numerical results from solving P-wave and SV-wave scattering problems in a half-plane and a semi-circular canyon have been obtained using the proposed model.

2.1 Formulation of Two-Dimensional Dynamic Infinite Elements and Wave Input Method

To derive the formulations of two-dimensional dynamic infinite elements, it is natural to consider wave motion equations in a half-plane. Since an earthquake wave can be decomposed into the sum of several harmonic waves, it is necessary to investigate the propagation behaviours of harmonic waves in a half-plane. Since material damping occurring in the soil/rock involves a frictional loss of energy, it can be considered as hysteretic damping, which is independent of frequency, by means of the correspondence principle (Wolf 1985). Using this principle, the damped solution of a system can be obtained from the elastic one by replacing the elastic constants with the corresponding complex ones. Under the assumption that the dynamic system is subjected to a harmonic wave loading and that the medium of the system exhibits hysteretic damping, the corresponding governing wave equations of the system can be expressed as follows:

$$G^*\nabla^2 u + \left(\lambda^* + G^*\right)\left(\frac{\partial^2 u}{\partial x^2} + \frac{\partial^2 v}{\partial x \partial y}\right) + f_x = \rho \frac{\partial^2 u}{\partial t^2}, \tag{2.1}$$

$$G^*\nabla^2 v + \left(\lambda^* + G^*\right)\left(\frac{\partial^2 u}{\partial x \partial y} + \frac{\partial^2 v}{\partial y^2}\right) + f_y = \rho \frac{\partial^2 v}{\partial t^2}, \tag{2.2}$$

$$G^* = (1 + i\eta_d)\, G, \quad \lambda^* = (1 + i\eta_d)\, \lambda, \tag{2.3}$$

where G is the shear modulus; λ is the Lamé constant; η_d is the hysteretic damping coefficient of the medium; u and v are displacements in the x and y directions; f_x and f_y are body forces in the x and y directions, respectively; ρ is the density of the medium; ∇^2 is the second-order two-dimensional Laplace operator.

Using the Galerkin weighted residual procedure and neglecting body forces in Eqs. (2.1) and (2.2), the discretized wave equation of the system can be derived as

$$-\,\omega^2\, [M]\, \{\Delta\} + (1 + i\eta_d)\, [K]\, \{\Delta\} = \{F_0\}, \tag{2.4}$$

where $\{\Delta\}$ is the unknown nodal displacement vector; ω is the circular frequency of the harmonic wave; $[M]$ and $[K]$ are the global mass and stiffness matrices of the system respectively; and $\{F_0\}$ is the amplitude vector of the applied harmonic load. $[M]$, $[K]$ and $\{F_0\}$ can be assembled from the following element submatrices and subvectors:

$$[M]^e = \iint_A [N]^T \rho\, [N]\, dA, \tag{2.5}$$

$$[K]^e = \iint_A [B]^T \left[D^*\right] [B]\, dA, \tag{2.6}$$

$$\{F_0\}^e = \int_S [N]^T \left\{\overline{X}_0\right\} dS + [N]^T \left\{\overline{P}_0\right\}, \tag{2.7}$$

where A and S are the area and boundary length of the element; $\{\bar{X}_0\}$ is the amplitude vector of element boundary traction; $\{\bar{P}_0\}$ is the amplitude vector of concentrated loads acting on the element; $[D^*]$ is the constitutive matrix of the element material; and $[B]$ and $[N]$ are the strain matrix and shape function matrix of the element. It needs to be pointed out that Eqs. (2.5), (2.6) and (2.7) are equally valid for both finite and dynamic infinite elements. Since the derivation of two-dimensional finite element formulation is well known (Zienkiewicz 1977; Rao 1989), only the formulation of two-dimensional dynamic infinite elements is derived below.

2.1.1 Formulation of Two-Dimensional Dynamic Infinite Elements

For dealing with wave propagation problems in infinite media of geometrical irregularities and geological complexities, the use of a coupled computational model of finite and dynamic infinite elements is very effective (Zhao 1987; Zhang and Zhao 1987; Zhao et al. 1989, 1991, 1992; Zhao and Valliappan 1993a, b, c, d, e, f). Considering a dynamic infinite element shown in Fig. 2.1, the corresponding coordinate mapping can be expressed as follows:

$$x = \sum_{i=1}^{5} M_i x_i, \tag{2.8}$$

$$y = \sum_{i=1}^{5} M_i y_i, \tag{2.9}$$

where M_i ($i = 1, 2, \ldots, 5$) is the following mapping function of the dynamic infinite element:

$$M_1 = \frac{1}{2}(\xi - 1)(\eta - 1), \tag{2.10}$$

$$M_2 = 0, \tag{2.11}$$

$$M_3 = -\frac{1}{2}(\xi - 1)(\eta + 1), \tag{2.12}$$

$$M_4 = \frac{1}{2}\xi(\eta + 1), \tag{2.13}$$

$$M_5 = -\frac{1}{2}\xi(\eta - 1). \tag{2.14}$$

The displacement field within this dynamic infinite element can be expressed as follows:

$$u = \sum_{i=1}^{3} N_i u_i, \tag{2.15}$$

$$v = \sum_{i=1}^{3} N_i v_i, \tag{2.16}$$

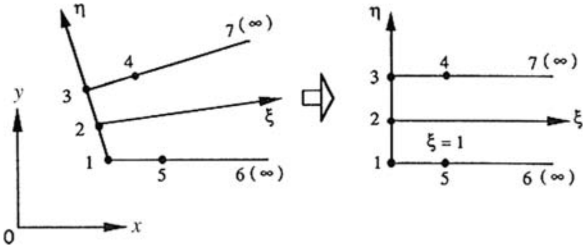

Fig. 2.1 Two-dimensional dynamic infinite element: nodes 1, 2 and 3 are the end nodes to be connected with a finite element; nodes 4 and 5 are the middle nodes with $\xi = 1$; nodes 6 and 7 are at infinity

where N_i ($i = 1$, 2 and 3) is the following displacement shape function of the dynamic infinite element:

$$N_1 = P(\xi)\frac{\eta(\eta - 1)}{2}, \tag{2.17}$$

$$N_2 = -P(\xi)(\eta - 1)(\eta + 1), \tag{2.18}$$

$$N_3 = P(\xi)\frac{\eta(\eta + 1)}{2}, \tag{2.19}$$

where $P(\xi)$ is the wave propagation function of the dynamic infinite element. From a harmonic wave propagation point of view, $P(\xi)$ can be expressed in the following form:

$$P(\xi) = \exp\left[-(\alpha + i\beta)\xi\right], \tag{2.20}$$

where α and β are the displacement–amplitude decay factor and nominal wavenumber of the dynamic infinite element in the local coordinate system. Physically, $\exp(-\alpha\xi)$ expresses the behaviour of displacement amplitude attenuation within the dynamic infinite element as a result of wave energy dissipation; while $\exp(-i\beta\xi)$ expresses the behaviour of phase delays as a result of wave propagation in the local coordinate system.

Equations (2.15) and (2.16) can be written in the matrix form as follows:

$$\begin{Bmatrix} u \\ v \end{Bmatrix}^e == [N]\{\Delta\}^e, \tag{2.21}$$

where $[N]$ is the shape function matrix of the dynamic infinite element; $\{\Delta\}^e$ is the nodal displacement vector of the element. They are of the following forms:

$$[N] = \begin{bmatrix} N_1 & 0 & N_2 & 0 & N_3 & 0 \\ 0 & N_1 & 0 & N_2 & 0 & N_3 \end{bmatrix},$$

$$\{\Delta\}^e = \left\{u_1 \ v_1 \ u_2 \ v_2 \ u_3 \ v_3\right\}^T. \tag{2.23}$$

Using the above definitions, the strain matrix of the dynamic infinite element can be expressed as follows:

$$\{\varepsilon\}^e = \begin{Bmatrix} \dfrac{\partial u}{\partial x} \\ \dfrac{\partial v}{\partial y} \\ \dfrac{\partial u}{\partial y} + \dfrac{\partial v}{\partial x} \end{Bmatrix} = \begin{bmatrix} \dfrac{\partial N_1}{\partial x} & 0 & \dfrac{\partial N_2}{\partial x} & 0 & \dfrac{\partial N_3}{\partial x} & 0 \\ 0 & \dfrac{\partial N_1}{\partial y} & 0 & \dfrac{\partial N_2}{\partial y} & 0 & \dfrac{\partial N_3}{\partial y} \\ \dfrac{\partial N_1}{\partial y} & \dfrac{\partial N_1}{\partial x} & \dfrac{\partial N_2}{\partial y} & \dfrac{\partial N_2}{\partial x} & \dfrac{\partial N_3}{\partial y} & \dfrac{\partial N_3}{\partial x} \end{bmatrix} = [B]\{\Delta\}^e, \tag{2.24}$$

where $[B]$ is the strain matrix of the dynamic infinite element; $\{\varepsilon\}^e$ is the strain vector of the element. The strain matrix of the dynamic infinite element can be further expressed as

$$[B] = \begin{bmatrix} \frac{\partial N_1}{\partial x} & 0 & \frac{\partial N_2}{\partial x} & 0 & \frac{\partial N_3}{\partial x} & 0 \\ 0 & \frac{\partial N_1}{\partial y} & 0 & \frac{\partial N_2}{\partial y} & 0 & \frac{\partial N_3}{\partial y} \\ \frac{\partial N_1}{\partial y} & \frac{\partial N_1}{\partial x} & \frac{\partial N_2}{\partial y} & \frac{\partial N_2}{\partial x} & \frac{\partial N_3}{\partial y} & \frac{\partial N_3}{\partial x} \end{bmatrix}. \tag{2.25}$$

To evaluate the strain matrix of the dynamic infinite element, it is necessary to calculate the first derivatives of the displacement shape functions with respect to the local ξ and η coordinates as follows:

$$\frac{\partial N_i}{\partial \xi} = \frac{\partial N_i}{\partial x}\frac{\partial x}{\partial \xi} + \frac{\partial N_i}{\partial y}\frac{\partial y}{\partial \xi} \qquad (i = 1, 2, 3), \tag{2.26}$$

$$\frac{\partial N_i}{\partial \eta} = \frac{\partial N_i}{\partial x}\frac{\partial x}{\partial \eta} + \frac{\partial N_i}{\partial y}\frac{\partial y}{\partial \eta} \qquad (i = 1, 2, 3). \tag{2.27}$$

Equations (2.26) and (2.27) can be readily expressed in the following matrix form:

$$\begin{Bmatrix} \frac{\partial N_i}{\partial \xi} \\ \frac{\partial N_i}{\partial \eta} \end{Bmatrix} = \begin{bmatrix} \frac{\partial x}{\partial \xi} & \frac{\partial y}{\partial \xi} \\ \frac{\partial x}{\partial \eta} & \frac{\partial y}{\partial \eta} \end{bmatrix} \begin{Bmatrix} \frac{\partial N_i}{\partial x} \\ \frac{\partial N_i}{\partial y} \end{Bmatrix} = [J] \begin{Bmatrix} \frac{\partial N_i}{\partial x} \\ \frac{\partial N_i}{\partial y} \end{Bmatrix} \qquad (i = 1, 2, 3), \tag{2.28}$$

where the matrix $[J]$, called the Jacobian matrix, is given by the following equation:

$$[J] = \begin{bmatrix} \frac{\partial x}{\partial \xi} & \frac{\partial y}{\partial \xi} \\ \frac{\partial x}{\partial \eta} & \frac{\partial y}{\partial \eta} \end{bmatrix}. \tag{2.29}$$

Substituting Eqs. (2.8) and (2.9) into Eq. (2.29) yields the final expression for the Jacobian matrix as follows:

$$[J] = \begin{bmatrix} \sum_{i=1}^{5} \left(\frac{\partial M_i}{\partial \xi} x_i \right) & \sum_{i=1}^{5} \left(\frac{\partial M_i}{\partial \xi} y_i \right) \\ \sum_{i=1}^{5} \left(\frac{\partial M_i}{\partial \eta} x_i \right) & \sum_{i=1}^{5} \left(\frac{\partial M_i}{\partial \eta} y_i \right) \end{bmatrix}. \tag{2.30}$$

Thus, the first derivatives of the displacement shape functions with respect to the global x and y coordinates can be expressed as follows:

$$\begin{Bmatrix} \dfrac{\partial N_i}{\partial x} \\ \dfrac{\partial N_i}{\partial y} \end{Bmatrix} = [J]^{-1} \begin{Bmatrix} \dfrac{\partial N_i}{\partial \xi} \\ \dfrac{\partial N_i}{\partial \eta} \end{Bmatrix} \qquad (i = 1,2,3). \tag{2.31}$$

Mathematically, there exists the following expression:

$$dA = dxdy = |J|\, d\xi d\eta, \tag{2.32}$$

where $|J|$ is the Jacobian determinant.

The displacement-amplitude decay factor, α, can be determined from elastic wave theory. Considering an elastic homogeneous half-plane under a concentrated harmonic excitation force as shown in Fig. 2.2 and assuming that no energy dissipation occurs in the elastic medium, the total wave energy passing through a cylindrical surface with radius R_1 should be equal to that with radius R_2. From a physical point of view, the energy flow density of a harmonic wave in an elastic medium can be defined as follows:

$$< I >= k\omega^2 A^2, \tag{2.33}$$

where k is the coefficient associated with the material property of the medium; ω is the circular frequency of excitation; and A is the displacement amplitude of the elastic wave.

Suppose the end nodal points (i.e. nodes 1, 2 and 3) and middle nodal points (i.e. nodes 4 and 5) of the dynamic infinite element pass through two cylindrical surfaces with radii R_1 and R_2 in the elastic homogeneous half-plane, the displacement amplitude of the harmonic wave at node 1 can be expressed as follows:

$$A_1 = |U_1| = |u_1 N_1|_{\xi=0} = |u_1| \exp(-\alpha\xi)|_{\xi=0} = |u_1| \tag{2.34}$$

where u_1 is the nodal displacement of node 1.

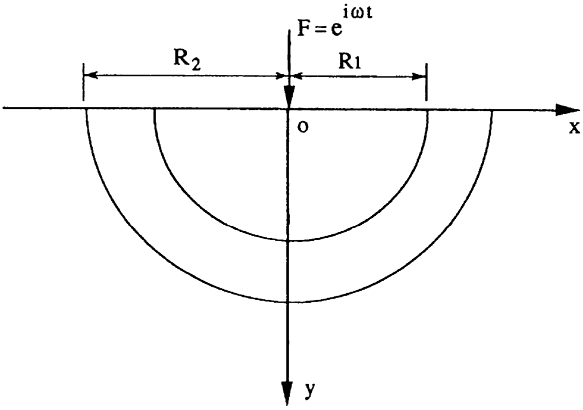

Fig. 2.2 Amplitude decay of harmonic waves in an infinite medium: owing to the wave energy conservation, the amplitude of a harmonic wave decreases as the radius of a cylindrical surface increases

Similarly, the displacement amplitude of the harmonic wave at node 5 can be expressed as follows:

$$A_2 = |U_5| = |u_1 N_1|_{\xi=1} = |u_1| \exp(-\alpha\xi)|_{\xi=1} = |u_1| \exp(-\alpha). \tag{2.35}$$

Therefore, the energy flow densities of the harmonic wave through these two cylindrical surfaces can be expressed as follows:

$$< I_1 >= k\omega^2 A_1^2 = k\omega^2 u_1^2 \qquad \text{(on the surface with node 1)}, \tag{2.36}$$

$$< I_2 >= k\omega^2 A_2^2 = k\omega^2 u_1^2 \exp(-2\alpha) \qquad \text{(on the surface with node 5)} \tag{2.37}$$

Considering the equality condition of wave energy through these two cylindrical surfaces yields the following equation:

$$< I_1 > \pi R_1 =< I_2 > \pi R_2. \tag{2.38}$$

Once Eqs. (2.36) and (2.37) are substituted into Eq. (2.38), the displacement-amplitude decay factor of the element can be obtained and expressed as follows:

$$\alpha = -\frac{1}{2} \ln\left(\frac{R_1}{R_2}\right). \tag{2.39}$$

Since the interface between a finite element and a dynamic infinite element is not exactly a cylindrical surface in a computational model, the following approximate formula can be used in the process of establishing the computational model:

$$\alpha = -\frac{1}{2} \ln\left(\frac{D_F}{D_F + \Delta D_F}\right), \tag{2.40}$$

where D_F is the length of the finite element region and ΔD_F is the distance between the middle and corner nodes of a two-dimensional dynamic infinite element.

Equation (2.39) or (2.40) clearly indicates the influence of the position of an arbitrarily chosen boundary (i.e. the near field boundary of a computational model) between a finite element and a dynamic infinite element on the displacement amplitude factor of the two-dimensional dynamic infinite element.

Based on Eqs. (2.5), (2.6) and (2.32), the mass and stiffness matrices of the dynamic infinite element can be rewritten as follows:

$$[M]^e = \int_{-1}^{1} \int_{0}^{\infty} [N]^T \rho [N] \, |J| \, d\xi d\eta, \tag{2.41}$$

$$[K]^e = \int_{-1}^{1} \int_{0}^{\infty} [B]^T \left[D^*\right] [B] \, |J| \, d\xi d\eta, \tag{2.42}$$

where $|J|$ is the Jacobian determinant.

Evaluation of Eqs. (2.41) and (2.42) involves the general integrals of the following form:

$$I = \int_0^\infty F(\xi)\exp\left[-2\,(\alpha + i\beta)\,\xi\right]d\xi. \tag{2.43}$$

The sufficient condition for the convergence of Eq. (2.43) is that $\alpha > 0$. From the physical point of view, wave propagation in an infinite medium is always accompanied by dispersion and attenuation. Thus, the convergent condition for Eq. (2.43) can be evidently satisfied.

The selection of integration points in the ξ direction is related to the function, $F(\xi)$. According to the shape functions of the dynamic infinite element, $F(\xi)$ is a polynomial with a power not greater than 3. Therefore, the four-point Newton–Cotes integration scheme, with ξ=2, 4, 6 and 8 as numerical integration points, is used and the corresponding weighting coefficients are as follows (Chow and Smith 1981):

$$W_1 = \frac{1}{24}\left(96\gamma - 52\gamma^2 + 18\gamma^3 - 3\gamma^4\right), \tag{2.44}$$

$$W_2 = \frac{1}{8}\left(-48\gamma + 38\gamma^2 - 16\gamma^3 + 3\gamma^4\right), \tag{2.45}$$

$$W_3 = \frac{1}{8}\left(32\gamma - 28\gamma^2 + 14\gamma^3 - 3\gamma^4\right), \tag{2.46}$$

$$W_4 = \frac{1}{24}\left(-24\gamma + 22\gamma^2 - 12\gamma^3 + 3\gamma^4\right), \tag{2.47}$$

where γ is the following function of α and β:

$$\gamma = \frac{1}{2}\left(\frac{\alpha - i\beta}{\alpha^2 + \beta^2}\right). \tag{2.48}$$

Note that W_1, W_2, W_3 and W_4 are complex numbers. They are related to the nominal wavenumber (β) of the dynamic infinite element in the local coordinate system.

Another important issue associated with the application of dynamic infinite elements to the numerical simulation of elastic wave propagation problems is that the displacement shape function of a dynamic infinite element contains, either implicitly or explicitly, the wavenumber of an elastic wave. In an elastic medium, there are at least two types of waves, S-waves and P-waves. Generally, it is difficult to separate the components of these two types of waves, because they are associated with all displacement components, especially for dealing with wave radiation problems in infinite media. Over the past, several schemes were used to overcome this difficulty. Medina and Taylor (1983) used a split scheme between wave components on the basis of analytical solutions. Chow and Smith (1981) assumed, arbitrarily, that the vertical component of a wave is associated with an S-wave and that the horizontal component of a wave is associated with a P-wave. Zhang and Zhao (1987) used, as an approximation, Rayleigh wavenumbers for the lateral infinite elements and S-wave numbers for the bottom infinite elements within a computational model of finite and dynamic infinite elements. Although some assumptions were used to choose wavenumbers for two-dimensional dynamic infinite elements, satisfactory numerical results were obtained from using the above-mentioned approaches for solving wave radiation problems in infinite media (Chow and Smith 1981; Zhang and Zhao 1987). As the types of incident waves are known for wave scattering problems, in contrast to wave radiation problems, the selections of wavenumbers for two-dimensional dynamic infinite elements are much easier, especially in dealing with vertical incident waves. In the case of dealing with a vertical incident wave, the wavenumber of the incident wave can be used as the wavenumber for all the two-dimensional dynamic infinite elements, because the type of the incident wave is a dominate wave type within the system.

2.1.2 *Wave Input Method for Simulating Wave Scattering Problems in Infinite Media*

Since natural earthquake waves can be decomposed into a large number of harmonic waves using the fast Fourier transform technique (i.e. FFT for short), a harmonic wave propagating in an infinite medium can be used for developing the wave input method. Figure 2.3 shows a typical dynamic soil–structure interaction problem during earthquakes. From the wave motion theory point of view, this problem can be essentially treated as a wave scattering problem due to geometrical irregularities and material property complexities in both the structure and the near field of the infinite medium. Using the coupled computational model of finite and dynamic infinite elements, the whole problem domain can be divided into an interior domain (i.e. Ω_I) and an exterior domain (i.e. Ω_E). The interior domain, which is simulated using finite elements, is comprised of both the structure and the near field of the infinite medium, while the exterior domain, which is simulated using dynamic infinite elements, is comprised of the far field of the infinite medium. Supposing a harmonic wave is propagating from the exterior domain into the interior domain, a horizontal boundary, which is a part of the interface between finite and dynamic infinite elements within the underlying rock, is defined as the wave input boundary, Γ_λ.

To obtain the dynamic response of the interior domain when an incident wave approaches from the far field, the model shown in Fig. 2.3(A) can be decomposed into two computational models that are shown in Figs. 2.3(B) and 2.3(C), respectively. In the computational model shown in Fig. 2.3(B), an artificially fixed boundary condition is applied to the wave input boundary, so that the incident wave reflects and, consequently, reaction forces (i.e. P_λ) are generated on the fixed boundary within the computational model. By adding the opposite of the reaction forces (i.e. – P_λ) on the wave input boundary within the computational model shown in

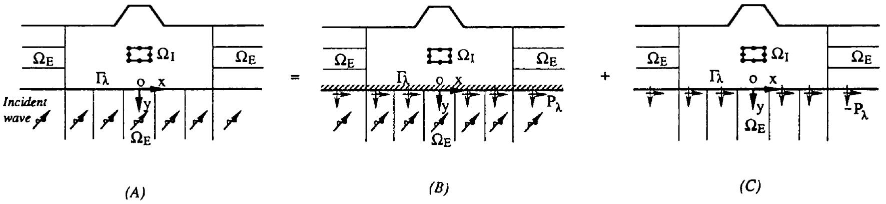

Fig. 2.3 Wave input method for simulating wave scattering problems in infinite media: (**A**) the model of the original problem; (**B**) the modified model with a fixed boundary; (**C**) the equivalent model for simulating the wave scattering problem

Fig. 2.3(C), the effect of the artificially fixed boundary condition can be eliminated. As there is no response in the interior domain of the computational model shown in Fig. 2.3(B), the one shown in Fig. 2.3(C) can be used to simulate the dynamic response of the interior domain of the whole system, instead of the original model shown in Fig. 2.3(A). However, the dynamic response of the exterior domain under the horizontal wave input boundary can be obtained only by superposition of the numerical results from using both the computational models shown in Figs. 2.3(B) and 2.3(C).

The major advantage of using the proposed wave input method is that full-space elastic wave theory can be used to describe an earthquake excitation by simply choosing a horizontal boundary within the underlying rock. Free boundary conditions on the surfaces of both the structure and the foundation can be easily satisfied by applying zero nodal forces to the surface nodes of the computational model. As a result, the proposed computational model (shown in Fig. 2.3(C)) is capable of simulating wave propagating and scattering mechanisms under any arbitrary geometrical and geological conditions within the region located above the horizontal wave input boundary.

Suppose the materials of an infinite medium have hysteretic damping, the discretized wave equation for the computational model shown in Fig. 2.3(C) can be expressed as follows:

$$\left\{-\omega^2\begin{bmatrix} M_{\lambda\lambda} & M_{\lambda 0} \\ M_{0\lambda} & M_{00} \end{bmatrix} + (1 + i\eta_d)\begin{bmatrix} K_{\lambda\lambda} & K_{\lambda 0} \\ K_{0\lambda} & K_{00} \end{bmatrix}\right\}\begin{Bmatrix} \Delta_\lambda \\ \Delta_0 \end{Bmatrix} = \begin{Bmatrix} P_\lambda \\ P_0 \end{Bmatrix}, \tag{2.49}$$

where Δ_λ and Δ_0 are the complex displacement vectors for the wave input boundary and the rest of the interior domain, respectively; η_d is the hysteretic damping coefficient; ω is the circular frequency of an incident wave; the elements in mass matrix $[M]$ and stiffness matrix $[K]$ represent the submatrices associated with Δ_λ and Δ_0; and $\{P_\lambda\}$ is the subvector of the equivalent nodal loads associated with Δ_λ. The equivalent nodal load vector for an element can be evaluated using the following equation:

$$\{P_\lambda\}^e = -\int_S [N]^T \{\sigma\}^e \, dS, \tag{2.50}$$

where $[N]$ is the displacement shape function of the element; and $\{\sigma\}^e$ is a generalized stress vector acting on the wave input boundary, S, of the element. This stress vector can be evaluated by considering incident wave types and wave reflection characteristics on a fixed boundary.

2.2 Incident P-wave and SV-wave Reflection Characteristics on a Fixed Boundary

To evaluate the reaction forces on the wave input boundary (i.e. $Y = 0$ in Fig. 2.3(B)), it is necessary to investigate both the incident P-wave and the incident SV-wave reflection characteristics on a fixed boundary. As shown in Fig. 2.4, it is assumed that either a plane harmonic P-wave or a plane harmonic SV-wave propagates in the space and impinges onto a fixed boundary. From wave motion theory (Graff 1975), the corresponding governing equations for this problem can be expressed as follows:

$$u = \frac{\partial \phi}{\partial x} + \frac{\partial \psi_z}{\partial y}, \tag{2.51}$$

$$v = \frac{\partial \phi}{\partial y} - \frac{\partial \psi_z}{\partial x}, \tag{2.52}$$

$$\nabla^2 \phi = \frac{1}{C_P^2} \frac{\partial^2 \phi}{\partial t^2}, \tag{2.53}$$

$$\nabla^2 \psi_z = \frac{1}{C_{SV}^2} \frac{\partial^2 \psi_z}{\partial t^2}, \tag{2.54}$$

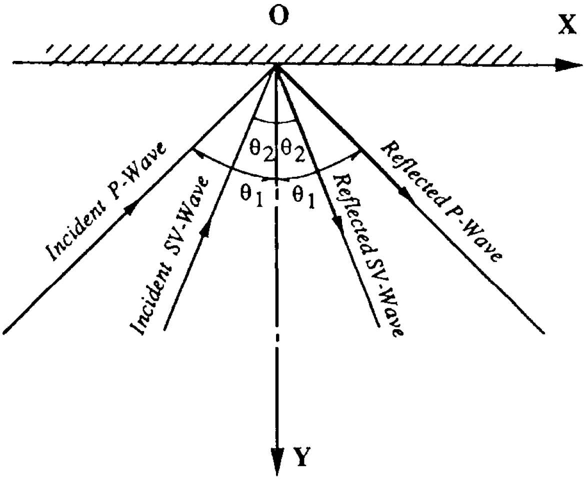

Fig. 2.4 P-wave and SV-wave reflections on a fixed boundary: θ_1 is the incident and reflection angles of a P-wave; θ_2 is the incident and reflection angles of an SV-wave

where u and v are the particle displacements in the x and y directions, respectively; ϕ and ψ_z are the scalar potential and the component of a vector potential (i.e. $\vec{\psi} = \psi_x\vec{i} + \psi_y\vec{j} + \psi_z\vec{k}$) in the z direction; C_P and C_{SV} are the P-wave and SV-wave velocities; and ∇^2 is a two-dimensional Laplace operator. Note that for the sake of convenience, it is assumed that the xoy coordinate system is coincident with the XOY one in this section.

The artificially fixed boundary has the following boundary conditions:

$$u = 0, \qquad v = 0 \qquad (\text{on } Y = 0). \tag{2.55}$$

For plane harmonic wave incidences, Eqs. (2.53) and (2.54) have the following analytical solutions:

$$\begin{aligned}\phi = {} & A_I^P \exp\left[i\gamma_P\left(-x\sin\theta_1 + y\cos\theta_1 + C_P t\right)\right]\\ & + A_R^P \exp\left[i\gamma_P\left(-x\sin\theta_1 - y\cos\theta_1 + C_P t\right)\right],\end{aligned} \tag{2.56}$$

$$\begin{aligned}\psi_z = {} & B_I^{SV} \exp\left[i\gamma_{SV}\left(-x\sin\theta_2 + y\cos\theta_2 + C_{SV} t\right)\right]\\ & + B_R^{SV} \exp\left[i\gamma_{SV}\left(-x\sin\theta_2 - y\cos\theta_2 + C_{SV} t\right)\right],\end{aligned} \tag{2.57}$$

where A_I^P and A_R^P are the potential amplitudes of the incident P-wave and reflected P-wave, respectively; B_I^{SV} and B_R^{SV} are the potential amplitudes of the incident SV-wave and reflected SV-wave, respectively; θ_1 is the P-wave incident or reflection angle; θ_2 is the SV-wave incident or reflection angle; and γ_P and γ_{SV} are the wavenumbers of the P-wave and SV-wave, respectively. By definition, these two wavenumbers can be expressed as follows:

$$\gamma_P = \frac{\omega}{C_P}, \tag{2.58}$$

$$\gamma_{SV} = \frac{\omega}{C_{SV}}. \tag{2.59}$$

From elastic wave theory, θ_1 and θ_2 satisfy the following relationship (Graff 1975):

$$\frac{\sin\theta_1}{\sin\theta_2} = \frac{C_P}{C_{SV}} = \frac{\gamma_{SV}}{\gamma_P} = D = \sqrt{\frac{2(1-\nu)}{1-2\nu}}, \tag{2.60}$$

where ν is Poisson's ratio of the elastic medium.

By considering Eqs. (2.53), (2.54), (2.55), (2.56) and (2.57) simultaneously, the ratios of related potential amplitudes can be determined. This leads to the following solutions:

(i) in the case of a P-wave incidence:

$$\frac{A_R^P}{A_I^P} = \frac{\cos\theta_1\cos\theta_2 - \sin\theta_1\sin\theta_2}{\cos\theta_1\cos\theta_2 + \sin\theta_1\sin\theta_2}, \tag{2.61}$$

$$\frac{B_R^{SV}}{A_I^P} = \frac{-\gamma_P\sin\theta_1\cos\theta_1}{\gamma_{SV}\left(\cos\theta_1\cos\theta_2 + \sin\theta_1\sin\theta_2\right)}. \tag{2.62}$$

Note that if the P-wave incident angle is identical to zero (i.e. $\theta_1 = 0$), then $B_R^{SV}/A_I^P = 0$, implying that no wave mode conversion takes place for this special vertical incident angle. Otherwise, when $\theta_1 \neq 0$, wave mode conversion takes place, so that a reflected SV-wave occurs.

(ii) For an SV-wave incidence, in which the incident angle (i.e. θ_2) is less than the critical incident angle (i.e. $\theta_{critical}$), the following solutions can be obtained:

$$\frac{B_R^{SV}}{B_I^{SV}} = \frac{\cos\theta_1 \cos\theta_2 - \sin\theta_1 \sin\theta_2}{\cos\theta_1 \cos\theta_2 + \sin\theta_1 \sin\theta_2}, \tag{2.63}$$

$$\frac{A_R^P}{B_I^{SV}} = \frac{2\gamma_{SV} \sin\theta_2 \cos\theta_2}{\gamma_P \left(\cos\theta_1 \cos\theta_2 + \sin\theta_1 \sin\theta_2\right)}. \tag{2.64}$$

Similarly as above, if the incident angle of the SV-wave is identical to zero (i.e. $\theta_2 = 0$), then $A_R^P/B_I^{SV} = 0$, indicating that no wave mode conversion takes place for this special vertical incident angle. Otherwise, when $\theta_2 \neq 0$, wave mode conversion takes place and a P-wave is generated.

From elastic wave theory, the stresses are given by the following relationships:

$$\sigma_x = (\lambda + 2G)\left(\frac{\partial^2\phi}{\partial x^2} + \frac{\partial^2\phi}{\partial y^2}\right) - 2G\left(\frac{\partial^2\phi}{\partial y^2} - \frac{\partial^2\psi_z}{\partial x \partial y}\right), \tag{2.65}$$

$$\sigma_y = (\lambda + 2G)\left(\frac{\partial^2\phi}{\partial x^2} + \frac{\partial^2\phi}{\partial y^2}\right) - 2G\left(\frac{\partial^2\phi}{\partial x^2} + \frac{\partial^2\psi_z}{\partial x \partial y}\right), \tag{2.66}$$

$$\tau_{xy} = G\left(2\frac{\partial^2\phi}{\partial x \partial y} + \frac{\partial^2\psi_z}{\partial y^2} - \frac{\partial^2\psi_z}{\partial x^2}\right), \tag{2.67}$$

where G is the shear modulus; λ is the Lamé constant of the medium; σ_x and σ_y are the normal stresses in the x and y directions; and τ_{xy} is the shear stress on the fixed boundary.

To determine the reaction forces on the fixed boundary (i.e. $Y = 0$), only the normal stress σ_y and shear stress τ_{xy} need to be considered. Using Eqs. (2.56), (2.57), (2.65), (2.66) and (2.67), the ratio of the total stress to the stress induced by an incident wave can be determined. This leads to the following solutions.

(i) For a P-wave incidence:

$$\frac{\sigma_y^P}{\sigma_{y0}^P} = 1 + \frac{A_R^P}{A_I^P} + \frac{B_R^{SV} G \gamma_{SV}^2 \sin(2\theta_2)}{A_I^P \gamma_P^2 \left[(\lambda + 2G) + 2G \sin^2\theta_1\right]} = 1 + \beta_\sigma^P, \tag{2.68}$$

$$\frac{\tau_{xy}^P}{\tau_{xy0}^P} = 1 - \frac{A_R^P}{A_I^P} - \frac{B_R^{SV} \gamma_{SV}^2 \cos(2\theta_2)}{A_I^P \gamma_P^2 \sin(2\theta_1)} = 1 + \beta_\tau^P, \tag{2.69}$$

where σ_y^P and τ_{xy}^P are the normal and shear stresses on the fixed boundary as a result of the P-wave incidence; β_σ^P and β_τ^P are the stress increase factors of the stresses σ_y^P

and τ_{xy}^{P} on the fixed boundary; and σ_{y0}^{P} and τ_{xy0}^{P} are the normal and shear stresses on the fixed boundary just before wave reflections take place.

(ii) For an SV-wave incidence, whose incident angle (i.e. θ_2) is less than the corresponding critical incident angle (i.e. $\theta_{critical}$), the following solutions can be obtained:

$$\frac{\sigma_y^{SV}}{\sigma_{y0}^{SV}} = 1 - \frac{B_R^{SV}}{B_I^{SY}} + \frac{A_R^P \gamma_P^2 \left(D^2 - 2\sin^2\theta_1\right)}{B_I^{SV}\gamma_{SV}^2 \sin(2\theta_2)} = 1 + \beta_\sigma^{SV}, \tag{2.70}$$

$$\frac{\tau_{xy}^{SV}}{\tau_{xy0}^{SV}} = 1 + \frac{B_R^{SV}}{B_I^{SV}} + \frac{A_R^P \gamma_P^2 \sin(2\theta_1)}{B_I^{SV}\gamma_{SV}^2 \cos(2\theta_2)} = 1 + \beta_\tau^{SV}, \tag{2.71}$$

$$D = \frac{C_P}{C_{SV}}, \tag{2.72}$$

where σ_y^{SV} and τ_{xy}^{SV} are the normal and shear stresses on the fixed boundary as a result of the SV-wave incidence; β_σ^{SV} and β_τ^{SV} are the stress increase factors of the stresses σ_y^{SV} and τ_{xy}^{SV} on the fixed boundary; and σ_{y0}^{SV} and τ_{xy0}^{SV} are the normal and shear stresses on the fixed boundary just before wave reflections take place.

Considering Eqs. (2.61), (2.62), (2.63), (2.64), (2.68), (2.69), (2.70) and (2.71) simultaneously yields the following results:

$$\beta_\sigma^P = \frac{\cos(\theta_1 + \theta_2)}{\cos(\theta_1 - \theta_2)} - \frac{D\sin(2\theta_1)\sin(2\theta_2)}{\cos(\theta_1 - \theta_2)\left(2\sin^2\theta_1 - D^2\right)}, \tag{2.73}$$

$$\beta_\tau^P = -\frac{\cos(\theta_1 + \theta_2)}{\cos(\theta_1 - \theta_2)} - \frac{D\cos(2\theta_2)}{\cos(\theta_1 - \theta_2)}, \tag{2.74}$$

$$\beta_\sigma^{SV} = -\frac{\cos(\theta_1 + \theta_2)}{\cos(\theta_1 - \theta_2)} - \frac{D^2 - 2\sin^2\theta_1}{D\cos(\theta_1 - \theta_2)}, \tag{2.75}$$

$$\beta_\tau^{SV} = \frac{\cos(\theta_1 + \theta_2)}{\cos(\theta_1 - \theta_2)} + \frac{\sin(2\theta_1)\sin(2\theta_2)}{D\cos(\theta_1 - \theta_2)\cos(2\theta_2)}. \tag{2.76}$$

Figure 2.5 shows the distributions of stress increase factors resulting from different wave modes, wave incident angles and Poisson's ratios of the medium material. From these analytical results, it can be concluded that (1) stress increase factors on a fixed boundary are highly dependent on the incident wave modes, wave incident angles and Poisson's ratio of the medium material; (2) if the incident angle is zero (i.e. either $\theta_1 = 0$ or $\theta_2 = 0$), both β_σ^P and β_τ^{SV} are equal to unity and independent of the Poisson's ratio of the medium material; and (3) for an SV-wave incidence, there exists a critical incident angle, $\theta_{critical}$, which is dependent on the Poisson's ratio of the medium material and can be determined from Eq. (2.43) with $\theta_1 = 90°$ as follows:

$$\sin\theta_1 = D\sin\theta_2 = 1, \quad \theta_{critical} = \sin^{-1}\left(\frac{1}{D}\right) = \sin^{-1}\left(\sqrt{\frac{1-2\nu}{2(1-\nu)}}\right). \tag{2.77}$$

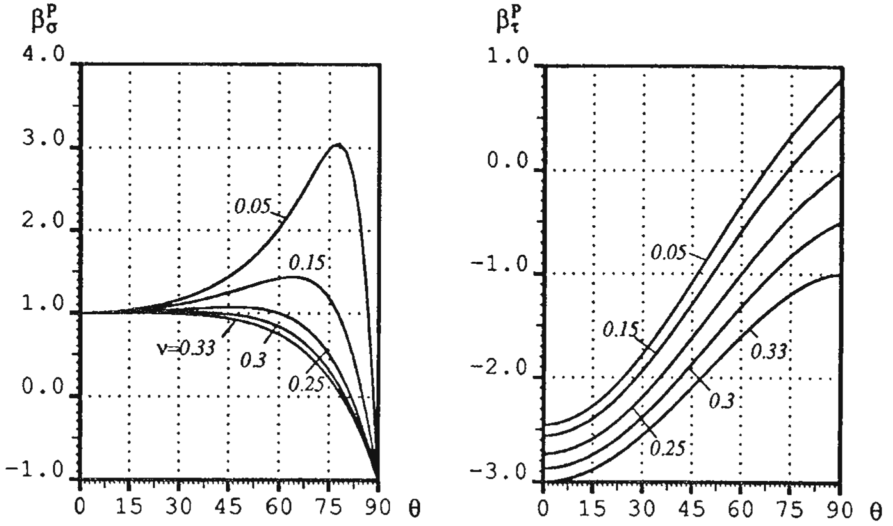

P-wave incidence

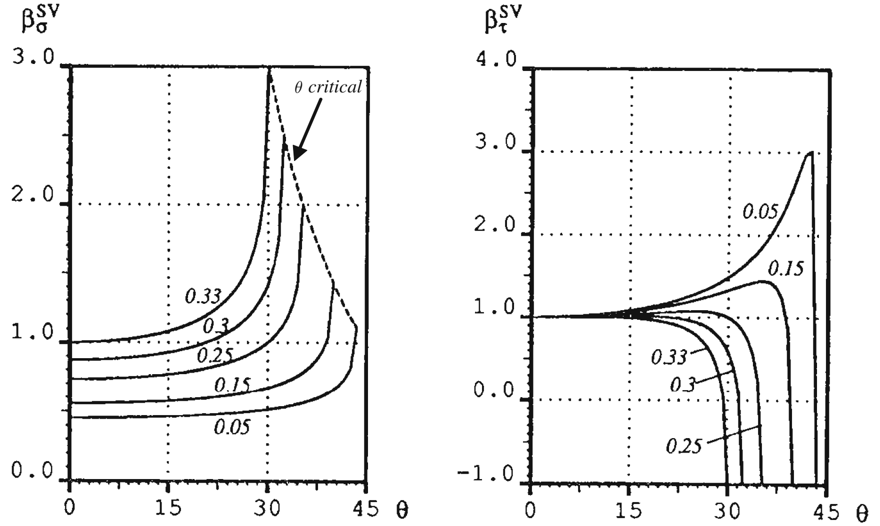

SV-wave incidence

Fig. 2.5 Distributions of stress increase factors arising from P-wave and SV-wave incidences on a fixed boundary: five different values of Poisson's ratio are considered in the figure

For example, when $\nu = 0.33$ (where ν is Poisson's ratio of the medium material), $\theta_{critical} = 30°$, while in the case of $\nu = 0.05$, $\theta_{critical} = 43.5°$. Moreover, when an SV-wave incident angle approaches the corresponding critical incident angle, two stress increase factors, namely β_σ^{SV} and β_τ^{SV}, will change dramatically.

2.3 Formulation of Generalized Stresses on the Wave Input Boundary

When the normal and shear stresses are determined on a fixed boundary (as shown in Fig. 2.4), the equivalent nodal load vector of an element on the wave input boundary can be evaluated using Eq. (2.33). To determine the total stresses (i.e. σ_y and τ_{xy}) on a fixed boundary, two original stresses (i.e. σ_{y0} and τ_{xy0}), which are generated by an incident wave just before the occurrence of wave reflection, need to be evaluated on the basis of elastic wave theory. Note that the xoy coordinate system is assumed to be coincident with the XOY one in this section.

2.3.1 SV-wave Incidence

Consider a plane SV-wave as shown in Fig. 2.6, propagating from the far field of a system into the near field of the system and arriving at a fixed boundary. Before the incident SV-wave reflects on the fixed boundary, the particle displacements of the incident SV-wave can be expressed as

$$u_{\lambda x} = u_\lambda \cos\theta, \tag{2.78}$$

$$u_{\lambda y} = u_\lambda \sin\theta, \tag{2.79}$$

where u_λ is the particle displacement of the incident plane SV-wave while arriving at the fixed boundary (i.e. $Y = 0$) before the reflection of the incident wave; $u_{\lambda x}$ and $u_{\lambda y}$ are the components of u_λ in the x and y directions, respectively; and θ is the incident angle of the plane SV-wave.

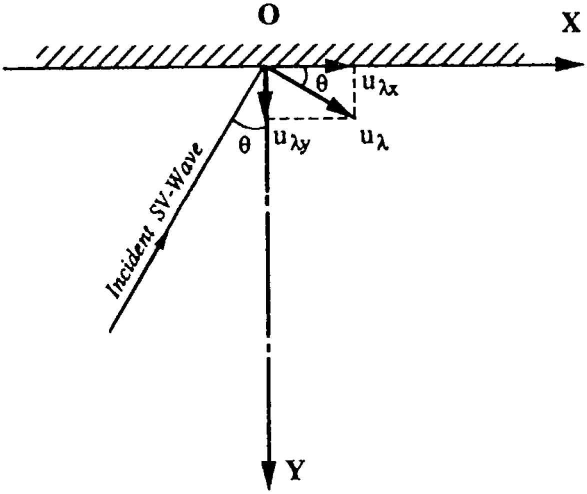

Fig. 2.6 Particle displacement on a fixed boundary for an SV-wave incidence

Assuming the incident plane SV-wave is a harmonic wave with unit amplitude, the displacement of this wave can be expressed as follows:

$$u_\lambda = \exp\left[i\omega\left(1 - \frac{x}{C_{SVx}} + \frac{y}{C_{SVy}}\right)\right], \tag{2.80}$$

where C_{SVx} and C_{SVy} are the apparent wave velocities of the incident plane SV-wave in the x and y directions, respectively:

$$C_{SVx} = \frac{C_{SV}}{\sin\theta}, \tag{2.81}$$

$$C_{SVy} = \frac{C_{SV}}{\cos\theta}. \tag{2.82}$$

From elastic wave theory, the strain vector resulting only from u_λ on the fixed boundary (i.e. $Y = 0$) can be expressed as follows:

$$\{\varepsilon_0\} = \left\{\begin{array}{c} \dfrac{\partial u_{\lambda x}}{\partial x} \\ \dfrac{\partial u_{\lambda y}}{\partial y} \\ \dfrac{\partial u_{\lambda x}}{\partial y} + \dfrac{\partial u_{\lambda y}}{\partial x} \end{array}\right\} = \frac{i\omega}{C_{SV}} \exp\left[i\omega\left(t - \frac{x}{C_{SVx}}\right)\right] \left\{\begin{array}{c} -\dfrac{1}{2}\sin(2\theta) \\ \dfrac{1}{2}\sin(2\theta) \\ \cos(2\theta) \end{array}\right\}. \tag{2.83}$$

The following relationship between stresses and strains exists in elastic wave theory:

$$\{\sigma_0\} = [D]\{\varepsilon_0\}, \tag{2.84}$$

where $\{\sigma_0\}$ is a stress vector resulting only from u_λ on the fixed boundary (i.e. $Y = 0$); and $[D]$ is a constitutive matrix of the medium. For plane strain problems, this constitutive matrix can be expressed in the following matrix form:

$$[D] = \frac{E}{1+\nu}\begin{bmatrix} \dfrac{1-\nu}{1-2\nu} & \dfrac{\nu}{1-2\nu} & 0 \\ \dfrac{\nu}{1-2\nu} & \dfrac{1-\nu}{1-2\nu} & 0 \\ 0 & 0 & \dfrac{1}{2} \end{bmatrix}, \tag{2.85}$$

where E and ν are the modulus of elasticity (i.e. Young's modulus) and Poisson's ratio of the medium, respectively.

Substituting Eqs. (2.83) and (2.85) into Eq. (2.84) yields the following equation:

$$\{\sigma_0\} = \begin{Bmatrix} \sigma_{x0} \\ \sigma_{y0} \\ \tau_{xy0} \end{Bmatrix} = \frac{iE\omega}{2C_{SV}(1+\nu)} \exp\left[i\omega\left(t - \frac{x}{C_{SVx}}\right)\right] \begin{Bmatrix} -\sin(2\theta) \\ \sin(2\theta) \\ \cos(2\theta) \end{Bmatrix}. \quad (2.86)$$

In the frequency domain analysis, the term, $e^{i\omega t}$, can be omitted so that σ_{y0}^{SV} and τ_{xy0}^{SV} can be expressed as follows:

$$\sigma_{y0}^{SV} = \frac{iE\omega\sin(2\theta)}{2C_{SV}(1+\nu)} \exp\left(-i\frac{\omega}{C_{SVx}}x\right), \quad (2.87)$$

$$\tau_{xy0}^{SV} = \frac{iE\omega\cos(2\theta)}{2C_{SV}(1+\nu)} \exp\left(-i\frac{\omega}{C_{SVx}}x\right). \quad (2.88)$$

Considering Eqs. (2.70), (2.71), (2.87) and (2.88) yields the following generalized stress vector (in Eq. (2.50)) as a result of the plane SV-wave incidence on the wave input boundary (i.e. $Y = 0$):

$$\{\sigma\}^e = \begin{Bmatrix} \sigma_y^{SV} \\ \tau_{xy}^{SV} \end{Bmatrix} = -\frac{iE\omega}{C_{SV}} \exp\left(-i\frac{\omega}{C_{SVx}}x\right) \begin{Bmatrix} f_\sigma^{SV} \\ f_\tau^{SV} \end{Bmatrix}, \quad (2.89)$$

where f_σ^{SV} and f_τ^{SV} are the stress factors resulting from the plane SV-wave incidence. They can be expressed as follows:

$$f_\sigma^{SV} = -\frac{\sin(2\theta)}{2(1+\nu)}\left(1 + \beta_\sigma^{SV}\right), \quad (2.90)$$

$$f_\tau^{SV} = -\frac{\cos(2\theta)}{2(1+\nu)}\left(1 + \beta_\tau^{SV}\right). \quad (2.91)$$

2.3.2 *P-wave Incidence*

The same procedure can be used to derive the generalized stress vector resulting from a plane P-wave incidence. As shown in Fig. 2.7, a plane P-wave propagates from the far field of a system into the near field of the system and arrives at a fixed boundary (i.e. $Y = 0$). Before the incident P-wave reflects on the fixed boundary, the displacement field of the incident P-wave can be expressed as:

$$u_{\lambda x} = u_\lambda \sin\theta, \quad (2.92)$$

$$u_{\lambda y} = -u_\lambda \cos\theta. \quad (2.93)$$

Under the assumption that the incident plane P-wave is a harmonic wave with unit amplitude, the displacement of this incident wave can be written in the form:

$$u_\lambda = \exp\left[i\omega\left(1 - \frac{x}{C_{Px}} + \frac{y}{C_{Py}}\right)\right], \quad (2.94)$$

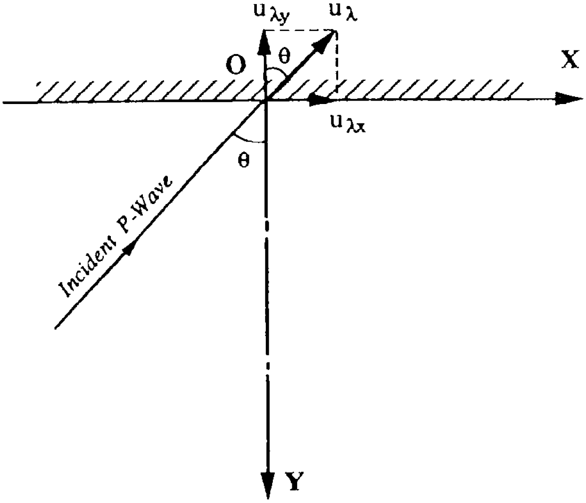

Fig. 2.7 Particle displacement on a fixed boundary for a P-wave incidence

where C_{Px} and C_{Py} are the apparent wave velocities of the incident plane P-wave in the x and y directions, respectively.

$$C_{Px} = \frac{C_P}{\sin\theta}, \tag{2.95}$$

$$C_{Py} = \frac{C_P}{\cos\theta}. \tag{2.96}$$

Elastic wave theory is used to determine the strain vector resulting only from the plane P-wave incidence on the fixed boundary (i.e. $Y = 0$):

$$\{\varepsilon_0\} = \begin{Bmatrix} \dfrac{\partial u_{\lambda x}}{\partial x} \\ \dfrac{\partial u_{\lambda y}}{\partial y} \\ \dfrac{\partial u_{\lambda x}}{\partial y} + \dfrac{\partial u_{\lambda y}}{\partial x} \end{Bmatrix} = \frac{i\omega}{C_P} \exp\left[i\omega\left(t - \frac{x}{C_{Px}}\right)\right] \begin{Bmatrix} -\sin^2\theta \\ -\cos^2\theta \\ \sin(2\theta) \end{Bmatrix}. \tag{2.97}$$

Substituting Eqs. (2.85) and (2.97) into Eq. (2.84) yields the following equation:

$$\{\sigma_0\} = \begin{Bmatrix} \sigma_{x0} \\ \sigma_{y0} \\ \tau_{xy0} \end{Bmatrix} = \frac{iE\omega}{C_P(1+\nu)} \exp\left[i\omega\left(t - \frac{x}{C_{SVx}}\right)\right] \begin{Bmatrix} -\dfrac{1-\nu}{1-2\nu}\left(\sin^2\theta + \dfrac{\nu}{1-\nu}\cos^2\theta\right) \\ -\dfrac{1-\nu}{1-2\nu}\left(\cos^2\theta + \dfrac{\nu}{1-\nu}\sin^2\theta\right) \\ \dfrac{1}{2}\sin(2\theta) \end{Bmatrix}. \tag{2.98}$$

If the analysis is carried out in the frequency domain, term $e^{i\omega t}$ is a common factor and can be omitted so that σ_{y0}^{P} and τ_{xy0}^{P} can be expressed as

$$\sigma_{y0}^{P} = -\frac{iE\omega(1-\nu)\left(\cos^2\theta + \frac{\nu}{1-\nu}\sin^2\theta\right)}{C_P(1+\nu)(1-2\nu)} \exp\left(-i\frac{\omega}{C_{SVx}}x\right), \tag{2.99}$$

$$\tau_{xy0}^{p} = \frac{iE\omega\sin(2\theta)}{2C_P(1+\nu)} \exp\left(-i\frac{\omega}{C_{SVx}}x\right). \tag{2.100}$$

Considering Eqs. (2.68), (2.69), (2.99) and (2.100) yields the following generalized stress vector (in Eq. (2.50)) as a result of the plane P-wave incidence on the wave input boundary (i.e. $Y = 0$):

$$\{\sigma\}^{e} = \begin{Bmatrix} \sigma_y^P \\ \tau_{xy}^P \end{Bmatrix} = -\frac{iE\omega}{C_P} \exp\left(-i\frac{\omega}{C_{SVx}}x\right) \begin{Bmatrix} f_\sigma^P \\ f_\tau^P \end{Bmatrix}, \tag{2.101}$$

where f_σ^P and f_τ^P are the stress factors resulting from the plane P-wave incidence. These stress factors can be expressed as

$$f_\sigma^P = \frac{(1-\nu)}{(1+\nu)(1-2\nu)}\left(\cos^2\theta + \frac{\nu}{1-\nu}\sin^2\theta\right)\left(1+\beta_\sigma^P\right), \tag{2.102}$$

$$f_\tau^P = -\frac{\sin(2\theta)}{2(1+\nu)}\left(1+\beta_\tau^P\right). \tag{2.103}$$

Although the stress factors expressed in Eqs. (2.90), (2.91), (2.102) and (2.103) are independent of the frequency of the incident wave, the resulting generalized stresses on the wave input boundary are dependent on the frequency of the incident wave. For a non-zero incident angle, θ, there exist phase differences along the wave input boundary. These phase differences are expressed by the exponential function terms in Eqs. (2.89) and (2.101).

Figure 2.8 shows the distribution of stress factors as a result of P-wave and SV-wave incidences. From the analytical results shown in this figure, it can be concluded that: (1) just like stress increase factors, stress factors on the wave input boundary are significantly dependent on the incident wave modes, wave incident angles and Poisson's ratio of the medium; (2) for a P-wave incidence, there exists a non-zero incident angle, θ, so that $f_\tau^P = 0$, indicating that no shear stress appears for this special incident angle because of wave-mode conversion on a fixed boundary; and (3) for vertical incidences of both, a P-wave and an SV-wave, $f_\tau^P = 0$ and $f_\sigma^{SV} = 0$, but the stress increase factors, β_τ^P and β_σ^{SV}, are not equal to zero (as shown in Fig. 2.5). This indicates that for a vertically incident P-wave, only normal stress appears on the wave input boundary, while for a vertically incident SV-wave, only shear stress appears on the wave input boundary. Thus, there is no wave mode conversion for vertically incident P-waves and SV-waves.

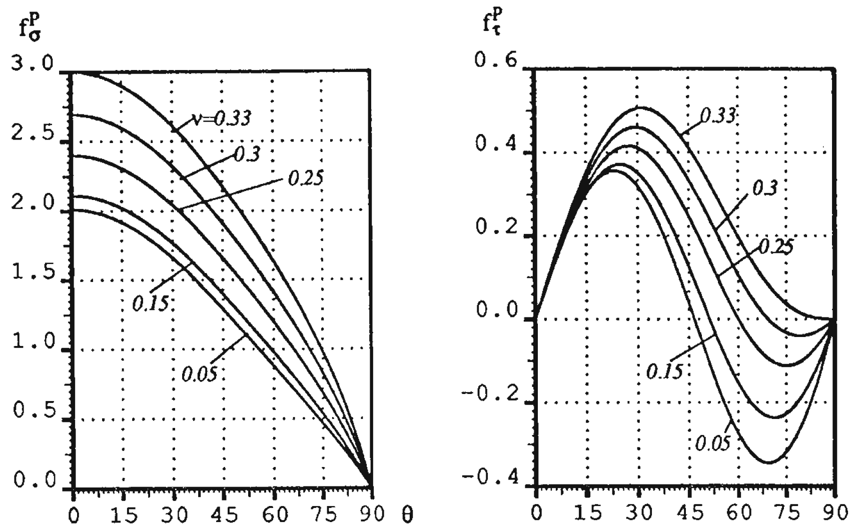

P-wave incidence

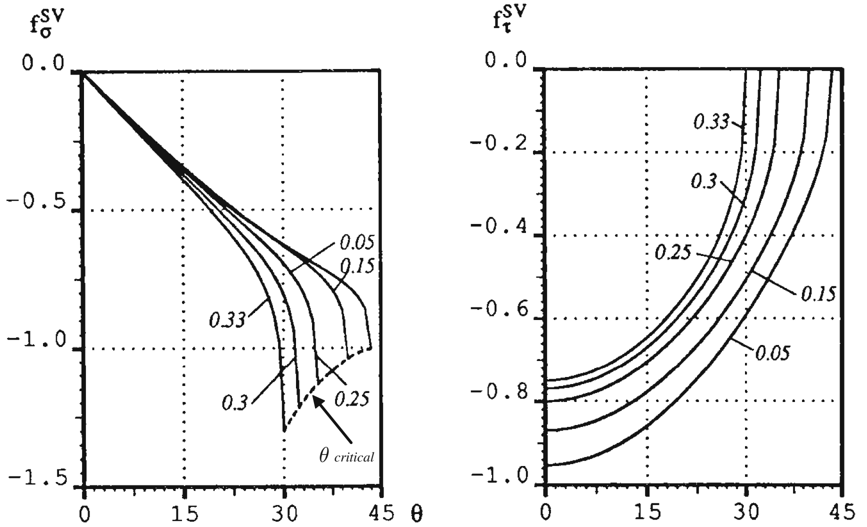

SV-wave incidence

Fig. 2.8 Distributions of stress factors arising from P-wave and SV-wave incidences on a fixed boundary: five different values of Poisson's ratio are considered in the figure

2.4 Verification of the Proposed Computational Model for Simulating Wave Scattering Problems in Infinite Media

Based on the proposed dynamic infinite element theory and wave input method, a computer program has been developed. As a result, the proposed computational model of finite elements and dynamic infinite elements can be used to investigate the dynamic responses of both a half-plane and a semi-circular canyon under P-wave and SV-wave incidences. Through comparison of the corresponding numerical results with theoretical results and Wong's analytical results (Wong 1982), the correctness and accuracy of the proposed computational model can be verified.

2.4.1 Wave Reflection on the Surface of an Elastic Half-Plane

To examine the correctness and accuracy of the proposed computational model for simulating wave scattering problems in infinite media, the reflection of both a plane harmonic SV-wave and a plane harmonic P-wave on the surface of an elastic half-plane is considered in this subsection. As shown in Fig. 2.9, the near field of the half-plane is simulated using eight-node isoparametric finite elements, while the far field is simulated by the proposed two-dimensional dynamic infinite elements. A horizontal line (i.e. $Y = 0$) is used as the wave input boundary. Both a unit plane harmonic SV-wave and a unit plane harmonic P-wave, which propagate vertically from the far field under the wave input boundary into the near field, are considered in the coupled computational model of finite elements and dynamic infinite elements. The wavenumbers of dynamic infinite elements are chosen as either SV-wavenumbers or P-wavenumbers, depending on the types of incident waves. For the purpose of investigating the effect of the wave input boundary length, modelled by finite elements, on the accuracy of the numerical results, three different lengths

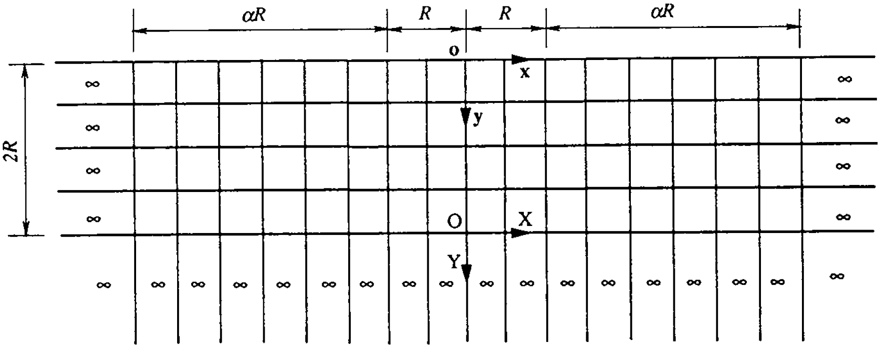

$(\alpha = 2, 3, 4)$

Fig. 2.9 Coupled model of finite and dynamic infinite elements for simulating wave reflection on the surface of a half-plane (i.e. α= 2, 3 and 4 in Fig. 2.9) are taken into account in the following computations. Since the sizes of the finite elements used in the near field can be determined by the size requirement criterion (Zienkiewicz 1977), no mesh refinement in the near field needs to be tested. However, to ensure the accuracy and convergence of the coupled computational model of finite elements and dynamic infinite elements, it is necessary to investigate the effect of the overall size of the near field on the numerical solutions. For α= 2, the near field and far field of the coupled computational model are simulated using 48 eight-node isoparametric elements and 22 dynamic infinite elements. When α= 4, they are simulated using 80 eight-node isoparametric elements and 30 dynamic infinite elements, respectively.

The following parameters are used for the computational model: the reference length of the problem (i.e. R) is 100 m; the elastic modulus of the medium (i.e. E) is 24×10^9Pa; the density of the medium (i.e. ρ) is 2400 kg m^{-3}; Poisson's ratio of the medium (i.e. ν) is $1/3$; the velocities of the P-wave and SV-wave in the medium are 3872 m s^{-1} and 1936 m s^{-1}, respectively.

Figure 2.10 shows the distribution of displacement amplitudes along the surface of the half-plane as a result of the vertical incidence of either a plane harmonic SV-wave or a plane harmonic P-wave. In this figure, A_U is the amplitude of the horizontal displacement on the surface of the half-plane, while A_V is the amplitude of the vertical displacement on the surface of the half-plane. For the vertical incidence of a unit plane harmonic SV-wave, the theoretical result indicates that the amplitude of horizontal displacement on the surface of the half-plane is identical to 2. Similarly, for the vertical incidence of a unit plane harmonic P-wave, the theoretical result indicates that the amplitude of the vertical displacement on the surface of the half-plane

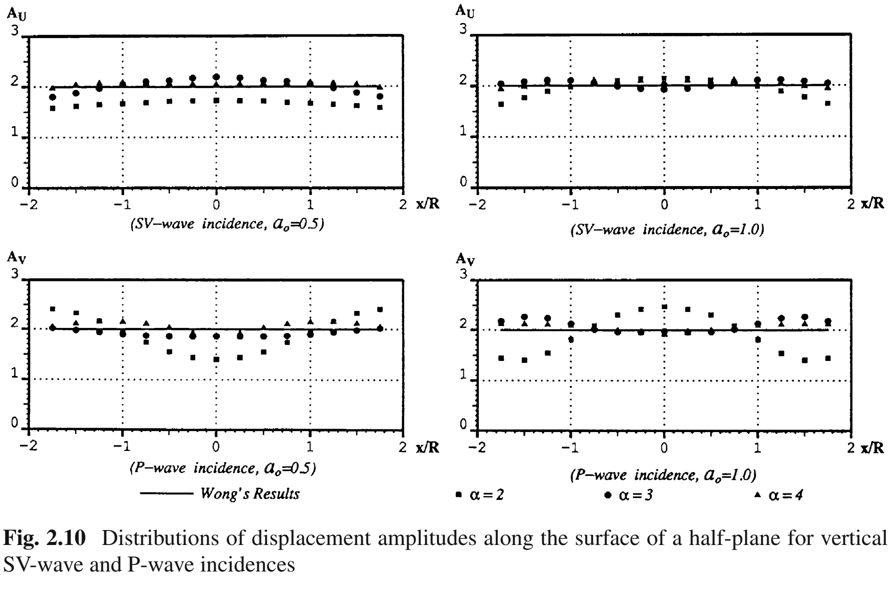

Fig. 2.10 Distributions of displacement amplitudes along the surface of a half-plane for vertical SV-wave and P-wave incidences

is also identical to 2. Note that a dimensionless frequency, $a_0 = \omega R/(\pi C_{SV})$, is used to show the numerical results in Fig. 2.10. Clearly, the related numerical results indicate that the wave input boundary length, which can be represented by α, has a significant effect on the accuracy of the numerical results. With the SV-wave vertical incidence and $a_0 = 0.5$ taken as an example, if $\alpha = 2$, the maximum relative error from the numerical results can reach 21%, while for $\alpha = 3$ and $\alpha = 4$, the maximum relative error can be reduced to 10 and 4%, respectively. The same phenomena can be observed from the numerical results when the P-wave vertical incidence and other different values of the dimensionless frequencies are considered in the computational model. This indicates that, so long as the wave input boundary modelled by finite elements is sufficiently long, accurate numerical results can be obtained from using the coupled computational model of finite elements and dynamic infinite elements for simulating wave scattering problems in infinite media.

2.4.2 Wave Scattering on the Surface of a Semi-circular Canyon

As the second example, a wave scattering problem on the surface of a semi-circular canyon is simulated using the proposed computational model of finite and dynamic infinite elements. For the purpose of verifying the computational model and the proposed wave input method, it is assumed that both a unit plane harmonic SV-wave and a unit plane harmonic P-wave propagate from the far field of a semi-circular canyon into the near field. Once the incident wave reaches the semi-circular canyon, it scatters and reflects on the surface of the semi-circular canyon. Since semi-analytical solutions are available for this problem (Wong 1982), the proposed computational model of finite and dynamic infinite elements can be verified through comparison of the current numerical solutions with Wong's semi-analytical solutions (Wong 1982). Figure 2.11 shows the computational model for simulating the wave scattering problem on the surface of a semi-circular canyon. In this computational model,

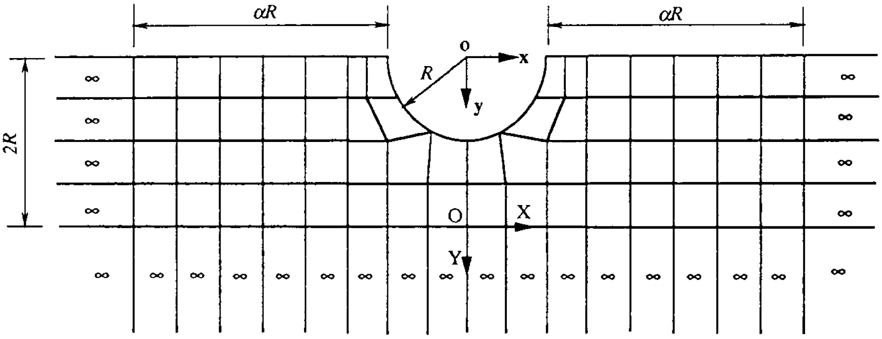

(α = 2, 3 ,4)

Fig. 2.11 Coupled model of finite and dynamic infinite elements for simulating wave scattering on the surface of a semi-circular canyon the near field of the semi-circular canyon is simulated using eight-node isoparametric finite elements, while the far field is simulated using two-dimensional dynamic infinite elements. A horizontal line (i.e. $Y = 0$) is used as the wave input boundary. The wavenumbers of the dynamic infinite elements are chosen as either SV-wavenumbers or P-wavenumbers, depending on the types of incident waves. The radius of the semi-circular canyon, which is equal to 100 m (i.e. $R = 100$ m), is defined as the reference length of this problem. Other material parameters of the

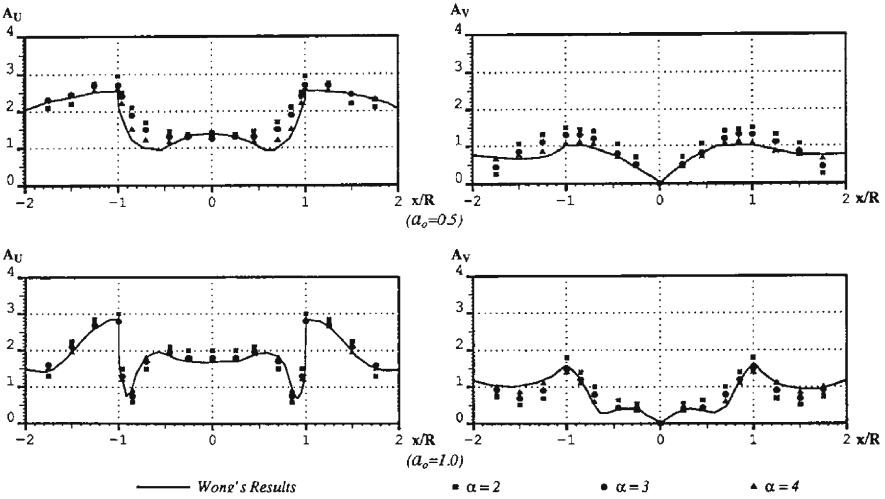

(A) $\theta=0°$

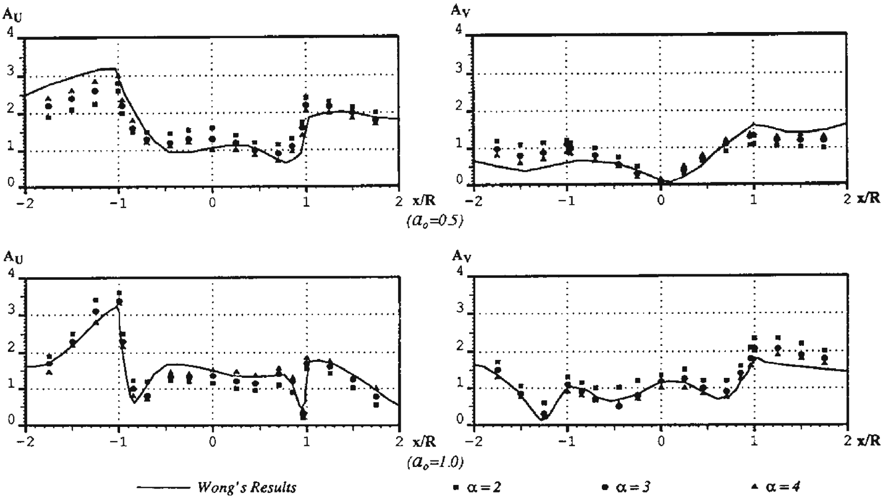

(B) $\theta=15°$

Fig. 2.12 Distributions of displacement amplitudes along the surface of a semi-circular canyon in the case of an SV-wave incidence: (**A**) $\theta = 0°$; (**B**) $\theta = 15°$

medium are the same as those used for the half-plane wave reflection problem in the previous subsection.

Figures 2.12 and 2.13 show the distributions of displacement amplitudes along the surface of the semi-circular canyon for cases of SV-wave and P-wave incidences. In these figures, a_0 is the dimensionless frequency; A_U and A_V are the amplitudes of displacements in the x and y directions, respectively. The related numerical results clearly indicate that the wave input boundary length, which is represented by α in the

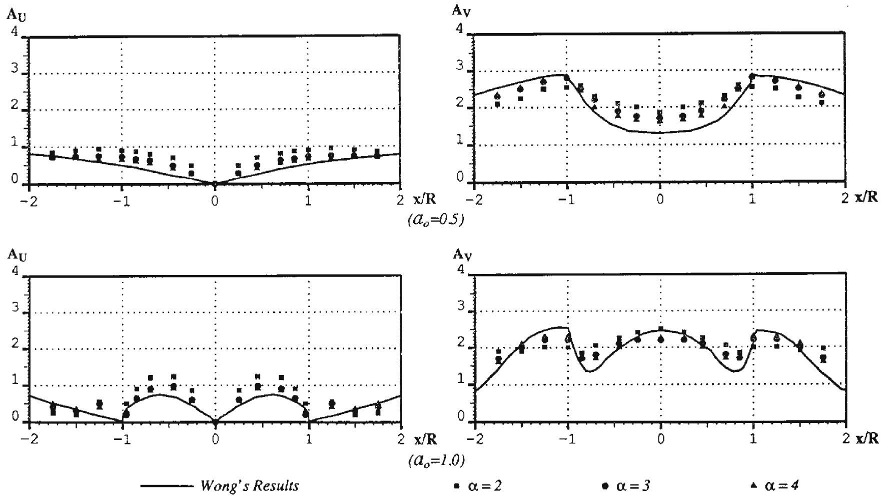

(A) $\theta = 0°$

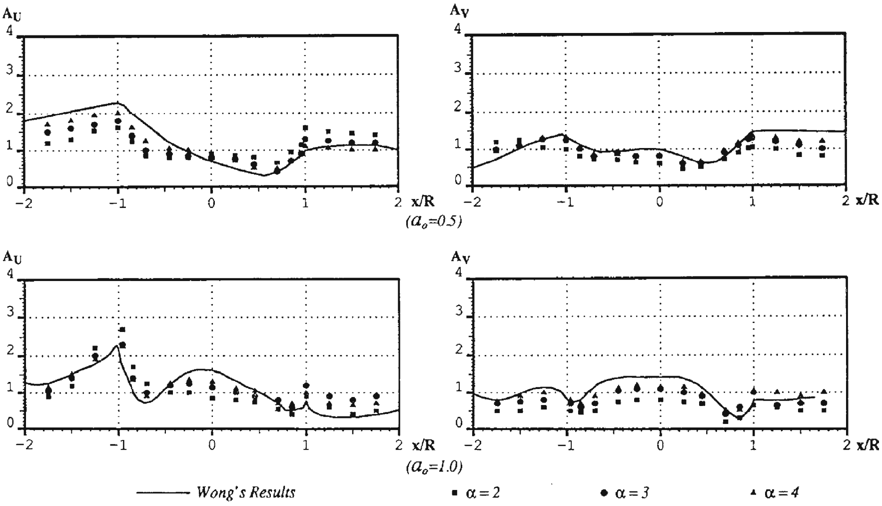

(B) $\theta = 60°$

Fig. 2.13 Distributions of displacement amplitudes along the surface of a semi-circular canyon for a P-wave incidence: (**A**) $\theta = 0°$; (**B**) $\theta = 60°$

computational model, has significant effects on the accuracy of the current numerical solutions. For $\alpha \geq 3$, the current numerical solutions are in good agreement with Wong's (1982) semi-analytical solutions, especially in the cases of SV-wave and P-wave vertical incidences. This is because the whole wave field of the system is dominated by the incident wave. For this reason, it is reasonable to use the wavenumber of the incident wave for dynamic infinite elements in the computational model. As expected, the current numerical solutions demonstrate that if the wave input boundary length modelled by using finite elements is long enough, the coupled computational model with the proposed wave input method can be used to produce accurate numerical solutions for simulating SV-wave and P-wave scattering problems in infinite media.

If the SV-wave incidence is vertical, vertical displacement components along the surface of a semi-circular canyon will be generated, even though only horizontal displacements are applied on the wave input boundary. This phenomenon is different from what was observed when the incident wave is an SH-wave (Zhang and Zhao 1988). For an SH-wave incidence, no wave-mode conversion occurs along the surface of a semi-circular canyon. However, since wave-mode conversion can occur for either SV-wave or P-wave oblique incidences on a surface, a similar phenomenon can be observed of the numerical solutions when the incident wave is a P-wave. For SV-wave and P-wave incidences, the displacement amplifications along the surface of a semi-circular canyon are significant, especially at the top corner of the semi-circular canyon.

2.4.3 Wave Scattering on the Surface of an Embankment Dam

The coupled computational model of finite elements and dynamic infinite elements can be used to simulate wave scattering and propagation mechanisms in heterogeneous media. To illustrate this point, the dynamic response of a 30-m high embankment dam under an SV-wave vertical incidence from the base rock is considered in this subsection. Figure 2.14 shows the geometry of this computational problem, in

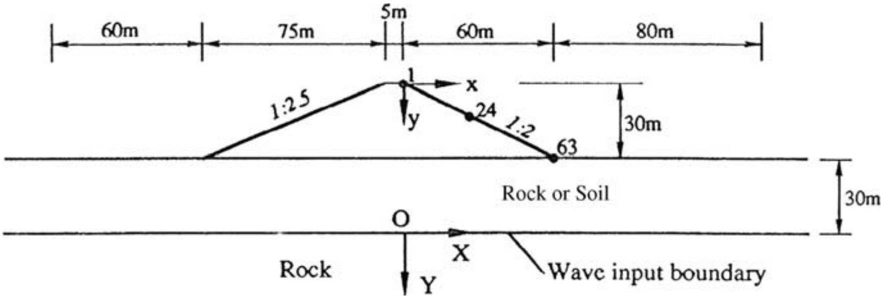

Fig. 2.14 Computational model for simulating wave scattering along the surface of an embankment dam: in the first case, the layer is comprised of rock; while in the second case, the layer is comprised of soil

which two cases are considered. In the first case the foundation of the embankment dam is comprised of a homogeneous elastic rock base, called the rock foundation, while in the second case the foundation of the embankment dam is comprised of a soil layer and a rock base, called the soil layer foundation.

The following parameters are used in the coupled computational model of finite elements and dynamic infinite elements. For both the soil embankment dam and the

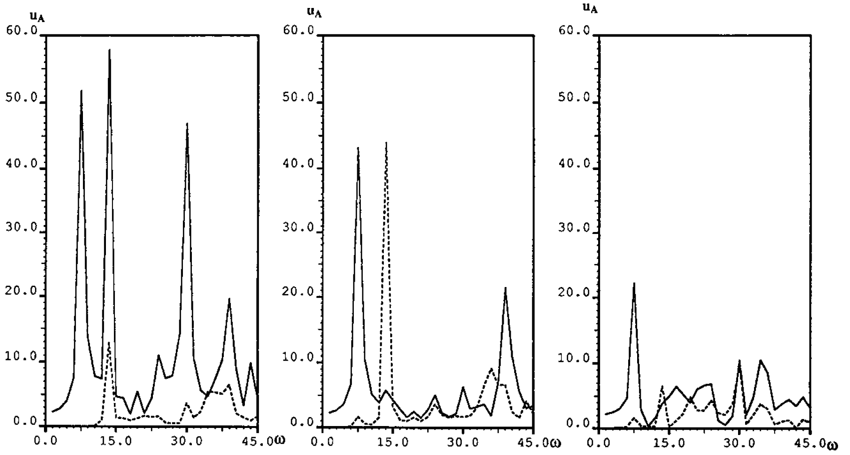

(a) Station 1 (b) Station 24 (c) Station 63

(A) Soil layer foundation

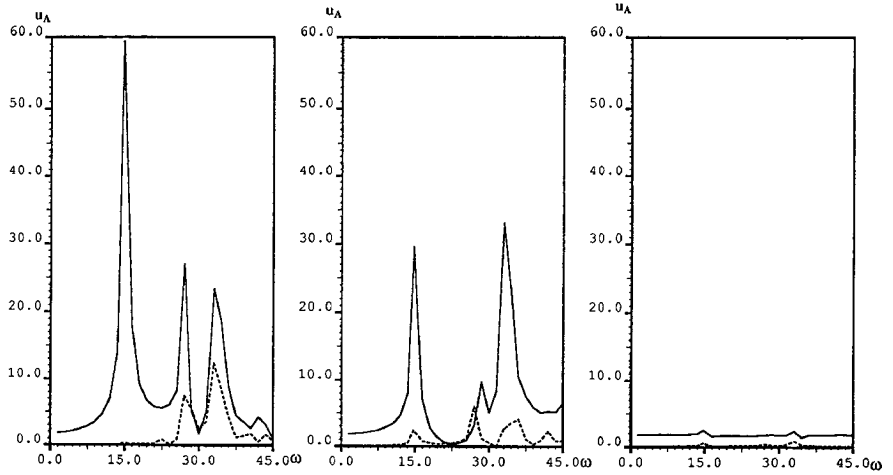

(a) Station 1 (b) Station 24 (c) Station 63

(B) Rock foundation

Fig. 2.15 Amplitude distributions of complex frequency functions for displacements of the dam: (**A**) soil layer foundation; (**B**) rock foundation. As shown in Fig. 2.14, Stations 1, 24 and 63 are located at the *top*, the *middle* and the *bottom* of the dam soil layer, the elastic modulus (E_s) is 0.252×10^9Pa; the value of Poisson's ratio (ν_s) is 0.3 and the density (ρ_s) is 2000 kg m^{-3}. For the rock, the elastic modulus (E_r) is 28.8×10^9Pa; Poisson's ratio (ν_r) is 0.2 and the density (ρ_r) is 2400 kg m^{-3}. To apply the incident SV-wave from the far field, a horizontal line ($Y = 0$) is used as the wave input boundary. From a structural dynamic analysis point of view, the complex frequency response function can be used to represent the dynamic response of the embankment dam. In this regard, a unit vertically incident harmonic SV-wave is applied on the wave input boundary of the computational model.

Figure 2.15 shows the amplitudes of the complex frequency response functions for the displacements of the embankment dam, which is located on the soil layer foundation and the rock foundation, respectively. In these two figures, solid lines and dashed lines represent the horizontal and vertical displacements of the embankment dam. Three different stations (i.e. stations 1, 24 and 63 shown in Fig. 2.14) are located at the top, the middle and the bottom of the embankment dam. For the rock foundation, the fundamental frequency of the dam–foundation system is 13.5 rad s^{-1}, whereas for the soil layer foundation, the fundamental frequency of the dam–foundation system is 7.5 rad s^{-1}. Compared with the dynamic response curve of the dam–rock foundation system, the dynamic response curve of the dam–soil layer–foundation system has more peaks because of the reflection and refraction of waves within the soil layer. For the rock foundation, the amplitude of the complex frequency response function at the dam–foundation interface (i.e. station 63 shown in Fig. 2.14) approaches a constant value, except for the resonance frequencies of the system. However, for the soil layer foundation, the dynamic response at the dam–foundation interface is very complicated, indicating that the effect of the dam–foundation interaction becomes stronger as the foundation of the embankment dam becomes softer. Generally, the dynamic response at the top (i.e. station 1 shown in Fig. 2.14) of the embankment dam is much stronger than that at the bottom (i.e. station 63) of the embankment dam. Although only horizontal displacements are applied on the wave input boundary of the computational model, vertical displacements appear in the dynamic response of an embankment dam because of the wave scattering effect of the embankment dam.

Chapter 3
Application of Two-Dimensional Dynamic Infinite Elements: Simulation of Dynamic Dam–Water–Foundation Interaction Problems

3.1 Simulation of Dynamic Gravity Dam–Water–Foundation Interaction Systems

Extensive studies on the dynamic response of concrete gravity dams due to earthquake loadings have demonstrated that their dynamic response is mainly affected by the following factors: (1) the interaction between the dam and impounded reservoir water (Chopra 1968; Chakarbarti and Chopra 1974; Liam-Finn et al. 1977); (2) the compressibility of the impounded water (Chopra and Gupta 1982); (3) the interaction between the dam and the foundation rock (Liam-Finn et al. 1977; Liam-Finn and Varoglu 1972a, b, 1975); and (4) the materials at the reservoir bottom (Hall and Copra 1982; Fenves and Chopra 1983, 1984, 1985; Lotfi et al. 1987; Medina et al. 1990). By means of a substructure method, Chopra and his colleagues considered the above factors and made some interesting conclusions on the dynamic response of concrete gravity dams due to earthquake loadings (Chopra 1968; Chakarbarti and Chopra 1974; Hall and Copra 1982; Fenves and Chopra 1983, 1984, 1985). Because of limitations of the substructure method, in which analytical solutions need to be employed to simulate an infinite reservoir in the upstream direction of a gravity dam–water–foundation system, materials at the reservoir bottom were assumed to have zero thickness. However, in certain circumstances such as the concrete gravity dams built in the Yellow River valley, China, not only materials at a reservoir bottom have considerable thicknesses, but also sediments at the reservoir bottom are comprised of very soft clay materials. Although some basic studies have been carried out to investigate how reservoir bottom sediments affect the dynamic response of concrete gravity dams (Medina et al. 1990; Zhao 1994), further studies are needed to investigate the detailed dynamic mechanisms associated with the effect of reservoir bottom sediments on the dynamic response of such dams. In view of this fact, a more realistic computational model, which is capable of including both the gravity dam–water–foundation interaction effect and the reservoir bottom sediment effect simultaneously, was developed (Valliappan and Zhao 1992; Zhao et al. 1995). In this computational model, a finite and dynamic infinite element coupling technique is used to simulate a whole gravity dam–water–foundation system, including the reservoir bottom sediment effect. Since reservoir bottom sediments may comprise

C. Zhao, *Dynamic and Transient Infinite Elements*, Advances in Geophysical and Environmental Mechanics and Mathematics, DOI 10.1007/978-3-642-00846-7_3,

very soft clay materials, it is assumed that they can be treated as visco-elastic solid materials in the corresponding computational models.

The main purpose of this section is to use a coupled computational model of finite and dynamic infinite elements for investigating the effects of reservoir bottom sediments on the dynamic response of concrete gravity dams. Since the coupled computational model keeps all the advantages of the conventional finite element method, the complicated geometries, complex physical and mechanical properties of a gravity dam–water–foundation system, including the reservoir bottom sediment effect, can be straightforwardly considered in the corresponding computational simulations. In addition, the use of dynamic infinite elements allows the infinite extension of both the reservoir and the foundation of a concrete gravity dam to be simulated more reasonably for the dynamic analysis of a gravity dam–water–foundation system. To examine how reservoir bottom sediments affect the dynamic response of a concrete gravity dam, their thickness, softness and damping are considered as the main parameters in the following parametric studies. Since the soft layer of reservoir bottom sediments has a significant amplification effect on an incident acceleration wave from the underlying rock, the amplitude of the acceleration wave at the water–sediment interface is much greater than that of the corresponding free-field motion, especially when the layer of reservoir bottom sediments is thick and soft. Consideration of the amplification effect of an incident earthquake wave due to reservoir bottom sediments makes this study different from the previous work (Hall and Copra 1982; Fenves and Chopra 1983, 1984, 1985; Lotfi et al. 1987; Medina et al. 1990). The free-field motion on the surface of an elastic half-plane is double the value of an incident wave under the assumption of either a P-wave or an SV-wave vertical incidence from the far field of the elastic half-plane (Graff 1975; Zhao et al. 1992; Zhao and Valliappan 1993a, b). Although wave energy, to some extent, can be dissipated (absorbed) by the damping of reservoir bottom sediments so as to reduce the dynamic response of a concrete gravity dam, the amplified acceleration at the water–sediment interface may result in a considerable increase in the dynamic response of the concrete gravity dam. Thus, the physical and mechanical properties of reservoir bottom sediments, which are considered approximately in the previous studies (Hall and Copra 1982; Fenves and Chopra 1983, 1984, 1985), can be simulated more reasonably and realistically using the coupled computational model of finite and dynamic infinite elements.

3.1.1 Computational Model of a Concrete Gravity Dam–Water–Foundation System Including Reservoir Bottom Sediments

At the bottom of a reservoir in the upstream direction of a concrete gravity dam, there usually exist highly variable layers of exposed bedrock, alluvium, silt, clay and other sedimentary materials. These sediments may be deposited to a significant thickness in some rivers over a long period of time before a concrete gravity dam is constructed. Generally, once the concrete gravity dam is put into operation, sediments can continue to be deposited at the reservoir bottom of the concrete gravity dam, especially when the latter is located in a river with more sediments and sands. During operation of the reservoir, the thickness of the reservoir bottom sediments increases gradually and may approach a constant value because sand-sluices are usually constructed in the dam system. As reservoir bottom sediments are complex and variable for most rivers, some simplification about their characteristics needs to be made in the computational model. Figure 3.1 shows the conceptual model of a gravity dam–water–foundation system, including reservoir bottom sediments. When reservoir bottom sediments are treated as visco-elastic solid materials, the whole gravity dam–water–foundation system can be divided into a water region, Ω_W, and a solid region, Ω_S. An interface between the water region and the solid region is defined as Γ_{WS}. Since the governing equations for the water region are different from those for the solid region, these two regions need to be considered separately in the process of deriving the formulations for the computational model. The solid region can be further divided into the following three subregions: a sediment subregion, Ω_{S1}, a dam subregion, Ω_{S2} and a foundation subregion, Ω_{S3}. Although these three subregions may have different geometrical shapes and material properties, their governing equations are exactly the same, according to elastic wave motion theory. Since both the water region and the solid region extend to infinity, the coupled computational model of finite and dynamic infinite elements (Saini et al. 1978; Chow and Smith 1981; Medina and Taylor 1983; Zhao 1987; Zhang and Zhao 1987, 1988; Zhao et al. 1987, 1989, 1992, 1995; Zhao and Valliappan 1991, 1993a, b, c, d, e) is more suitable for simulating this problem.

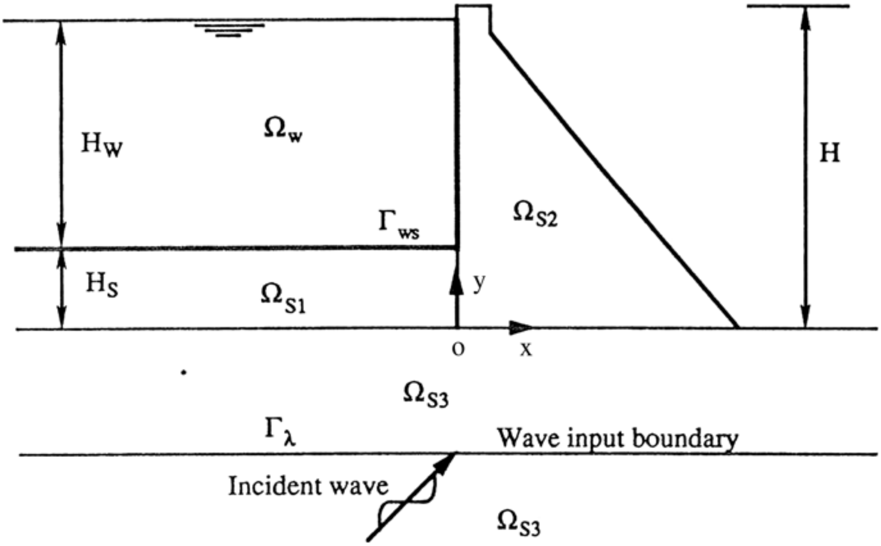

Fig. 3.1 Geometry of the concrete gravity dam–water–foundation system including reservoir bottom sediments

3.1.1.1 Computational Simulation of the Water Region

For the water region, the wave equation can be expressed as follows:

$$\frac{\partial^2 p}{\partial x^2} + \frac{\partial^2 p}{\partial y^2} = \frac{1}{C_W^2}\frac{\partial^2 p}{\partial t^2}, \tag{3.1}$$

where p is the pressure in the water region; C_W is the wave velocity of water. If the reservoir is full, the corresponding boundary conditions can be written in the following form:

$$p = 0 \qquad (\text{on}\, y = H), \tag{3.2}$$

$$\frac{\partial p}{\partial n} = -\rho_W \frac{\partial^2 u_n}{\partial t^2} \qquad (\text{on } \Gamma_{WS}), \tag{3.3}$$

where ρ_W is the density of water; n represents the direction normal to the boundary, Γ_{WS}; and u_n is the displacement in the n direction.

By means of the Galerkin weighted-residual method, the discretized equation of motion for the water region can be expressed as follows:

$$\left(-\omega^2 [Q] + [H]\right)\{P\} = \{B\}, \tag{3.4}$$

where ω is the circular frequency of excitation; $[Q]$, $[H]$ and $\{B\}$ are the property matrices and vector for the water region. The elements in these property matrices and vector can be evaluated using the following equations:

$$H_{ij} = \sum\nolimits_e h_{ij}, \tag{3.5}$$

$$Q_{ij} = \sum\nolimits_e q_{ij}, \tag{3.6}$$

$$B_i = \sum\nolimits_e b_i, \tag{3.7}$$

where $\sum_e$ implies a summation over all elements in the water region. From a computational point of view, h_{ij}, q_{ij} and b_i can be expressed as follows:

$$h_{ij} = \int_A \left[\frac{\partial N_i'}{\partial x}\frac{\partial N_j'}{\partial x} + \frac{\partial N_i'}{\partial y}\frac{\partial N_j'}{\partial y}\right] dA, \tag{3.8}$$

$$q_{ij} = \frac{1}{C_W^2}\int_A \left[N_i' N_j'\right] dA, \tag{3.9}$$

$$b_i = \int_{S_W} \left[N_i' \frac{\partial p}{\partial n}\right] dS_W, \tag{3.10}$$

where N_i' is the shape function for the water element; A and S_W are, respectively, the area of the water element and the contact length between water and solid for the water element.

Equation (3.4) can be rewritten in the following partition form:

$$\begin{bmatrix} [E_{11}] & [E_{12}] \\ [E_{21}] & [E_{22}] \end{bmatrix} \begin{Bmatrix} \{P_{WS}\} \\ \{P_I\} \end{Bmatrix} = \begin{Bmatrix} \{B_{WS}\} \\ \{0\} \end{Bmatrix}, \tag{3.11}$$

where $\{P_{WS}\}$ and $\{P_1\}$ are the nodal pressure vectors corresponding to the water–solid interface and the interior domain of the water region, respectively; $\lfloor E_{ij} \rfloor$ and $\{B_{WS}\}$ are, respectively, the corresponding property matrix and vector for the water region and the water–solid interface.

Using the dynamic condensation technique, the nodal pressure vector on the water–solid interface can be expressed as follows:

$$\{P_{WS}\} = [E_C]^{-1} \{B_{WS}\}, \tag{3.12}$$

$$[E_C] = [E_{11}] - [E_{12}] [E_{22}]^{-1} [E_{21}]. \tag{3.13}$$

3.1.1.2 Computational Simulation of the Solid Region

For the solid region, assuming the solid material is of hysteretic damping and neglecting the body force of the solid medium, the corresponding wave equations of motion can be expressed in the following form:

$$G^* \left(\frac{\partial^2 u}{\partial x^2} + \frac{\partial^2 u}{\partial y^2} \right) + (\lambda^* + G^*) \left(\frac{\partial^2 u}{\partial x^2} + \frac{\partial^2 v}{\partial x \partial y} \right) = \rho \frac{\partial^2 u}{\partial t^2}, \tag{3.14}$$

$$G^* \left(\frac{\partial^2 v}{\partial x^2} + \frac{\partial^2 v}{\partial y^2} \right) + (\lambda^* + G^*) \left(\frac{\partial^2 u}{\partial x \partial y} + \frac{\partial^2 v}{\partial y^2} \right) = \rho \frac{\partial^2 v}{\partial t^2}, \tag{3.15}$$

$$G^* = (1 + i\eta_d)G, \qquad \lambda^* = (1 + i\eta_d)\lambda, \tag{3.16}$$

where G is the shear modulus; λ is the Lamé constant; η_d is the hysteretic damping coefficient of the solid medium; u and v are the displacements of the solid medium in the x and y directions; ρ is the density of the solid medium.

Equations (3.14) and (3.15) can be discretized using the coupled computational method of finite and dynamic infinite elements. As a result, the discretized equation of motion for the solid region can be expressed as

$$\left(-\omega^2 [M] + (1 + i\eta_d) [K] \right) \{\Delta\} = \{F_0\}, \tag{3.17}$$

where $[M]$ and $[K]$ are the global mass and stiffness matrices of the solid region, respectively; $\{\Delta\}$ is the global nodal displacement vector of the solid region; $\{F_0\}$

is the amplitude vector of the input harmonic load. These matrices and vector can be evaluated by assembling the corresponding elemental property matrices and vectors of the solid region (Zhao et al. 1989, 1992, 1995; Zhao and Valliappan 1991, 1993a, b, c, d).

To derive the coupling equation between the solid region and the water region, Eq. (3.7) is rewritten in the following partition form:

$$\left(-\omega^2\begin{bmatrix}[M_{WW}] & [M_{W\lambda}] & [M_{WO}]\\ [M_{\lambda W}] & [M_{\lambda\lambda}] & [M_{\lambda O}]\\ [M_{OW}] & [M_{O\lambda}] & [M_{OO}]\end{bmatrix}+(1+i\eta_d)\begin{bmatrix}[K_{WW}] & [K_{W\lambda}] & [K_{WO}]\\ [K_{\lambda W}] & [K_{\lambda\lambda}] & [K_{\lambda O}]\\ [K_{OW}] & [K_{O\lambda}] & [K_{OO}]\end{bmatrix}\right)\begin{Bmatrix}\{\Delta_W\}\\ \{\Delta_\lambda\}\\ \{\Delta_O\}\end{Bmatrix}=\begin{Bmatrix}\{P_W\}\\ \{P_\lambda\}\\ \{0\}\end{Bmatrix}, \tag{3.18}$$

where $\{\Delta_W\}$, $\{\Delta_\lambda\}$ and $\{\Delta_O\}$ are the nodal displacement vectors corresponding to the water–solid interface, the wave input boundary (Γ_λ) and the rest of the solid region, respectively. Submatrices in the global mass matrix $[M]$ and global stiffness matrix $[K]$ are related to vectors $\{\Delta_W\}$, $\{\Delta_\lambda\}$ and $\{\Delta_O\}$. $\{P_\lambda\}$ is the driving force vector due to an incident wave and can be evaluated from elastic wave theory (Zhao et al. 1992; Valliappan and Zhao 1992; Zhao and Valliappan 1993a, b). $\{P_W\}$ is the coupling force vector on the water–solid interface.

3.1.1.3 Determination of the Coupling Force between the Water and the Solid Regions

In previous subsections, the equations of motion (i.e. Eqs. (3.11) and (3.18)) for both the water region and the solid region have been derived independently. Since there is an interaction effect between the water region and the solid region, these equations of motion cannot be solved directly. For example, in Eq. (3.11), the vector $\{B_{WS}\}$ depends on the displacement of the solid region, while in Eq. (3.18), the vector $\{P_W\}$, in turn, depends on the pressure acting on the water–solid interface. Thus, in order to obtain solutions for either the water region or the solid region, Eqs. (3.11) and (3.18) need to be solved simultaneously.

As shown in Fig. 3.2, if it is assumed that the water–solid interface is simulated using a three-node line element, which is, in fact, a side of an eight-node isoparametric finite element, a pressure–displacement relationship on this interface can be determined as follows.

For the reservoir water, the following equation holds:

$$\ddot{u}_n=\frac{\partial^2 u_n}{\partial t^2}=\frac{\partial^2 u}{\partial t^2}\sin\alpha-\frac{\partial^2 v}{\partial t^2}\cos\beta=m\frac{\partial^2 u}{\partial t^2}-l\frac{\partial^2 v}{\partial t^2}, \tag{3.19}$$

where $\ddot{u}_n$ is the acceleration in the normal direction of the water–solid interface; $\ddot{u}=\partial^2 u/(\partial t^2)$ and $\ddot{v}=\partial^2 v/(\partial t^2)$ are the accelerations in the x and y directions,

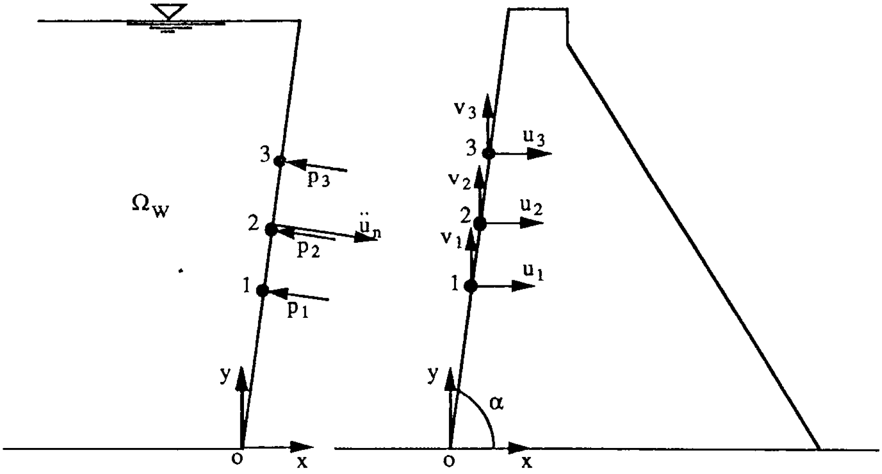

Fig. 3.2 Interaction effect on the water–solid interface

respectively. For a three-node (water) element, these accelerations can be expressed, at the element level, as follows:

$$\left\{\begin{matrix}\ddot{u}\\ \ddot{v}\end{matrix}\right\}^e = \left[[N_{S1}]\ [N_{S2}]\ [N_{S3}]\right]\left\{\ddot{\Delta}_W\right\}^e = [N_S]\left\{\ddot{\Delta}_W\right\}^e, \tag{3.20}$$

where $\left\{\ddot{\Delta}_W\right\}^e$ is the acceleration vector of the element; $[N_S]$ is the displacement shape function matrix of the element. Submatrix $[N_{Si}]$ in matrix $[N_S]$ can be written in the form:

$$[N_{Si}] = \begin{bmatrix} N_i & 0 \\ 0 & N_i \end{bmatrix} \qquad (i = 1{,}2{,}3). \tag{3.21}$$

Substituting Eqs. (3.3), (3.19) and (3.20) into Eq. (3.10) yields the following element vector, $\{B_{WS}\}^e$, on the water–solid interface:

$$\{B_{WS}\}^e = -\rho_W\,[L]^e\left\{\ddot{\Delta}_W\right\}^e, \tag{3.22}$$

$$[L]^e = \int_{S_W}\left([N_W]^T\,[m\ -l]\,[N_S]\right)dS_W, \tag{3.23}$$

where $[L]^e$ is a matrix expressing the pressure–displacement relation on the water–solid interface. $[N_W]$ is the following pressure shape function of the water element:

$$[N_W] = [N_1 \quad N_2 \quad N_3]. \tag{3.24}$$

By assembling the element vector $\{B_{WS}\}^e$ on the water–solid interface, the global matrix $\{B_{WS}\}$ on this interface can be expressed as

$$\{B_{WS}\} = -\rho_W\,[L]\left\{\ddot{\Delta}_W\right\}. \tag{3.25}$$

Substituting Eq. (3.25) into Eq. (3.12) yields

$$\{P_{WS}\} = -\rho_W [E_C]^{-1} [L] \left\{\ddot{\Delta}_W\right\}. \tag{3.26}$$

Consequently, the equivalent nodal force of the element on the water–solid interface can be derived as

$$\{P_W\}^e = \left([L]^e\right)^T \{P_{WS}\}^e. \tag{3.27}$$

Similarly, assembling the equivalent nodal force vector for all the elements on the water–solid interface yields the global vector on this interface in the form:

$$\{P_W\} = [L]^T \{P_{WS}\} = \omega^2 \rho_W [L]^T [E_C]^{-1} [L] \{\Delta_W\}. \tag{3.28}$$

Note that the relation

$$\left\{\ddot{\Delta}_W\right\} = -\omega^2 \{\Delta_W\} \tag{3.29}$$

was used to derive the above equation. Substituting Eq. (3.29) into Eq. (3.18) yields the coupling equation between the water and the solid regions:

$$\left(-\omega^2 \begin{bmatrix} \left[M^*_{WW}\right] & [M_{W\lambda}] & [M_{WO}] \\ [M_{\lambda W}] & [M_{\lambda\lambda}] & [M_{\lambda O}] \\ [M_{OW}] & [M_{O\lambda}] & [M_{OO}] \end{bmatrix} + (1 + i\eta_d) \begin{bmatrix} [K_{WW}] & [K_{W\lambda}] & [K_{WO}] \\ [K_{\lambda W}] & [K_{\lambda\lambda}] & [K_{\lambda O}] \\ [K_{OW}] & [K_{O\lambda}] & [K_{OO}] \end{bmatrix}\right) \begin{Bmatrix} \{\Delta_W\} \\ \{\Delta_\lambda\} \\ \{\Delta_O\} \end{Bmatrix} = \begin{Bmatrix} \{0\} \\ \{P_\lambda\} \\ \{0\} \end{Bmatrix}, \tag{3.30}$$

$$\left[M^*_{WW}\right] = [M_{WW}] + \rho_W [L]^T [E_C]^{-1} [L]. \tag{3.31}$$

Note that since the total values of the nodal displacement vectors $\{\Delta_W\}$, $\{\Delta_\lambda\}$ and $\{\Delta_O\}$ are used as fundamental variables in Eq. (3.30), the interaction effect between the water and solid regions can be simulated using frequency-dependent masses on the water–solid interface in the coupled computational model of finite and dynamic infinite elements. This differs from the conventional dynamic analysis of concrete gravity dam–water–foundation systems (Hall and Copra 1982; Fenves and Chopra 1983, 1984, 1985), in which the relative values of nodal displacements of a discretized system is used as fundamental variables, so that the free-field motion can be employed to describethe input earthquake acceleration wave on interfaces between the dam and the foundation as well as between the reservoir water and the foundation.

3.1.2 *Effects of Reservoir Bottom Sediments on the Dynamic Response of Concrete Gravity Dams due to Unit Harmonic Wave Incidences*

Reservoir bottom sediments can be characterized by the following parameters: the thickness, Poisson's ratio and the damping coefficient of the sediments. Since each of these parameters may have different effects on the dynamic response of concrete gravity dams, it is necessary to consider each of them separately, so that the dynamic mechanisms associated with how reservoir bottom sediments affect the dynamic response of concrete gravity dams can be recognized. From this point of view, a concrete gravity dam, which is comprised of a homogeneous and isotropic material and is founded on an elastic half-plane, is considered in this subsection. As the complex frequency response function of a dam body is capable of representing the dynamic behaviour of the dam–water–foundation system, including reservoir bottom sediments, both a unit acceleration harmonic P-wave and a unit acceleration harmonic SV-wave are used as incident waves on the wave input boundary of the computational model (Zhao et al. 1992, 1995; Zhao and Valliappan 1993a, b). For ease of making comparison with previous studies (Hall and Copra 1982; Fenves and Chopra 1983, 1984, 1985), these incident acceleration waves are assumed to propagate vertically from the far field to the near field of the dam–water–foundation system.

Figure 3.3 shows the coupled computational model of finite and dynamic infinite elements for simulating the dam–water–foundation system. An incident unit

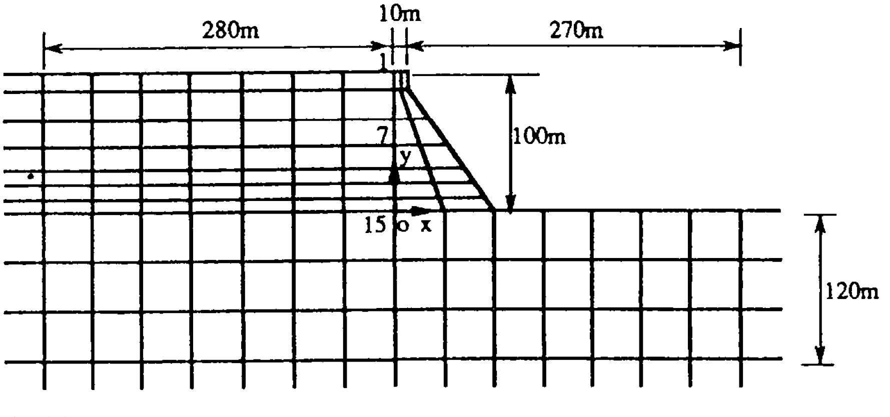

Fig. 3.3 Computational model of the concrete gravity dam–water–foundation system: the near field is simulated using finite elements, while the far field is simulated using dynamic infinite elements

harmonic wave, which is either an SV-wave or a P-wave, is applied to the wave input boundary (i.e. a horizontal line) within the computational model. A detailed explanation of the wave input method can be found in Chap. 2. The following parameters are used for the coupled computational model. For the concrete gravity dam and rock foundation, the elastic modulus is 28.8×10^9 Pa; the value of Poisson's ratio is 0.2; the density of the concrete and rock is $2400\,\mathrm{kg\,m^{-3}}$; the corresponding shear-wave velocity in the dam and rock foundation is $2236\,\mathrm{ms^{-1}}$. For the reservoir water, the density is $2400\,\mathrm{kg\,m^{-3}}$; the corresponding P-wave velocity is $1436\,\mathrm{m\,s^{-1}}$. For the reservoir bottom sediment, different parameters, which are given in the following subsections, are used to investigate their effects on the dynamic response of the dam–water–foundation system. To facilitate the investigations of the effects of reservoir bottom sediments, a dam–foundation without reservoir water (i.e. an empty reservoir) is used as a basic problem for comparison.

Figure 3.4 shows the amplitude distributions of the complex frequency response function for the acceleration of the concrete gravity dam at three different stations, namely stations 1, 7 and 15 shown in Fig. 3.3. These three stations are located at the top (i.e. station 1), the middle (i.e. station 7) and the bottom (i.e. station 15) of the dam. In this figure, $\ddot{u}_A$ and $\ddot{v}_A$ are the acceleration amplitudes in the horizontal and vertical directions, respectively. Since a unit acceleration wave is used as the incident wave, the acceleration shown in Fig. 3.4 can be viewed as dimensionless. It is clear that there is a response peak occurring at station 1 when $\omega \approx 20\,\mathrm{rad\,s^{-1}}$, indicating that the predominant circular frequency of the concrete gravity dam is about $20\,\mathrm{rad\,s^{-1}}$. As the current numerical results are very similar to the previous

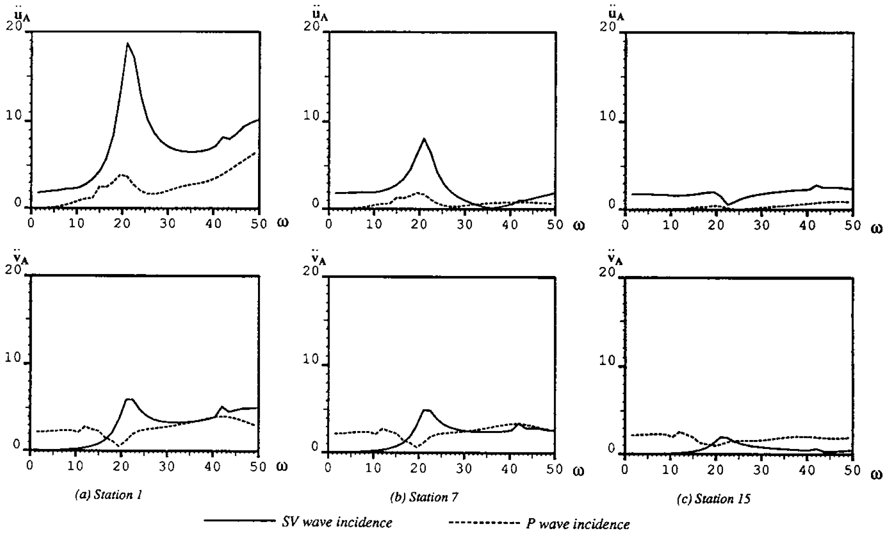

(a) Station 1 (b) Station 7 (c) Station 15

Fig. 3.4 Amplitude distributions of the complex frequency response function for the acceleration of the concrete gravity dam (empty reservoir): the peak value of the dynamic response at station 1 shows that the predominant circular frequency of the system is about 20 rad $\mathrm{s^{-1}}$.

results (Hall and Copra 1982; Fenves and Chopra 1983, 1984, 1985), the coupled computational model of finite and dynamic infinite elements is suitable for dealing with concrete dam–foundation interaction problems. Since absolute accelerations at the nodes of elements in the coupled computational model are used as fundamental variables, the dynamic response of the concrete dam is expressed using the absolute acceleration, which includes both the ground acceleration and the relative acceleration (to the ground surface) for a given nodal point in the coupled computational model. For the unit harmonic acceleration wave of a vertical incident angle propagating in an elastic half-plane, the value of the resulting acceleration is doubled on the surface of the elastic half-plane due to the reflection of the incident wave. This double-valued acceleration on the surface of the elastic half-plane, which is called the free-field motion, is the equivalent ground acceleration applied to the computational model. Note that this equivalent ground acceleration was used as the input acceleration in the previous analysis (Hall and Copra 1982; Fenves and Chopra 1983, 1984, 1985). If the value of the ground acceleration, which is equal to two in this situation, is subtracted from the current numerical results, the relative acceleration for the dynamic response of the concrete gravity dam can be obtained from the current computational model. Nevertheless, for the purpose of investigating the dynamic response of a concrete gravity dam–water–foundation system, either the absolute acceleration or the relative acceleration can be used as the fundamental variable, only depending on the wave input method employed in the computational model.

3.1.2.1 Effects of Sediment Thickness on the Dynamic Response of Concrete Gravity Dams due to Unit Harmonic Wave Incidences

To investigate the effect of the reservoir bottom sediment thickness on the dynamic response of the concrete gravity dam, three different ratios of the sediment thickness (H_S) to the dam height (H), namely $H_S/H = 0$, 0.1 and 0.2, are considered in the corresponding computational models. Assuming the reservoir bottom sediment is composed of a soft clay layer, the following parameters are used for the sediment material: the elastic modulus is 0.252×10^9 Pa; the value of Poisson's ratio is 0.3; the density is $2000\,\mathrm{kg\,m^{-3}}$; the corresponding shear-wave velocity is $220\,\mathrm{m\,s^{-1}}$.

Figure 3.5 shows the effects of sediment thicknesses on the amplitude distributions of the complex frequency response function for the acceleration of the concrete gravity dam at the same three different stations (shown in Fig. 3.3) due to SV-wave and P-wave vertical incidences from the far field of the concrete gravity dam–water–foundation system. In this figure, cases 1, 2 and 3 represent the numerical results when the ratios of the sediment thickness (H_S) to the dam height (H) is equal to 0, 0.1 and 0.2, respectively. When $H_S/H = 0$, the whole reservoir is filled with water so that there is no sediment at the reservoir bottom. For an SV-wave vertical incidence, the acceleration value of the concrete gravity dam with a thin sediment layer (i.e. case 2) is smaller than that without sediment (i.e. case 1). This observation is similar to what was observed from the previous results (Hall and Copra 1982; Fenves and Chopra 1983, 1984, 1985). However, the acceleration value

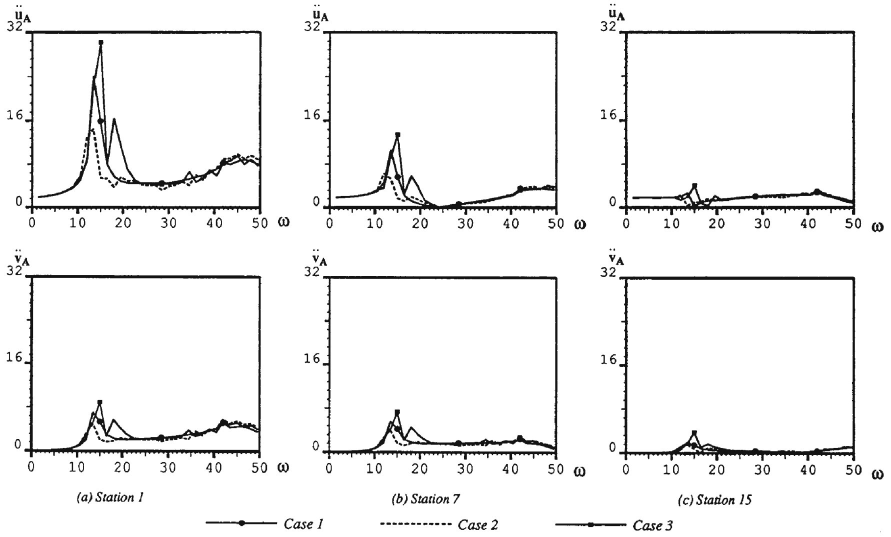

(A) SV-wave incidence

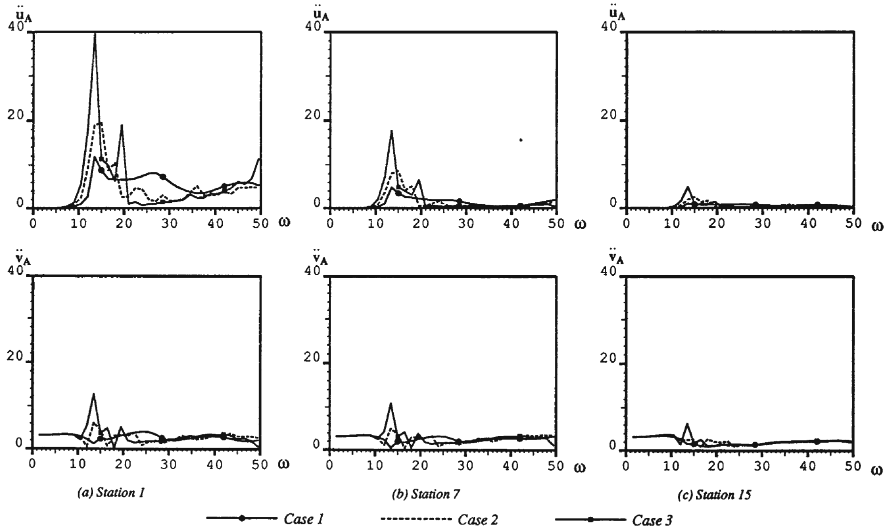

(B) P-wave incidence

Fig. 3.5 Effects of sediment thickness on the amplitude distribution of the complex frequency response function for the acceleration of the concrete gravity dam: (**A**) SV-wave incidence; (**B**) P-wave incidence

of the concrete gravity dam with a thicker sediment layer (i.e. case 3) is greater than that without sediment (i.e. case 1). This opposite behavior is due to the fact that when the sediment thickness is considered in the computational model, it has two main effects on the dynamic response of the concrete gravity dam–water–foundation system. The first effect is to dissipate the wave energy of the system due to both the sediment material damping and the radiation damping within the sediment layer, so that the dynamic response of the concrete gravity dam is reduced. The second effect is to amplify the acceleration at the water–sediment interface. This can cause an increase in dynamic water pressure on the upstream surface of the concrete gravity dam, so that the dynamic response of the concrete gravity dam is increased. For a given sediment material, since the amplification of the reservoir bottom sediment layer to the incident wave is dependent on both the sediment layer thickness and the sediment material properties, the thicker the sediment layer is, the greater will be the acceleration on the water–sediment interface.

For an SV-wave vertical incidence, both the scattered vertical acceleration on the water–sediment interface and the amplified horizontal acceleration on the dam–sediment interface can result in an increase in the dynamic response of the concrete gravity dam. When the sediment layer thickness is small, the scattered vertical acceleration and the amplified horizontal acceleration are small, so that they do not play a dominant role in controlling the dynamic response of the concrete gravity dam–water–foundation system. In this situation, energy dissipation (absorption) within the sediment layer plays a dominant role, so that the acceleration of the concrete gravity dam–water–foundation system is decreased. However, when the sediment layer is thicker, both the scattered vertical acceleration and the horizontal acceleration within the sediment layer become stronger, resulting in a stronger response of the concrete gravity dam–water–foundation system.

For a P-wave vertical incidence, the amplified vertical acceleration on the water–sediment interface has a profound effect on the dynamic response of the concrete gravity dam–water–foundation system, compared with what is observed for an SV-wave vertical incidence. The reason is that a vertical acceleration is the primary component for the P-wave vertical incidence considered in the computational model, while it is a ramification for the SV-wave vertical incidence due to the wave mode conversion on the water–sediment interface. For a P-wave vertical incidence, even a small thickness of the reservoir bottom sediment layer (e.g. $H_S/H = 0.1$) can produce a stronger vertical acceleration on the water–sediment interface, resulting in both a greater dynamic water pressure on the upstream surface of a concrete gravity dam and a stronger dynamic response of the concrete gravity dam–water–foundation system. It can be concluded that the thickness of a reservoir bottom layer has a greater effect on the dynamic response of the concrete gravity dam for a P-wave vertical incidence than it has for an SV-wave vertical incidence. Therefore, for the sake of making a safer design of a concrete gravity dam, it is suggested that both the reservoir bottom sediment thickness and material properties of the sediment be carefully considered in the computational model. Nevertheless, it seems that the reservoir bottom sediment thickness has little influence on the resonant frequency of a concrete gravity dam–water–foundation system.

Compared with the numerical results obtained for the empty reservoir case (i.e. Fig. 3.4), the existence of reservoir water and reservoir bottom sediments can cause a reduction in the resonant frequency of a concrete gravity dam–water–foundation system. For example, the predominant circular frequency of the dam–water–foundation system is about 14 rad s^{-1}, as shown in Fig. 3.5. However, the predominant circular frequency of the empty reservoir case is about 20 rad s^{-1}. Such predominant circular frequencies are clearly displayed by the response peaks (at station 1) in Figs. 3.4 and 3.5. This is because in the current computational model the reservoir water can be simulated as added (frequency-dependent) masses on the water–solid interface. Owing to the existence of the reservoir water and reservoir bottom sediments, the horizontal acceleration of the concrete gravity dam is greater than the vertical one, even for a P-wave vertical incidence, as shown by the numerical results in Fig. 3.5. The dynamic response on the dam–foundation interface (e.g. station 15) is relatively small for both the empty reservoir case (i.e. Fig. 3.4) and the full reservoir cases with reservoir bottom sediments (i.e. Fig. 3.5). Generally, the higher the location at the body of a concrete gravity dam, the stronger the dynamic response of the concrete gravity dam (Hall and Copra 1982; Fenves and Chopra 1983, 1984, 1985; Valliappan and Zhao 1992; Zhao et al. 1995)

3.1.2.2 Effects of Sediment Elastic Properties on the Dynamic Response of Concrete Gravity Dams due to Unit Harmonic Wave Incidences

For the purpose of investigating the effects of reservoir bottom sediments on the dynamic response of the concrete gravity dam–water–foundation system (shown in Fig. 3.3), the ratio of the sediment thickness to the dam height is kept constant at $H_S/H = 0.1$, while three different elastic moduli of the sediment material, namely 0.252×10^9 Pa, 1.4×10^9 Pa and 0.252×10^{10} Pa, are considered as cases 1, 2 and 3, respectively, in the corresponding computational models. The same Poisson's ratio ($\nu_s = 0.3$) and the same density of the sediment material ($\rho_s = 2000\,\mathrm{kg\,m^{-3}}$) are used in these three cases.

Figure 3.6 shows the effects of sediment elastic modulus on the amplitude distributions of the complex frequency response function for the acceleration of the concrete gravity dam at the same three different stations (as shown in Fig. 3.3) due to SV-wave and P-wave vertical incidences. For an SV-wave vertical incidence and the given thickness of the reservoir bottom sediment layer ($H_S/H = 0.1$), an increase in the elasticity of the sediment material results in an increase in the accelerations of the concrete gravity dam. Such an increase becomes negligible small for the higher values of elastic moduli of the sediment material. The reason is that for a small value of the sediment-layer thickness, as explained in the previous subsection, the existence of the sediment layer can play an important role in dissipating the wave energy of the concrete gravity dam–water–foundation system, resulting in a considerable decrease in the dynamic response of the concrete gravity dam. This observation is in good coincidence with the previous conclusion stating that a softer sediment layer usually results in greater wave energy dissipation within the concrete gravity dam–water–foundation system (Hall and Copra 1982; Fenves and Chopra 1983, 1984, 1985; Valliappan and Zhao 1992; Zhao et al. 1995).

For a P-wave vertical incidence, the amplification of a sediment layer to the incident wave plays a major role in controlling the dynamic response of a concrete

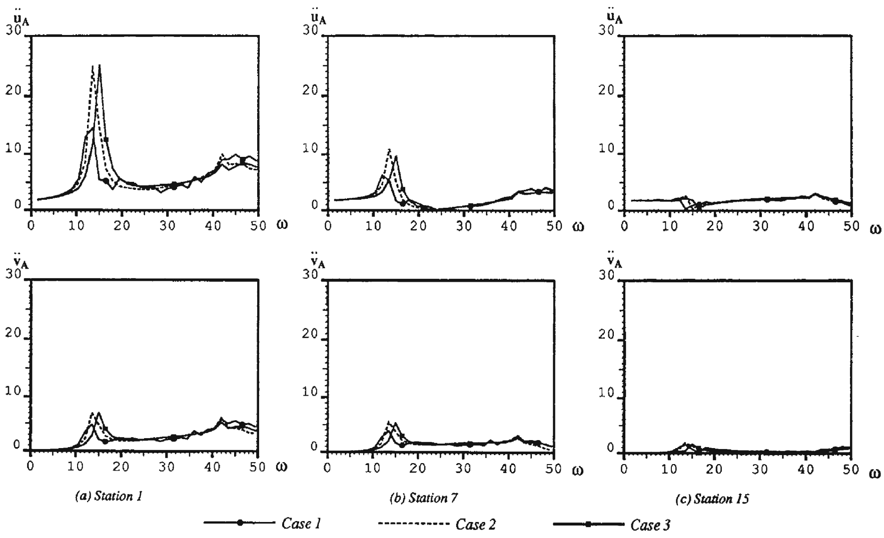

(A) SV-wave incidence

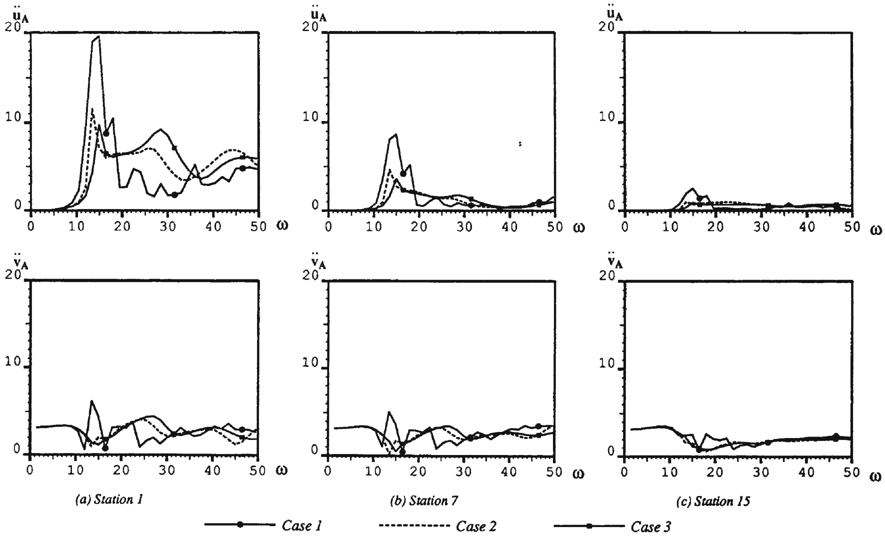

(B) P-wave incidence

Fig. 3.6 Effects of sediment elastic modulus on the amplitude distribution of the complex frequency response function for the acceleration of the concrete gravity dam: (**A**) SV-wave incidence; (**B**) P-wave incidence

gravity dam. As the elastic modulus of the sediment material increases, the amplification of the sediment layer to the incident wave decreases. Consequently, the dynamic water pressure on the upstream surface of the concrete gravity dam decreases, resulting in a decrease in the dynamic response of the concrete gravity dam. With a further increase in the elastic modulus of the sediment material, the dynamic response curve of the concrete gravity dam becomes smoother for both SV-wave and P-wave vertical incidences. Since a small difference between the elastic modulus of the sediment material and that of the foundation rock can only cause a similar response of the concrete gravity dam, a much smoother response curve of the concrete gravity dam is obtained in the empty reservoir case (i.e. Fig. 3.4). For both SV-wave and P-wave vertical incidences, the strongest response of a concrete gravity dam always takes place at the crest of the concrete gravity dam, while the weakest response occurs at the heel of the concrete gravity dam.

3.1.2.3 Effects of Poisson's Ratios of the Sediment on the Dynamic Response of Concrete Gravity Dams due to Unit Harmonic Wave Incidences

Further study is carried out to investigate the effects of Poisson's ratios of the reservoir bottom sediment material on the dynamic response of the concrete gravity dam–water–foundation system. By keeping other parameters of the sediment material unchanged, three different Poisson's ratios of the sediment material, namely 0.2, 0.3 and 0.4, are used in cases 1, 2 and 3 for the corresponding computational models. The unchanged parameters of the sediment material in the computational models are as follows: the elastic modulus of the sediment material is 0.252×10^9 Pa; the density of the sediment material is $2000\,\mathrm{kg\,m^{-3}}$; the ratio of the sediment thickness to the dam height is 0.1.

Figure 3.7 shows the effects of the sediment Poisson's ratios on the amplitude distributions of the complex frequency response function for the acceleration of the concrete gravity dam at the given three different stations (in Fig. 3.3) due to SV-wave and P-wave vertical incidences. For an SV-wave vertical incidence, the overall trend of the effects of Poisson's ratios on the dynamic response of the concrete gravity dam is that with an increase in Poisson's ratio of the sediment material, the acceleration value of the concrete gravity dam is increased. Since a higher Poisson's ratio of the sediment material can cause a greater vertical deformation on the water–sediment interface due to the wave scattering effect, more energy of the input wave can be changed into the vertical movement of the particle on this interface. As a result, the scattered vertical acceleration becomes stronger as Poisson's ratio of the sediment material becomes greater. On the other hand, a stronger vertical acceleration can cause a higher dynamic water pressure on the upstream surface of the concrete gravity dam, so that a greater dynamic response of the concrete gravity dam is obtained.

For a P-wave vertical incidence, although a higher Poisson's ratio of the sediment material can result in a greater horizontal movement of the particle on the water–sediment interface, a stronger scattered horizontal acceleration on this interface has little effects on the dynamic response of the concrete gravity dam. However, since the wave energy of the incident wave is changed into the horizontal movement of the particles on the water–sediment interface, the vertical acceleration of the particles on this interface becomes smaller under the condition that the total energy

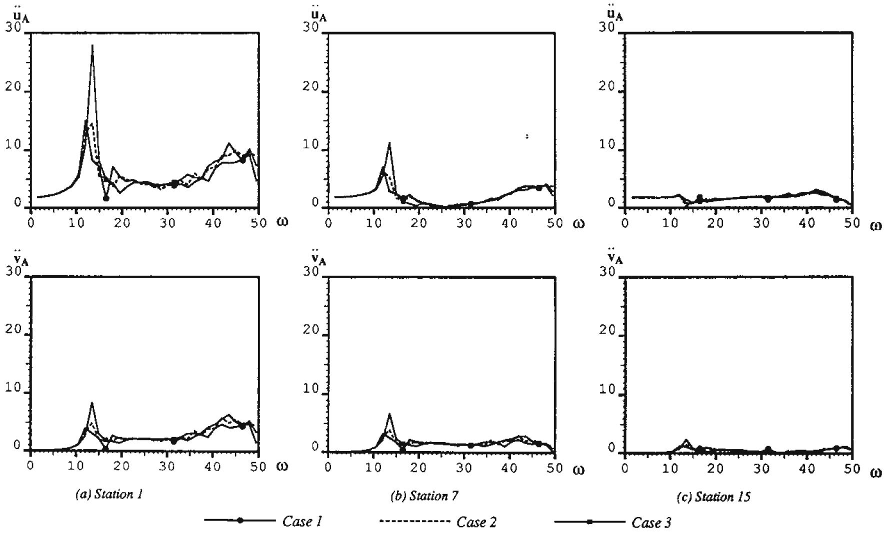

(A) SV-wave incidence

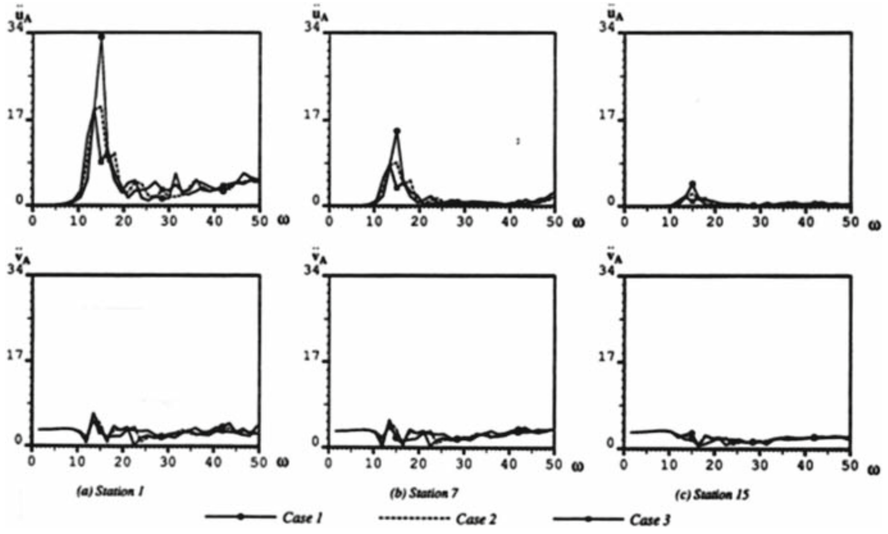

(B) P-wave incidence

Fig. 3.7 Effects of sediment Poisson's ratios on the amplitude distribution of the complex frequency response function for the acceleration of the concrete gravity dam: (**A**) SV-wave incidence; (**B**) P-wave incidence

of the particles should be conservative on this interface. Therefore, in the case of the P-wave vertical incidence, the dynamic response of the concrete gravity dam decreases as Poisson's ratio of the sediment material increases. This phenomenon can be clearly observed from the numerical results shown in Fig. 3.7.

3.1.2.4 Effects of the Sediment Damping Coefficients on the Dynamic Response of Concrete Gravity Dams due to Unit Harmonic Wave Incidences

Assuming the damping characteristic of the reservoir bottom sediment is hysteretic, three different damping coefficients, namely 0, 0.1 and 0.2 in cases 1, 2 and 3, respectively, are considered for investigating the effects of sediment damping coefficients on the dynamic response of the concrete gravity dam–water–foundation system. Other parameters of the sediment material are exactly the same as those used in Sect. 3.1.2.3, exempt for a constant of 0.3 being used for Poisson's ratio of the sediment material in all the three cases.

Figure 3.8 shows the effects of sediment damping coefficients on the amplitude distributions of the complex frequency response function for the acceleration of the concrete gravity dam at the three different stations (shown in Fig. 3.3) due to SV-wave and P-wave vertical incidences. Since the dynamic response of a concrete gravity dam is more sensitive to the vertical acceleration on a water–sediment interface than to the horizontal acceleration on this interface, the sediment damping coefficient has little effect on the dynamic response of the concrete gravity dam due to an SV-wave vertical incidence, even though it may cause a considerable reduction in the horizontal acceleration on the water–sediment interface located far away from the concrete gravity dam. This interpretation is supported by the numerical results shown in Fig. 3.8. For a P-wave vertical incidence, a larger sediment damping coefficient can result in a greater decrease in the vertical acceleration on the water–sediment interface, so that a decrease in the horizontal acceleration of the concrete gravity dam can be observed from the corresponding numerical results. It is concluded that the sediment damping coefficient can have a remarkable effect on the dynamic response of the concrete gravity dam due to a P-wave vertical incidence. However, for both SV-wave and P-wave vertical incidences, the sediment damping coefficient has little influence on the fundamental resonant frequency of the concrete gravity dam–water–foundation system.

3.1.3 Transient Response of Concrete Gravity Dams due to Earthquake Wave Incidences

Using the coupled computational model of finite and dynamic infinite elements for simulating wave scattering problems due to P-wave and SV-wave incidences (Zhao et al. 1992, 1995), it is convenient to investigate the transient seismic response of a concrete gravity dam–water–foundation system in the frequency domain (Zhao and Valliappan 1993a; Zhao et al. 1995). A transient incident earthquake wave, which is assumed to be a plane acceleration wave, can be decomposed into a series of harmonic waves (Clough and Penzien 1975; Wolf 1985; Zhao and Valliappan 1993a; Zhao et al. 1995). The amplitude of each harmonic wave can be expressed as follows:

$$\ddot{U}_I(\omega) = \int_{-\infty}^{+\infty} \ddot{u}_I(t) e^{-i\omega t} dt, \tag{3.32}$$

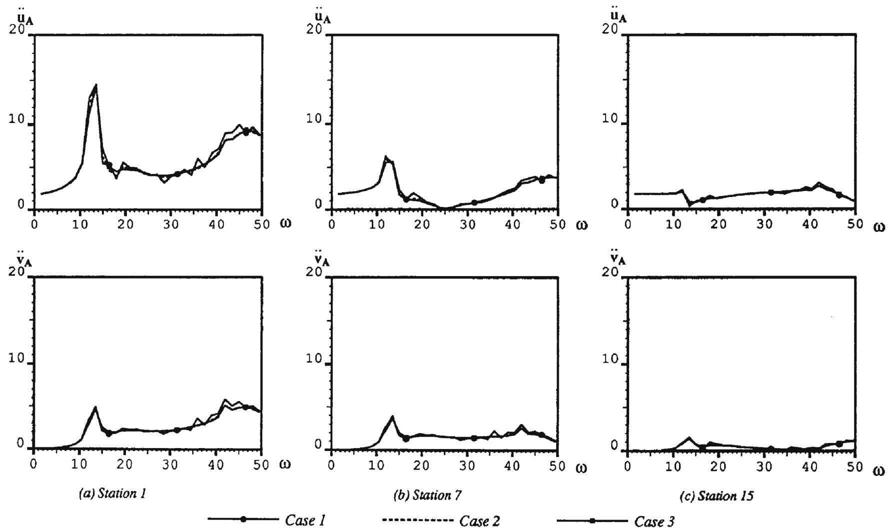

(a) Station 1 (b) Station 7 (c) Station 15

(A) SV-wave incidence

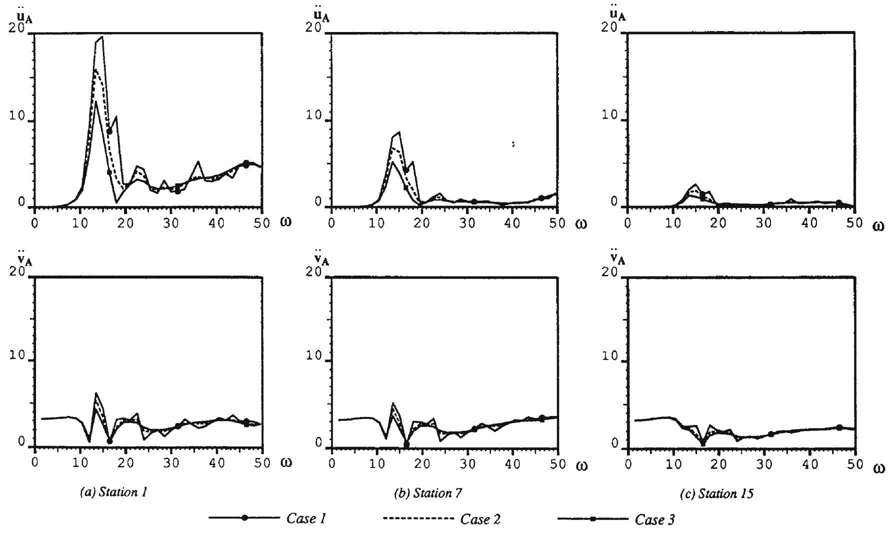

(a) Station 1 (b) Station 7 (c) Station 15

(B) P-wave incidence

Fig. 3.8 Effects of sediment damping on the amplitude distribution of the complex frequency response function for the acceleration of the concrete gravity dam: (**A**) SV-wave incidence; (**B**) P-wave incidence

where $\ddot{u}_I(t)$ is the acceleration of the incident earthquake wave; ω is the circular frequency of a decomposed harmonic wave; $\ddot{U}_I(\omega)$ is the Fourier spectrum amplitude of the decomposed harmonic wave.

As Eq. (3.32) is the Fourier transform integral, its inverse form can be expressed using the following equation:

$$\ddot{u}_I(t) = \frac{1}{2\pi} \int_{-\infty}^{+\infty} \ddot{U}_I(\omega) e^{i\omega t} d\omega. \tag{3.33}$$

After an incident acceleration wave is decomposed, a unit harmonic wave with frequency ω can be used to compute the complex frequency response function, $H_j(\omega)$, for nodal point j in the concrete gravity dam–water–foundation system (Zhao et al. 1992, 1995; Zhao and Valliappan 1993a).

To obtain the transient seismic response for any points in the concrete gravity dam–water–foundation system, an arbitrary nodal point, namely nodal point j, is considered to illustrate the related procedures. For this nodal point, the harmonic response due to a given decomposed harmonic acceleration wave with amplitude $\ddot{U}_I(\omega)$ and circular frequency ω can be evaluated:

$$\ddot{U}_{R_j}(\omega) = H_j(\omega) \ddot{U}_I(\omega), \tag{3.34}$$

where $\ddot{U}_{R_j}(\omega)$ is the acceleration amplitude of the harmonic response for nodal point j in the concrete gravity dam–water–foundation system due to the decomposed harmonic acceleration-wave incidence (Zhao et al. 1992, 1995; Zhao and Valliappan 1993a).

By superposition of the harmonic responses for all the decomposed harmonic waves, the transient seismic response for nodal point j in the concrete gravity dam–water–foundation system due to the earthquake acceleration-wave incidence can be obtained as follows:

$$\ddot{u}_{R_j}(t) = \frac{1}{2\pi} \int_{-\infty}^{+\infty} \ddot{U}_{R_j}(\omega) e^{i\omega t} d\omega, \tag{3.35}$$

where $\ddot{u}_{R_j}(t)$ is the acceleration of the transient seismic response of the nodal point j in the concrete gravity dam–water–foundation system.

From a computational point of view, the discretized Fourier transform is used in the coupled computational model of finite and dynamic infinite elements for simulating the concrete gravity dam–water–foundation system due to earthquake acceleration-wave incidences. For this reason, the incident acceleration wave, $\ddot{u}_I(t)$, is usually assumed to be periodic with a finite period, T. To make use of the fast Fourier transform (i.e. FFT) technique, this period (T) is divided into n equal intervals of Δt, where n is selected as a power of 2. The variable frequency (ω) is also divided into the same number of intervals $\Delta\omega$ as the time variable (t). The lowest and highest frequencies in the numerical analysis can be expressed in the following equations:

$$\omega_{\min} = \Delta\omega = \frac{2\pi}{T}, \tag{3.36}$$

$$\omega_{\max} = \frac{n}{2}\Delta\omega = \frac{\pi}{\Delta t}, \tag{3.37}$$

where $\omega_{\max}$ is called the cut-off frequency or the Nyquist frequency, which is related to the interval of time (Δt) and can be determined from the characteristics of an incident acceleration wave.

To derive the discretized form for Eqs. (3.32) and (3.35), the following relationships are introduced:

$$t_k = k\Delta t = \frac{kT}{n} \qquad (k = 0, 1, 2, \ldots, n-1), \tag{3.38}$$

$$\omega_q = q\Delta\omega = \frac{2\pi q}{T} \qquad (q = 0, 1, 2, \ldots, n-1). \tag{3.39}$$

Substituting Eqs. (3.38) and (3.39) into Eqs. (3.32) and (3.35) yields

$$\ddot{U}_I(\omega_q) = \Delta t \sum_{k=0}^{n-1} \ddot{u}_I(t_k) e^{-2\pi i(qk/n)} \qquad (q = 0, 1, 2, \ldots, n-1), \tag{3.40}$$

$$\ddot{u}_{R_j}(t_k) = \frac{\Delta\omega}{2\pi} \sum_{q=0}^{n-1} \ddot{U}_{R_j}(\omega_q) e^{2\pi i(qk/n)} \qquad (k = 0, 1, 2, \ldots, n-1). \tag{3.41}$$

3.1.3.1 Selection of an Earthquake for the Transient Response of Concrete Gravity Dams due to Earthquake Wave Incidences

Earthquakes are very complicated and complex phenomena in nature. Their time histories recorded on natural ground are quite irregular. This is because of complexities of sources mechanisms, wave reflections and refractions at irregular interfaces, wave dispersions along their travelling paths. The state-of-the-art techniques for selecting input earthquake waves in engineering practice include the following two aspects. If the recorded history data of an earthquake are available at a specific structure site under consideration, then this earthquake can be used as an input earthquake for the seismic analysis of the structure. However, if there are no earthquake records available at a specific structure site under consideration, then the so-called engineering analogy method is used to produce an artificial input earthquake wave. In this case, for a given structure site, it is necessary to investigate the topological and geological conditions of the structure site and the activities of faults (i.e. potential earthquake sources) near the structure site. An earthquake time history, which is recorded at a similar site to the structure site under consideration, is selected as an input earthquake wave, even though necessary modifications are needed to make this selected earthquake wave suitable for reproducing the design earthquake intensity of the given structure site.

For the purpose of investigating the effects of reservoir bottom sediments on the transient seismic response of a concrete gravity dam–water–foundation system, one could select an arbitrary earthquake motion as the input earthquake wave. From this point of view, the acceleration time history of an S25W component of the Parkfield, California earthquake (McEvilly et al. 1967; Trifunac and Udwadia 1974; Zhao and

Valliappan 1993a), is selected as the input earthquake wave for investigating the effects of reservoir bottom sediments on the transient seismic response of the concrete gravity dam–water–foundation system, which is already considered in the previous subsections. This selected earthquake took place on 27 June 1966 and the peak value of the S25W acceleration component was $-3.408\,\mathrm{m\,s^{-2}}$. For convenience of the seismic analysis, this acceleration time history is normalized through dividing the acceleration by the absolute value of the peak magnitude, 3.408, resulting in a unit earthquake acceleration wave. This unit earthquake acceleration wave has the same frequency characteristics as the original one.

Figure 3.9 shows the acceleration, Fourier spectrum and acceleration response spectrum of the selected unit earthquake acceleration wave. In this figure, a is used to represent the acceleration; F-S the Fourier spectrum; ξ the damping ratio of a one-degree-of-freedom dynamic system; and S_a the acceleration spectrum. To make use of the FFT technique, an equal time interval, $\Delta t = 0.02\,\mathrm{s}$, is adopted and 1024 pairs of data are used to represent this unit earthquake acceleration wave, resulting in the lowest frequency of $0.3068\,\mathrm{rad\,s^{-1}}$ (i.e. $\omega_{\mathrm{min}} = 0.3068\,\mathrm{rad\,s^{-1}}$) and the highest frequency of $157.08\,\mathrm{rad\,s^{-1}}$ (i.e. $\omega_{\mathrm{max}} = 157.08\,\mathrm{rad\,s^{-1}}$), respectively. As can be seen from the Fourier spectrum in Fig. 3.9, the predominant circular frequency is about $17\,\mathrm{rad\,s^{-1}}$, which has a corresponding predominant period of 0.37 s. In engineering practice, the acceleration response spectrum, which expresses the maximum acceleration response of a one-degree-of-freedom dynamic system excited by a given earthquake acceleration wave, can be used to represent roughly the dynamic response of a structure under the given earthquake acceleration wave. In other words, the acceleration response spectrum can be used as a kind of measurement of the structural response intensity due to a given input earthquake wave, to judge roughly the dynamic response intensity for a series of structures of different fundamental frequencies.

3.1.3.2 Transient Seismic Response of a Concrete Gravity Dam–Water–Foundation System Including Reservoir Bottom Sediment Effects

In this subsection, the same coupled computational model of finite and dynamic infinite elements as that shown in Fig. 3.3 is used to investigate the transient seismic response of the concrete gravity dam–water–foundation system, including reservoir bottom effects. The following parameters are used in the coupled computational model. For both the concrete gravity dam and the underlying rock foundation, the elastic modulus is 28.8×10^9 Pa; the value of Poisson's ratio is 0.2; the density of the medium is $2400\,\mathrm{kg\,m^{-3}}$. These parameters results in a shear wave velocity of $2236\,\mathrm{m\,s^{-1}}$ within both the concrete gravity dam and the underlying rock foundation. For the reservoir water, the density is $1000\,\mathrm{kg\,m^{-3}}$; the compressional wave velocity of water is assumed to be $1436\,\mathrm{m\,s^{-1}}$. For the reservoir bottom sediment, the elastic modulus is 0.252×10^9 Pa; the value of Poisson's ratio is 0.3; the density of the sediment material is $2000\,\mathrm{kg\,m^{-3}}$. These parameters results in a shear-wave velocity of $220\,\mathrm{m\,s^{-1}}$ within the reservoir bottom sediment layer. To consider the

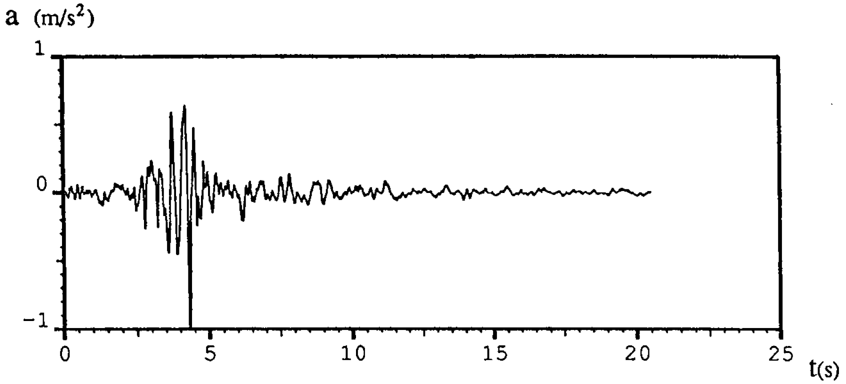

(a) Input earthquke accelerogram

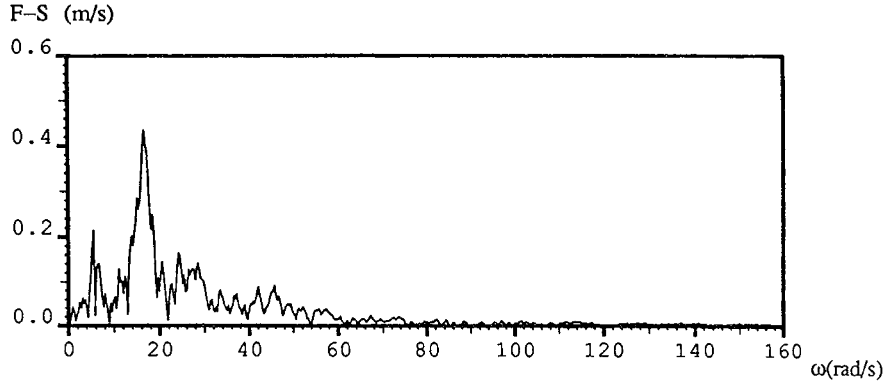

(b) Fourier spectrum

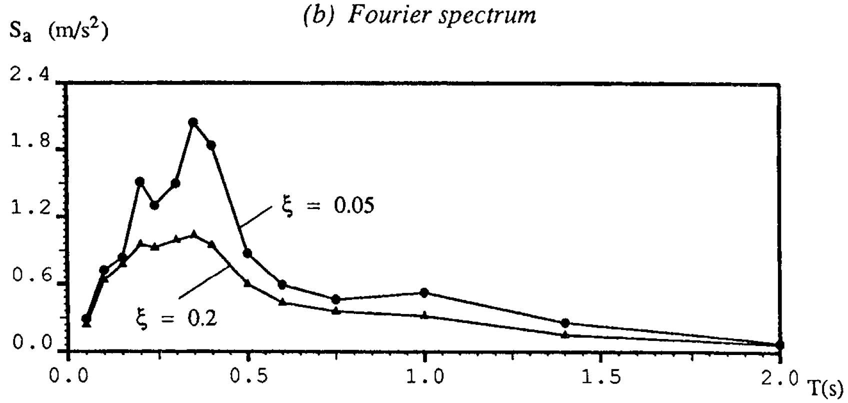

(c) Response spectrum

Fig. 3.9 The acceleration time history, Fourier spectrum and response spectrum of the selected input earthquake wave: (**a**) input earthquake accelerogram; (**b**) Fourier spectrum; and (**c**) response spectrum effect of the reservoir bottom sediment on the transient seismic response of the concrete gravity dam, a constant of 0.1 for the ratio of the sediment-layer thickness to the dam height, namely $H_S/H = 0.1$, is used in the coupled computational model of finite and dynamic infinite elements. Without loss of generality, the selected unit earthquake acceleration wave (Fig. 3.13) in the previous subsection is applied, as either an input SV-wave or an input P-wave, to the wave input boundary of the coupled computational model.

Figures 3.10 and 3.11 show the acceleration distributions at three typical stations of the concrete gravity dam due to the seismic SV-wave vertical incidence. The numerical results shown in Fig. 3.10 are obtained for the full-reservoir model without reservoir bottom sediments (i.e. $H_S/H = 0$), while the numerical results shown in Fig. 3.11 are obtained for the full reservoir with reservoir bottom sediments (i.e. $H_S/H = 0.1$). In these figures, a_x and a_y are the horizontal and vertical components of the acceleration response of the concrete gravity dam. As shown in Fig. 3.3, stations 1, 7 and 15 are located at the crest, the middle height position and the heel of the concrete gravity dam, respectively. For both the full reservoir with reservoir bottom sediments and the full reservoir without reservoir bottom sediments, the seismic response at the crest of the concrete gravity dam is much stronger than that at the heel of the concrete gravity dam. Due to the predominant role of energy dissipation in a sediment layer, the seismic response of the concrete gravity dam without reservoir bottom sediments is stronger than that with reservoir bottom sediments, indicating that these sediments have a significant effect on the transient seismic response of the concrete gravity dam–water–foundation system. For the full reservoir without reservoir bottom sediments, the amplitude of the horizontal acceleration at the crest (station 1) of the concrete gravity dam is about $9\,\mathrm{m\,s^{-2}}$, while for the full reservoir with reservoir bottom sediments, the amplitude of the horizontal acceleration at the crest (station 1) of the concrete gravity dam is about $5\,\mathrm{m\,s^{-2}}$. These amplitudes take place at about 4.6 s in the coupled computational model. Since a considerable difference in horizontal accelerations along the height of a concrete gravity dam can result in rotation and bending of the dam, it can be concluded that for the seismic SV-wave vertical incidence, the neglect of the reservoir bottom sediment effect in a concrete gravity dam–water–foundation system is conservative for the seismic design of the concrete gravity dam, because the consideration of reservoir bottom sediments can result in a remarkable increase in the damping of the whole concrete gravity dam–water–foundation system.

Figures 3.12 and 3.13 show the acceleration distributions at three typical stations, namely stations 1, 7 and 15 in Fig. 3.3, of the concrete gravity dam due to the seismic P-wave vertical incidence. The numerical results shown in Fig. 3.12 are obtained from the full reservoir model without reservoir bottom sediments (i.e. $H_S/H = 0$), while the numerical results shown in Fig. 3.13 are obtained from the full reservoir with reservoir bottom sediments (i.e. $H_S/H = 0.1$). When reservoir bottom sediments are considered in the coupled computational model of the concrete gravity dam-water-foundation system, the overall acceleration response of the concrete gravity dam due to the seismic P-wave vertical incidence is stronger than that due to the seismic SV-wave vertical incidence. For example, the amplitude of

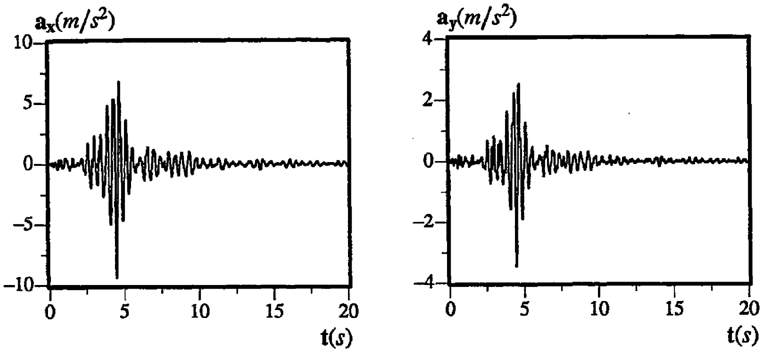

(Station 1)

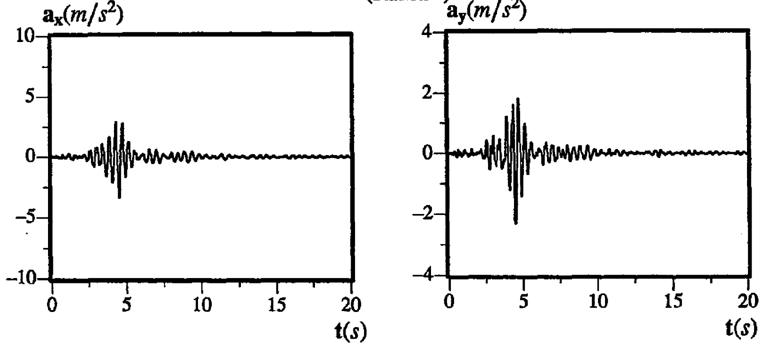

(Station 7)

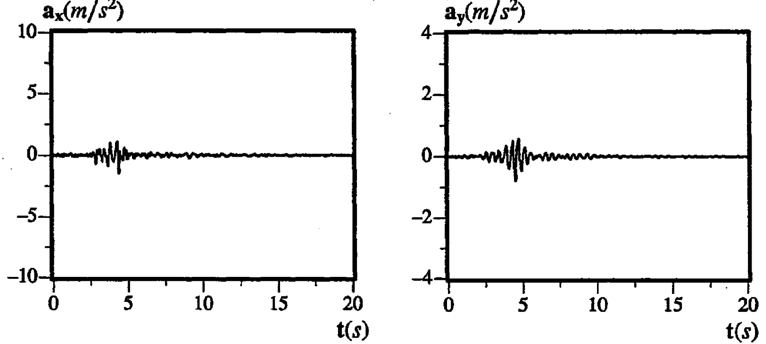

(Station 15)

Fig. 3.10 Acceleration response of the concrete gravity dam due to the seismic SV-wave incidence (without sediments): as shown in Fig. 3.3, stations 1, 7 and 15 are located at the *top*, the *middle* and the *bottom* of the dam

the horizontal acceleration at the crest of the concrete gravity dam (in Fig. 3.13) is about $12\,\mathrm{m\,s^{-2}}$ in the case of the seismic P-wave vertical incidence, while it is about $5\,\mathrm{m\,s^{-2}}$ in the case of the seismic SV-wave vertical incidence, as shown in Fig. 3.11. Due to the predominant role of reservoir bottom sediments in the amplification of the input seismic wave, the horizontal acceleration response of the

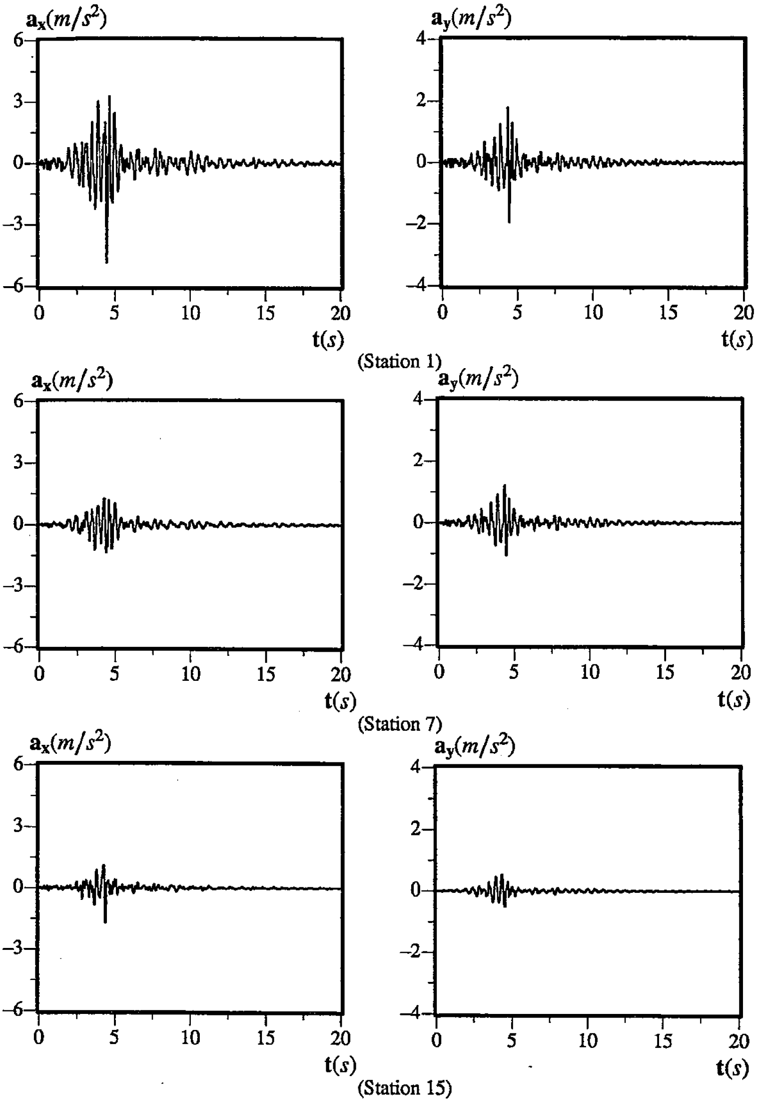

Fig. 3.11 Acceleration response of the concrete gravity dam due to the seismic SV-wave incidence (with sediments): as shown in Fig. 3.3, stations 1, 7 and 15 are located at the *top*, the *middle* and the *bottom* of the dam

concrete gravity dam is stronger than the vertical acceleration response of the concrete gravity dam, even though the vertical seismic acceleration wave is applied to the wave input boundary of the coupled computational model as a result of the seismic P-wave vertical incidence. This indicates that the consideration of reservoir bottom sediments is important for the seismic design of a concrete gravity dam

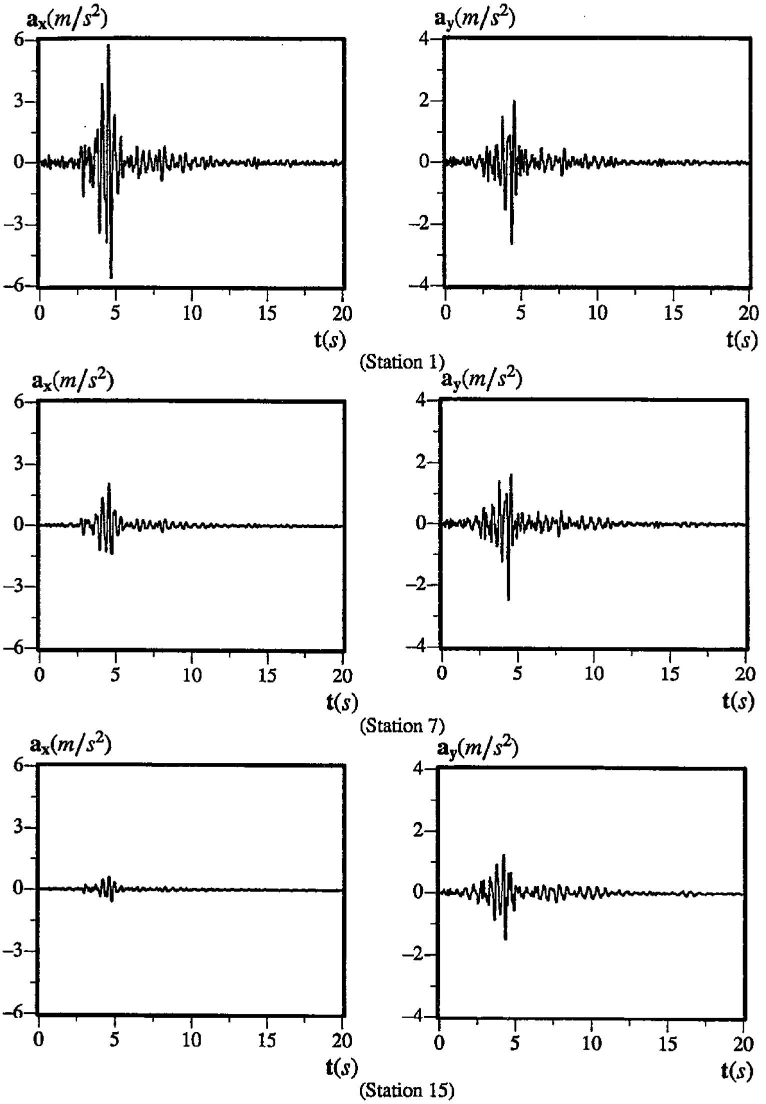

Fig. 3.12 Acceleration response of the concrete gravity dam due to the seismic P-wave incidence (without sediments): as shown in Fig. 3.3, stations 1, 7 and 15 are located at the *top*, the *middle* and the *bottom* of the dam

under the seismic P-wave vertical incidence. Since the seismic response of a concrete gravity dam for a seismic P-wave vertical incidence is significantly different from that for a seismic SV-wave vertical incidence, it is suggested that the type of an incident seismic wave be carefully considered for the seismic design of the concrete gravity dam.

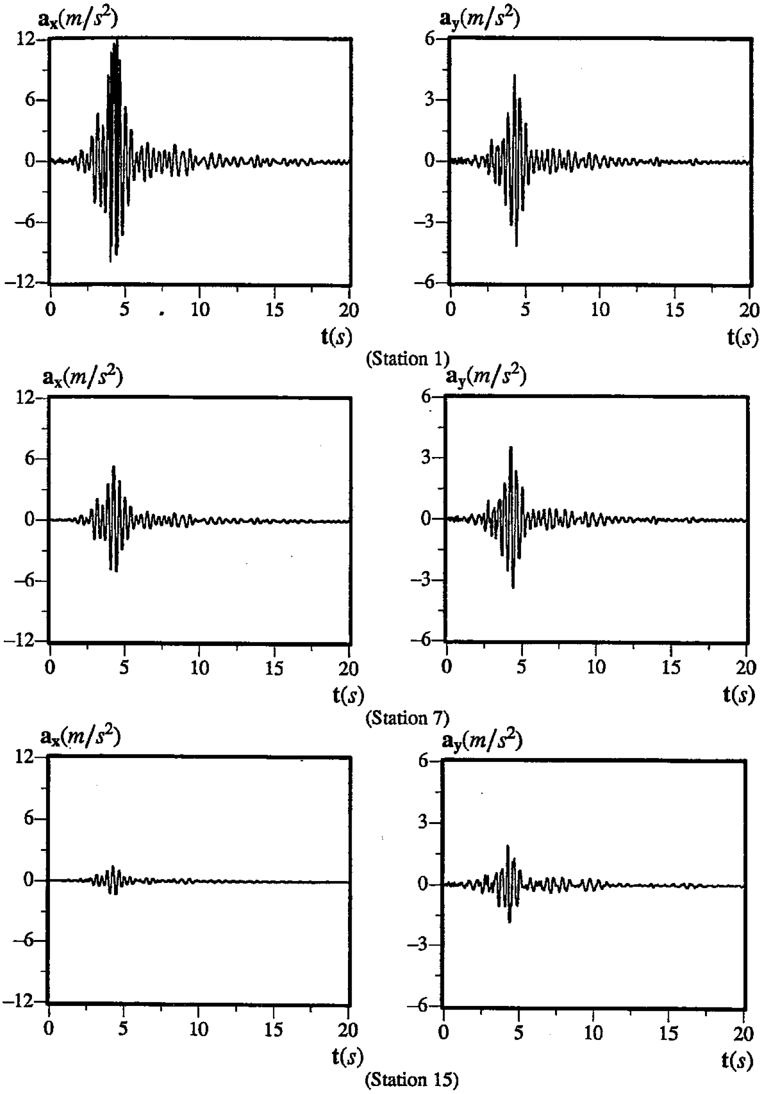

Fig. 3.13 Acceleration response of the concrete gravity dam due to the seismic P-wave incidence (with sediments): as shown in Fig. 3.3, stations 1, 7 and 15 are located at the *top*, the *middle* and the *bottom* of the dam

3.2 Simulation of Dynamic Embankment Dam–Water–Foundation Interaction Systems

Embankment dams can be found widely around the world. Some of them have been built in high seismic activity areas. The Lubuge Dam in Yunnan province, the Miyun Dam in Beijing, the Xiaolongdi Dam in Henan province and the Shimen

Dam in Shaanxi province are typical examples. These dams are not only built in the region where the seismic intensity for the design of embankment dams is 8° or higher, but also their heights are above 60 m. Due to ever-increasing demand for both water supply and flood protection, demand for construction of embankment dams in high-seismic-activity regions still exists even today. On the other hand, the accurate risk evaluation associated with existing dams and the successful designs for future dams are highly dependent on the appropriate understanding of their dynamic behaviours under earthquake loadings. Due to the possibility of disastrous consequences resulting from the failure of an embankment dam, the seismic design of embankment dams has become an important topic in the field of dam engineering. The major sliding in the Lower San Fernando Dam during the California Earthquake in 1971 resulted in a loss of about 10 m of freeboard, while the sliding of the upstream inclined clay apron in the Miyun Dam during the Tangshan Earthquake in 1976 jeopardized the safety of the dam. This indicates that further understanding of the seismic behaviours of embankment dams remains a major task for dam engineers.

Some important aspects that may affect the dynamic response of embankment dams under earthquake loadings have been recognized as follows: (1) since embankment dams undergo deformation that influences the motion of reservoir water, the embankment dam–water interaction must be taken into account (Chopra 1968; Liam-Finn et al. 1977); (2) when embankment dams are built on deformable (soil) foundations, the embankment dam–foundation interaction needs to be considered (Liam-Finn and Varoglu 1972a, b; Chopra and Gupta 1982; Zhao et al. 1993); (3) as water pressure on a reservoir bottom can affect the motion of the foundation that in turn affect the dynamic response of the embankment dam (Hall and Chopra 1982; Zhao 1994), the water–foundation interaction should be included in the dynamic response of an embankment dam–water–foundation system; and (4) reservoir bottom sediments can have a significant effect on incident waves, especially for incident P-waves (Fenves and Chopra 1983, 1984; Lofti et al. 1987; Medina et al. 1990; Valliappan and Zhao 1992; Zhao et al. 1993, 1995). Thus, it is necessary to consider the above four factors for dealing with the dynamic response of an embankment dam–water–sediment–foundation system.

One of the most likely effects of an earthquake on an embankment dam is to cause damage of the impervious member of the dam, resulting in reservoir-water leakage through the impervious member of the embankment dam. The failure of an impervious member of the embankment dam is usually caused by remarkable differential displacements in the impervious member of the embankment dam. Since different parts of an embankment dam may have different amplification effects on an incident earthquake wave, a better design for the location of an impervious member within an embankment dam is beneficial to the safety of the embankment dam. It is common practice to use different configurations of impervious members within embankment dams. Typical examples of the impervious member configurations are central clay cores, central concrete cores, upstream inclined impervious aprons and upstream concrete watertight protection. From a wave motion point of view, all the impervious members may have different advantages and disadvantages for a particular embankment dam–water–sediment–foundation system. For this reason, it is imperative to carry out a systematic study for investigating the effect of impervious members on the dynamic response of an embankment dam–water–sediment–foundation system.

When an embankment dam is built across a valley of a river with considerable sediments, a remarkable thickness of soft materials (i.e. sediments) can be accumulated at the reservoir bottom during the lifetime of the embankment dam. The effect of reservoir bottom sediments on the dynamic response of a concrete gravity dam–water–foundation system has been investigated in previous studies. Medina et al. (1990) solved the dynamic gravity dam–water–sediment–foundation interaction problem using a combination of the finite element and the boundary element methods. Fenves and Chopra (1983, 1984) used an absorptive reservoir bottom condition to represent the reservoir bottom effect in the finite element model of a concrete gravity dam–water–foundation system. Valliappan and Zhao (1992) proposed a more realistic computational model, in which a concrete gravity dam–water–foundation system including the thickness and material properties of the reservoir bottom sediment is simulated using finite elements and dynamic infinite elements. They concluded that the effect of reservoir bottom sediments on the dynamic response of concrete gravity dams is quite significant during earthquake wave incidences, especially during seismic P-wave incidences (Zhao et al. 1995). Nevertheless, only limited work has been done for investigating the effect of reservoir bottom sediments on the dynamic response of an embankment dam–water–sediment–foundation system (Zhao et al. 1993).

Due to the complexity of an embankment dam–water–sediment–foundation system, the coupled computational model of finite and dynamic infinite elements (Zhao et al. 1987, 1989, 1991; Zhao and Valliappan 1991; Valliappan and Zhao 1992) provides an effective and efficient way for investigating the dynamic response of the embankment dam–water–sediment–foundation system. Using the coupled computational model, not only can the infinite extension of both reservoir and dam foundation be simulated realistically, but also the input mechanism of an incident seismic wave can be simulated more appropriately (Zhao et al. 1992, 1995; Zhao and Valliappan 1993a, b, c; Valliappan and Zhao 1992). As the far field of an embankment dam–water–sediment–foundation system is simulated using dynamic infinite elements, the use of the coupled computational model of finite and dynamic infinite elements can reduce computer efforts significantly. Another advantage in using the coupled computational model of finite and dynamic infinite elements is that an incident wave coming from the far field of the system is transformed into equivalent nodal forces on the input wave boundary, where the scattered waves from the near field of the system can be transmitted back into the far field of the system through dynamic infinite elements. Owing to these advantages, the coupled computational model of finite and dynamic infinite elements is used to investigate the effects of both impervious member types and reservoir bottom sediments on the dynamic response of embankment dams in the following subsections.

3.2.1 Effects of Impervious Member Types on the Dynamic Response of an Embankment Dam–Foundation System

In dam engineering practice, central clay cores and upstream inclined impervious aprons are used as two primary ways to prevent reservoir water from leaking through embankment dams. From an embankment-dam design point of view, both dam configurations and materials are quite different for these two types of impervious members. This means that the type of impervious members may affect the dynamic response of an embankment dam–foundation system.

Figure 3.14 shows a typical embankment dam profile with either a central clay core or an upstream inclined concrete apron. In this figure, the height of the dam is 60 m; the slope of the upstream surface of the dam is 1:2 from the top to the bottom of the dam; the slopes of the downstream surface of the dam are 1:2 for the upper part and 1:3 for the lower part of the dam; the width of the dam crest is 10 m; the width of the dam bottom is 300 m. A berm of 7.5 m width is constructed at the level of 37.5 m, which is measured from the dam bottom. For the purpose of investigating the effect of foundation materials on the dynamic response of the embankment dam–foundation system (shown in Fig. 3.14), both a layered foundation and a homogeneous soil foundation are considered in the corresponding coupled computational model of finite and dynamic infinite elements. The embankment dam and the near field of the foundation are simulated using eight-node isoparametric finite elements, while the far field of the foundation is simulated using dynamic infinite elements. The horizontal interface between finite elements and dynamic infinite elements is used as the wave input boundary, where the incident waves coming from the far field of the system are transmitted into equivalent nodal forces using elastic wave theory (Zhao et al. 1992). As scattered waves from the embankment dam due to complicated dam configurations and various material properties can be transmitted from the near field back into the far field of the system, spurious reflected waves can be avoided on the wave input boundary. Since the main purpose of this subsection is to investigate the effect of impervious member types on the dynamic response of embankment dams, vertically incident unit harmonic P-waves and SV-waves are considered in the coupled computational model.

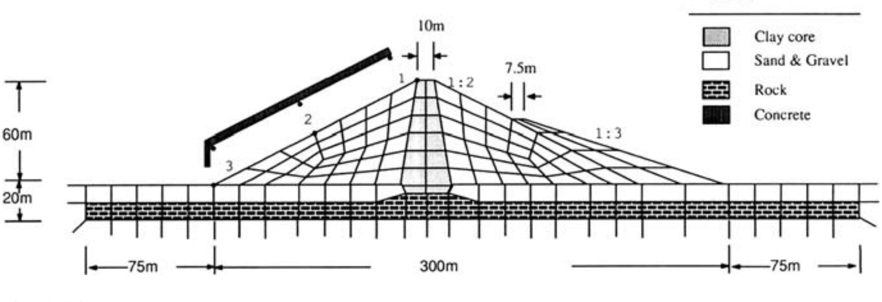

Fig. 3.14 Computational model of an embankment dam with either a central clay core or an upstream inclined concrete apron

The following material properties are used throughout this subsection. For both the crust of the embankment dam and the underlying soil layer, which are usually comprised of sands and gravels, the elastic modulus is 200×10^6 Pa; the value of Poisson's ratio is 0.33; the density of the material is $2070\,\mathrm{kg\,m^{-3}}$; the hysteretic damping coefficient is 0.2. These parameters result in a shear wave of $189\,\mathrm{m\,s^{-1}}$ within the crust of the embankment dam and the underlying soil layer. For the clay core, the elastic modulus is 90×10^6 Pa; the value of Poisson's ratio is 0.41; the density of the material is $2020\,\mathrm{kg\,m^{-3}}$; the hysteretic damping coefficient is 0.2. These parameters result in a shear wave of $125\,\mathrm{m\,s^{-1}}$ within the central clay core of the embankment dam. For the inclined concrete apron, the elastic modulus is 20×10^9 Pa; the value of Poisson's ratio is 0.16; the density of the material is $2380\,\mathrm{kg\,m^{-3}}$; the hysteretic damping coefficient is 0.05; the corresponding shear wave within the upstream inclined concrete apron of the embankment dam is $1871\,\mathrm{m\,s^{-1}}$. For the rock foundation, the elastic modulus is 30×10^9 Pa; the value of Poisson's ratio is 0.16; the density of the material is $2400\,\mathrm{kg\,m^{-3}}$; the hysteretic damping coefficient is 0.05; the corresponding shear wave within the rock foundation of the embankment dam is $2321\,\mathrm{m\,s^{-1}}$. Since shear wave velocities are different for the different parts of the embankment dam–foundation system, the maximum size of finite elements is determined by the softest material, so that the requirement for using an appropriate element size due to wave propagation is satisfied for all the finite elements used in the coupled computational model of finite and dynamic infinite elements.

Figures 3.15 and 3.16 show the dynamic response of an embankment dam with empty reservoir on a layered foundation due to SV-wave and P-wave vertical incidences, respectively. In these figures, the solid lines represent the amplification factors of the horizontal accelerations at three different positions of the embankment dam, while the dashed lines denote the amplification factors of the vertical accelerations at three different positions of the embankment dam. Note that the resonant frequency of the embankment dam–foundation system with an upstream inclined concrete apron is different from that with a central clay core. As an upstream inclined concrete apron is much stiffer than a central clay core, the fundamental resonant frequency of the embankment dam with the upstream inclined concrete apron is greater than that with the central clay core. However, since the thickness of an upstream inclined concrete apron is relatively small, which is 0.5 m in the coupled computational model, an increase in the fundamental resonant frequency of the embankment dam is not profound, even though this increase deserves to be considered in the dynamic analysis of the embankment dam–foundation system. For instance, the fundamental resonant frequency of the embankment dam with a clay core is about $8\,\mathrm{rad\,s^{-1}}$, while it is about $9\,\mathrm{rad\,s^{-1}}$ for the same embankment dam with an upstream inclined concrete apron.

In terms of the (acceleration) amplification factors of the embankment dam–foundation system, different impervious member types have a significant influence on the dynamic response of the embankment dam in the lower frequency range of excitation, but they have little effect on the dynamic response of the embankment dam in the higher frequency range of excitation. As was pointed out in a previous

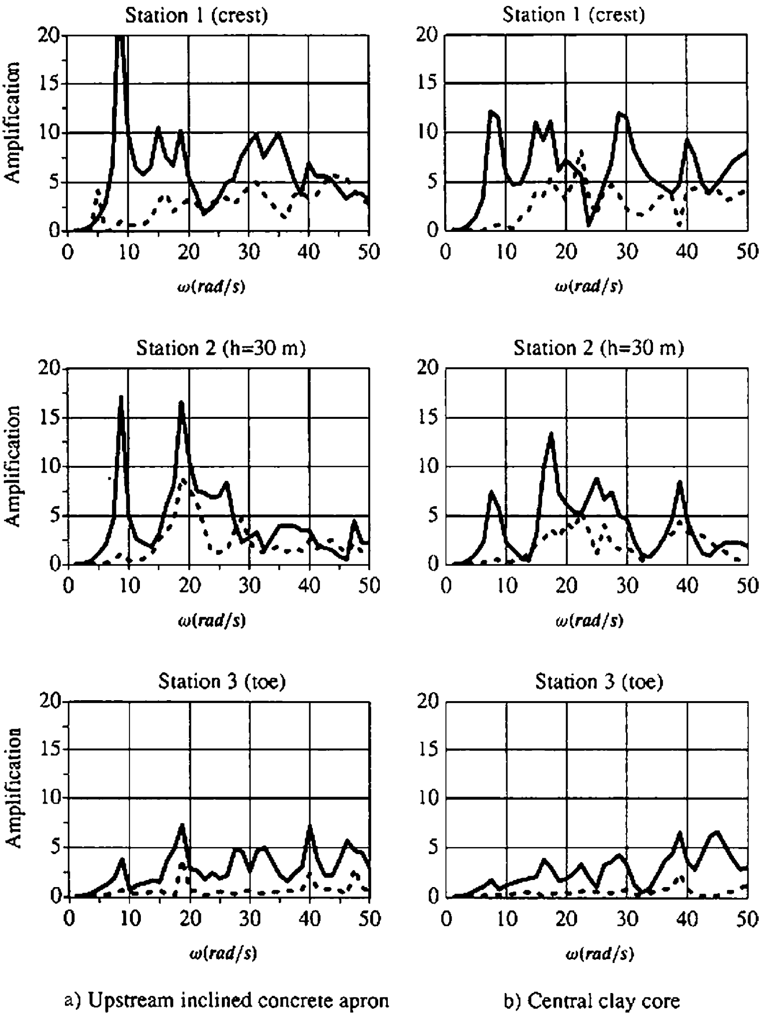

Fig. 3.15 Response of the empty embankment dam on a layered foundation due to the SV-wave vertical incidence

study (Zhao and Valliappan, 1991), the material damping of a dynamic system plays a more important role in controlling the dynamic response of the system for lower frequency excitation than it plays for higher frequency excitation. For an embankment dam with an upstream inclined concrete apron, the total material damping of the embankment dam–foundation system decreases as a result of a decrease in the hysteretic damping coefficient of the related material, compared with the embankment dam with a central clay core. For this reason, both the (acceleration) amplification factor and the dynamic response of the embankment dam with an upstream

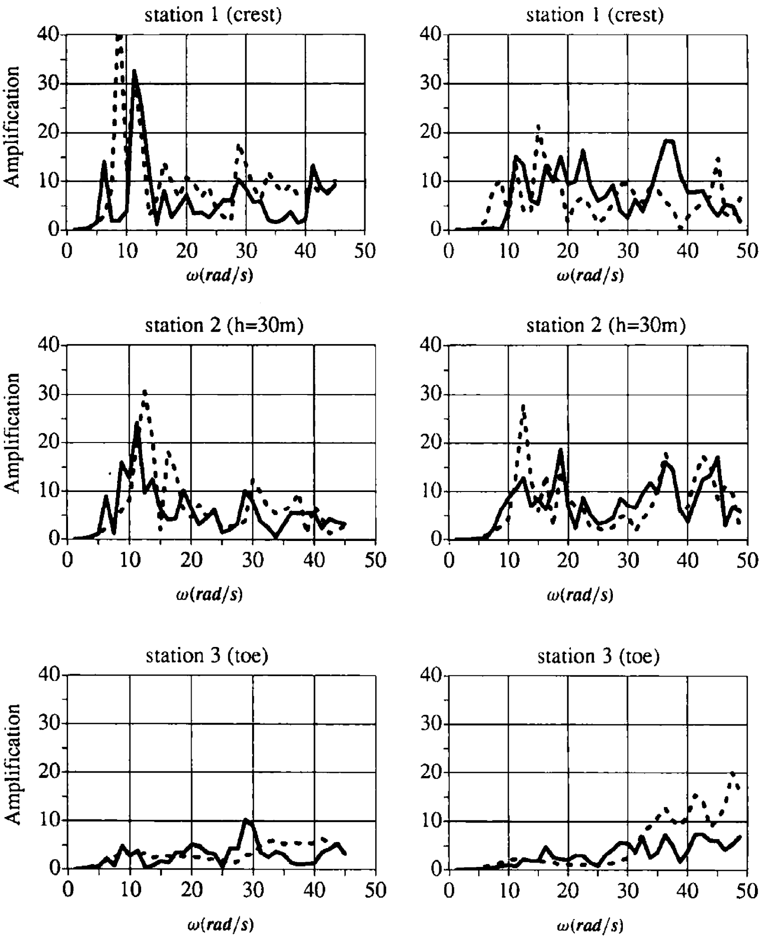

a) Upstream inclined concrete apron

b) Central clay core

Fig. 3.16 Response of the empty embankment dam on a layered foundation due to the P-wave vertical incidence

inclined concrete apron increase in the lower frequency range of excitation. It can be concluded that from the seismic resistance point of view, central clay cores are more suitable as impervious members for embankment dams. Since the dynamic response of an embankment dam–foundation system is dominated by the radiation damping of the system for higher frequency excitation, the (acceleration) amplification factors of the embankment dam with an upstream inclined concrete apron are almost the same as those with a central clay core because of the identical radiation damping of the foundation for both the upstream inclined concrete apron and the central clay core cases.

As shown in Figs. 3.15 and 3.16, there are many peaks in the dynamic response curves of the empty embankment dam on a layered foundation due to the unit harmonic SV-wave and P-wave vertical incidences. As the incident harmonic wave is applied on the wave input boundary consisting of a horizontal line, which is an interface between the finite elements and dynamic infinite elements, in the coupled computational model, it may result in significant different responses on the surfaces of two different foundation models. For the layered foundation model, the incident harmonic wave is applied to a wave input boundary within the underlying rock, instead of within the soil layer. When an incident harmonic wave propagates through the soil layer, the characteristics of the incident harmonic wave is changed significantly, so that the response curve on the top surface of the soil layer appears as many peaks due to the wave reflection and refraction within the soil layer. It is the propagating mechanism of an incident wave within a soil layer that makes the (acceleration) response curves of the embankment dam–layered foundation system with many peaks.

When the embankment dam is located on a homogeneous soil foundation, the (acceleration) response curves of the embankment dam–foundation system are comparatively smooth, as demonstrated in Figs. 3.17 and 3.18. This indicates that if the propagating mechanism of an incident wave, which propagates for the far field into the near field of the foundation, is considered in the coupled computational model, the foundation material has a significant influence on the dynamic response of the embankment dam–foundation system. Since the embankment dam and its layered foundation are considered as a whole system, the (acceleration) amplification factors of the embankment dam are quite high due to the amplification effect of the soil layer on the incident wave.

Figures 3.17 and 3.18 show the dynamic response of an empty embankment dam on a homogeneous soil foundation due to the unit harmonic SV-wave and P-wave vertical incidences. Again, the amplification factors of both the horizontal acceleration (marked by solid lines) and the vertical acceleration (marked by dashed lines) are used to display the dynamic response of the embankment dam–foundation system. In terms of the effect of impervious member types on the fundamental resonant frequency and amplification factors of the embankment dam, the same conclusions as those obtained in the layered foundation case can be made for the homogeneous soil foundation case. However, the (acceleration) amplification factors of the embankment dam on a homogeneous soil foundation are much smaller than those on a layered foundation. As mentioned previously, soil layers can cause greater amplification to the incident wave, resulting in an increase in the amplification factors of the embankment dam. Since the soil/rock layered foundation is much stiffer than the homogeneous soil foundation, the fundamental resonant frequency of the embankment dam on a homogeneous soil foundation is much smaller than that on a layered foundation. This indicates that the foundation material has a significant effect on the dynamic response of the embankment dam–foundation system. With an increase in the height of an embankment dam, the amplification factors of the embankment dam increase in most cases, due to the reflection and refraction of the incident wave on the surface of the embankment dam.

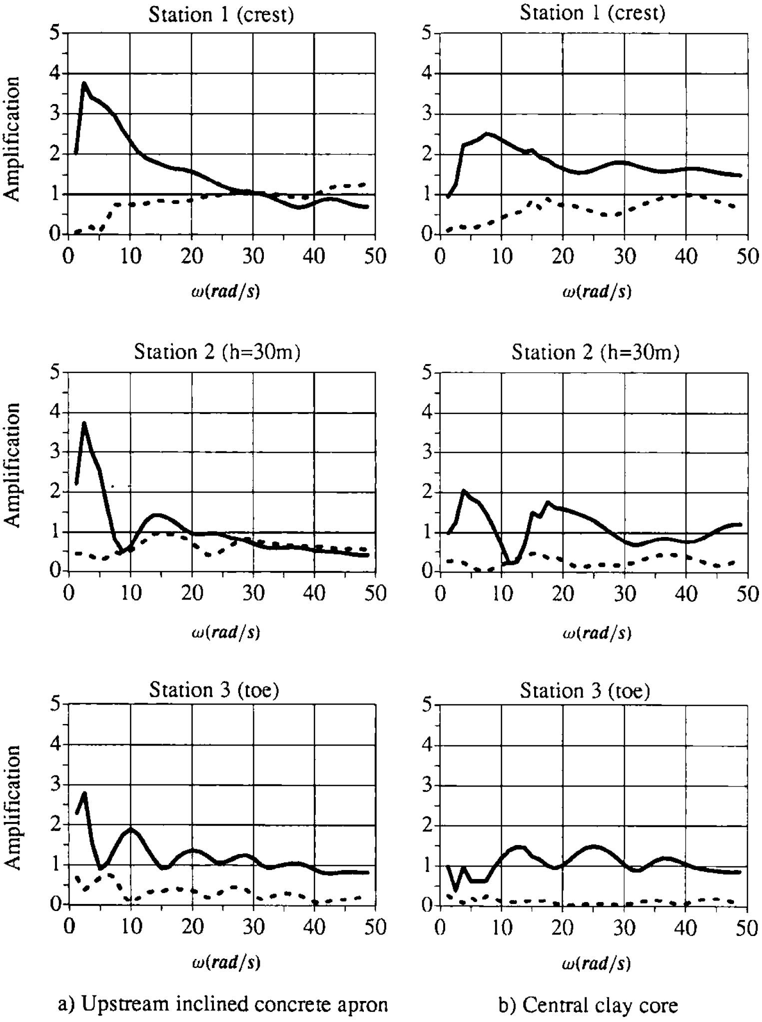

a) Upstream inclined concrete apron

b) Central clay core

Fig. 3.17 Response of the empty embankment dam on a homogeneous soil foundation due to the SV-wave vertical incidence

Figures 3.19, 3.20, 3.21 and 3.22 show the deformed shapes of different embankment dam–foundation systems due to SV-wave and P-wave vertical incidences with two different circular frequencies. It may be desired that these deformed shapes be plotted at the different fundamental resonant frequencies for different embankment dam–foundation systems. Since the fundamental resonant frequencies are different for the different embankment dam–foundation systems under consideration, for the purpose of demonstrating the effects of both impervious member types and foundation materials, the deformed shapes of different embankment dam–foundation systems are plotted for two circular frequencies, namely $\omega = 15\,\mathrm{rad\,s^{-1}}$ and

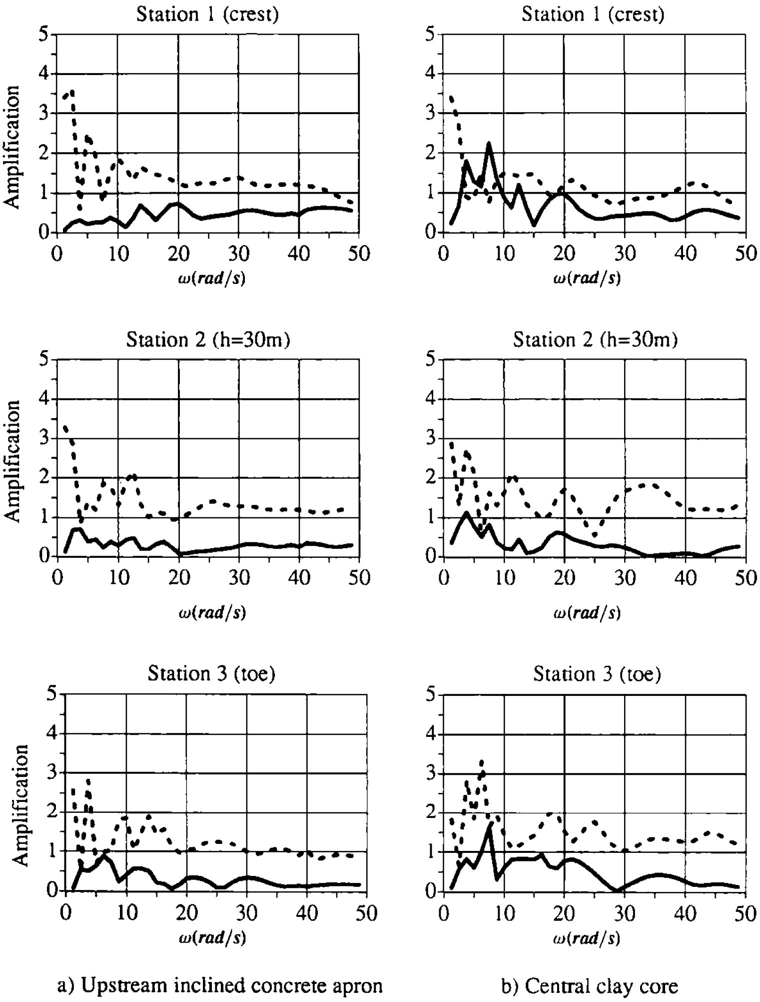

Fig. 3.18 Response of the empty embankment dam on a homogeneous soil foundation due to the P-wave vertical incidence

$\omega = 30\,\mathrm{rad\,s^{-1}}$. Note that the deformations in these figures have been exaggerated for the purpose of clear illustration.

For the vertically incident SV-wave with a circular frequency, $\omega = 15\,\mathrm{rad\,s^{-1}}$, the deformed shapes of the embankment dam are significantly affected by the foundation material rather than the impervious member type. However, for the vertically incident SV-wave with a higher circular frequency, $\omega = 30\,\mathrm{rad\,s^{-1}}$, the deformed shapes of the embankment dam depend on both the impervious member type and the foundation material. Since the frequencies considered for incident harmonic waves are within an appropriate range of a natural earthquake wave, it can be concluded

Fig. 3.19 Deformed shapes of the embankment dam due to the SV-wave vertical incidence ($\omega = 15\,\mathrm{rad\,s^{-1}}$)

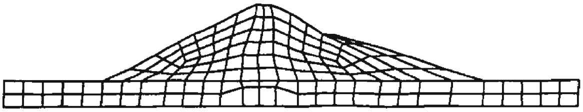

(a) Empty reservoir on homogeneous foundation
(Central clay core)

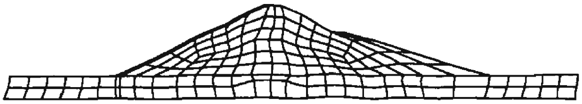

(b) Empty reservoir on homogeneous foundation
(Upstream inclined apron)

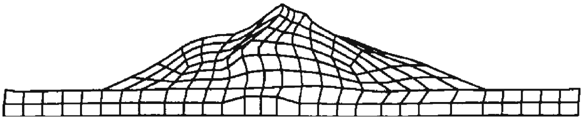

(c) Empty reservoir on layered foundation
(Central clay core)

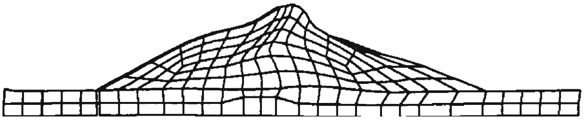

(d) Empty reservoir on layered foundation
(Upstream inclined apron)

that both the impervious member type and the foundation material have a significant effect on the seismic response of an embankment dam–foundation system. Compared with the SV-wave vertical incidence, the deformed shapes of the embankment dam due to the P-wave vertical incidence are different for all the cases studied, implying that incident wave types can have a significant influence on the dynamic response of an embankment dam–foundation system. Generally, the deformed shape of an embankment dam on a layered foundation is more complicated than that on a homogeneous soil foundation. This phenomenon is caused by the multiple reflection and refraction of waves within both the embankment dam and the layered soil.

3.2.2 Effects of Reservoir Bottom Sediments on the Dynamic Response of an Embankment Dam–Foundation System

For a central clay core dam with full impounded reservoir water, the water table within the dam body is too high to be neglected for the dynamic analysis of the embankment dam. However, when an embankment dam with an upstream inclined concrete apron is considered, even for a full impounded reservoir water, the water table behind the upstream inclined concrete apron is so low that it can be ignored

Fig. 3.20 Deformed shapes of the embankment dam due to the SV-wave vertical incidence ($\omega = 30$ rad s^{-1})

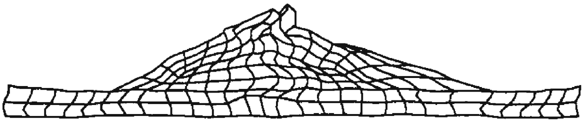

(a) Empty reservoir on homogeneous foundation
(Central clay core)

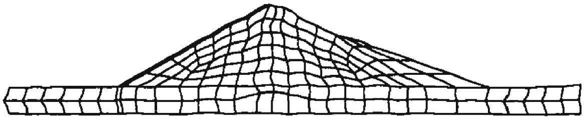

(b) Empty reservoir on homogeneous foundation
(Upstream inclined apron)

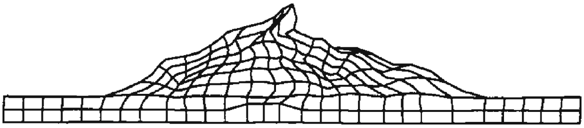

(c) Empty reservoir on layered foundation
(Central clay core)

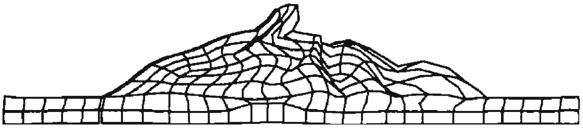

(d) Empty reservoir on layered foundation
(Upstream inclined apron)

for the dynamic analysis of the embankment dam without causing any considerable loss of accuracy.

Since the main purpose of this subsection is to investigate the effect of reservoir bottom sediments on the dynamic response of embankment dams, an embankment dam with an upstream inclined concrete apron, as shown in Fig. 3.23, is considered in this subsection. To emphasize the effect of reservoir bottom sediments, some factors, which may affect the dynamic response of embankment dams, such as the liquefaction of an embankment dam and the nonlinear behaviour of an embankment dam–foundation system, are neglected here. The material properties of the embankment dam and foundation are exactly the same as those used in the previous subsection. It is assumed that the reservoir bottom sediment is comprised of soft clay materials under unsaturated conditions, which is the most dangerous case (Cheng 1986) and may give a maximum estimation for the effect of reservoir bottom sediments on the dynamic response of the embankment dam.

For the reservoir bottom sediment, the following parameters are used in the coupled computational model of finite and dynamic infinite elements (in Fig. 3.23): the elastic modulus is 70×10^6 Pa; the value of Poisson's ratio is 0.3; the density of the sediment is $1750\,\mathrm{kg\,m^{-3}}$; the thickness is 5 m; the hysteretic damping coefficient

Fig. 3.21 Deformed shapes of the embankment dam due to the P-wave vertical incidence ($\omega = 15$ rad s^{-1})

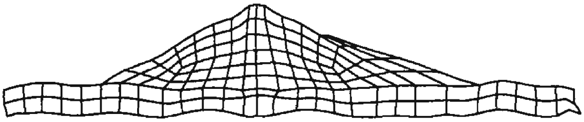

(a) Empty reservoir on homogeneous foundation (Central clay core)

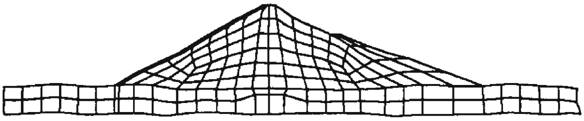

(b) Empty reservoir on homogeneous foundation (Upstream inclined apron)

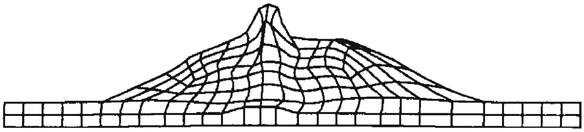

(c) Empty reservoir on layered foundation (Central clay core)

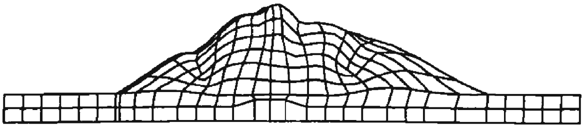

(d) Empty reservoir on layered foundation (Upstream inclined apron)

is 0.2; the corresponding shear wave within the rock foundation of the embankment dam is $124\,\mathrm{m\,s^{-1}}$. In order to examine the effect of incident wave types on the dynamic response of the embankment dam–water–sediment–foundation system, both a unit harmonic SV-wave and a unit harmonic P-wave are used as the incident waves for the coupled computational model of finite and dynamic infinite elements. To obtain accurate numerical results, the finite element mesh, which is used to simulate the near field of the whole embankment dam–water–sediment–foundation system, is fine enough to capture the travelling waves of minimum wavelength in the range of frequencies used in this subsection.

Figures 3.24 and 3.25 show the dynamic response of the embankment dam with an upstream inclined concrete apron due to the unit harmonic SV-wave and P-wave vertical incidences. In these figures, the amplification factor, which is defined as the ratio of the movement of a nodal point in the embankment dam to that of the incident wave, is used to exhibit the dynamic response of the embankment dam. To investigate the effect of reservoir bottom sediments on the dynamic response of the embankment dam, numerical results for three different cases, namely an empty reservoir, a full-reservoir-without-sediment and a full-reservoir-with-sediment, are displayed in these two figures (i.e. Figs. 3.24 and 3.25), where the solid and dashed lines represent the horizontal and vertical movements of a nodal point

Fig. 3.22 Deformed shapes of the embankment dam due to the P-wave vertical incidence ($\omega = 30$ rad s^{-1})

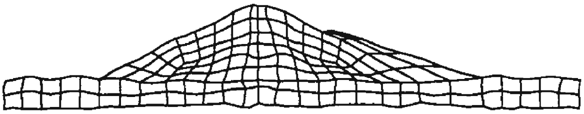

(a) Empty reservoir on homogeneous foundation (Central clay core)

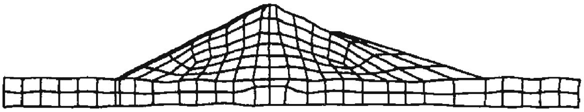

(b) Empty reservoir on homogeneous foundation (Upstream inclined apron)

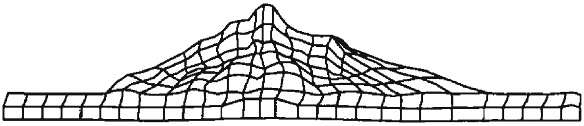

(c) Empty reservoir on layered foundation (Central clay core)

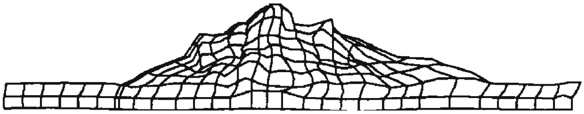

(d) Empty reservoir on layered foundation (Upstream inclined apron)

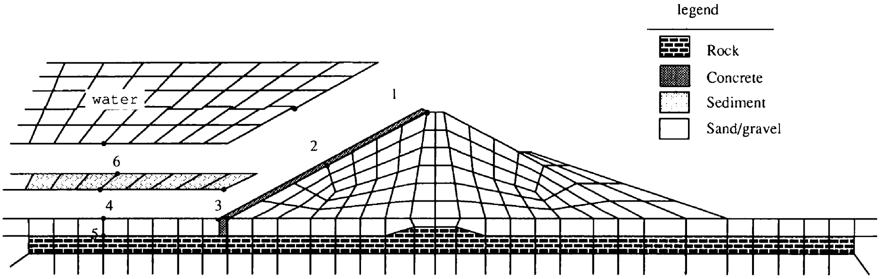

Fig. 3.23 Computational model of an embankment dam–water–sediment–foundation system

in the embankment dam. Compared with the empty reservoir case, the fundamental resonant frequency of the embankment dam–water–sediment–foundation system becomes small for a full reservoir with or without reservoir bottom sediments.

For a full reservoir, the total mass of the system including the reservoir water becomes somewhat larger, while the total stiffness of the embankment dam remains unchanged, compared with the empty reservoir case. Since the embankment dam–water–sediment–foundation is considered as a whole system, the reservoir water,

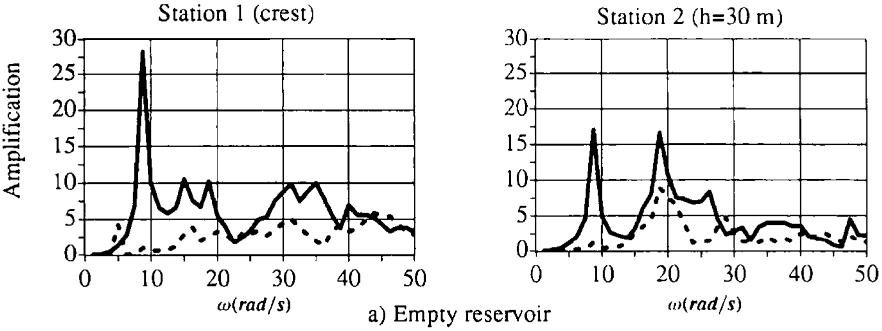

a) Empty reservoir

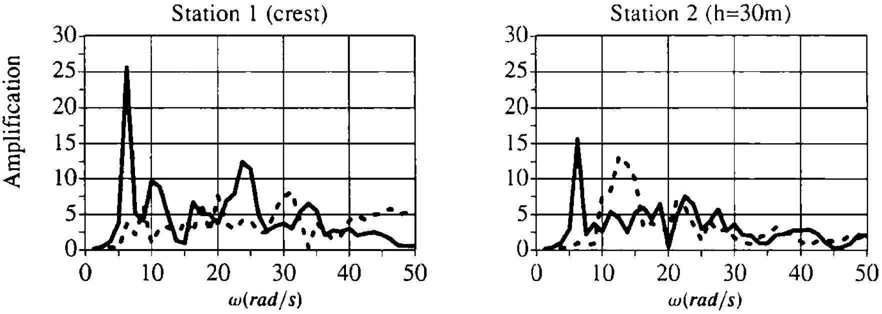

b) Full reservoir without sediment

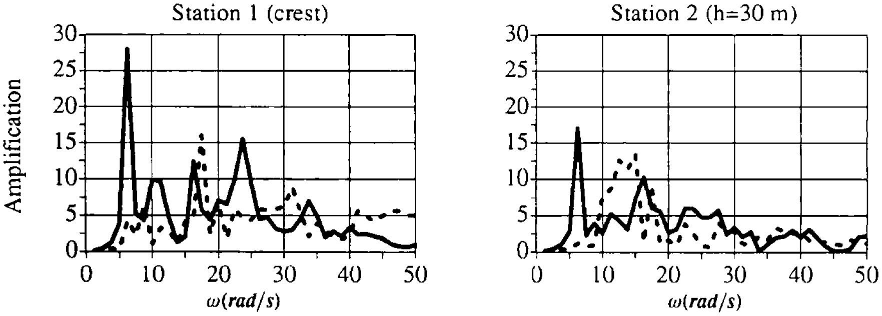

c) Full reservoir with sediment

Fig. 3.24 Response of the embankment dam with an upstream inclined concrete apron due to the SV-wave vertical incidence

which is assumed to extend through to infinity in the upstream direction of the embankment dam, can make a considerable contribution to the total mass of the system for an SV-wave vertical incidence. For the coupled computational model of finite and dynamic infinite elements (Zhao et al. 1987, 1989, 1991, 1992, 1995;

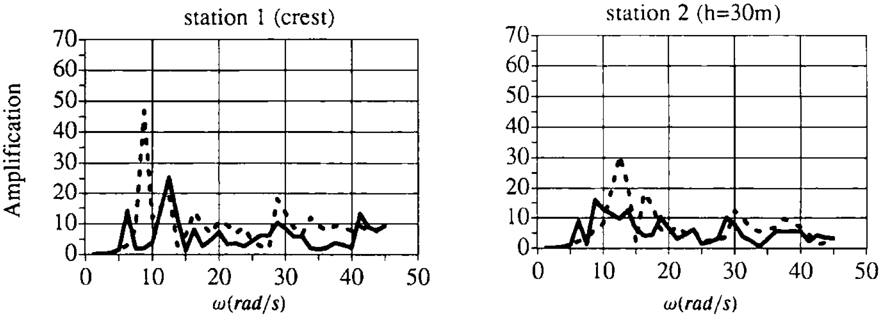

a) Empty reservoir

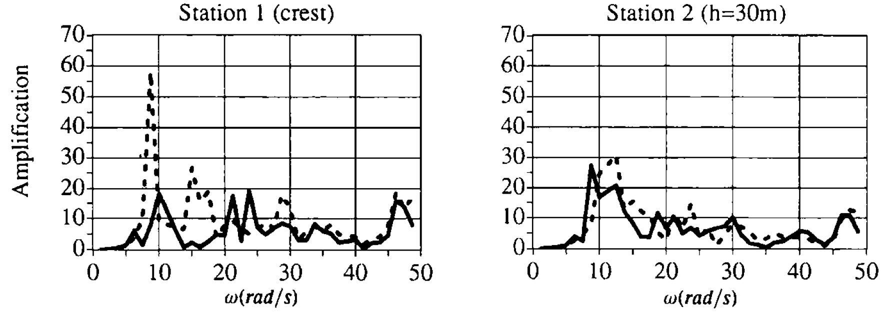

b) Full reservoir without sediment

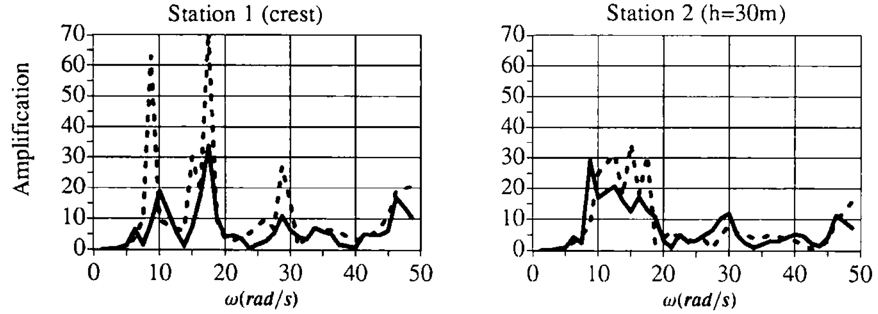

c) Full reservoir with sediment

Fig. 3.25 Response of the embankment dam with an upstream inclined concrete apron due to the P-wave vertical incidence

Zhao and Valliappan 1991, 1993a, b, c, Zhao and Xu 1994), the interaction effect at a water–solid interface can be treated as frequency-dependent masses, which are applied to the upstream surface of an embankment dam and the upper surface of a reservoir bottom sediment layer. For this reason, the coupled computational model of finite and dynamic infinite elements differs from the conventional dynamic

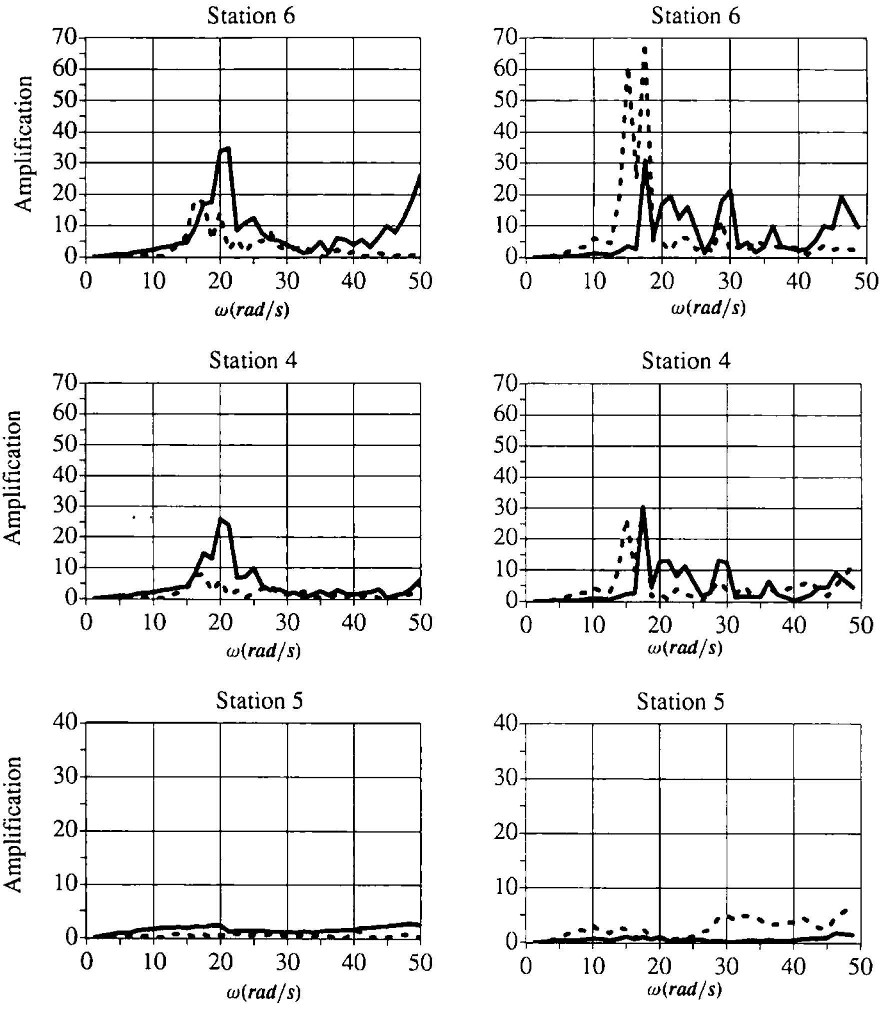

a) SV–wave incidence b) P–wave incidence

Fig. 3.26 Amplification effect of incident waves due to reservoir bottom sediments

analysis model (Hall and Copra 1982; Fenves and Chopra 1983, 1984, 1985), where either the domain of reservoir water is considered as a finite domain or the contribution of reservoir water to the mass of the upper surface of the reservoir bottom sediment layer is neglected.

For the SV-wave vertical incidence, the overall trend of the amplification factor of a nodal point in the embankment dam for the full-reservoir-without-sediment case is similar to that for the full-reservoir-with-sediment case, indicating that the reservoir bottom sediment has little influence on the amplification factor of the embankment dam–water–sediment–foundation system.

Since the reservoir bottom sediment has a little amplification to the incident SV-wave (Valliappan and Zhao 1992; Zhao et al. 1995), the induced hydrodynamic pressure on the inclined upstream surface of an embankment dam is smaller than that on the vertical upstream surface of a concrete gravity dam.

However, for the P-wave vertical incidence, the amplification factor of a nodal point in the embankment dam for the full-reservoir-with-sediment case is greater than that for the full-reservoir-without-sediment case, especially in the range of frequencies that are greater than the fundamental resonant frequency of the embankment dam–water–sediment–foundation system. This indicates that the reservoir bottom sediment has a considerable effect on the dynamic response of the embankment dam–water–sediment–foundation system for a P-wave vertical incidence. In order to gain insight into how the reservoir bottom sediment amplifies the incident wave on the upper surface of the sediment layer, the related numerical results are shown in Fig. 3.26, where the solid and dashed lines represent the horizontal and vertical movements respectively. In this figure, stations 4 and 6 denote the sediment–soil interface and the water–sediment interface, respectively, while station 5 denotes the soil–rock interface within the dam foundation.

These numerical results indicate that the reservoir bottom sediment has little amplification effect on the vertically incident SV-wave. For example, the maximum value of the amplification factor due to the sediment layer itself is about 35/25, which is the ratio of the maximum value of the amplification at the water–sediment interface (i.e. station 6) to that at the sediment–soil interface (i.e. station 4). However, for the P-wave vertical incidence, the maximum value of the amplification factor due to the sediment layer itself is about 68/25, indicating that the movement at the water–sediment interface for the P-wave vertical incidence is stronger than that for the SV-wave vertical incidence. Since the vertical movement at the water–sediment interface due to a P-wave vertical incidence has a much greater influence on the hydrodynamic pressure (at the upstream surface of the embankment dam) than the horizontal movement at the water–sediment interface due to an SV-wave vertical incidence, the dynamic response of the embankment dam–water–sediment–foundation system due to the P-wave vertical incidence is much stronger than that due to the SV-wave vertical incidence. This indicates that consideration of the incident wave type is important for the dynamic analysis of embankment dams when the dynamic embankment dam–water–sediment–foundation interaction is included in the coupled computational model of finite and dynamic infinite elements.

Figures 3.27 and 3.28 show the deformed shapes of the embankment dam with an upstream inclined concrete apron due to the unit harmonic SV-wave and P-wave vertical incidences with several frequencies, respectively. The related numerical results indicate that the deformed shapes obtained from the full-reservoir-without-sediment case are considerably different from those obtained from the full-reservoir-with-sediment case, implying that the reservoir bottom sediment has a considerable effect on the deformed shapes of the embankment dam for both SV-wave and P-wave vertical incidences. This further demonstrates that the consideration of the reservoir bottom sediment is important for the dynamic stability analysis of embankment dams.

Fig. 3.27 Deformed shapes of the embankment dam with an upstream inclined concrete apron due to the SV-wave vertical incidence

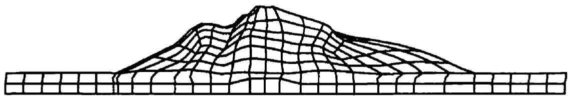

a) Full reservoir without sediment (ω =15 rad/s)

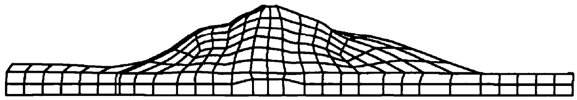

b) Full reservoir with sediment (ω=15 rad/sec)

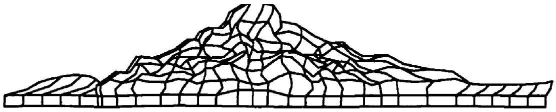

c) Full reservoir without sediment (ω =30 rad/s)

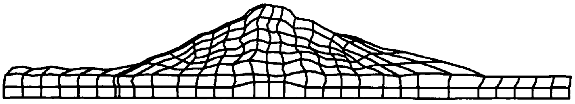

d) Full reservoir with sediment (ω=30 rad/s)

Fig. 3.28 Deformed shapes of the embankment dam with an upstream inclined concrete apron due to the P-wave vertical incidence

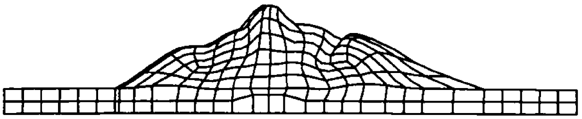

a) Full reservoir without sediment (ω=15 red/s)

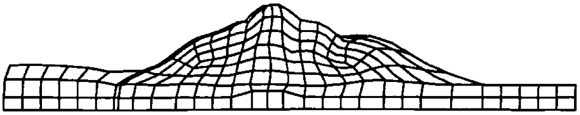

b) Full reservoir with sediment (ω =15 rad/s)

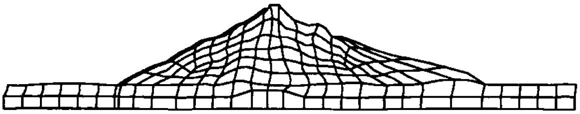

c) Full reservoir without sediment (ω=30 rad/s)

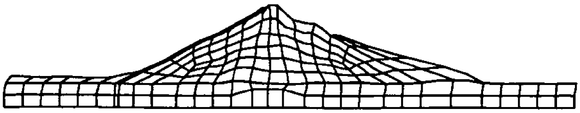

d) Full reservoir with sediment (ω=30 rad/s)

Chapter 4
Application of Two-Dimensional Dynamic Infinite Elements: Simulation of Wave Scattering Effects under Different Canyon Topographical and Geological Conditions

Previous studies related to the surface motion of wave propagation demonstrated that the topographical and geological features of a canyon have a significant influence on the motions of the ground (Bouchon 1973; Rogers et al. 1974; Datta and El-Akily 1978; Bard 1982; Shah et al. 1982, 1983; Dravinski 1983; Toki and Sato 1983; Ohtsuki and Harumi 1984; Zahradnik and Urban 1984; Sanchez-Sesma et al. 1985; Wong et al. 1985; Geli et al. 1988; Zhao and Valliappan 1993a, b). This fact may have an important impact on the dynamic response of such large-scale structures as dams and bridges, because free-field motions have obviously different amplitudes and phases along an abutment on which a structure is founded. One of the key questions associated with the selection of a dam or bridge site is to investigate which kind of canyon is more beneficial to the cost and safety of a structure, from a seismic resistance point of view. As illustrated in previous studies (Zhao 1987; Zhang and Zhao 1988), the amplitude and phase differences of the ground motion can affect the dynamic response of a massive structure dramatically, so that it is necessary to carry out a detailed study on the distribution of the free-field motion along a natural canyon. This work may have great significance in engineering practice.

From the point of view of wave motion theory, the analysis of a free-field motion can be attributed to a wave scattering problem in an infinite medium. An earthquake wave usually originates from an epicentre and propagates in the infinite medium. When the earthquake wave reaches a canyon or a structure, wave reflection and scattering take place, so that the resulting free-field motion should be a sum of the incident earthquake-wave field and the scattered wave field. As an earthquake wave propagating in an elastic medium can be decomposed into a sum of several harmonic waves, it is convenient to use a harmonic wave for investigating the distribution characteristics of free-field motions. Once a dynamic analysis for the distribution characteristics of free-field motions due to harmonic waves is made, it is straightforward to extend the analysis to an earthquake-wave-incident case using the FFT (i.e. Fast Fourier Transform) technique. For this reason, both harmonic and seismic waves are used to examine the effects of canyon topographical and geological conditions on ground motions due to P-wave and SV-wave incidences from the far field of the canyon.

C. Zhao, *Dynamic and Transient Infinite Elements*, Advances in Geophysical and Environmental Mechanics and Mathematics, DOI 10.1007/978-3-642-00846-7_4,

Regarding the effects of the canyon topographical and geological conditions on the ground motions, theoretical studies, which were initiated in the 1960s, were mainly devoted to the reflection and diffraction behaviours of SH-waves on ground surfaces (Asano 1966; McIvor 1969; Boor 1972). Trifunac (1973) and Wong and Trifunac (1974) obtained analytical solutions for SH-wave scattering along semi-circular and semi-elliptical canyons using both variable separation techniques and special functions. Because of the complexity of the problem, pure analytical solutions were restricted not only to very simple topographical and geological conditions, but also to the incidences of simple wave types such as SH-waves. With the development of computational techniques, many different numerical methods, such as the discrete wavenumber method (Aki and Larner 1970), the finite element method (Reimer et al. 1974; Smith 1975), the boundary integral equation method (Wong and Jennings 1975; Sanchez-Sesma 1983), the general inverse method (Wong 1982), the wave function approach (Eshraghi and Dravinski 1989a, b) and the discrete wavenumber boundary element method (Kawase 1988; Khair et al. 1989) were presented for solving wave scattering problems along canyons of more complicated geometrical shapes. Among these methods, the finite element method is very powerful, because the complexities of geometrical and geological conditions in a natural canyon can be easily simulated.

Using the finite element method for wave scattering problems, Reimer et al. (1974) and Smith (1975) conducted some pioneering work. In the work of Reimer et al. (1974), finite elements were used to simulate a dam and its foundation. Using the assumption of a massless foundation, a uniform earthquake model, in which the wave-propagation effects in the foundation were ignored, was used to input the earthquake load. This wave input model has obvious drawbacks and has been improved by Clough et al. (1985). In Smith's work on the wave-propagation problem (Smith 1975), finite elements and non-reflecting boundaries were used to simulate the infinite foundation, and initial displacements were applied to the wave input boundary of the finite element model. The common drawbacks of using these early finite element models to simulate an infinite foundation is that one cannot consider both the simulation of the infinite foundation and the earthquake-wave-input mechanism appropriately at the same time. To overcome these drawbacks, Zhao (1987) presented a wave-input procedure for wave propagation in an infinite foundation. In Zhao's wave-input procedure, a natural infinite foundation was simulated using a coupled computational model of finite and dynamic infinite elements, and an earthquake wave was applied to a wave-input boundary within the coupled computational model. For ease of computation, the wave-input boundary was assumed to be a horizontal line in the underlying rock (Zhao 1987; Zhao et al. 1992; Zhao and Valliappan 1993a, b). The seismic force on the wave-input boundary can be evaluated by considering the characteristics of the input earthquake wave. Zhao's original work was used to simulate SH-wave, SV-wave and P-wave scattering problems in infinite foundations (Zhang and Zhao 1988; Zhao and Valliappan 1993a, b).

Taking into consideration both geometrical and geological complexities and the infinite extent of natural canyons, a coupled computational model of finite and dynamic infinite elements is used, in this chapter, for investigating the effects of canyon topographical and geological conditions on the ground motions due to P- and SV-wave incidences. In the coupled computational model, the near field of a canyon is simulated using finite elements, while the far field of the canyon is simulated using dynamic infinite elements. Several topographical conditions, represented by trapezoidal and V-shaped canyons with different ratios of top width to height (L/H), are considered in the corresponding coupled computational models, when both P- and SV-waves with different incident angles propagate from the far fields into the near fields of these different canyons. The amplification factors and distribution patterns of displacements along canyon surfaces are used to show the effects of canyon topographical conditions on the ground motions. To examine the effects of geological conditions on the ground motions, weathered rock layers on the canyon surfaces are considered in the corresponding coupled computational models, in which the different ratio of the elastic modulus of a weathered rock layer to that of the underlying rock is used to represent different geological conditions of the canyon.

4.1 Simulation of Infinite Domain of a Canyon

In dealing with wave-propagation problems in infinite domains with geometrical and geological complexities, the coupled computational model of finite and dynamic infinite elements has been proven very effective (Chow and Smith 1981; Medina and Taylor 1983; Zhang and Zhao 1987, 1988; Zhao et al. 1989, 1991, 1992; Zhao and Valliappan 1993a, b). In this chapter, eight-node isoparametric finite elements are used to simulate the near field of a canyon. Their formulations are well known (Zienkiewicz 1977) and therefore, need not to be repeated. Since the previous two-dimensional dynamic infinite element (Zhang and Zhao 1987, 1988; Zhao et al. 1992) has only one wavenumber to represent the displacement shape function of the element, it is necessary to develop another kind of two-dimensional dynamic infinite element, in which both the P wavenumber and SV wavenumber are used to express the displacement shape function of the element due to the coexistence of these two waves in wave-scattering problems along a canyon.

For the two-dimensional six-node dynamic infinite element shown in Fig. 4.1, since the sides of the element in the ξ direction can be represented by straight lines, four nodes are sufficient to describe exactly the geometry of the two-dimensional six-node dynamic infinite element in the global coordinate system. The

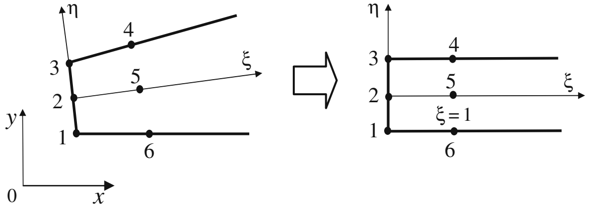

Fig. 4.1 Two-dimensional six-node dynamic infinite element: nodes 1, 2 and 3 are the end nodes to be connected with a finite element; nodes 4, 5 and 6 are the middle nodes with $\xi = 1$

mapping relationship between the global and local coordinate systems for this two-dimensional six-node dynamic infinite element can be expressed as follows:

$$x = \sum_{q=1}^{6} M_q x_q, \tag{4.1}$$

$$y = \sum_{q=1}^{6} M_q y_q, \tag{4.2}$$

where x_q and y_q are the nodal coordinates of the two-dimensional six-node dynamic infinite element in the x and y directions, respectively; M_q (q=1, 2, ..., 6) is the mapping function of the two-dimensional six-node dynamic infinite element:

$$M_1 = \frac{1}{2}(\xi - 1)(\eta - 1), \tag{4.3}$$

$$M_2 = M_5 = 0, \tag{4.4}$$

$$M_3 = -\frac{1}{2}(\xi - 1)(\eta + 1), \tag{4.5}$$

$$M_4 = \frac{1}{2}\xi(\eta + 1), \tag{4.6}$$

$$M_6 = -\frac{1}{2}\xi(\eta - 1). \tag{4.7}$$

Note that for the convenience of expressing the coordinate mapping relationship, M_2 and M_5 are set to zero for the two-dimensional six-node dynamic infinite element.

Consideration of the displacement compatibility condition on the connected interface between a two-dimensional eight-node isoparametric finite element and a two-dimensional six-node dynamic infinite element yields the following displacement shape functions for the two-dimensional six-node dynamic infinite element:

$$N_q = P_q(\xi)\frac{\eta(\eta - 1)}{2} \qquad (q = 1, 6), \tag{4.8}$$

$$N_q = -P_q(\xi)(\eta + 1)(\eta - 1) \qquad (q = 2, 5), \tag{4.9}$$

$$N_q = P_q(\xi)\frac{\eta(\eta + 1)}{2} \qquad (q = 3, 4), \tag{4.10}$$

where $P_q(\xi)$ ($q = 1, 2, \ldots, 6$) is the wave-propagation function of the two-dimensional six-node dynamic infinite element; N_q ($q = 1, 2, \ldots, 6$) is the displacement shape function of the two-dimensional six-node dynamic infinite element. It can be determined by investigating the harmonic wave-propagation behaviour in an infinite medium (Zhao et al. 1992; Zhao and Valliappan 1993b). When an isotropic homogeneous elastic half-space is subjected to a harmonic loading, the induced harmonic waves propagate from the vibration source into the far field of the half-space. The analytical solution for this problem can be expressed using the special functions, known as Bessel functions and Hankel functions (Graff 1975; Medina and Taylor 1983). For the far field of the half-space, the asymptotic behaviour of these special functions can be approximately expressed as a combination of several exponential functions. The physical explanation for this is that the induced waves in the far field of the half-space can be approximately represented using superposition of plane harmonic waves. Based on this recognition and consideration of the induced wave with multiple wavenumbers, the general form of the wave propagation function for the two-dimensional six-node dynamic infinite element can be expressed as follows:

$$P_q(\xi) = \exp(-\alpha\xi)\left[c_1\exp(-i\beta_1\xi) + c_2\exp(-i\beta_2\xi)\right] \qquad (q = 1, 2, \ldots, 6), \tag{4.11}$$

where α is the nominal decay coefficient that is used to express the wave amplitude attenuation due to both the wave energy dissipation in the two-dimensional six-node dynamic infinite element and the geometric divergence of the two-dimensional six-node dynamic infinite element. Note that the determination of α was addressed in Chap. 2. β_1 and β_2 are two nominal wavenumbers corresponding to an S-wave and P-wave in the two-dimensional six-node dynamic infinite element. These nominal wavenumbers are used to express the phase characteristics of the wave propagation in the two-dimensional six-node dynamic infinite element. c_1 and c_2 are two constants to be determined by matching the displacement field of the two-dimensional six-node dynamic infinite element with that of the infinite medium.

Based on the equality condition of nodal displacements at any infinite side of the two-dimensional six-node dynamic infinite element in the ξ direction, c_1 and c_2 in Eq. (4.11) can be determined. With one side of the two-dimensional six-node dynamic infinite element (with nodes 1 and 6) taken as an example, the following relationships exist:

$$\begin{Bmatrix} u_1 \\ u_6 \end{Bmatrix} = \begin{bmatrix} 1 & 1 \\ \exp[-(\alpha + i\beta_1)] & \exp[-(\alpha + i\beta_2)] \end{bmatrix} \begin{Bmatrix} c_1 \\ c_2 \end{Bmatrix} = [C] \begin{Bmatrix} c_1 \\ c_2 \end{Bmatrix}. \tag{4.12}$$

Solving Eq. (4.12) yields the following solution for c_1 and c_2:

$$\begin{Bmatrix} c_1 \\ c_2 \end{Bmatrix} = [C]^{-1} \begin{Bmatrix} u_1 \\ u_6 \end{Bmatrix}. \tag{4.13}$$

If Eqs. (4.8), (4.9), (4.10), (4.11), (4.12) and (4.13) are considered simultaneously, then $P_q(\xi)$ (q=1, 2, …, 6) can be expressed as follows:

$$P_q(\xi) = \frac{1}{\Delta}\{\exp[-(\alpha + i\beta_2)]\exp[-(\alpha + i\beta_1)\xi] \\ - \exp[-(\alpha + i\beta_1)]\exp[-(\alpha + i\beta_2)\xi]\} \qquad (q = 1, 2, 3), \tag{4.14}$$

$$P_q(\xi) = \frac{1}{\Delta}\{-\exp[-(\alpha + i\beta_1)\xi] + \exp[-(\alpha + i\beta_2)\xi]\} \qquad (q = 4, 5, 6), \tag{4.15}$$

$$\Delta = \exp[-(\alpha + i\beta_2)] - \exp[-(\alpha + i\beta_1)]. \tag{4.16}$$

Note that a sufficient condition for the existence of $P_q(\xi)$ ($q = 1, 2, \ldots, 6$) in the two-dimensional six-node dynamic infinite element is that β_1 and β_2 are two different constants. This condition can be satisfied for simulating wave-propagation problems in an infinite medium, because an S-wave and a P-wave have two different wavenumbers in the infinite medium.

In addition, the following expression for the wave-propagation function of the two-dimensional six-node dynamic infinite element holds:

$$P_q(\xi_r) = \delta_{qr} \qquad (q = 1, 2, \ldots, 6;\ r = 1, 2, \ldots, 6), \tag{4.17}$$

where δ_{qr} is the Kronecker delta. This implies that for any displacement shape function N_q ($q = 1, 2, \ldots, 6$), $N_q = 1$ when $\xi = \xi_q$ and $\eta = \eta_q$, while $N_q = 0$ when $\xi = \xi_r$ and $\eta = \eta_r$, where $r \neq q$.

By following the same procedures as those used in the finite element method (Zienkiewicz 1977; Zhao et al. 1992), both the mass matrix and the stiffness matrix of the two-dimensional six-node dynamic infinite element can be expressed as follows:

$$[M]^e = \int_{-1}^{1}\int_{0}^{\infty} [N]^T \rho [N]\, |J|\, d\xi d\eta, \tag{4.18}$$

$$[K]^e = \int_{-1}^{1}\int_{0}^{\infty} [B]^T [D^*][B]\, |J|\, d\xi d\eta, \tag{4.19}$$

where $[B]$ and $[N]$ are the strain matrix and shape function matrix of the two-dimensional six-node dynamic infinite element; $[D^*]$ is the constitutive matrix of the element material; $|J|$ is the Jacobian determinant, which can be determined using the mapping relationship of the element (in Eqs. (4.1) and (4.2)); ρ is the density of the element material.

Using the displacement shape functions expressed in Eqs. (4.8), (4.9) and (4.10), the displacement field within this two-dimensional six-node dynamic infinite element can be expressed as follows:

$$u = \sum_{q=1}^{6} N_q u_q, \tag{4.20}$$

$$v = \sum_{q=1}^{6} N_q v_q, \tag{4.21}$$

where N_q ($q = 1, 2, \ldots, 6$) is the displacement shape functions of the two-dimensional six-node dynamic infinite element.

Equations (4.20) and (4.21) can be written in the matrix form:

$$\begin{Bmatrix} u \\ v \end{Bmatrix}^e == [N]\{\Delta\}^e, \tag{4.22}$$

where $[N]$ is the shape function matrix of the two-dimensional six-node dynamic infinite element; $\{\Delta\}^e$ is the nodal displacement vector of the element. They are of the following forms:

$$[N] = \begin{bmatrix} N_1 & 0 & N_2 & 0 & N_3 & 0 & N_4 & 0 & N_5 & 0 & N_6 & 0 \\ 0 & N_1 & 0 & N_2 & 0 & N_3 & 0 & N_4 & 0 & N_5 & 0 & N_6 \end{bmatrix}, \tag{4.23}$$

$$\{\Delta\}^e = \left\{ u_1 \; v_1 \; u_2 \; v_2 \; u_3 \; v_3 \; u_4 \; v_4 \; u_5 \; v_5 \; u_6 \; v_6 \right\}^T. \tag{4.24}$$

Using the above definitions, the strain matrix of the two-dimensional six-node dynamic infinite element can be expressed as follows:

$$\{\varepsilon\}^e = \begin{Bmatrix} \frac{\partial u}{\partial x} \\ \frac{\partial v}{\partial y} \\ \frac{\partial u}{\partial y} + \frac{\partial v}{\partial x} \end{Bmatrix} = [B]\{\Delta\}^e, \tag{4.25}$$

where $[B]$ is the strain matrix of the two-dimensional six-node dynamic infinite element; $\{\varepsilon\}^e$ is the strain vector of the element. The strain matrix of the dynamic infinite element can be further expressed as

$$[B] = \begin{bmatrix} \frac{\partial N_1}{\partial x} & 0 & \frac{\partial N_2}{\partial x} & 0 & \frac{\partial N_3}{\partial x} & 0 & \frac{\partial N_4}{\partial x} & 0 & \frac{\partial N_5}{\partial x} & 0 & \frac{\partial N_6}{\partial x} & 0 \\ 0 & \frac{\partial N_1}{\partial y} & 0 & \frac{\partial N_2}{\partial y} & 0 & \frac{\partial N_3}{\partial y} & 0 & \frac{\partial N_4}{\partial y} & 0 & \frac{\partial N_5}{\partial y} & 0 & \frac{\partial N_6}{\partial x} \\ \frac{\partial N_1}{\partial y} & \frac{\partial N_1}{\partial x} & \frac{\partial N_2}{\partial y} & \frac{\partial N_2}{\partial x} & \frac{\partial N_3}{\partial y} & \frac{\partial N_3}{\partial x} & \frac{\partial N_4}{\partial y} & \frac{\partial N_4}{\partial x} & \frac{\partial N_5}{\partial y} & \frac{\partial N_5}{\partial x} & \frac{\partial N_6}{\partial y} & \frac{\partial N_6}{\partial x} \end{bmatrix}. \tag{4.26}$$

To evaluate the strain matrix of the two-dimensional six-node dynamic infinite element, it is necessary to calculate the first derivatives of the displacement shape functions with respect to the local ξ and η coordinates as follows:

$$\frac{\partial N_q}{\partial \xi} = \frac{\partial N_q}{\partial x}\frac{\partial x}{\partial \xi} + \frac{\partial N_q}{\partial y}\frac{\partial y}{\partial \xi} \qquad (q = 1, 2, \ldots, 6), \tag{4.27}$$

$$\frac{\partial N_q}{\partial \eta} = \frac{\partial N_q}{\partial x}\frac{\partial x}{\partial \eta} + \frac{\partial N_q}{\partial y}\frac{\partial y}{\partial \eta} \qquad (q = 1, 2, \ldots, 6). \tag{4.28}$$

Equations (4.27) and (4.28) can be readily expressed in the following matrix form:

$$\begin{Bmatrix} \frac{\partial N_q}{\partial \xi} \\ \frac{\partial N_q}{\partial \eta} \end{Bmatrix} = \begin{bmatrix} \frac{\partial x}{\partial \xi} & \frac{\partial y}{\partial \xi} \\ \frac{\partial x}{\partial \eta} & \frac{\partial y}{\partial \eta} \end{bmatrix} \begin{Bmatrix} \frac{\partial N_q}{\partial x} \\ \frac{\partial N_q}{\partial y} \end{Bmatrix} = [J] \begin{Bmatrix} \frac{\partial N_q}{\partial x} \\ \frac{\partial N_q}{\partial y} \end{Bmatrix} \qquad (q = 1, 2, \ldots, 6), \tag{4.29}$$

where the matrix $[J]$, called the Jacobian matrix, is given by the following equation:

$$[J] = \begin{bmatrix} \frac{\partial x}{\partial \xi} & \frac{\partial y}{\partial \xi} \\ \frac{\partial x}{\partial \eta} & \frac{\partial y}{\partial \eta} \end{bmatrix}. \tag{4.30}$$

Substituting Eqs. (4.1) and (4.2) into Eq. (4.30) yields the final expression for the Jacobian matrix as follows:

$$[J] = \begin{bmatrix} \sum\limits_{q=1}^{6} \left(\frac{\partial M_q}{\partial \xi} x_q \right) & \sum\limits_{q=1}^{6} \left(\frac{\partial M_q}{\partial \xi} y_q \right) \\ \sum\limits_{q=1}^{6} \left(\frac{\partial M_q}{\partial \eta} x_q \right) & \sum\limits_{q=1}^{6} \left(\frac{\partial M_q}{\partial \eta} y_q \right) \end{bmatrix}. \tag{4.31}$$

Therefore, the first derivatives of the displacement shape functions with respect to the global x and y coordinates can be expressed as follows:

$$\begin{Bmatrix} \frac{\partial N_q}{\partial x} \\ \frac{\partial N_q}{\partial y} \end{Bmatrix} = [J]^{-1} \begin{Bmatrix} \frac{\partial N_q}{\partial \xi} \\ \frac{\partial N_q}{\partial \eta} \end{Bmatrix} \qquad (q = 1, 2, \ldots, 6). \tag{4.32}$$

Mathematically, the value of the Jacobian determinant $|J|$ can be determined from the Jacobian matrix $[J]$.

For the plane strain problem, the constitutive matrix of the element material can be expressed in the following form:

$$\left[D^*\right] = \frac{E(1 + i\eta_d)}{1 + \mu} \begin{bmatrix} \frac{1-\mu}{1-2\mu} & \frac{\mu}{1-2\mu} & 0 \\ \frac{\mu}{1-2\mu} & \frac{1-\mu}{1-2\mu} & 0 \\ 0 & 0 & \frac{1}{2} \end{bmatrix}, \tag{4.33}$$

where E and μ are the elastic modulus and Poisson's ratio of the element material, respectively; η_d is the hysteretic damping coefficient of the element material.

Substituting Eqs. (4.23), (4.26) and (4.33) into Eqs. (4.18) and (4.19) yields the following generalized integral for the evaluation of the mass and stiffness matrices of the two-dimensional six-node dynamic infinite element:

$$I = \int_0^{\infty} F(\xi) \exp\left[-(2\alpha + i\beta_q + i\beta_r)\xi\right] d\xi \qquad (q = 1, 2;\ r = 1, 2). \tag{4.34}$$

To evaluate the generalized integral using the numerical integration technique (Chow and Smith 1981; Zhang and Zhao 1987), the following definition is introduced:

$$\beta = \frac{\beta_q + \beta_r}{2} \qquad (q = 1, 2;\ r = 1, 2). \tag{4.35}$$

As a result, Eq. (4.34) can be evaluated using the numerical integration technique described in Sect. 2.1.1.

To investigate the accuracy of the proposed two-dimensional six-node dynamic infinite element, a coupled computational model of two-dimensional eight-node finite elements and six-node dynamic infinite elements is used for simulating a wave propagation problem in an elastic half-plane under a unit harmonic SV-wave vertical incidence. Figure 4.2 shows the coupled computational model, in which the near field of the half-plane is simulated using two-dimensional eight-node isoparametric finite elements, while the far field of the half-plane is simulated using two-dimensional six-node dynamic infinite elements. The two bottom corners of the computational model are simulated using two degenerated two-dimensional six-node dynamic infinite elements, in which nodes 1, 2 and 3 are coincident. The horizontal line ($Y = 0$) of infinite length is used as the wave-input boundary (Zhao et al. 1992; Zhao and Valliappan 1993a, b), which can be divided into two parts. The first part is comprised of the horizontal interface (at $Y = 0$) between finite and dynamic infinite elements, while the second part is comprised of the interfaces between two normal dynamic infinite elements and two degenerated dynamic infinite elements. A unit harmonic wave is considered to propagate vertically from the far field beneath the wave input boundary into the near field of the computational model. For the purpose of investigating the horizontal length effects of the first part of the wave-input boundary on the accuracy of numerical results, three different lengths represented by three different values of α (i.e. $\alpha = 2$, 3 and 4 in Fig. 4.2) are considered in the

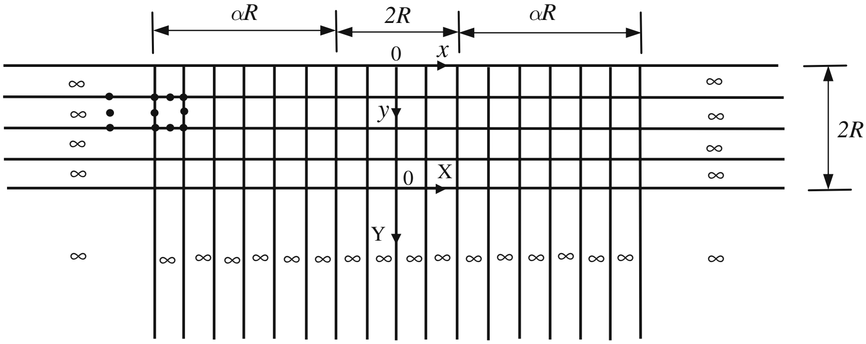

Fig. 4.2 Computational model of eight-node finite and six-node infinite elements for a wave-reflection problem in an elastic half-plane ($\alpha = 2, 3, 4$): the near field is simulated using eight-node finite elements, while the far field is simulated using six-node dynamic infinite elements

corresponding computational models. Note that with an increase in the value of α, the number of the two-dimensional eight-node finite elements is increased accordingly, so that the critical element size requirement is satisfied.

Tables 4.1 and 4.2 show the distribution of displacement amplitudes along the surface of the half-plane due to plane SV-wave vertical incidences with two different frequencies. In these two tables, A_U is the amplitude of the horizontal displacement; δ_1 is the relative error; and a_0 is a dimensionless frequency with the following definition: $a_0 = \omega R/(\pi C_{SV})$, where ω and C_{SV} are the circular frequency and velocity of the incident SV-wave, respectively. Note that for a unit harmonic SV-wave vertical incidence, the theoretical value for the amplitude of the horizontal displacement on the surface of an elastic homogeneous half-plane is equal to 2 (Graff 1975; Zhao et al. 1992).

As expected, the horizontal length of the first part of the wave-input boundary, which is represented by the value of α, has a significant effect on the accuracy of the numerical results. With the SV-wave vertical incidence and $a_0 = 0.5$ taken as an example, when $\alpha = 2$, the maximum relative error can reach 19%, while for $\alpha = 3$ and $\alpha = 4$, the corresponding maximum relative error can be reduced to 9.5 and 4%, respectively. This demonstrates that so long as the horizontal length of the first part of the wave-input boundary is appropriate, accurate numerical results can be obtained from the coupled computational model of two-dimensional eight-node finite elements and six-node dynamic infinite elements.

For the SV-wave vertical incidence with a higher frequency, $a_0 = 1.0$, for most observation points represented by different values of x/R, the relative error increases as α increases from 3 to 4. This implies that the wave-input method, which is used in the coupled computational model of two-dimensional eight-node finite elements and six-node dynamic infinite elements, is more suitable for simulating low-frequency than high-frequency wave-propagation problems. Since the primary components of

Table 4.1 Distribution of displacement amplitudes along the half-plane surface (SV-wave vertical incidence, $a_0 = 0.5$)

	$\alpha = 2$		$\alpha = 3$		$\alpha = 4$	
x/R	A_U	$\delta_1(\%)$	A_U	$\delta_1(\%)$	A_U	$\delta_1(\%)$
–1.5	1.62	19.0	1.88	6.0	2.04	2.0
–1.25	1.65	17.5	1.97	1.5	2.07	3.5
–1.0	1.67	16.5	2.05	2.5	2.08	4.0
–0.75	1.69	15.5	2.10	5.0	2.07	3.5
–0.5	1.71	14.5	2.12	6.0	2.06	3.0
–0.25	1.72	14.0	2.17	8.5	2.05	2.5
0.0	1.73	13.5	2.19	9.5	2.04	2.0
0.25	1.72	14.0	2.17	8.5	2.05	2.5
0.5	1.71	14.5	2.12	6.0	2.06	3.0
0.75	1.69	15.5	2.10	5.0	2.07	3.5
1.0	1.67	16.5	2.05	2.5	2.08	4.0
1.25	1.65	17.5	1.97	1.5	2.07	3.5
1.5	1.62	19.0	1.88	6.0	2.04	2.0

Table 4.2 Distribution of displacement amplitudes along the half-plane surface (SV-wave vertical incidence, $a_0 = 1.0$)

	$\alpha = 2$		$\alpha = 3$		$\alpha = 4$	
x/R	A_U	$\delta_1(\%)$	A_U	$\delta_1(\%)$	A_u	$\delta_1(\%)$
–1.5	1.77	11.5	2.08	4.0	1.98	1.0
–1.25	1.89	5.5	2.11	5.5	2.05	2.5
–1.0	1.98	1.0	2.10	5.0	2.10	5.0
–0.75	2.05	2.5	2.05	2.5	2.10	5.0
–0.5	2.10	5.0	1.99	0.5	2.08	4.0
–0.25	2.13	6.5	1.94	3.0	2.09	4.5
0.0	2.14	7.0	1.92	4.0	2.06	3.0
0.25	2.13	6.5	1.94	3.0	2.09	4.5
0.5	2.10	5.0	1.99	0.5	2.08	4.0
0.75	2.05	2.5	2.05	2.5	2.10	5.0
1.0	1.98	1.0	2.10	5.0	2.10	5.0
1.25	1.89	5.5	2.11	5.5	2.05	2.5
1.5	1.77	11.5	2.08	4.0	1.98	1.0

an earthquake incident wave in a rock foundation are within a low-frequency range, the wave-input method (Zhao 1987; Zhang and Zhao 1988; Zhao et al. 1992) is suitable for the seismic-response analysis of canyons and structures.

4.2 Effects of Canyon Topographical Conditions on the Ground Motions due to Harmonic Wave Incidences

As natural canyon shapes are complicated and diversified, it is impossible to include all possible canyon shapes in a study. For the sake of simplicity, two typical canyon shapes, namely V-shaped canyons and trapezoidal canyons, are considered in this study. By varying the following two canyon geometrical parameters, height H and top width L, the effects of their topographical conditions on the ground motions due to harmonic wave incidences can be investigated using the coupled computational model of two-dimensional eight-node isoparametric finite elements and six-node dynamic infinite elements (Zhao et al. 1992; Zhao and Valliappan 1993a, b).

4.2.1 Free-Field Motions along V-shaped Canyons due to Harmonic Wave Incidences

In this subsection, a V-shaped canyon with three different ratios of the top width to the height of the canyon, namely L/H=1, 3 and 5, is considered to investigate the effects of the topographical conditions on the free-field motions due to harmonic wave incidences. As shown in Fig. 4.3, the near field of the canyon is simulated using two-dimensional eight-node isoparametric finite elements, while the far field

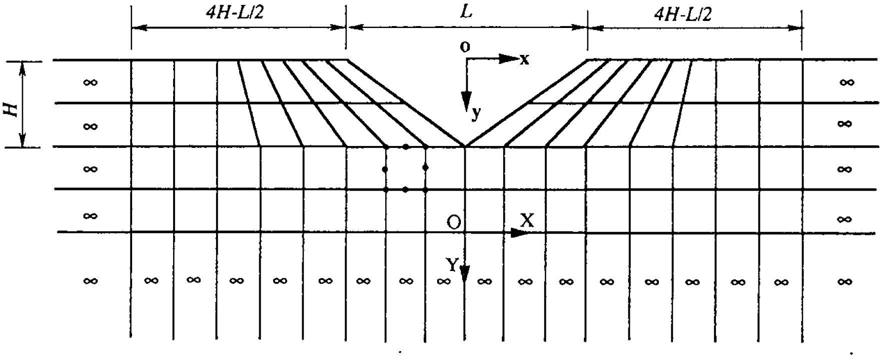

Fig. 4.3 Computational model of a V-shaped canyon: the near field is simulated using eight-node finite elements, while the far field is simulated using six-node dynamic infinite elements

of the canyon is simulated using two-dimensional six-node dynamic infinite elements. Since a displacement distribution pattern along the canyon can be used to represent the free-field motion, a unit plane harmonic displacement SV-wave, which has different frequencies and different incident angles, is used in the coupled computational model of two-dimensional eight-node isoparametric finite elements and six-node dynamic infinite elements. By means of the wave-input method (Zhao 1987; Zhao et al. 1992; Zhao and Valliappan 1993a, b), a horizontal line (i.e. $Y = 0$) in the coupled computational model is used as the wave-input boundary, where the incident harmonic displacement SV-wave can be transformed into dynamic nodal loads for the related finite and dynamic infinite elements using elastic wave theory (Graff 1975; Zhao 1987; Zhao et al. 1992). An angle between the normal of the front of the incident plane harmonic SV-wave and a vertical line coincident with the y axis of the coordinate system (in Fig. 4.3) is defined as the wave incident angle, θ, for the coupled computational model. Thus, $\theta = 0^{\circ}$ means that the plane harmonic SV-wave is vertically propagating to the wave-input boundary, while a non-zero incident angle (i.e. $\theta \neq 0^{\circ}$) means that the plane harmonic SV-wave is obliquely propagating to the wave-input boundary. To examine the effects of wave incident angles on the free-field motion along the canyon surface, two different incident angles, namely $\theta = 0^{\circ}$ and $\theta = 15^{\circ}$, are used in the corresponding coupled computational model.

The following parameters are used: the height of the V-shaped canyon is 100 m; the elastic modulus of the surrounding rock of the canyon is 24×10^9 Pa; the Poisson's ratio of the surrounding rock is 1/3 and the density of the surrounding rock is 2400 kg m^{-3}.

To investigate the effect of the incident SV-wave frequency on the free-field motion along the surface of the V-shaped canyon, a dimensionless frequency a_0 is defined as

$$a_0 = \frac{\omega H}{\pi C_{SV}}, \tag{4.36}$$

where ω is the circular frequency of the incident harmonic SV-wave; H is the height of the V-shaped canyon; and C_{SV} is the SV-wave velocity in the surrounding rock of the canyon.

The numerical results for the free-field motion can be represented using the following expressions for the displacement amplitudes at surface nodal points of the coupled computational model:

$$A_u = \sqrt{[\mathrm{Re}(u)]^2 + [\mathrm{Im}(u)]^2}, \tag{4.37}$$

$$A_v = \sqrt{[\mathrm{Re}(v)]^2 + [\mathrm{Im}(v)]^2}, \tag{4.38}$$

where A_u and A_v are the nodal displacement amplitudes in the x and y directions; u and v are the corresponding displacements in the x and y directions, respectively; Re and Im are the real part and imaginary part of the displacement.

Using the displacement amplitudes defined in Eqs. (4.37) and (4.38), not only can the displacement distribution pattern along the canyon surface be described, but also the amplification factor of the displacement can be expressed as a result of the unit plane harmonic displacement SV-wave incidence.

Figure 4.4 shows the displacement amplitude distributions along the V-shaped canyon due to harmonic plane SV-wave incidences with two different incident angles. For the SV-wave vertical incidence (i.e. Fig. 4.4(A)), the symmetry of the displacement distribution pattern along the canyon surface is maintained due to the symmetric feature of the problem. Both the maximum value and the distribution patterns of the displacement amplitudes along the canyon surface are different for different ratios of the top width to the height of the V-shaped canyon (i.e. L/H). This is especially so for the incident SV-wave with the higher frequency (i.e. $a_0 = 1.0$). This indicates that the canyon topographic condition can have a significant effect on the free-field motion along the surface of a natural canyon.

For the SV-wave vertical incidence, the maximum value of the displacement amplitude along the canyon surface can reach values above 3. This maximum value occurs at the top (i.e. $x/H = 0.5$) of the most narrow canyon (i.e. $L/H = 1$). Even though a vertical incident plane harmonic SV-wave is considered, both A_u and A_v are not equal to zero due to wave-mode conversion and scattering on the surface of the V-shaped canyon. This phenomenon is different from what is observed for a plane harmonic SH-wave incidence (Zhang and Zhao 1988).

For an oblique incident SV-wave, the non-symmetry of the displacement distribution pattern along the surface of the V-shaped canyon is displayed in Fig. 4.4(B). The distribution pattern of the nodal displacement amplitude along the canyon surface is clearly different for the three different ratios of the canyon top width to the canyon height (i.e. L/H). For the plane harmonic SV-wave oblique incidence (i.e. Fig. 4.4(B)), the shield effect of the V-shaped canyon is not obvious, compared with what is observed from the plane harmonic SH-wave oblique incidence (Zhang and Zhao 1988). This phenomenon can be attributed to the wave-mode conversion in the case of plane harmonic SV-wave oblique incidence. Since the numerical results

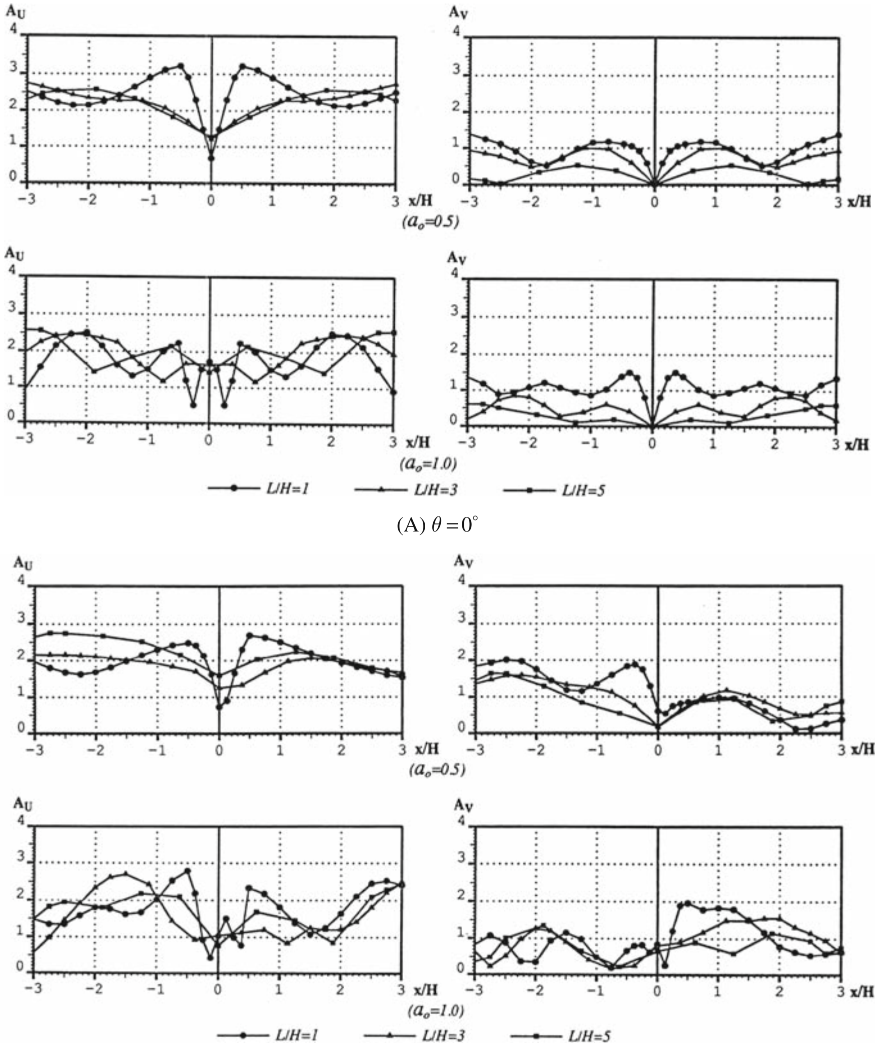

(A) $\theta = 0^\circ$

(B) $\theta = 15^\circ$

Fig. 4.4 Distributions of displacement amplitudes along V-shaped canyons due to the harmonic SV-wave incidence: (**A**) $\theta = 0^\circ$; (**B**) $\theta = 15^\circ$

obtained from the coupled computational model due to the plane harmonic SV-wave vertical incidence (i.e. Fig. 4.4(A)) are remarkably different from those due to the plane harmonic SV-wave oblique incidence (i.e. Fig. 4.4(B)), it can be concluded that wave incident angles have significant effects on the free-field motion along the surface of a natural canyon.

4.2.2 Free-Field Motions along Trapezoidal Canyons due to Harmonic Wave Incidences

In this subsection, the coupled computational model of two-dimensional eight-node isoparametric finite elements and six-node dynamic infinite elements is used to simulate wave propagation and scattering along a typical trapezoidal canyon. Figure 4.5 shows the discretized mesh. To represent the shape of the trapezoidal canyon, a new parameter, L_1, is introduced to express the bottom width of the canyon, so that a ratio, L_1/L, can be used as a canyon shape indicator. Two extreme values, namely $L_1/L = 0$ and $L_1/L = 1$, can be used to represent a V-shaped canyon and a rectangular canyon, respectively. By keeping the ratio of the canyon top width to canyon height unchanged (i.e. L/H=3 in this subsection), three different values of L_1/L, namely $L_1/L = 0$, 1/3 and 1, are considered in the coupled computational model of two-dimensional eight-node isoparametric finite elements and six-node dynamic infinite elements. The selection of the wave-input boundary and parameters of the surrounding rock for the computational model used in this subsection is exactly the same as that in Sect. 4.2.1. The unit plane harmonic displacement waves with different wave types, different frequencies and different incident angles are considered as input waves for the coupled computational model of two-dimensional eight-node isoparametric finite elements and six-node dynamic infinite elements.

Figure 4.6 shows the displacement amplitude distributions along a V-shaped canyon ($L_1/L = 0$), a trapezoidal canyon ($L_1/L = 1/3$) and a rectangular canyon ($L_1/L = 1$) due to unit plane harmonic (displacement) SV-wave and P-wave vertical incidences with two different frequencies. Note that both SV-wave and P-wave oblique incidences were also considered previously (Zhao and Valliappan 1993a, b). For a trapezoidal canyon, the canyon shape can affect the distribution pattern of displacement amplitudes along the canyon surface dramatically, especially for the rectangular canyon. Compared with both the V-shaped canyon and the trapezoidal canyon (with $L_1/L = 1/3$), the rectangular canyon results in a different

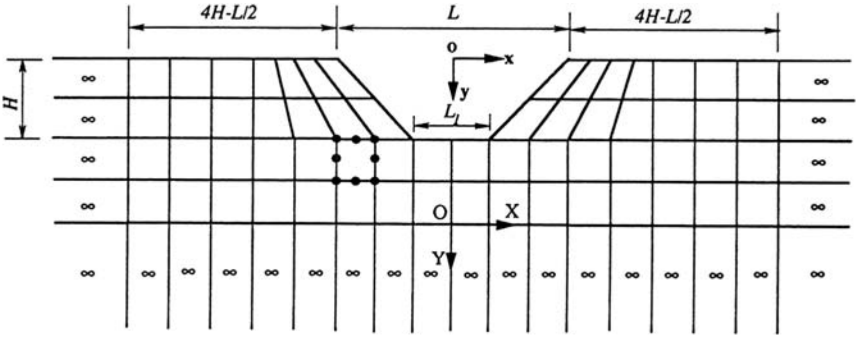

Fig. 4.5 Computational model for a typical trapezoidal canyon: the near field is simulated using eight-node finite elements, while the far field is simulated using six-node dynamic infinite elements

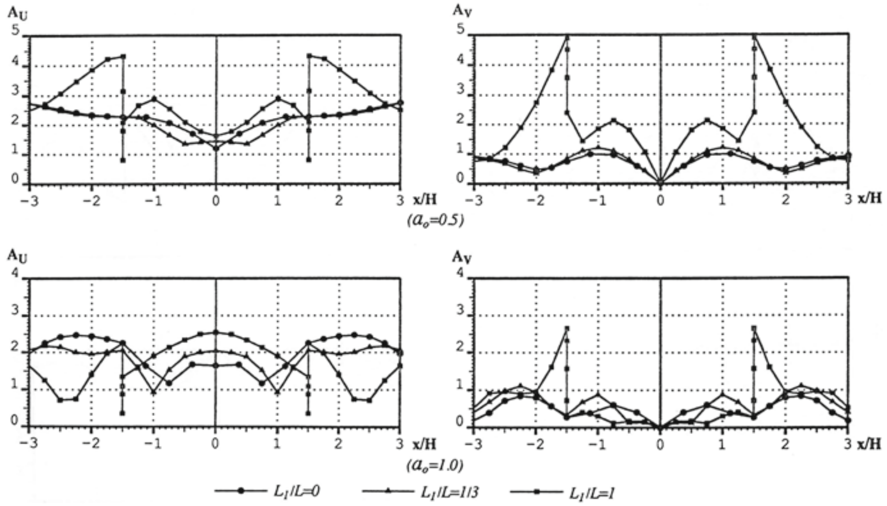

(A) Harmonic SV-wave vertical incidence

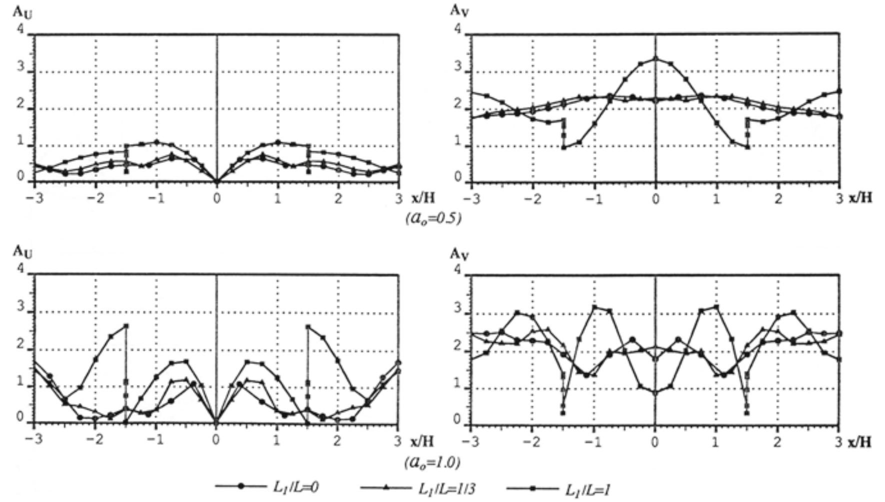

(B) Harmonic P-wave vertical incidence

Fig. 4.6 Distributions of displacement amplitudes along differently shaped canyons due to the harmonic SV-wave and P-wave vertical incidences ($\theta = 0°$): (**A**) harmonic SV-wave vertical incidence; (**B**) harmonic P-wave vertical incidence

distribution pattern of the free-field motion due to the abrupt change in the shape of the canyon bank.

The maximum value of the displacement amplitude along the canyon surface, which can reach 5 (in Fig. 4.6(A)) for the plane harmonic (displacement) SV-wave vertical incidence and 3.4 (in Fig. 4.6(B)) for the plane harmonic (displacement) P-wave vertical incidence, is observed at the top corners of the rectangular canyon. This indicates that a rectangular canyon can result in a greater amplification effect of the ground motion than either a V-shaped canyon or a trapezoidal canyon. As a rapid change in the shape of the canyon bank can induce an extreme value for the free-field motion along the canyon surface, it should carefully be considered in the seismic analysis of structures. Note that the V-shaped and trapezoidal canyons result, roughly, in a similar overall trend of the ground motion, although some differences may exist between the maximum displacement amplitude along the V-shaped canyon and that along the trapezoidal canyon. The symmetry and asymmetry of the distribution of the free-field motion along the canyon surface can be clearly observed for vertical and oblique incident waves. Since the canyon shape indicator, L_1/L, and the ratio of the canyon top width to height, L/H, of a natural canyon are basically within the range studied in this subsection, the above results likely provide a realistic insight into and an understanding of how topographical conditions affect the free-field motions. However, the fact that different amplification effects exist for different canyon shapes suggested that two-dimensional computational models may not be appropriate for some natural canyons, where topographical irregularities along the longitudinal directions of canyons are significant. In this case, three-dimensional models are needed to simulate the dynamic behaviour of three-dimensional wave-scattering problems.

4.3 Effects of Canyon Geological Conditions on Ground Motions due to Harmonic Wave Incidences

In the real world, not only can the shapes of natural canyons be diversified and variable, but also the geological conditions of natural canyons are changeable. On the surface of a natural canyon, some alluvial or pluvial materials and weathered rocks can exist. The existence of such soft materials may affect the free-field motion along the surface of the natural canyon. The main purpose of this subsection is to investigate the effects of a weathered rock stratum on the free-field motion along the surface of the canyon, rather than to conduct a general discussion on the effects of geological conditions in a broader sense.

As shown in Fig. 4.7, a weathered V-shaped canyon, which has a height of 100 m (i.e. $H = 100$ m) and a top-width-to-height ratio of 3 (i.e. $L/H = 3$), is simulated by the coupled computational model of two-dimensional eight-node isoparametric finite elements and six-node dynamic infinite elements. The shaded area in this figure is the weathered rock stratum with a thickness of 20 m. The ratio of the elastic modulus of the normal (fresh) rock to that of the weathered rock, E_n/E_w, can be used to express the softness of the weathered rock stratum.

The following parameters are used for the coupled computational model: the elastic modulus of the normal rock (E_n) is 24×10^9 Pa; Poisson's ratio is 1/3 for both the normal rock and the weathered rock; the density of both the normal rock and the weathered rock is 2400 kg m^{-3}. A unit plane harmonic displacement wave

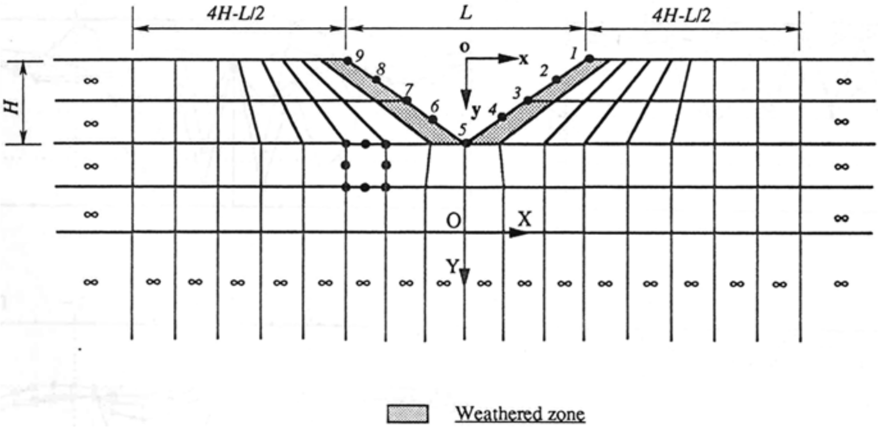

Fig. 4.7 Computational model for a weathered V-shaped canyon: the near field is simulated using eight-node finite elements, while the far field is simulated using six-node dynamic infinite elements; stations 1 and 5 are used as two observation stations in this chapter

with different wave types, different frequencies and different incident angles is used as the input wave for the coupled computational model of eight-node isoparametric finite elements and six-node two-dimensional dynamic infinite elements. The wave-input method used for the coupled computational model in this subsection is exactly the same as that in Sect. 4.2. To investigate the effects of the weathered rock stratum on the free-field motion along the canyon surface, four different values for E_n/E_w, namely $E_n/E_w = 1$, 5, 10 and 20, are used in the corresponding coupled computational model. Note that $E_n/E_w = 1$ means that the surrounding rock of the canyon is homogeneous, so that the numerical results obtained for this particular case can be used as a basis for comparison with those obtained for other weather rock cases.

Figure 4.8 shows the displacement amplitude distributions along the weathered canyon surface due to unit plane harmonic SV-wave and P-wave incidences. These numerical results clearly indicate that the existence of the weathered rock stratum has a significant influence on the free-field motion along the weathered canyon surface. Generally, the softer the weathered rock stratum, the greater the displacement amplitude of the free-field motion along the weathered canyon surface. For most weathered rock stratum cases, the maximum value of the free-field motion takes place at the upper part of the canyon bank surface. This phenomenon is different from what is observed in the case of homogeneous rock ($E_n/E_w = 1$), where the maximum value of the free-field motion usually occurs at the top corners of the canyon bank.

Both the frequency and the angle of incident waves can also affect the displacement amplitude distributions of the free-field motion along the weathered canyon surface. For the lower frequency ($a_0 = 0.5$), the displacement amplification distribution on each bank of the weathered canyon surface (i.e. $-1.5 < x/H < 0$ or $0 < x/H < 1.5$) has only one peak, while for the higher frequency ($a_0 = 1.0$), it has

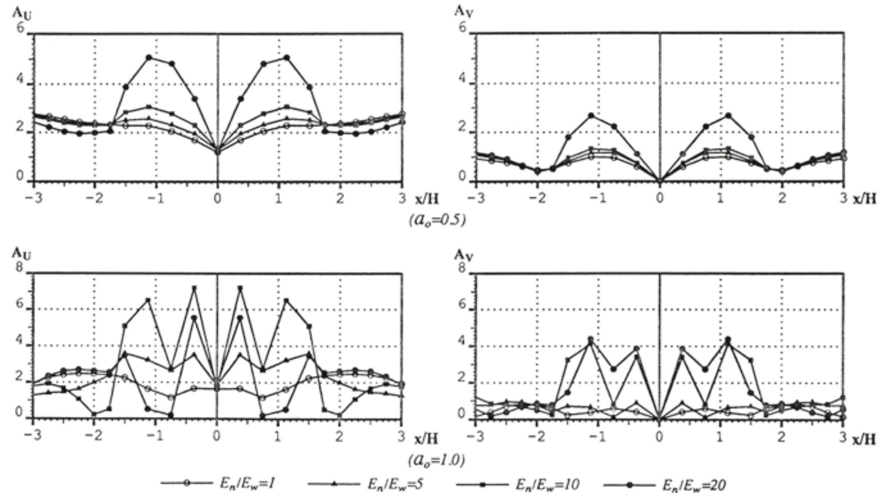

(A) Harmonic SV-wave vertical incidence

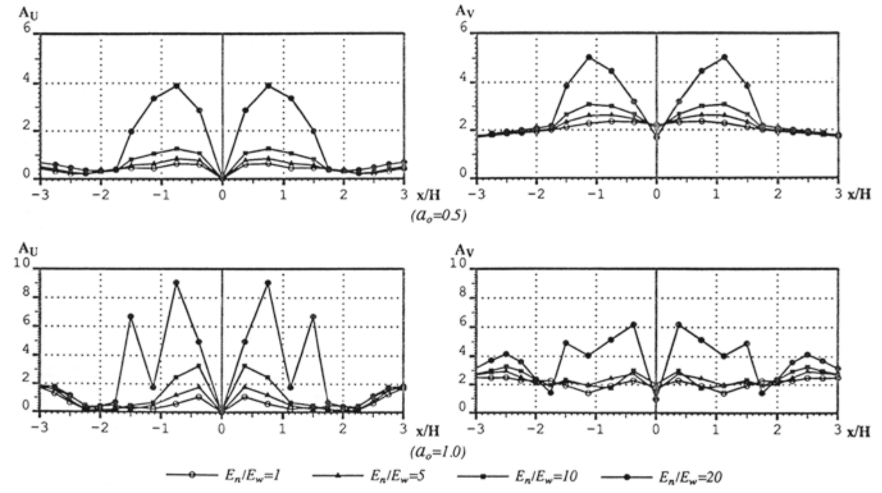

(B) Harmonic P-wave vertical incidence

Fig. 4.8 Distributions of displacement amplitudes along weathered V-shaped canyons due to the harmonic SV-wave and P-wave vertical incidences ($\theta = 0°$): (**A**) harmonic SV-wave vertical incidence; (**B**) harmonic P-wave vertical incidence

two peaks, indicating that the frequency of an incident wave has a remarkable effect on the free-field motion along a weathered canyon surface. For the two frequencies used, the maximum value of the displacement amplitude along the weathered canyon surface can reach about 7.3 and 9.2 for the unit harmonic SV-wave incidence (in Fig. 4.8(A)) and the unit harmonic P-wave incidence (in Fig. 4.8(B)), respectively. This demonstrates that the incident wave type can significantly affect the free-field motion along the weathered canyon surface. Note that for a homogeneous canyon ($E_n/E_w = 1$), the maximum value of the displacement amplitude along the canyon surface is just 2.8 for both the unit harmonic SV-wave incidence (in Fig. 4.8(A)) and the unit harmonic P-wave incidence (in Fig. 4.8(B)). Since the maximum value of the displacement amplitude along a weathered canyon surface is significantly different from that along an un-weathered canyon surface, it is concluded that the geological condition of a natural canyon can have remarkable effects on the free-field motion along the surface of the natural canyon. Thus, an engineering treatment, such as the removal of weathered rocks by excavation or the cement grouting on the abutment of an arch dam or a large span bridge, is not only necessary for the static stability of the structure under static loads, but also beneficial to the earthquake resistance of the structure as a result of a much weaker free-field motion on sound rock abutments.

A further study is carried out to examine the characteristics of the complex frequency response along the weathered V-shaped canyon due to unit plane harmonic (displacement) SV-wave and P-wave incidences. Figure 4.9 shows the distributions of the complex response functions at different stations on the weathered V-shaped canyon surface. For a homogeneous canyon ($E_n/E_w = 1$), there is little repeated wave reflection occurring near the canyon surface, so that no considerable resonant frequency appears in the complex frequency response curve of the homogeneous canyon. When the incident wave arrives at the homogeneous canyon surface, it reflects and scatters due to the free surface condition of the homogeneous canyon. The resulting reflected and scattered waves are then propagating from the homogeneous canyon surface into the far field of the homogeneous canyon through two-dimensional eight-node finite elements and six-node dynamic infinite elements used in the coupled computational model. This fact demonstrates that the two-dimensional six-node dynamic infinite element is capable of propagating waves in an appropriate manner. For the weathered canyon, resonance takes place as a result of the come-and-go reflection effect of the wave within the weathered rock stratum. The resonant phenomenon is very obvious for the softer weathered rock stratum ($E_n/E_w = 20$).

The curves of the complex frequency response functions are different at different observation stations along the weathered canyon surface, implying that different parts of a dam–canyon interface may undergo different earthquake motions due to the wave-scattering effect along the canyon surface. These curves depend on the incident wave type, the incident angle and the ratio of the elastic modulus of the normal (fresh) rock to that of the weathered rock, E_n/E_w. Since an arch dam is a highly static indeterminate structure, a displacement difference in the free-field motion along the dam–canyon interface can result in remarkable stresses within the dam. Therefore, from a seismic design point of view, both phase and amplitude differences in the free-field motion along an arch dam–canyon interface should be considered in the computational model of the arch dam system. To reduce the dynamic stress level within an arch dam, it is necessary to take some measures for strengthening the weathered rock along the surface of a natural canyon.

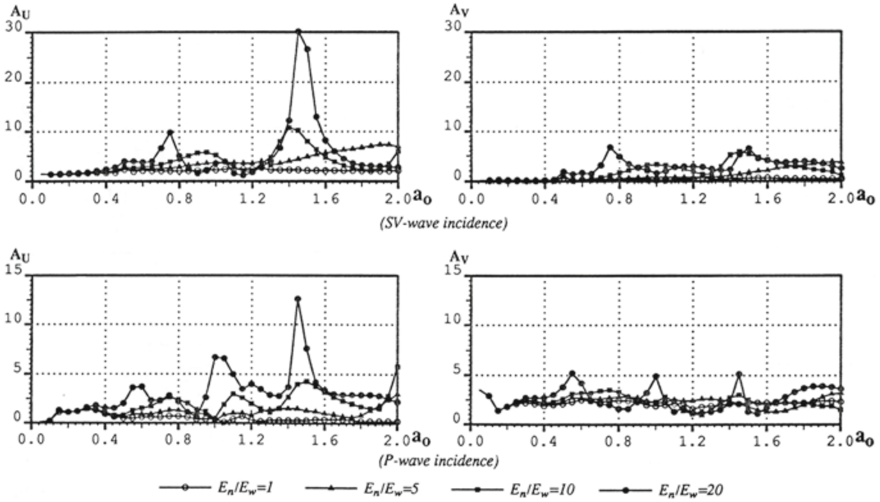

(A) Station 1

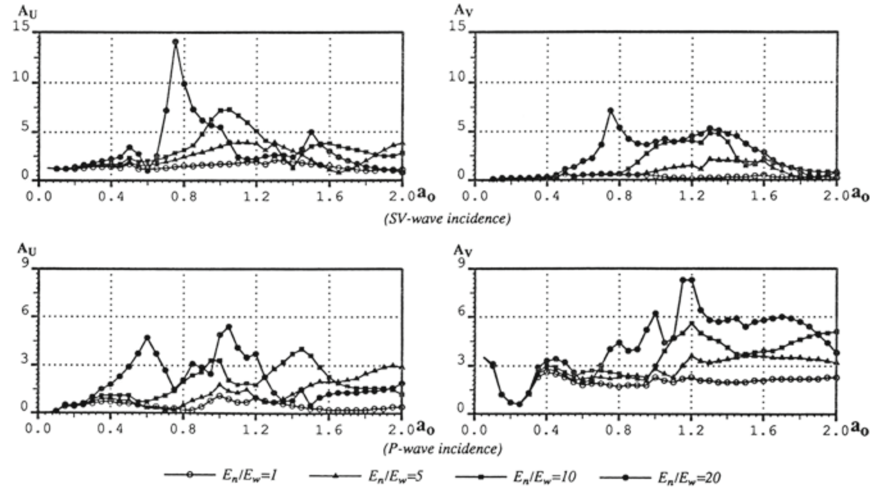

(B) Station 4

Fig. 4.9 Distributions of complex response functions along weathered V-shaped canyons: (**A**) Station 1; (**B**) Station 4. The locations of these two stations are shown in Fig. 4.7

4.4 Effects of Canyon Topographical Conditions on Ground Motions due to Seismic Wave Incidences

To compare the numerical results obtained in this section with those obtained in Sect. 4.3, the same consideration of canyon shapes and computational models as that in Sect. 4.3 is adopted. For this reason, two typical canyon shapes, namely a

V-shaped canyon and a trapezoidal canyon, are used to represent approximately the geometrical aspects of natural canyons. By changing both the height and top width of a canyon, the effects of topographical conditions on the free-field motion due to seismic wave incidences can be investigated.

4.4.1 Free-Field Motions along V-shaped Canyons due to Seismic Wave Incidences

The same coupled computational model for a typical V-shaped canyon, as shown in Fig. 4.3, is used here to investigate the effect of canyon shape on the free-field motion along the canyon surface due to seismic wave incidences. Three different top width to height ratios of the canyon, namely $L/H = 1$, 3 and 5, are considered in the corresponding coupled computational model of two-dimensional eight-node isoparametric finite elements and six-node dynamic infinite elements. Under the assumption of either a plane seismic SV-wave or a plane seismic P-wave propagating vertically from the far field to the near field of the canyon, a horizontal line (i.e. $Y = 0$ in Fig. 4.3) is used as the wave-input boundary within the coupled computational model (Zhao 1987; Zhao et al. 1992; Zhao and Valliappan 1993a, b).

For the purpose of investigating the effects of topographical and geological conditions on the free-field motions along the canyon surfaces, one could select an arbitrary earthquake motion as the input seismic wave. We shall use the acceleration time history of an S25W component of the Parkfield, California earthquake as the input seismic wave for investigating the effects of topographical and geological conditions on the free-field motions along the canyon surfaces. This earthquake took place on 27 June 1966, and the peak value of the S25W acceleration component was –3.408 m s^{-2}. For convenience of conducting the seismic analysis, this acceleration time history is normalized by dividing the acceleration by the absolute value of the peak magnitude, 3.408, resulting in a unit earthquake acceleration wave. This wave has the same frequency characteristics as the original one. Note that this wave has been used to investigate the effects of reservoir bottom sediments on the transient seismic response of a concrete gravity dam–water–foundation system in Chap. 3, where both the seismic analysis methodology and the seismic wave selection principles are discussed in detail. Figure 3.13 shows the acceleration, Fourier spectrum and acceleration response spectrum of the selected unit earthquake acceleration wave. In this figure, a is the acceleration; F-S is the Fourier spectrum; ξ is the damping ratio of a one-degree-of-freedom dynamic system; S_a is the acceleration spectrum.

Similar to Sect. 4.2.1, the following parameters are used in the coupled computational model: the height of the V-shaped canyon is 100 m; the elastic modulus of the surrounding rock of the canyon is 24×10^9 Pa; the Poisson's ratio of the surrounding rock is 1/3; the density of the surrounding rock is 2400 kg m^{-3}.

Figure 4.10 shows the earthquake accelerogram and the corresponding response spectrum at two different observation stations (i.e. stations 1 and 5 shown in Fig. 4.7) along the canyon surface due to the plane seismic SV-wave incidence. In these

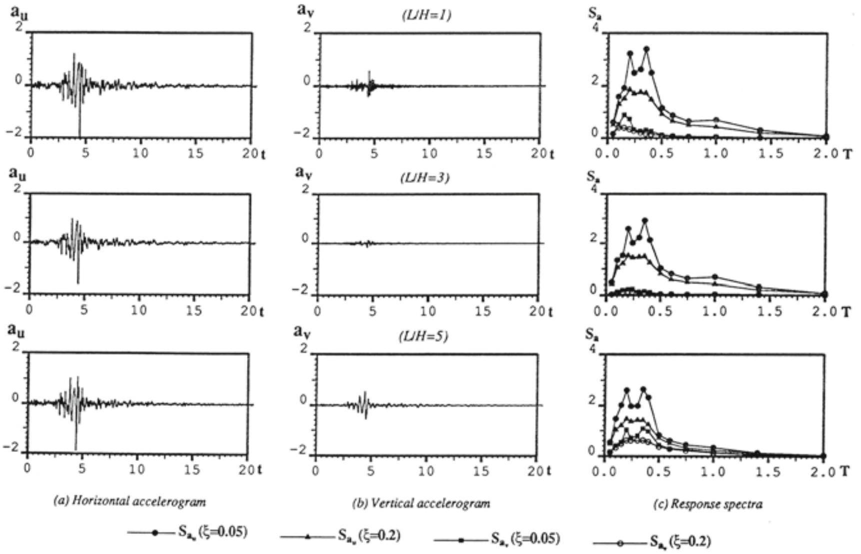

(A) Station 1

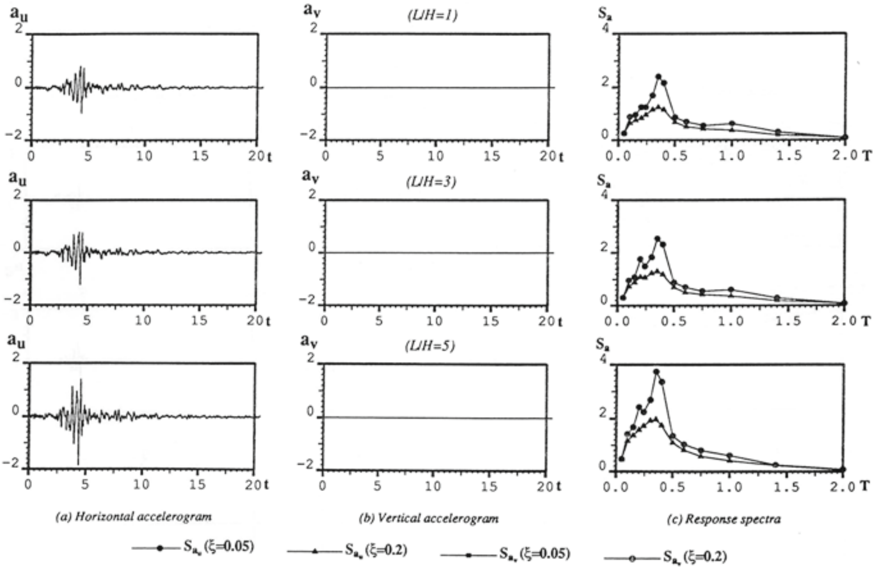

(B) Station 5

Fig. 4.10 Distributions of acceleration time-history and response spectrum along V-shaped canyons (seismic SV-wave vertical incidence): (**A**) Station 1; (**B**) Station 5. The locations of these two stations are shown in Fig. 4.7

figures, a_u and a_v are the horizontal and vertical components of the ground acceleration; S_{a_u} and Sa_v are the acceleration response spectra corresponding to a_u and a_v, respectively. Although the input wave motion on the wave-input boundary is only in the horizontal direction under the assumption of the plane seismic SV-wave incidence, the vertical acceleration (a_v) at station 1 (in Fig. 4.10(A)) is not equal to zero as a result of wave-mode conversion on the canyon surface. As expected, the vertical acceleration (a_v) at station 5 (in Fig. 4.10(B)) is equal to zero due to the symmetric feature of the V-shaped canyon. This phenomenon is also observed in plane harmonic SV-wave incidences (Zhao and Valliappan 1993a, b).

The peak values of the horizontal acceleration component (a_u) on the upper section of the canyon at station 1 (in Fig. 4.10(A)) approaches –2 m s^{-2} for all the three V-shaped canyons with different top–width-to-height ratios, indicating that the acceleration-amplification factor at this part of the canyon is about 2 because the peak value of the incident wave applied to the wave-input boundary is –1 m s^{-2}. At the lower section of the canyon at station 5 (in Fig. 4.10(B)), the peak value of the horizontal acceleration component is obviously different for all the three V-shaped canyons with different top-width-to-height ratios. In this case, the peak value of the horizontal acceleration component has a peak value of –1.85 m s^{-2} when the top-width–to-height ratio of the canyon is equal to 5 (i.e. $L/H=5$), while it has a peak value of –0.98 m s^{-2} and –1.22 m s^{-2} when the top-width-to-height ratios of the canyon are equal to 1 and 3, respectively. This clearly demonstrates that under plane seismic SV-wave incidences, the top-width-to-height ratio (L/H) of a canyon can affect the free-field motion along the canyon surface.

Compared with a plane harmonic SV-wave incidence, a plane seismic SV-wave incidence can result in a smaller amplification factor to the free-field motion along the canyon surface due to the average self-healing effect caused by a series of different harmonic waves arising from an incident earthquake wave. The frequency distribution characteristics of the free-field motion along the canyon surface can be investigated from the numerical results (shown in Figs. 4.10(A) and 4.10(B)). For the horizontal acceleration component of the free-field motion along the canyon surface, the distribution curves of the response spectrum (S_{a_u}) at the lower part of the canyon (i.e. station 5 in Fig. 4.10(B)) have similar shapes to those of the incident seismic SV-wave. At the upper part of the canyon (i.e. station 1 in Fig. 4.10(A)), the higher frequency component becomes stronger, so that there is a slight difference between the response spectrum (Sa_u) of the free-field motion along the canyon surface and that of the incident seismic SV-wave.

Although a vertical acceleration component (a_v) appears at the free-field motion along the upper part of the canyon surface due to the plane seismic SV-wave incidence, the peak value of this vertical acceleration component is much smaller than that of the corresponding horizontal acceleration component (a_u). The high-frequency component of the vertical acceleration component (a_v) for a narrow canyon ($L/H = 1$) is more obvious than that for a broader canyon ($L/H = 5$). Evidently, canyon shapes have significant effects on the frequency components of free-field motions along canyon surfaces.

Under the plane seismic P-wave vertical incidence, the overall trends of the horizontal and vertical acceleration components, a_u and a_v, are different from those under plane seismic SV-wave vertical incidence. Figure 4.11 shows the earthquake accelerogram and the corresponding response spectrum at two different observation stations (i.e. stations 1 and 5 shown in Fig. 4.7) along the canyon surface due to the plane seismic P-wave incidence. In this situation, the vertical acceleration component (a_v) is much greater than the horizontal acceleration component (a_u). The peak value of the vertical acceleration component reaches –3 m s^{-2} for $L/H = 5$ at station 1 (in Fig. 4.11(A)), which is greater than that for either $L/H = 1$ or 3. This indicates that both different canyon shapes and incident seismic wave types have different amplification effects on free-field motions along canyon surfaces. Since the amplification factor of a canyon depends on both the canyon shape and the incident seismic wave, the maximum amplification factor of a canyon can take place when the canyon and the incident seismic wave have the same predominant frequency. This phenomenon can be observed from the numerical results obtained for $L/H = 5$ due to the plane seismic P-wave incidence. In this situation, the maximum values of the vertical acceleration response spectrum (S_{av}) can reach 6 and 3 m s^{-2} for $\xi = 0.05$ and 0.2 respectively.

By comparing the numerical results obtained from the consideration of the plane seismic SV-wave incidence (i.e. Fig. 4.10(A), (B)) with those of the plane seismic P-wave incidence (i.e. Fig. 4.11(A), (B)), it can be concluded that the wave-mode conversion effect is more obvious when the plane seismic P-wave incidence is considered in the coupled computational model of two-dimensional eight-node isoparametric finite elements and six-node dynamic infinite elements. The peak value of the horizontal acceleration component (a_u) due to the plane seismic P-wave incidence is greater than that of the vertical acceleration component (a_v) due to the plane seismic SV-wave incidence, especially for the narrow canyon ($L/H = 1$).

As expected, the horizontal acceleration component (a_u) due to the plane seismic P-wave vertical incidence vanishes at station 5 (in Fig. 4.11(B)) because of the symmetry of the V-shaped canyon. Although different amplification effects exist in the upper part of the canyon at station 1 (in Fig. 4.11(A)) for three different values of the top-width-to-height ratio of the canyon (L/H), similar distribution patterns of the free-field motion in the lower part of the canyon at station 5 (in Fig. 4.11(B)) occur for all three values of the top-width-to-height ratio of the canyon. This indicates that different parts of a canyon have different amplification effects on the incident seismic waves, even though the canyon is of regular V shape.

4.4.2 Free-Field Motions along Trapezoidal Canyons due to Seismic Wave Incidences

The same coupled computational model for a typical trapezoidal canyon as shown in Fig. 4.5 is used to investigate the effect of topographical conditions on the free-field motion along the canyon surface due to seismic wave incidences.

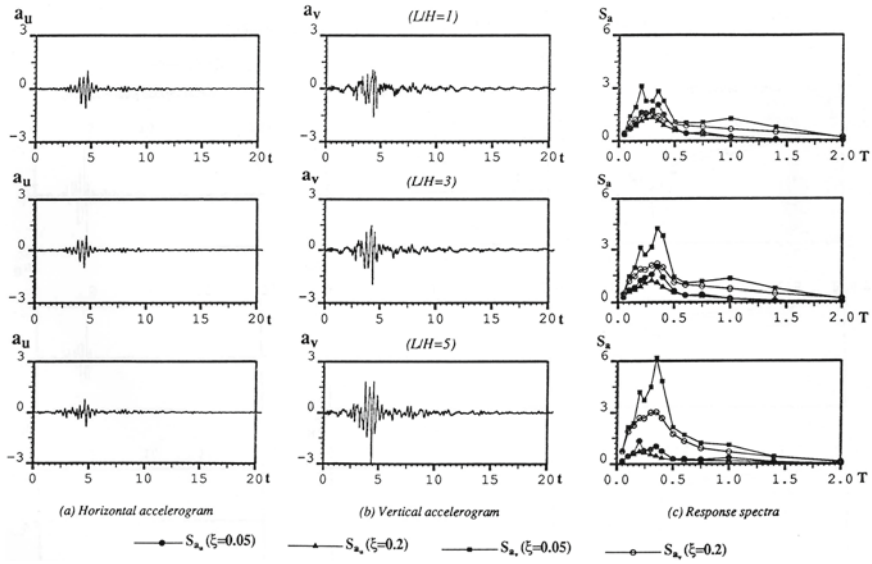

(A) Station 1

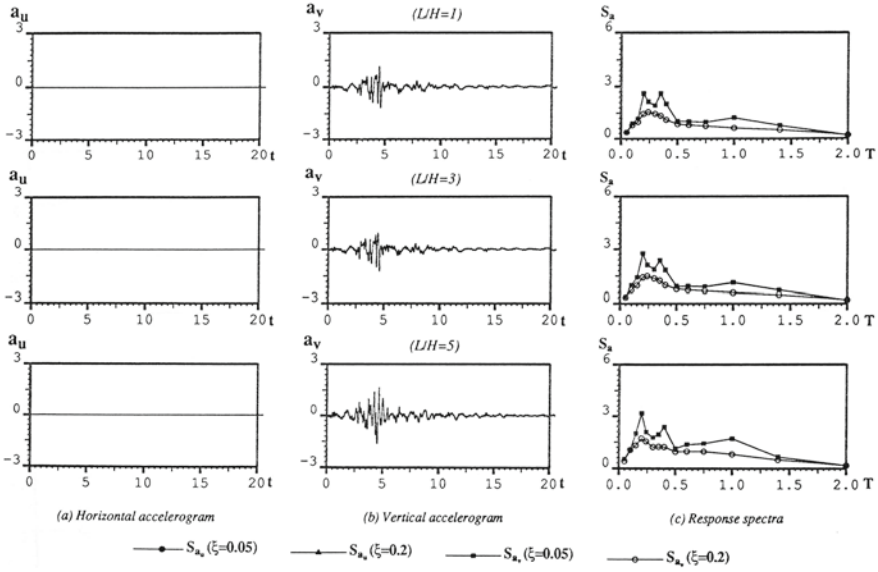

(B) Station 5

Fig. 4.11 Distributions of acceleration time-history and response spectrum along V-shaped canyons (seismic P-wave vertical incidence) (**A**) Station 1; (**B**) Station 5. The locations of these two stations are shown in Fig. 4.7

The same parameters as those used in Sect. 4.2.2 are used in this subsection. The only difference between this subsection and Sect. 4.2.2 is that in the latter, plane harmonic wave incidences are considered in the coupled computational model, while in the former, plane seismic wave incidences are considered. The same incident plane seismic wave as that used in Sect. 4.4.1 is used in this subsection.

Figure 4.12 shows the canyon surface earthquake accelerogram and the corresponding response spectrum at two different observation stations (i.e. stations 1 and 5 shown in Fig. 4.7) for a V-shaped canyon (i.e. $L_1/L = 0$), a trapeqoidal canyon (i.e. $L_1/L = 1/3$) and a rectangular canyon (i.e. $L_1L = 1$) due to the unit plane seismic SV-wave indidence. For the trapezoidal and V-shaped canyons, similar time-histories of the horizontal acceleration component (at a given observation station) can be observed from these numerical results. The peak value of the vertical acceleration component is small for either a trapezodial canyon or a V-shaped canyon. Although a similar trend exists for the distribution pattern of the horizontal acceleration component (a_u) at the same observation station along the surfaces of the three different canyons, the wave mode conversion effect is more conspicuous when the rectangular canyon is considered. This phenomenon is also observed for a plane harmonic SV-wave incidence (Zhao and Valliappan 1993a, b).

An abrupt change in the slope of a canyon bank can result in a stronger wave-mode conversion effect. For example, at the top of the rectangular canyon (i.e. station 1 in Fig. 4.12(A)), the peak value of the vertical acceleration component (a_v) can reach –1.38 m s^{-2}, while the peak value of the horizontal acceleration component (a_u) is –1.81 m s^{-2}. The wave-mode conversion effect is different for different observation stations along the canyon surface. This indicates that for a structure built on the top of a steeper canyon bank, not only a stronger horizontal acceleration component but also a stronger vertical acceleration component should be considered in the seismic design of the structure, irrespective of the fact that a vertical incident seismic SV-wave has only a horizontal acceleration component.

For a similar observation station, located on the surface of the three different canyons, the frequency component distribution of the horizontal acceleration component is different, as can be seen from the corresponding response spectrum shown in Fig. 4.12(A), (B). As expected, the vertical acceleration component vanishes at station 5 (in Fig. 4.12(B)) due to both the symmetric feature of the canyon and the vertical incidence of the seismic wave.

For the plane seismic P-wave vertical incidence, the rectangular canyon results in different distribution patterns for the acceleration time-history and the corresponding response spectrum at the two observation stations on the canyon surface, when compared with the trapezoidal and V-shaped canyons. Figure 4.13 shows the canyon surface accelerogram and the corresponding response spectrum (at the two observation stations) for the three canyons of different shapes due to the plane seismic P-wave vertical incidence. Clearly, the rectangular canyon results in the strongest acceleration response among the three different canyons, especially at the upper part of the rectangular canyon (i.e. station 1 in Fig. 4.13(A)). The peak value of the

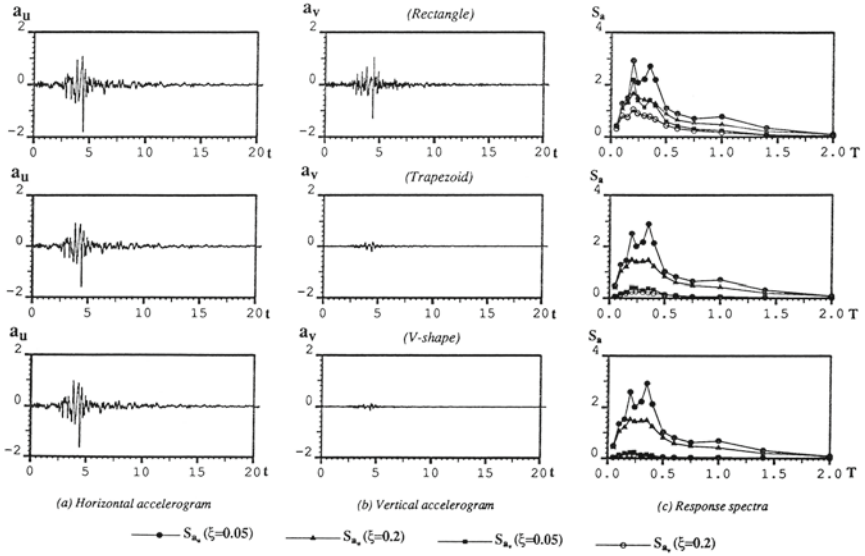

(A) Station 1

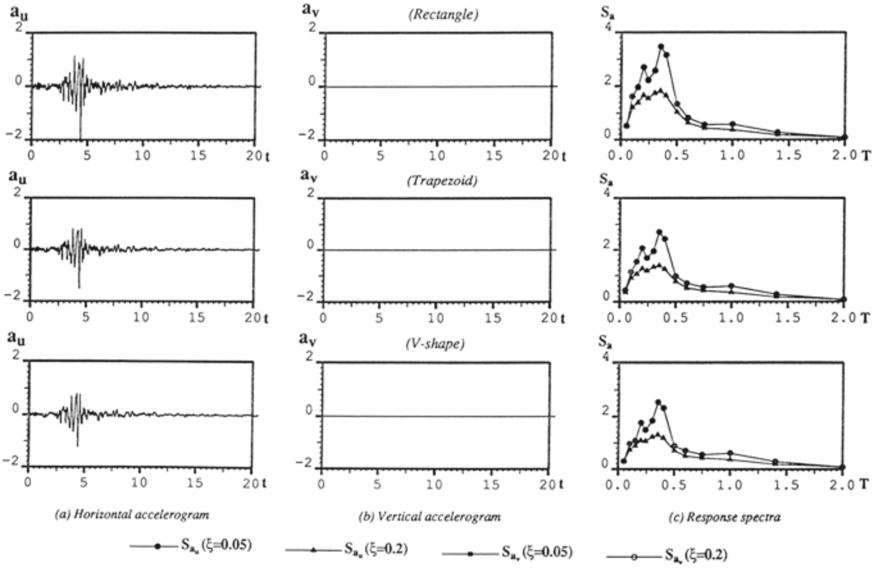

(B) Station 5

Fig. 4.12 Distributions of acceleration time-history and response spectrum due to different canyon shapes (seismic SV-wave vertical incidence): (**A**) Station 1; (**B**) Station 5. The locations of these two stations are shown in Fig. 4.7

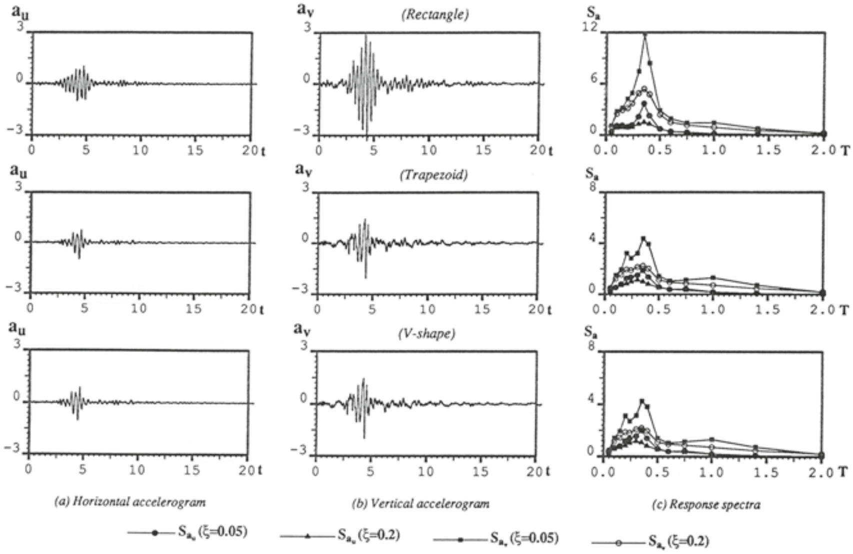

(A) Station 1

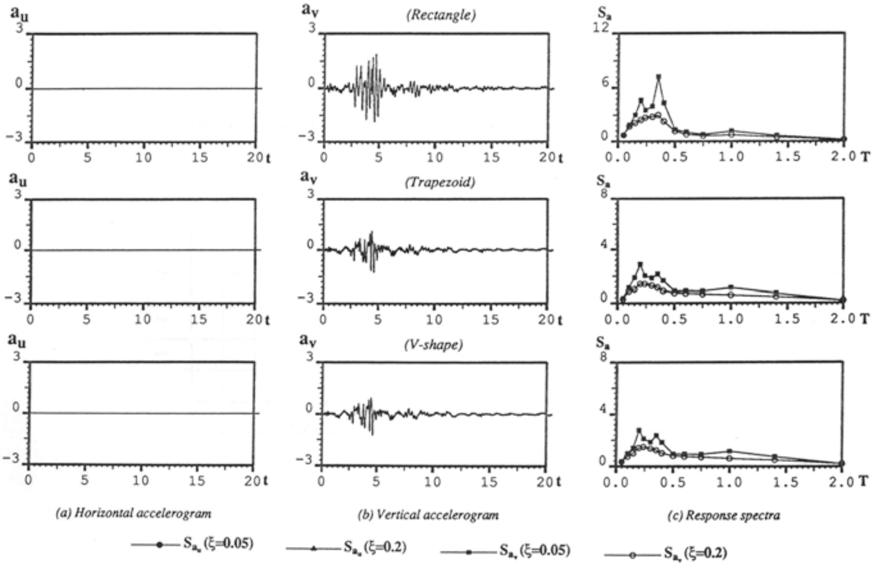

(B) Station 5

Fig. 4.13 Distributions of acceleration time-history and response spectrum due to different canyon shapes (seismic P-wave vertical incidence): (**A**) Station 1; (**B**) Station 5. The locations of these two stations are shown in Fig. 4.7

vertical acceleration component (a_v) is –3.2 m s^{-2} for the rectangular canyon, while for the trapezoidal and V-shaped canyons, the peak values of the vertical acceleration components are –2.1 m s^{-2} and –2 m s^{-2}, respectively. This indicates that for a given vertical incident seismic P-wave, the rectangular canyon results in a higher amplification factor for the free-field motion on the canyon surface than the trapezoidal and V-shaped canyons, although the amplification factor varies at different observation stations on the canyon surface.

For the seismic P-wave vertical incidence, the free-field motion at the top of a canyon is stronger than that at the bottom of the canyon. The maximum value of the vertical acceleration response spectrum (S_{a_v}) can reach 12 ms^{-2} for the rectangular canyon (Fig. 4.13(A)), while the maximum values of the horizontal acceleration response spectrum (S_{a_u}) are 4.5 and 4.4 ms^{-2} for the trapezoidal and V-shaped canyons, respectively. This implies that a structure located near the top corner of a rectangular canyon is subjected to stronger ground motion during an earthquake. For the trapezoidal and V-shaped canyons, similar acceleration time-history curves and the corresponding response spectrum curves are obtained from the corresponding computational models.

Although the incident seismic P-wave has only a vertical acceleration component on the wave-input boundary in the computational model, the resulting horizontal acceleration component of the free-field motion on the canyon surface is not equal to zero (in Fig. 4.13(A)) due to the wave-mode conversion effect. Compared with the plane seismic SV-wave vertical incidence, the plane seismic P-wave vertical incidence can result in a little weaker wave-mode conversion effect for the rectangular canyon. This demonstrates that the canyon amplification to an incident seismic wave depends also on the incident wave type. Since one type of incident seismic wave can excite another type of seismic wave on the canyon surface, horizontal and vertical acceleration components of the free-field motion always exist simultaneously on the canyon surface during a natural earthquake. This implies that for the safe seismic design of either a large arch dam or a large bridge, both the horizontal and the vertical components of an earthquake should be considered at the same time.

In summary, the shape of a canyon may have a significant effect on the free-field motion along the canyon surface during earthquake wave incidences. The amplification effect of a canyon mainly depends on the location of an observation station on the surface of the canyon, the incident angle of a seismic wave and the magnitude and type of an incident seismic wave. Compared with an incident seismic wave, the frequency components of the free-field motion on the surface of a canyon are considerably different as a result of wave reflection and scattering on the surface of the canyon. A canyon can result in the strongest free-field motion when the predominant frequency of the canyon coincides with that of the incident earthquake wave. Both horizontal and vertical components of the free-field motion are simultaneously excited on the surface of a canyon, although a vertical incident seismic wave has only one vertical or horizontal component, depending on the type of the vertical incident seismic wave. In comparison with harmonic wave incidences (Zhao and Valliappan 1993a, b), the amplification of a canyon to an incident seismic wave is a little smaller because of an averaged self-healing effect arising from a series of harmonic waves in the incident seismic wave. Generally, the amplification factor at the top of a canyon is greater than that at the bottom of the canyon during an earthquake event. A steeper canyon bank can result in stronger wave-mode conversion, and hence the slope of the canyon bank should be considered carefully for the seismic design of a structure.

4.5 Effects of Canyon Geological Conditions on Ground Motions due to Seismic Wave Incidences

This section is an extension of Sect. 4.3, in which the effects of canyon geological conditions on the ground motions due to harmonic wave incidences are investigated using the coupled computational model of two-dimensional eight-node isoparametric finite elements and six-node dynamic infinite elements. The same parameters, computational models and wave input methods as those used in Sect. 4.3 are employed in this section. The only difference between this section and Sect. 4.3 is that in Sect. 4.3, plane harmonic waves are considered as incident waves in the computational model, while in this section, plane seismic waves are used as incident waves in the computational model of two-dimensional eight-node isoparametric finite elements and six-node dynamic infinite elements. The same incident plane seismic wave as that used in Sect. 4.4.1 is used here.

Figure 4.14 shows the canyon surface earthquake accelerogram and the corresponding response spectrum at two observation stations for three different weathered stratum cases due to plane seismic SV-wave vertical incidence. In this figure, the ratio of the elastic modulus of the normal (fresh) rock to that of the weathered rock, E_n/E_w, is used to express the softness of the weathered stratum. These results clearly indicate that the weathered rock stratum of the canyon has a significant influence on the free-field motion along the canyon surface. For a given incident seismic wave, the softer the weathered rock stratum is, the stronger will be the free-field motion along the canyon surface. With station 1 (in Fig. 4.14(A)) taken as an example, the peak value of the horizontal acceleration component (a_u) is –2.55, –2.25 and –1.6 m s^{-2} for $E_n/E_w = 20$, 10 and 1, respectively. This indicates that since a unit plane seismic wave is used in the coupled computational model, the amplification factor of the canyon to the incident seismic wave can reach 2.55 when $E_n/E_w = 20$. The strongest free-field motion takes place in the upper part of the canyon, as can be seen from the numerical results shown at station 1 in Fig. 4.14(A). The similar phenomenon is also observed in the numerical results of Sect. 4.3, where a unit plane harmonic wave is considered as the incident wave for the coupled computational model.

Compared with the horizontal acceleration component (a_u) due to the plane seismic SV-wave vertical incidence, the vertical acceleration component (a_v) is a little smaller, but is still worth considering for a softer weathered rock stratum (i.e. $E_n/E_w = 20$). The response spectra of the free-field motion at station 1 (in

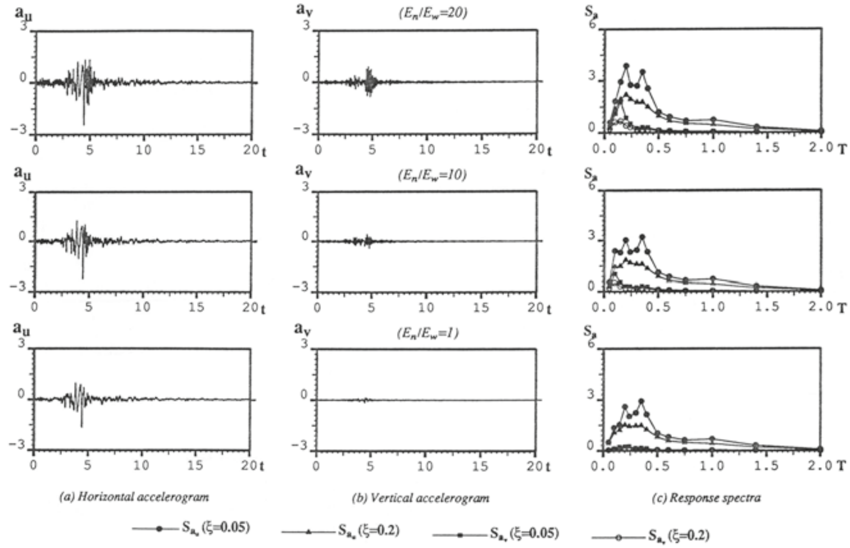

(A) Station 1

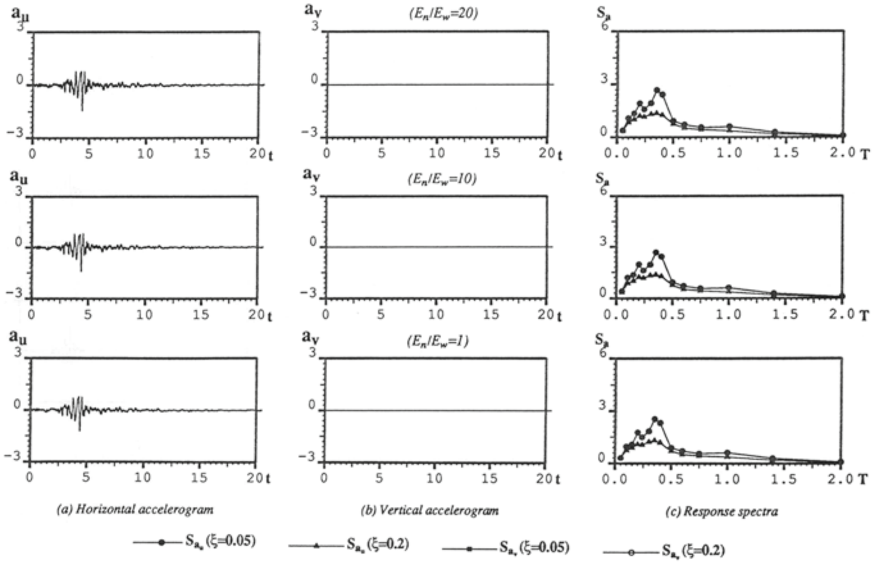

(B) Station 5

Fig. 4.14 Distributions of acceleration time-history and response spectrum due to different weathered strata (seismic SV-wave vertical incidence): (**A**) Station 1; (**B**) Station 5. The locations of these two stations are shown in Fig. 4.7

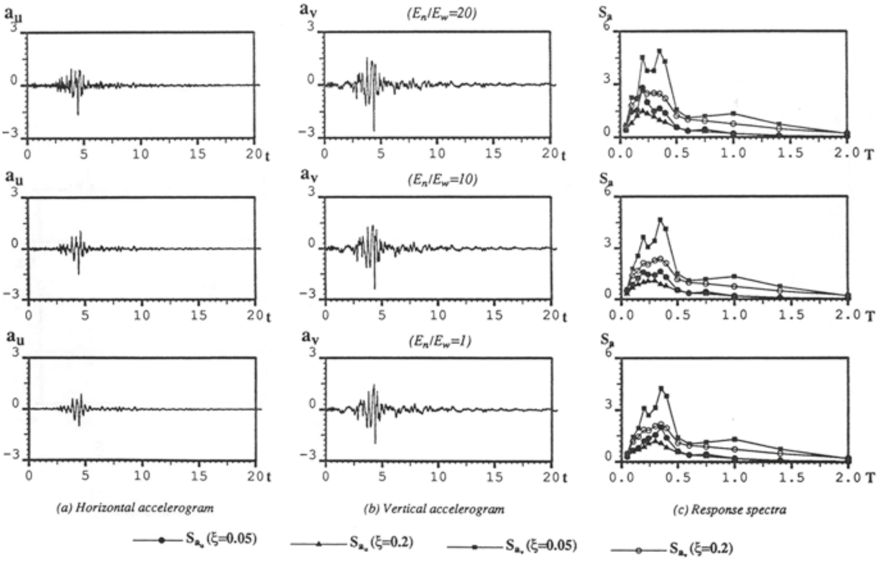

(A) Station 1

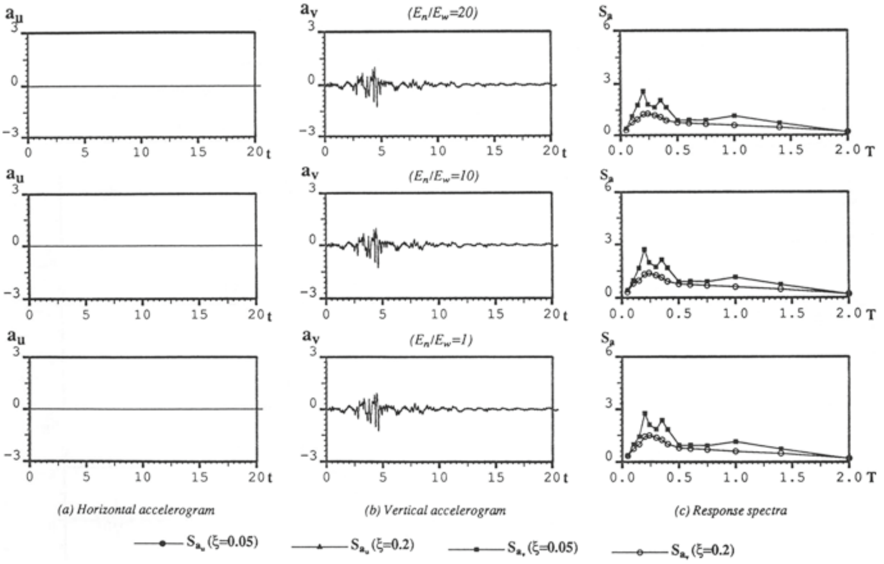

(B) Station 5

Fig. 4.15 Distributions of acceleration time-history and response spectrum due to different weathered strata (seismic P-wave vertical incidence): (**A**) Station 1; (**B**) Station 5. The locations of these two stations are shown in Fig. 4.7

Fig. 4.14(A)) are similar to those of the incident seismic SV-wave for a homogeneous rock canyon (i.e. $E_n/E_w = 1$) but are different for the weathered rock stratum on the surface of the fresh rock of the canyon. For station 5 shown in Fig. 4.14(B), the earthquake accelerogram and the corresponding response spectrum are almost the same for all three values of E_n/E_w. As expected, the vertical acceleration component remains zero at station 5 as a result of both the canyon symmetry and the vertical incident seismic SV-wave. Compared with a plane harmonic SV-wave incidence, a plane seismic SV-wave incidence can result in a smaller amplification factor to the free-field motion along the weathered canyon surface due to the average self-healing effect caused by a series of different harmonic waves arising from the incident seismic SV-wave.

To investigate the effect of the incident seismic wave type on the free-field motion along the weathered canyon surface, a unit vertically incident seismic P-wave, which has the same acceleration time-history as that used for the unit vertically incident seismic SV-wave, is used in the coupled computational model. Figure 4.15 shows the canyon surface earthquake accelerogram and the corresponding response spectrum at two observation stations for the three different weathered stratum cases due to the plane seismic P-wave vertical incidence. The wave mode conversion effect of the weathered canyon due to the plane seismic P-wave vertical incidence is stronger than that due to the plane seismic SV-wave vertical incidence. The softer the weathered rock stratum of a canyon, the stronger the wave mode conversion of the canyon. The peak values of the horizontal and vertical acceleration components (a_u and a_v) are almost the same at station 1 in Fig. 4.15(A), while the peak value of the horizontal acceleration component is even greater than that of the vertical acceleration component at station 3, which is located at the middle of the weathered canyon surface. This indicates that the wave-mode conversion effect depends not only on the incident seismic wave type and the weathered stratum material on the fresh rock surface of the canyon, but also on the location of an observation station along the weathered canyon surface. For the seismic P-wave vertical incidence and $E_n/E_w = 10$ (in Fig. 4.15(A)), the maximum amplification factor of the weathered canyon to the incident seismic P-wave is about 3, which is equivalent to the value obtained for the seismic SV-wave vertical incidence and $E_n/E_w = 20$ (in Fig. 4.13(A)). For all three values of the softness of the weathered stratum (E_n/E_w) under consideration, similar results for the free-field acceleration and the corresponding response spectrum are obtained at station 5 in Fig. 4.15(B), indicating that the value of E_n/E_w has little effect on the free-field motion at station 5 during an earthquake event.

In summary, the geological conditions of a canyon can significantly affect the free-field motion along the canyon surface during earthquakes. Both the peak value and the frequency component of the free-field motion along the surface of a natural canyon mainly depend on the softness of the weathered stratum (E_n/E_w), the location of an observation station along the canyon surface and the incident seismic wave. The softer the weathered rock stratum of a canyon, the greater the amplification of the canyon to an incident seismic wave. A softer weathered stratum on the surface of a canyon can result in a stronger wave-mode conversion effect, especially for seismic P-wave vertical incidences.

Chapter 5
Theory of Three-Dimensional Dynamic Infinite Elements for Simulating Wave Propagation Problems in Infinite Media

Numerical simulation of infinite media is an important topic in dynamic soil–structure interaction problems. This topic arose from numerous practical problems, such as numerical simulation of building structural foundations, offshore structural foundations, dam foundations, nuclear power station foundations, just to name a few. The study of this topic becomes more important when the structure is large and the effects of earthquake waves are considered. Owing to the importance of dynamic soil–structure interaction effects, a large amount of research has been carried out in the past few decades (Elorduy et al. 1967; Lysmer and Kuhlemyer 1969; Kausel 1974; Zienkiewicz and Bettess 1975; Wong and Luco 1976; White et al. 1977; Cundall et al. 1978; Chow and Smith 1981; Hamidzadeh-Eraghi and Grootenhuis 1981; Medina and Taylor 1983; Liao et al. 1984; Wolf 1985, 1988; Zhao et al. 1987, 1989; Zhang and Zhao 1987; Zhao and Liu 2002, 2003). The general methodology of dealing with a dynamic soil–structure interaction problem is to divide the whole infinite foundation of the problem into a near field, which is comprised of a limited region of the infinite foundation, and a far field, which is comprised of the remaining part of the infinite foundation. As the near field is usually simulated by using the finite element method, both the geometrical irregularity and the non-homogeneity of an infinite foundation can be considered to determine the boundary of the near field. Since the far field is usually simplified as an isotropic, homogeneous, elastic medium, its effect on the near field can be represented either by some special artificial boundaries (Lysmer and Kuhlemyer 1969; Kausel 1974; White et al. 1977; Cundall et al. 1978; Liao et al. 1984; Zhao and Liu 2002, 2003) or by some special elements (Ungless 1973; Zienkiewicz and Bettess 1975; Bettess 1977, 1980; Chow and Smith 1981; Medina and Taylor 1983; Zhao et al. 1987, 1989). Through applying these special artificial boundaries or elements on the interface between the near field and the far field, the effect of the far field on the near field can be considered in the corresponding computational models.

From the wave-propagation point of view, there are two typical kinds of problems: a kind of wave radiation problem and a kind of wave scattering problem. For a wave radiation problem, the vibration source of the problem is located within the interior region of the near field, while for a wave scattering problem, the vibration source of the problem is located within the exterior region of the near field.

C. Zhao, *Dynamic and Transient Infinite Elements*, Advances in Geophysical and Environmental Mechanics and Mathematics, DOI 10.1007/978-3-642-00846-7_5,

The artificial boundary technique works well for dealing with wave radiation problems in infinite foundations, but it often fails in solving wave scattering problems in infinite foundations. Since the seismic analysis of a structure can be treated as a wave scattering problem, it is very difficult, if not impossible, to use the artificial boundary technique for solving dynamic soil–structure interaction problems, where earthquake waves are coming from the far fields of structural foundations. In such a case, the use of special elements such as dynamic infinite elements and boundary elements is a potential way for dealing with dynamic soil–structure interaction problems under earthquake loadings. Although the boundary element method is an efficient way to simulate wave scattering problems in a homogeneous medium due to a significant reduction in the total number of degrees-of-freedom of the system, the dynamic infinite element method is more suitable for simulating wave scattering problems in a non-homogeneous medium due to the banded and symmetrical nature of the resulting global mass and stiffness matrices of the system. On the other hand, for large structures such as arch dams, especially for double-curvature arch dams with smaller thicknesses and complicated configurations, a few finite elements are usually enough to simulate the thickness of a double-curvature arch dam so that the total number of degrees-of-freedom of the double-curvature arch dam cannot be greatly reduced when it is simulated using the boundary element method. In this case, the boundary element method loses its computational advantage in comparison to the finite element method, implying that for the seismic analysis of arch dams, the coupled computational method of finite elements and dynamic infinite elements (Zhao et al. 1989, 1992; Zhao and Valliappan 1991, 1993d, e) is more appropriate for simulating both an arch dam and the infinite foundation.

The concept of static infinite elements was initially presented in the seventies of the last century (Ungless 1973; Bettess 1977). Further work was carried out to apply the coupled computational model of finite elements and static infinite elements to the solution of static problems in engineering practice (Beer and Meek 1981; Zhao et al. 1986). The fundamental idea behind construction of a static infinite element is either to derive a special element displacement shape function, which is the production of a Lagrange interpolation function and a decay function, or to use special mapping techniques to map the infinite element into a finite one. The same idea has been used to develop two-dimensional dynamic infinite elements (Chow and Smith 1981; Medina and Taylor 1983; Zhao et al. 1987, 1992). Owing to the complicated mechanism of wave propagation in an infinite medium, the decay function for the static infinite element needs to be replaced by a wave propagation function for the dynamic infinite element. For simulating infinite solid media, several forms of two-dimensional dynamic infinite elements, which differ from the selection of the corresponding wave-propagation function of a dynamic infinite element, are presented by different authors (Chow and Smith 1981; Medina and Taylor 1983; Zhao et al. 1987, 1992). Nevertheless, early work on the development of dynamic infinite elements (Chow and Smith 1981; Medina and Taylor 1983) was mainly attributed to numerical simulation of two-dimensional and axisymmetrical wave radiation problems in infinite media. Although a previous three-dimensional dynamic infinite element (Zhao et al. 1989) was used to simulate a wavescattering problem for an arch dam–

foundation system, it has only one wavenumber so that it cannot be used to simulate efficiently and simultaneously wave-propagation problems of multiple wavenumbers (Zhao 1987). This means that for a given incident earthquake wave, one must first separate this wave into SH-wave, SV-wave and P-wave components and then use the wavenumber of each wave component to evaluate the stiffness and mass matrices of a dynamic infinite element. As a result, the stiffness and mass matrices of the previous three-dimensional dynamic infinite element need to be evaluated three times since only one wavenumber can be exactly represented each time by the previous three-dimensional dynamic infinite element.

Based on the above considerations, the theory of three-dimensional dynamic infinite elements is presented in this chapter. The wavenumbers of SH-waves, SV-waves and P-waves are used in the proposed three-dimensional dynamic infinite element. As a result, the coupled computational model of three-dimensional finite elements and three-dimensional dynamic infinite elements are better suited for simulating seismic wave propagation problems in the infinite foundations of arch dams. Owing to the use of a mapping technique in the process of developing the three-dimensional dynamic infinite element, it is feasible to use the coupled computational model of three-dimensional finite elements and three-dimensional dynamic infinite elements for dealing with dynamic arch dam–foundation interaction problems in a rectangular coordinate system. Two vibration problems, namely the vibration of a square rigid plate on a homogeneous elastic half-space and the vibration of a square rigid plate on a layered foundation, are considered as benchmark problems for the verification of the coupled computational model of three-dimensional finite elements and dynamic infinite elements.

5.1 Coupled Computational Model for Simulating Three-Dimensional Wave Propagation Problems in Infinite Foundations of Structures

For the numerical simulation of wave propagation problems in infinite foundations of structures, it is necessary to investigate the propagating mechanisms of harmonic waves in the infinite foundations of structures, because an arbitrary wave can be decomposed into the sum of several harmonic waves. The understanding of the detailed mechanisms of harmonic wave propagation in an infinite foundation can provide important insights into the fundamental behaviours and characteristics of a dynamic structure–foundation interaction system. After harmonic wave propagation problems in the infinite foundation are solved, the seismic analysis of a structure–foundation system can be straightforwardly carried out using the fast Fourier transform (FFT) and inverse Fourier transform (IFFT) techniques. Both the frequency domain method and the hybrid frequency-time domain method can be used for the linear and nonlinear dynamic analysis of a dynamic structure–foundation interaction system (Wolf 1985, 1988). Since an iteration technique is used for the hybrid frequency-time domain method, a nonlinear dynamic system, at each iteration, can be approximately simulated as a linear one, so that the nonlinear effect of the dynamic system can be represented by pseudo-forces. These forces compensate for the difference between the internal forces obtained from the pseudo-linear system and those obtained from the original nonlinear system. The iteration can be continued until the convergence is achieved. For these reasons, harmonic waves are used to establish the theoretical basis of three-dimensional dynamic infinite elements in this section.

Assuming an infinite foundation is subjected to a harmonic loading and that the material of the infinite foundation exhibits hysteretic damping, the governing equations of wave motion of the system can be expressed as follows:

$$G^*\nabla^2 u + (\lambda^* + G^*)\left(\frac{\partial^2 u}{\partial x^2} + \frac{\partial^2 v}{\partial x \partial y} + \frac{\partial^2 w}{\partial x \partial z}\right) + f_x = \rho\frac{\partial^2 u}{\partial t^2}, \tag{5.1}$$

$$G^*\nabla^2 v + (\lambda^* + G^*)\left(\frac{\partial^2 u}{\partial x \partial y} + \frac{\partial^2 v}{\partial y^2} + \frac{\partial^2 w}{\partial y \partial z}\right) + f_y = \rho\frac{\partial^2 v}{\partial t^2}, \tag{5.2}$$

$$G^*\nabla^2 w + (\lambda^* + G^*)\left(\frac{\partial^2 u}{\partial x \partial z} + \frac{\partial^2 v}{\partial y \partial z} + \frac{\partial^2 w}{\partial z^2}\right) + f_z = \rho\frac{\partial^2 w}{\partial t^2}, \tag{5.3}$$

$$G^* = (1 + i\eta_d)G, \qquad \lambda^* = (1 + i\eta_d)\lambda, \tag{5.4}$$

where G is the shear modulus; λ is the Lamé constant; η_d is the hysteretic damping coefficient of the medium; u, v and w are the displacements in the x, y and z directions; f_x, f_y and f_z are the body force components in the x, y and z directions respectively; ρ is the density of the medium; ∇^2 is the second-order three-dimensional Laplace operator.

By making use of the Galerkin weighted residual method and neglecting the body forces in Eqs. (5.1), (5.2) and (5.3), the following discretized equations of wave motion of the system can be obtained:

$$-\omega^2[M]\{\Delta\} + (1 + i\eta_d)[K]\{\Delta\} = \{F_0\}, \tag{5.5}$$

where $\{\Delta\}$ is the unknown nodal displacement vector; ω is the circular frequency of a harmonic wave; $[M]$ and $[K]$ are the global mass and stiffness matrices of the system, respectively; and $\{F_0\}$ is the amplitude vector of the applied harmonic load. $[M]$, $[K]$ and $\{F_0\}$ can be assembled from the following element submatrices and subvectors:

$$[M]^e = \iiint_V [N]^T \rho [N] dV, \tag{5.6}$$

$$[K]^e = \iiint_V [B]^T [D^*][B] dV, \tag{5.7}$$

$$\{F_0\}^e = \iint_A [N]^T\{\overline{X}_0\}dA + [N]^T\{\overline{P}_0\}, \tag{5.8}$$

where V and A are the volume and surface area of the element; $\{\overline{X}_0\}$ is the amplitude vector of the element boundary traction; $\{\overline{P}_0\}$ is the amplitude vector of concentrated loads acting on the element; $[D^*]$ is the constitutive matrix of the element material; $[B]$ and $[N]$ are the strain matrix and shape function matrix of the element.

It needs to be pointed out that Eqs. (5.6), (5.7) and (5.8) are equally valid for both the finite and dynamic infinite elements. Although the volume of the dynamic infinite element can approach infinity, the mass and stiffness matrices of the element are still of finite values (Chow and Smith 1981; Medina and Taylor 1983; Zhao et al. 1987, 1989). This is because both the displacement shape function and strain matrices of the dynamic infinite element have a common term, known as the wave propagation function, whose value tends to zero as the volume of the dynamic infinite element approaches infinity. Since the derivation of three-dimensional finite element formulation is well known (Zienkiewicz 1977; Rao 1989), only the formulation of three-dimensional dynamic infinite elements is derived in the next section.

5.2 Formulation of Three-Dimensional Dynamic Infinite Elements

In terms of simulating a continuum system numerically, the continuous displacement field of the system is approximately represented by a discretized displacement field. The accuracy of the discretized model depends, to a large extent, on both the element size and the extent to which the displacement shape function of an element approaches the continuous displacement field of the original system. In the finite element analysis, the restriction of the construction of the displacement shape function for a finite element can be somewhat relaxed if a fine mesh of smaller elements is used to simulate the discretized system. However, the use of smaller elements can result in a significant increase in the total number of degrees-of-freedom of the discretized system so that both the computer CPU time and storage requirement for a given problem will increase remarkably. On the other hand, it is possible to construct an element using a more accurate displacement shape function to match the continuous displacement field of a real system so as to reduce significantly the total number of degrees-of-freedom of the discretized model of the system. This is the basic idea behind the construction of some special elements such as the finite strip element (Cheung 1976) and the boundary element (Brebbia 1978). When these special elements are used appropriately in the numerical simulation of a system, both computer CPU times and storage requirements are reduced significantly, compared with the finite element simulation of the same system. This basic idea is also applicable to the construction of a three-dimensional dynamic infinite element and, therefore, the key issue associated with the construction of a three-dimensional dynamic infinite element is how to choose an accurate displacement shape function for the element.

5.2.1 *Mapping Functions of Three-Dimensional Dynamic Infinite Elements*

To make the resulting three-dimensional dynamic infinite element more suitable for simulating both the geometrical irregularity and the material variety of a natural arch-dam foundation, a coordinate mapping technique is used to map a three-dimensional dynamic infinite element in the global coordinate system into a typical parent dynamic infinite element in the local coordinate system. Through the theoretical analysis of this typical parent dynamic infinite element, the mass and stiffness matrices of the three-dimensional dynamic infinite element can be derived.

For the three-dimensional dynamic infinite element shown in Fig. 5.1, the four sides of the infinite element in the direction of approaching infinity can be represented by straight lines, so that only eight nodes are sufficient to describe the geometry of the three-dimensional dynamic infinite element in the global coordinate system. However, to represent the wave propagation behaviour within the infinite element appropriately, 12 nodes are used to describe the displacement field of the three-dimensional dynamic infinite element. For this reason, the mapping relationship between the global coordinate system and the local coordinate system for the three-dimensional dynamic infinite element can be expressed as follows:

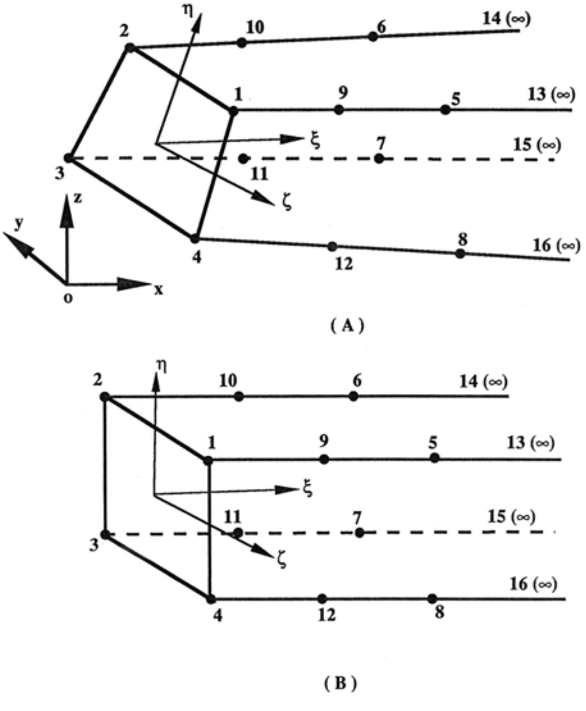

Fig. 5.1 Geometry of a three-dimensional 12-node dynamic infinite element: (**A**) the physical element; (**B**) the parent element

$$x = \sum_{q=1}^{8} M_q x_q, \tag{5.9}$$

$$y = \sum_{q=1}^{8} M_q y_q, \tag{5.10}$$

$$z = \sum_{q=1}^{8} M_q z_q, \tag{5.11}$$

where x_q, y_q and z_q are the nodal coordinates of the three-dimensional dynamic infinite element in the x, y and z directions, respectively; M_q ($q = 1,2, \ldots, 8$) is the mapping function of the three-dimensional dynamic infinite element.

$$M_1 = \frac{1}{4}(1-\xi)(1+\eta)(1+\zeta), \tag{5.12}$$

$$M_2 = \frac{1}{4}(1-\xi)(1+\eta)(1-\zeta), \tag{5.13}$$

$$M_3 = \frac{1}{4}(1-\xi)(1-\eta)(1-\zeta), \tag{5.14}$$

$$M_4 = \frac{1}{4}(1-\xi)(1-\eta)(1+\zeta), \tag{5.15}$$

$$M_5 = \frac{1}{4}\xi(1+\eta)(1+\zeta), \tag{5.16}$$

$$M_6 = \frac{1}{4}\xi(1+\eta)(1-\zeta), \tag{5.17}$$

$$M_7 = \frac{1}{4}\xi(1-\eta)(1-\zeta), \tag{5.18}$$

$$M_8 = \frac{1}{4}\xi(1-\eta)(1+\zeta). \tag{5.19}$$

Note that since the mapping functions of the three-dimensional dynamic infinite element are different from the displacement shape functions of the element, the three-dimensional dynamic infinite element is not an isoparametric element.

5.2.2 Displacement Shape Functions of Three-Dimensional Dynamic Infinite Elements

Consideration of the displacement compatibility condition on the connected interface between a three-dimensional eight-node isoparametric finite element (Zienkiewicz 1977) and a three-dimensional 12-node dynamic infinite element

(Zhao et al. 1993d) yields the following displacement field for the three-dimensional 12-node dynamic infinite element:

$$u = \sum_{q=1}^{12} N_q u_q, \tag{5.20}$$

$$v = \sum_{q=1}^{12} N_q v_q, \tag{5.21}$$

$$w = \sum_{q=1}^{12} N_q w_q, \tag{5.22}$$

where N_q $(q = 1, 2, \ldots, 12)$ is the displacement shape function of the three-dimensional 12-node dynamic infinite element as follows:

$$N_q = P_q(\xi)\left[\frac{1}{4}(1+\eta)(1+\zeta)\right] \qquad (q = 1, 5, 9), \tag{5.23}$$

$$N_q = P_q(\xi)\left[\frac{1}{4}(1+\eta)(1-\zeta)\right] \qquad (q = 2, 6, 10), \tag{5.24}$$

$$N_q = P_q(\xi)\left[\frac{1}{4}(1-\eta)(1-\zeta)\right] \qquad (q = 3, 7, 11), \tag{5.25}$$

$$N_q = P_q(\xi)\left[\frac{1}{4}(1-\eta)(1+\zeta)\right] \qquad (q = 4, 8, 12), \tag{5.26}$$

where $P_q(\xi)$ $(q = 1, 2, \ldots, 12)$ is the wave propagation function of the three-dimensional 12-node dynamic infinite element; N_q $(q = 1, 2, \ldots, 12)$ is the displacement shape function of the three-dimensional 12-node dynamic infinite element. The wave propagation function of the three-dimensional 12-node dynamic infinite element can be determined by investigating the harmonic wave propagation behaviour in an infinite medium (Zhao and Valliappan 1993d). When an isotropic, homogeneous and elastic half-space is subjected to a harmonic loading, the induced harmonic waves propagate from the vibration source into the far field of the half-space. The analytical solution for this problem can be expressed using the special functions, known as Bessel functions and Hankel functions (Graff 1975; Medina and Taylor 1983). For example, for P-waves and S-waves propagating with spherical symmetry, the harmonic free-vibration solution for spherically symmetrical waves traveling in a homogeneous, isotropic and elastic medium, away from the origin of a vibration source, is expressed as follows (Medina and Taylor 1983):

$$u = B_1 h_1^{(2)}(k_p R), \tag{5.27}$$

$$v = B_2 h_0^{(2)}(k_s R), \tag{5.28}$$

$$w = B_3 h_0^{(2)}(k_s R), \tag{5.29}$$

$$R = \sqrt{x^2 + y^2 + z^2}, \tag{5.30}$$

where $h_0^{(2)}$ and $h_1^{(2)}$ are the zeroth order and first-order spherical Hankel functions of the second kind; B_1, B_2 and B_3 are three constants; k_p and k_s are the wavenumbers of a P-wave and an S-wave, respectively.

Note that the asymptotic behaviour of $h_0^{(2)}$ and $h_1^{(2)}$ can be expressed using the following equations (Graff 1975; Medina and Taylor 1983):

$$h_0^{(2)}(x) = \frac{1}{x} \exp\left[i\left(x - \frac{\pi}{4}\right)\right] + O\left(|x|^{-2}\right), \tag{5.31}$$

$$h_1^{(2)}(x) = \frac{1}{x} \exp\left[i\left(x - \frac{3\pi}{4}\right)\right] + O\left(|x|^{-2}\right). \tag{5.32}$$

Equations (5.27), (5.28), (5.29), (5.31) and (5.32) clearly indicate that the wave propagation behaviour in the far field of a half-space can be approximately represented by exponential functions. A similar conclusion can be obtained when a cylindrical Rayleigh wave (i.e. R-wave) propagating in a homogeneous, isotropic and elastic half-space is considered. Therefore, in the far field of a half-space, the asymptotic behaviour of these special functions can be approximately expressed as a combination of several exponential functions. The physical explanation for this is that the induced waves in the far field of the half-space can be approximately represented using the superposition of plane harmonic waves. Based on this recognition and consideration of induced waves with multiple wavenumbers, the general form of the wave propagation function for the three-dimensional 12-node dynamic infinite element can be expressed as

$$\begin{aligned} P_q(\xi) = \exp(-\alpha\xi) \ \big[&c_1 \exp(-i\beta_1\xi) + c_2 \exp(-i\beta_2\xi) \\ &+ c_3 \exp(-i\beta_3\xi)\big] \quad (q = 1, 2, \ldots, 12), \end{aligned} \tag{5.33}$$

where α is the nominal decay coefficient that is used to express the wave amplitude attenuation due to both the wave energy dissipation in the three-dimensional 12-node dynamic infinite element and the geometrical divergence of the three-dimensional 12-node dynamic infinite element. Note that the determination of the value of α was addressed in Chap. 2. β_1, β_2 and β_3 are three nominal wavenumbers corresponding to R-, S- and P-waves in the three-dimensional 12-node dynamic infinite element. These nominal wavenumbers are used to express the phase characteristics of wave propagation in the three-dimensional 12-node dynamic infinite element. c_1, c_2 and c_3 are three constants to be determined by matching the displacement field of the three-dimensional 12-node dynamic infinite element with that of the infinite medium.

Although R-waves, S-waves and P-waves decay with distance from the point of excitation at different rates, previous studies (Zhang and Zhao 1987; Zhao et al. 1989) have demonstrated that the decay rates of different waves in a dynamic infinite element are not sensitive to the numerical results. Thus, the same decay rate is used for all three waves involved in the construction of the wave propagation function of the three-dimensional 12-node dynamic infinite element. Regarding the exponential decay of the Rayleigh wave with the depth from ground surface, it is reasonable to represent this phenomenon approximately by using piecewise interpolation in the η and ζ directions for the three-dimensional 12-node dynamic infinite element.

To determine the constants c_1, c_2 and c_3, the displacement field of the three-dimensional 12-node dynamic infinite element needs to be considered. Letting nodal displacements for the nodes located at an infinite side in the ξ direction of the element be equal to the element displacement field expressed in Eqs. (5.20), (5.21) and (5.22), these three constants can be determined. For instance, if the side of the three-dimensional 12-node dynamic infinite element with nodes 1 ($\xi = 0$), 5 ($\xi = 1/2$) and 9 ($\xi = 1$) is considered, the following relationships emerge:

$$\begin{Bmatrix} u_1 \\ u_5 \\ u_9 \end{Bmatrix} = \begin{bmatrix} 1 & 1 & 1 \\ -\exp\left[-\frac{1}{2}\left(\alpha + i\beta_1\right)\right] & -\exp\left[-\frac{1}{2}\left(\alpha + i\beta_2\right)\right] & -\exp\left[-\frac{1}{2}\left(\alpha + i\beta_3\right)\right] \\ \exp\left[-\left(\alpha + i\beta_1\right)\right] & \exp\left[-\left(\alpha + i\beta_2\right)\right] & \exp\left[-\left(\alpha + i\beta_3\right)\right] \end{bmatrix} \begin{Bmatrix} c_1 \\ c_2 \\ c_3 \end{Bmatrix} = [C] \begin{Bmatrix} c_1 \\ c_2 \\ c_3 \end{Bmatrix}. \tag{5.34}$$

Solving Eq. (5.34) yields the following matrix equation:

$$\begin{Bmatrix} c_1 \\ c_2 \\ c_3 \end{Bmatrix} = [C]^{-1} \begin{Bmatrix} u_1 \\ u_5 \\ u_9 \end{Bmatrix} = [E] \begin{Bmatrix} u_1 \\ u_5 \\ u_9 \end{Bmatrix}. \tag{5.35}$$

After these three constants are determined, the wave-propagation function for the three-dimensional 12-node dynamic infinite element can be further expressed as follows:

$$\begin{aligned} P_q(\xi) = {} & E_{11} \exp\left[-\left(\alpha + i\beta_1\right)\xi\right] + E_{21} \exp\left[-\left(\alpha + i\beta_2\right)\xi\right] \\ & + E_{31} \exp\left[-\left(\alpha + i\beta_3\right)\xi\right] \qquad (q = 1, 2, 3, 4), \end{aligned} \tag{5.36}$$

$$\begin{aligned} P_q(\xi) = {} & E_{12} \exp\left[-\left(\alpha + i\beta_1\right)\xi\right] + E_{22} \exp\left[-\left(\alpha + i\beta_2\right)\xi\right] \\ & + E_{32} \exp\left[-\left(\alpha + i\beta_3\right)\xi\right] \qquad (q = 5,6,7,8), \end{aligned} \tag{5.37}$$

$$\begin{aligned} P_q(\xi) = {} & E_{13} \exp\left[-\left(\alpha + i\beta_1\right)\xi\right] + E_{23} \exp\left[-\left(\alpha + i\beta_2\right)\xi\right] \\ & + E_{33} \exp\left[-\left(\alpha + i\beta_3\right)\xi\right] \qquad (q = 9, 10, 11, 12), \end{aligned} \tag{5.38}$$

where

$$E_{11} = \frac{1}{\Delta} \exp\left[-\frac{1}{2}\left(3\alpha + i\beta_2 + i\beta_3\right)\right]\left[\exp\left(-\frac{i}{2}\beta_3\right) - \exp\left(-\frac{i}{2}\beta_2\right)\right], \tag{5.39}$$

$$E_{21} = \frac{1}{\Delta} \exp\left[-\frac{1}{2}\left(3\alpha + i\beta_1 + i\beta_3\right)\right]\left[\exp\left(-\frac{i}{2}\beta_1\right) - \exp\left(-\frac{i}{2}\beta_3\right)\right], \quad (5.40)$$

$$E_{31} = \frac{1}{\Delta} \exp\left[-\frac{1}{2}\left(3\alpha + i\beta_1 + i\beta_2\right)\right]\left[\exp\left(-\frac{i}{2}\beta_2\right) - \exp\left(-\frac{i}{2}\beta_1\right)\right], \quad (5.41)$$

$$E_{12} = \frac{1}{\Delta} \exp\left(-\alpha\right)\left[\exp\left(-i\beta_2\right) - \exp\left(-i\beta_3\right)\right], \quad (5.42)$$

$$E_{22} = \frac{1}{\Delta} \exp\left(-\alpha\right)\left[\exp\left(-i\beta_3\right) - \exp\left(-i\beta_1\right)\right], \quad (5.43)$$

$$E_{32} = \frac{1}{\Delta} \exp\left(-\alpha\right)\left[\exp\left(-i\beta_1\right) - \exp\left(-i\beta_2\right)\right], \quad (5.44)$$

$$E_{13} = \frac{1}{\Delta} \exp\left(-\frac{1}{2}\alpha\right)\left[\exp\left(-\frac{i}{2}\beta_3\right) - \exp\left(-\frac{i}{2}\beta_2\right)\right], \quad (5.45)$$

$$E_{23} = \frac{1}{\Delta} \exp\left(-\frac{1}{2}\alpha\right)\left[\exp\left(-\frac{i}{2}\beta_1\right) - \exp\left(-\frac{i}{2}\beta_3\right)\right], \quad (5.46)$$

$$E_{33} = \frac{1}{\Delta} \exp\left(-\frac{1}{2}\alpha\right)\left[\exp\left(-\frac{i}{2}\beta_2\right) - \exp\left(-\frac{i}{2}\beta_1\right)\right], \quad (5.47)$$

$$\begin{aligned}\Delta = {} & \exp\left(-\frac{3}{2}\alpha\right)\left\{\exp\left[-\frac{i}{2}\left(\beta_2 + \beta_3\right)\right]\left[\exp\left(-\frac{i}{2}\beta_3\right) - \exp\left(-\frac{i}{2}\beta_2\right)\right]\right\} \\ & + \exp\left(-\frac{3}{2}\alpha\right)\left\{\exp\left[-\frac{i}{2}\left(\beta_1 + \beta_2\right)\right]\left[\exp\left(-\frac{i}{2}\beta_2\right) - \exp\left(-\frac{i}{2}\beta_1\right)\right]\right\}. \\ & + \exp\left(-\frac{3}{2}\alpha\right)\left\{\exp\left(-\frac{i}{2}\left(\beta_1 + \beta_3\right)\right)\left[\exp\left(-\frac{i}{2}\beta_1\right) - \exp\left(-\frac{i}{2}\beta_3\right)\right]\right\}\end{aligned} \quad (5.48)$$

Note that a sufficient condition for the existence of $P_q(\xi)$ (q= 1, 2, ..., 12) in the three-dimensional 12-node dynamic infinite element is that β_1, β_2 and β_3 are three different constants. This condition can be satisfied for simulating wave-propagation problems in an infinite medium, because, from the physical point of view, R-, S- and P-waves have three different wavenumbers in the infinite medium.

In addition, the following expression for the wave propagation function of the three-dimensional 12-node dynamic infinite element exists:

$$P_q(\xi_r) = \delta_{qr} \qquad (q = 1, 2, \ldots, 12;\ r = 1, 2, \ldots, 12), \quad (5.49)$$

where δ_{qr} is the Kronecker delta. This implies that for any displacement shape function, N_q ($q = 1, 2, \ldots, 12$), $N_q = 1$ when $\xi = \xi_q$, $\eta = \eta_q$ and $\zeta = \zeta_q$, while $N_q = 0$ when $\xi = \xi_r$, $\eta = \eta_r$ and $\zeta = \zeta_r$, where $r \neq q$.

Supposing the velocities of the P-wave, S-wave and R-wave in an elastic infinite medium are 3000, 1500 and 1398 m s^{-1}, respectively, and that the excitation circular

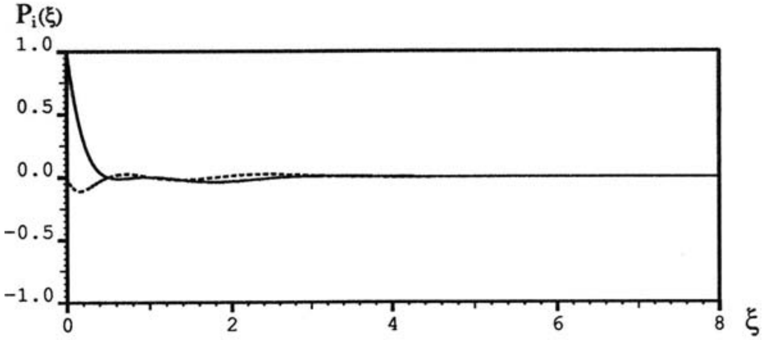

(a) i=1, 2, 3, 4

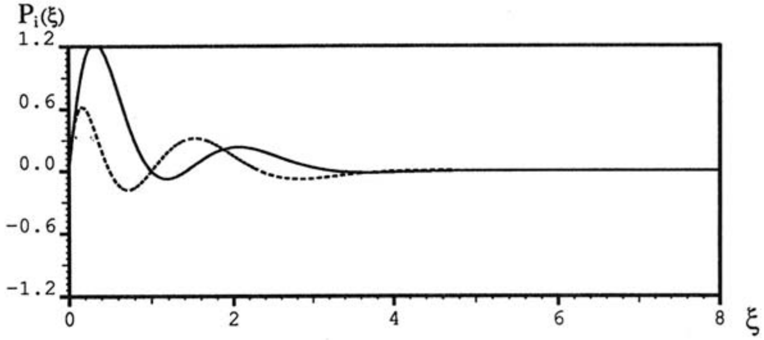

(b) i=5, 6, 7, 8

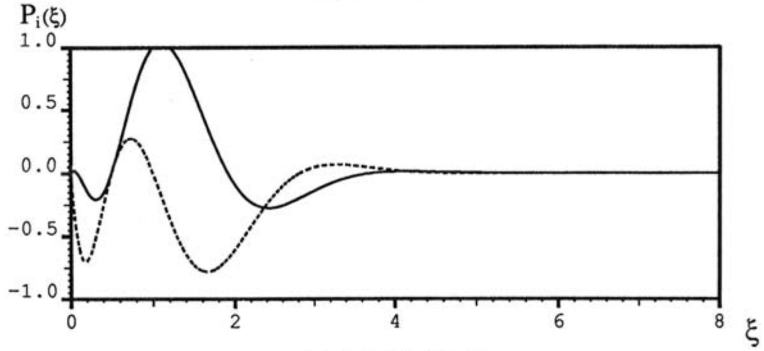

(c) i=9, 10, 11, 12

Fig. 5.2 Distributions of wave-propagation functions in a three-dimensional 12-node dynamic infinite element: the *solid lines* represent the real parts of the wave-propagation function, while the *dashed lines* represent the imaginary parts of the wave-propagation function frequency is 30 rad s^{-1}, the corresponding wavenumbers for the P-wave, S-wave and R-wave are 0.01, 0.02 and 0.0215, respectively. If these wavenumbers are multiplied by 100, which means that the global coordinates of the three-dimensional 12-node dynamic infinite element is divided by 100 in the ξ direction, the distributions of the wave propagation functions (i.e. $P_q(\xi)$ ($q = 1, 2, \ldots, 12$)), which are used in the three-dimensional 12-node dynamic infinite element, are shown in Fig. 5.2, where $\alpha = 2.2$, $\beta_1 = 1$, $\beta_2 = 2$ and $\beta_3 = 2.25$. In this figure, the solid and dashed lines are the real and imaginary parts of the wave-propagation functions, which are used to express the element-displacement pattern for the three-dimensional 12-node dynamic infinite element. From the wave-propagation point of view, it is the wave-propagation function that describes how waves in the three-dimensional 12-node dynamic infinite element propagate from the element nodes to the far field of the infinite medium.

Another characteristic of the three-dimensional 12-node dynamic infinite element is that real (physical) wavenumbers in a global coordinate system can be adjusted by changing the locations of element side nodes 5, 6, 7 and 8 in the global coordinate system. This technique is helpful when the three-dimensional 12-node dynamic infinite element is used to simulate wave-propagation problems in non-homogeneous infinite foundations (Zhao et al. 1987, 1989).

5.2.3 Mass and Stiffness Matrices of Three-Dimensional Dynamic Infinite Elements

If the same procedures as those used in the finite element method (Zienkiewicz 1977; Zhao et al. 1992) are used, both the mass matrix and the stiffness matrix of the three-dimensional 12-node dynamic infinite element can be expressed as follows:

$$[M]^e = \int_{-1}^{1}\int_{-1}^{1}\int_{0}^{\infty} [N]^T \rho [N]\,|J|\,d\xi d\eta d\zeta, \tag{5.50}$$

$$[K]^e = \int_{-1}^{1}\int_{-1}^{1}\int_{0}^{\infty} [B]^T [D^*][B]\,|J|\,d\xi d\eta d\zeta, \tag{5.51}$$

where $[B]$ and $[N]$ are the strain matrix and shape function matrix of the three-dimensional 12-node dynamic infinite element; $[D^*]$ is the constitutive matrix of the element material; $|J|$ is the Jacobian determinant which can be determined using the mapping relationship of the element (in Eqs. (5.9), (5.10) and (5.11)); and ρ is the density of the element material.

To determine the shape function matrix, Eqs. (5.20), (5.21) and (5.22) can be written in the matrix form:

$$\begin{Bmatrix} u \\ v \\ w \end{Bmatrix}^e = [N]\,\{\Delta\}^e, \tag{5.52}$$

where $[N]$ is the shape function matrix of the three-dimensional 12-node dynamic infinite element; $\{\Delta\}^e$ is the nodal displacement vector of the element. They are of the following forms:

$$[N] = \left[[N_1]\ [N_2]\ [N_3]\ [N_4]\ [N_5]\ [N_6]\ [N_7]\ [N_8]\ [N_9]\ [N_{10}]\ [N_{11}]\ [N_{12}] \right], \tag{5.53}$$

$$\{\Delta\}^e = \left\{ \{\Delta_1\}\ \{\Delta_2\}\ \{\Delta_3\}\ \{\Delta_4\}\ \{\Delta_5\}\ \{\Delta_6\}\ \{\Delta_7\}\ \{\Delta_8\}\ \{\Delta_9\}\ \{\Delta_{10}\}\ \{\Delta_{11}\}\ \{\Delta_{12}\} \right\}^T, \tag{5.54}$$

where $\left[N_q\right]$ and $\left\{\Delta_q\right\}$ are the corresponding submatrix and subvector related to the node q $(q = 1, 2, \ldots, 12)$ of the three-dimensional 12-node dynamic infinite element. They can be expressed as follows:

$$\left[N_q\right] = \begin{bmatrix} N_q & 0 & 0 \\ 0 & N_q & 0 \\ 0 & 0 & N_q \end{bmatrix} \qquad (q = 1,2,\ldots,12), \tag{5.55}$$

$$\left\{\Delta_q\right\} = \begin{Bmatrix} u_q \\ v_q \\ w_q \end{Bmatrix} \qquad (q = 1,2,\ldots,12), \tag{5.56}$$

where N_q $(q = 1, 2, \ldots, 12)$ is the displacement shape function of node q; u_q, v_q and w_q $(q = 1, 2, \ldots, 12)$ are the displacement components of node q in the x, y and z directions, respectively.

Using the above definitions, the strain matrix of the three-dimensional 12-node dynamic infinite element can be expressed as follows:

$$\{\varepsilon\}^e = \begin{Bmatrix} \varepsilon_x \\ \varepsilon_y \\ \varepsilon_z \\ \gamma_{xy} \\ \gamma_{yz} \\ \gamma_{zx} \end{Bmatrix} = \begin{Bmatrix} \partial u/\partial x \\ \partial v/\partial y \\ \partial w/\partial z \\ \partial u/\partial y + \partial v/\partial x \\ \partial v/\partial z + \partial w/\partial y \\ \partial w/\partial x + \partial u/\partial z \end{Bmatrix} = [B]\{\Delta\}^e, \tag{5.57}$$

where $[B]$ is the strain matrix of the three-dimensional 12-node dynamic infinite element; and $\{\varepsilon\}^e$ is the strain vector of the element. The strain matrix of the three-dimensional 12-node dynamic infinite element can be further expressed as

$$[B] = \left[[B_1]\ [B_2]\ [B_3]\ [B_4]\ [B_5]\ [B_6]\ [B_7]\ [B_8]\ [B_9]\ [B_{10}]\ [B_{11}]\ [B_{12}] \right], \tag{5.58}$$

where $\left[B_q\right]$ is the corresponding strain submatrix related to the node q $(q = 1, 2, \ldots, 12)$ of the three-dimensional 12-node dynamic infinite element. It can be expressed as follows:

$$[B_q] = \begin{bmatrix} \partial N_q/\partial x & 0 & 0 \\ 0 & \partial N_q/\partial y & 0 \\ 0 & 0 & \partial N_q/\partial z \\ \partial N_q/\partial y & \partial N_q/\partial x & 0 \\ 0 & \partial N_q/\partial z & \partial N_q/\partial y \\ \partial N_q/\partial z & 0 & \partial N_q/\partial x. \end{bmatrix} \qquad (q = 1, 2, \ldots, 12). \tag{5.59}$$

To evaluate the strain matrix of the three-dimensional 12-node dynamic infinite element, it is necessary to calculate the first derivatives of the displacement shape functions with respect to the local ξ, η and ζ coordinates as follows:

$$\frac{\partial N_q}{\partial \xi} = \frac{\partial N_q}{\partial x}\frac{\partial x}{\partial \xi} + \frac{\partial N_q}{\partial y}\frac{\partial y}{\partial \xi} + \frac{\partial N_q}{\partial z}\frac{\partial z}{\partial \xi} \qquad (q = 1, 2, \ldots, 12), \tag{5.60}$$

$$\frac{\partial N_q}{\partial \eta} = \frac{\partial N_q}{\partial x}\frac{\partial x}{\partial \eta} + \frac{\partial N_q}{\partial y}\frac{\partial y}{\partial \eta} + \frac{\partial N_q}{\partial z}\frac{\partial z}{\partial \eta} \qquad (q = 1, 2, \ldots, 12), \tag{5.61}$$

$$\frac{\partial N_q}{\partial \zeta} = \frac{\partial N_q}{\partial x}\frac{\partial x}{\partial \zeta} + \frac{\partial N_q}{\partial y}\frac{\partial y}{\partial \zeta} + \frac{\partial N_q}{\partial z}\frac{\partial z}{\partial \zeta} \qquad (q = 1, 2, \ldots, 12). \tag{5.62}$$

Equations (5.60), (5.61) and (5.62) can be readily expressed in the following matrix form:

$$\begin{aligned} \begin{Bmatrix} \partial N_q/\partial \xi \\ \partial N_q/\partial \eta \\ \partial N_q/\partial \zeta \end{Bmatrix} &= \begin{bmatrix} \partial x/\partial \xi & \partial y/\partial \xi & \partial z/\partial \xi \\ \partial x/\partial \eta & \partial y/\partial \eta & \partial z/\partial \eta \\ \partial x/\partial \zeta & \partial y/\partial \zeta & \partial z/\partial \zeta \end{bmatrix} \begin{Bmatrix} \partial N_q/\partial x \\ \partial N_q/\partial y \\ \partial N_q/\partial z \end{Bmatrix} \\ &= [J] \begin{Bmatrix} \partial N_q/\partial x \\ \partial N_q/\partial y \\ \partial N_q/\partial z \end{Bmatrix} \qquad (q = 1, 2, \ldots, 12), \end{aligned} \tag{5.63}$$

where the matrix $[J]$, called the Jacobian matrix, is given by the following equation:

$$[J] = \begin{bmatrix} \partial x/\partial \xi & \partial y/\partial \xi & \partial z/\partial \xi \\ \partial x/\partial \eta & \partial y/\partial \eta & \partial z/\partial \eta \\ \partial x/\partial \zeta & \partial y/\partial \zeta & \partial z/\partial \zeta \end{bmatrix}. \tag{5.64}$$

Substituting Eqs. (5.9), (5.10) and (5.11) into Eq. (5.64) yields the final expression for the Jacobian matrix as follows:

$$[J] = \begin{bmatrix} \sum\limits_{q=1}^{8} \left[\left(\partial M_q/\partial \xi\right) x_q\right] & \sum\limits_{q=1}^{8} \left[\left(\partial M_q/\partial \xi\right) y_q\right] & \sum\limits_{q=1}^{8} \left[\left(\partial M_q/\partial \xi\right) z_q\right] \\ \sum\limits_{q=1}^{8} \left[\left(\partial M_q/\partial \eta\right) x_q\right] & \sum\limits_{q=1}^{8} \left[\left(\partial M_q/\partial \eta\right) y_q\right] & \sum\limits_{q=1}^{8} \left[\left(\partial M_q/\partial \eta\right) z_q\right] \\ \sum\limits_{q=1}^{8} \left[\left(\partial M_q/\partial \zeta\right) x_q\right] & \sum\limits_{q=1}^{8} \left[\left(\partial M_q/\partial \zeta\right) y_q\right] & \sum\limits_{q=1}^{8} \left[\left(\partial M_q/\partial \zeta\right) z_q\right] \end{bmatrix}. \tag{5.65}$$

Therefore, the first derivatives of the displacement shape functions with respect to the global x, y and z coordinates can be expressed as follows:

$$\begin{Bmatrix} \partial N_q/\partial x \\ \partial N_q/\partial y \\ \partial N_q/\partial z \end{Bmatrix} = [J]^{-1} \begin{Bmatrix} \partial N_q/\partial \xi \\ \partial N_q/\partial \eta \\ \partial N_q/\partial \zeta \end{Bmatrix}. \qquad (q = 1, 2, \ldots, 12). \tag{5.66}$$

Mathematically, the value of the Jacobian determinant $|J|$ can be determined from the Jacobian matrix $[J]$.

For three-dimensional solids with hysteretic damping, the constitutive matrix of the element material can be expressed in the following form:

$$[D^*] = \frac{E(1 + i\eta_d)}{(1+\mu)(1-2\mu)} \begin{bmatrix} 1-\mu & \mu & \mu & 0 & 0 & 0 \\ \mu & 1-\mu & \mu & 0 & 0 & 0 \\ \mu & \mu & 1-\mu & 0 & 0 & 0 \\ 0 & 0 & 0 & (1-2\mu)/2 & 0 & 0 \\ 0 & 0 & 0 & 0 & (1-2\mu)/2 & 0 \\ 0 & 0 & 0 & 0 & 0 & (1-2\mu)/2 \end{bmatrix}, \tag{5.67}$$

where E and μ are the elastic modulus and Poisson's ratio of the element material, respectively; η_d is the hysteretic damping coefficient of the element material.

Substituting Eqs. (5.53), (5.58) and (5.67) into Eqs. (5.50) and (5.51) yields the following generalized integral for the evaluation of the mass and stiffness matrices of the three-dimensional 12-node dynamic infinite element:

$$I = \int_0^\infty F(\xi) \exp\left[-(2\alpha + i\beta_q + i\beta_r)\xi\right] d\xi \qquad (q = 1, 2, 3;\ r = 1, 2, 3). \tag{5.68}$$

To evaluate the generalized integral using the numerical integration technique (Chow and Smith 1981; Zhang and Zhao 1987), the following definition

$$\beta = \frac{\beta_q + \beta_r}{2} \qquad (q = 1, 2, 3;\ r = 1, 2, 3) \tag{5.69}$$

is introduced. As a result, Eq. (5.68) can be evaluated using the numerical integration technique described in Sect. 2.1.1.

5.3 Verification of Three-Dimensional Dynamic Infinite Elements

The first numerical example for verifying the proposed three-dimensional 12-node dynamic infinite element is to simulate the dynamic response of a square massless rigid plate resting on a homogeneous, isotropic and elastic half-space. If the square massless plate is rigid, the analytical solutions for the compliance of the plate are available (Wong and Luco 1976; Hamidzadeh-Eraghi and Grootenhuis 1981). In the process of deriving the analytical solutions, the rigid plate is considered by assuming that the whole plate has the same translational and rotational deformations. This means that an elastic modulus of infinity is equivalently used in the related theoretical analysis. However, from the computational point of view, the elastic modulus of a finite value needs to be used for simulating the plate. To compare the emerging numerical results with the analytical solutions, the value of the elastic modulus of the plate must be several orders higher than that of the underlying rock in the coupled computational model of three-dimensional finite and dynamic infinite elements (Zhao et al. 1989, 1992, 1993d). This implies that only a "relatively rigid" plate is simulated in the corresponding computational models.

Figure 5.3 shows the computational model of a square massless plate resting on a homogeneous, isotropic and elastic half-space, in which only a quarter of the plate-foundation system is simulated using three-dimensional finite and dynamic infinite elements due to the symmetrical nature of the problem. The symmetry boundary condition is applied to the *xz* (i.e. $y=0$) and *yz* (i.e. $x=0$) planes for the vertical vibration of the square massless plate, while the symmetry boundary condition is applied to the *xz* (i.e. $y=0$) plane and the anti-symmetry boundary condition is applied to the *yz* (i.e. $x=0$) plane for the horizontal and rocking vibration of the square massless plate. To compare the current numerical results with the previous solutions (Wong and Luco 1976; Hamidzadeh-Eraghi and Grootenhuis 1981), the same assumptions as those used in the previous work are adopted for the coupled computational model of three-dimensional finite and dynamic infinite elements (Zhao et al. 1989, 1992, 1993d).

The following parameters are used in the coupled computational model of the plate-foundation system. For the rock foundation, the elastic modulus (E_r) is 24×10^9 Pa; the value of Poisson's ratio (ν_r) is 1/3; the rock density (ρ_r) is $2400\,\text{kg m}^{-3}$. For the square massless plate, the elastic modulus (E_p) is 24×10^{12} Pa so that the plate is "relatively rigid" to the rock foundation; the half-width of the

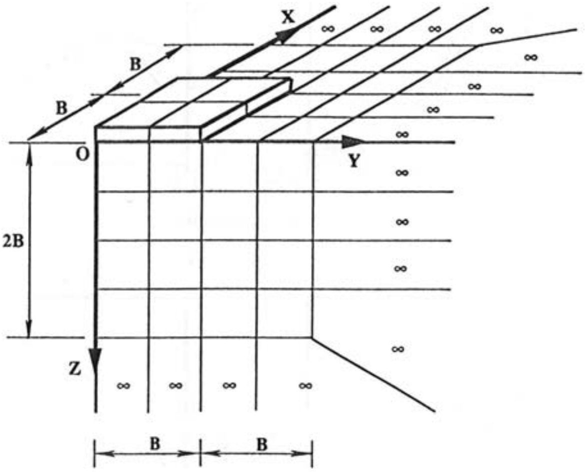

Fig. 5.3 Computational model of a massless plate resting on a homogeneous, isotropic and elastic half-space: the near field is simulated using plate and solid finite elements, while the far field is simulated using dynamic infinite elements

plate (B) is 10 m; the thickness of the plate is $B/10$. According to these parameters, the decay factor (α) used in the three-dimensional dynamic infinite elements is assumed to be 0.028, while the P-wave, S-wave and R-wave velocities, which can be determined from elastic wave theory (Graff 1975), are 3872, 1936 and 1804m s^{-1} in the rock foundation, respectively. Based on these wave velocities and the harmonic circular frequency of excitation, the three wavenumbers used in the three-dimensional dynamic infinite elements can be evaluated.

In the coupled computational model of the plate-foundation system, the square massless plate is simulated either by thick plate elements or by a combination of thick plate elements and plane stress elements (Hamidzadeh-Eraghi and Grootenhuis 1981). The near field of the rock foundation is simulated using three-dimensional eight-node solid finite elements, while the far field of the rock foundation is simulated using three-dimensional 12-node dynamic infinite elements. The resulting numerical solutions are compared with the “exact” solutions of Wong and Luco (1976), Hamidzadeh-Eraghi and Grootenhuis (1981) using the following parameters:

$$C_{HH}(a_0) = \frac{GB\Delta_1}{P_0}, \tag{5.70}$$

$$C_{VV}(a_0) = \frac{GB\Delta_3}{P_0}, \tag{5.71}$$

$$C_{MM}(a_0) = \frac{GB^3\theta_x}{M_x}, \tag{5.72}$$

$$C_{HM}(a_0) = \frac{GB^2\Delta_1}{M_x}, \tag{5.73}$$

where C_{HH} and C_{VV} are the dimensionless compliances of the plate due to the concentrated dynamic load (P_0) applied at the plate centre in the x and z directions, respectively; Δ_1 and Δ_3 are the corresponding complex displacements of the plate in the x and z directions; C_{MM} and C_{HM} are the dimensionless compliances of the plate due to the dynamic moment (M_x) applied at the plate centre; θ_x is the rotation angle of the plate corresponding to the applied moment (M_x) with respect to the x axis; G is the shear modulus of the rock foundation; a_0 is a dimensionless frequency with the following definition:

$$a_0 = \frac{\omega B}{C_S}, \tag{5.74}$$

where ω is the circular frequency of the excitation load; C_s is the S-wave velocity in the rock foundation.

Figure 5.4 shows the comparison between the current numerical results and the previous ones. In this figure, the solid and dashed lines, which are used for the representation of C_{HH} and C_{VV}, are cited from the work carried out by Wong and Luco (1976), while the solid and dashed lines, which are used for the representation of C_{MM} and C_{HM}, are cited from the work carried out by Hamidzadeh-Eraghi

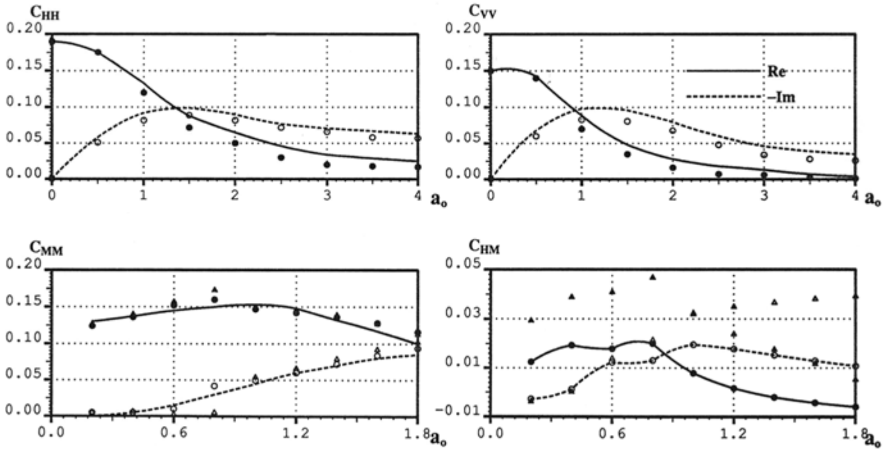

Fig. 5.4 Comparison of current results with previous results (Massless plate resting on a homogeneous, isotropic and elastic half-space)

and Grootenhuis (1981). For the computation of C_{MM} and C_{HM}, Poisson's ratio of the rock foundation is assumed to be 0.25 so that the corresponding wavenumbers for the P-wave, S-wave and R-wave need to be changed accordingly in the three-dimensional 12-node dynamic infinite elements. The solid dots and circles are used to express the numerical results obtained from the coupled computational model, in which the plate is simulated using a combination of thick plate elements and plane stress elements, while the solid triangles and hollow triangles are used to express the numerical results obtained from the coupled computational model, in which the plate is simulated only using thick plate elements. There is good agreement between the current numerical results and the previous ones when the plate is simulated using a combination of thick plate elements and plane stress elements, indicating that the accurate numerical results can be obtained from the coupled computational model of three-dimensional finite (plate) elements and dynamic infinite elements. However, when the plate is subjected to either a horizontal or a rocking loading and simulated only using thick plate elements, a significant discrepancy between the current numerical results and the previous ones is observed because the sway modes of the plate cannot be appropriately simulated by thick plate elements alone. Therefore, it is recommended that in the seismic analysis of a plate subjected to horizontal earthquakes, shell elements or a combination of thick plate elements and plane stress elements be used in the coupled computational model of three-dimensional finite (plate) elements and dynamic infinite elements.

The second numerical example for verifying the proposed three-dimensional 12-node dynamic infinite element is to simulate the dynamic response of a square massless plate resting on a visco-elastic layered foundation. This example, in essence, belongs to a wave propagation problem in a non-homogeneous infinite foundation. Figure 5.5 shows the computational model of the plate-foundation

Fig. 5.5 Computational model of a massless plate resting on a layered foundation: the near field is simulated using plate and solid finite elements, while the far field is simulated using dynamic infinite elements

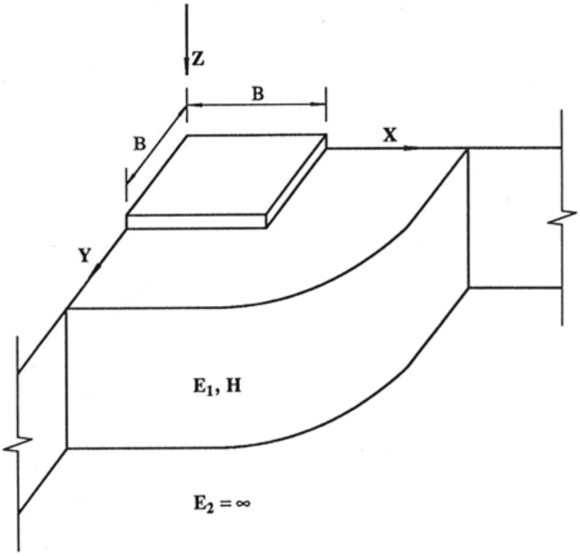

system. Owing to the symmetrical nature of the plate-foundation system, only a quarter of the plate-foundation system is simulated using three-dimensional finite (plate) elements and dynamic infinite elements. The same parameters as those used for the first verification example are employed in the computational model of the plate and layered foundation system. Since a layer resting on the rigid base rock is considered, the ratio of the layer depth to the plate width is assumed to be 2 in the coupled computational model of three-dimensional finite (plate) elements and dynamic infinite elements.

Figure 5.6 shows the comparison between the current numerical results with the previous ones (Chow 1987). In this figure, K and C are the dynamic stiffness coefficient and damping coefficient of the plate, respectively. The solid line is used to express the previous results (Chow 1987), while the solid dots are used to express the current numerical results obtained from the coupled computational model of three-dimensional finite (plate) elements and dynamic infinite elements. Generally, there is good agreement between the current numerical results and the previous ones, indicating that accurate numerical results can be obtained from the application of the coupled computational model of three-dimensional finite (plate) elements and dynamic infinite elements for solving three-dimensional wave-propagation problems in layered infinite foundations. Note that if the foundation of a plate/structure can be treated as a homogeneous, isotropic and visco-elastic half-space, the previous analytical and semi-analytical methods are computationally cheaper, compared with the coupled computational model used in this chapter. However, if the foundation of a plate/structure can be only treated as a non-homogeneous infinite medium, the previous analytical procedures (Wong and Luco 1976; Brebbia 1978; Hamidzadeh-Eraghi and Grootenhuis 1981; Chow 1987) are no longer directly applicable for

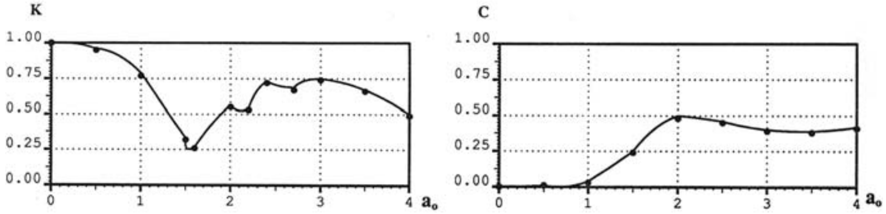

Fig. 5.6 Comparison of current results with previous results (massless plate resting on a layered foundation): the *solid lines* represent the previous solutions, while the *solid dots* represent the current results

dealing with dynamic plate/structure–foundation interaction problems, especially when dealing with dynamic arch dam—foundation interaction problems. In this case, the coupled computational model of three-dimensional finite (plate) elements and dynamic infinite elements can still work well through simply altering the parameters of different material regions, which are simulated by the three-dimensional finite (plate) elements and dynamic infinite elements.

Chapter 6
Application of Three-Dimensional Dynamic Infinite Elements: Simulation of Dynamic Structure–Foundation Interaction Problems

Numerical simulation of dynamic structure–foundation interaction problems has been an important research topic in many scientific and engineering fields (Zhao et al. 1991, 1992; Zhao and Valliappan 1991, 1993c, e). In terms of a structure–foundation interaction system, the foundation is referred to as the natural or built-up formation of soil, subsoil or rock upon which a building or structure is supported. If a structure is founded on a soft soil foundation, the dynamic structure–foundation interaction problem is also called the dynamic soil–structure interaction problem (Mita and Takanashi 1983; Wolf 1985, 1988). For example, the dynamic analysis of an embankment dam–foundation system is a typical dynamic soil–structure interaction problem. Owing to the vast diversity of structural configurations and foundation materials, it is impossible to deal with all the dynamic structure–foundation interaction problems in one chapter. For the purpose of illustrating how the three-dimensional dynamic infinite elements can be used for the numerical simulation of dynamic structure–foundation interaction problems, the following two application examples are considered in this chapter. The first application example is to simulate a dynamic plate–foundation interaction system using the coupled computational model of three-dimensional finite (plate) elements and dynamic infinite elements, while the second application example is to investigate the effects of both the raft foundation flexibility and the underlying rock property on the dynamic response of a three-dimensional framed structure.

6.1 Numerical Simulation of Plate Foundation Vibration on a Visco-elastic Half-Space

The dynamic behaviour of a three-dimensional plate foundation, which can be viewed as the lowest part of a structure and is usually made up of concrete or reinforced concrete materials, has been investigated using analytical methods (Elorduy et al. 1967; Wong and Luco 1976; Kitamura and Sakurai 1979; Adeli et al. 1981; Hamidzadeh-Eraghi and Grootenhuis 1981; Chow 1986). In these analytical methods, the plate foundation was often assumed to be rigid so as to derive analytical solutions. The efficiency and accuracy of the analytical methods depend mainly on

C. Zhao, *Dynamic and Transient Infinite Elements*, Advances in Geophysical and Environmental Mechanics and Mathematics, DOI 10.1007/978-3-642-00846-7_6,

how the complex flexibility influence coefficients for a rigid-plate foundation vibration problem are determined. Further development of the analytical method is to use the boundary integral equation approach to evaluate the dynamic stiffness of rectangular foundations in the frequency and time domains, respectively (Dominquez and Roesset 1978; Karabalis and Beskos 1984). For investigating the dynamic response of simple shaped (i.e. strip or circular) foundations on a layered half-space, analytical methods (Luco 1974, 1976, 1986) and semi-analytical methods (Gazetas and Roesset 1979; Luco and Aspel 1983) are also available in the literature. To improve the existing methods for dealing with vibration problems of three-dimensional rigid plate foundations on layered infinite media, Chow (1987) presented an approximate procedure under an assumption that the square sub-regions of a rigid plate foundation can be replaced approximately by circular sub-regions with equivalent areas. In this procedure, the complex flexibility influence coefficients of an arbitrary-shaped foundation are evaluated directly from the analysis of a smooth, rigid circular foundation resting on a layered soil medium using the finite element method with a viscous boundary (Lysmer and Kuhlemyer 1969). Although this method can be used to geometrically simulate a foundation with any shape, it is suitable only for vertical vibration of a rigid foundation resting on the surface of a horizontally layered soil medium of lateral infinite extension. For more general cases of foundation vibration problems, the coupled computational method of three-dimensional finite elements and dynamic infinite elements is more appropriate for simulating vibration problems of arbitrarily shaped "relatively rigid" and flexible foundations on layered infinite media (Zhao et al. 1989, 1992; Zhao and Valliappan 1991, 1993d, e). Note that in the process of deriving the analytical solutions, the rigid plate is considered by assuming that the whole plate has the same translational and rotational deformations. This means that the plate has an equivalent elastic modulus of infinity. However, from the computational point of view, the elastic modulus of a finite value needs to be used for simulating the plate. To compare the numerical results with the analytical solutions, the value of the elastic modulus of the plate must be several orders higher than that of the underlying rock in the coupled computational model of three-dimensional finite and dynamic infinite elements (Zhao et al. 1989, 1992, 1993d). This implies that only a "relatively rigid" plate can be simulated in the corresponding computational models. Since both the geometrical and the mechanical properties of a plate foundation–underlying foundation system can be represented easily using three-dimensional finite and dynamic infinite elements, detailed studies on the dynamic response of a square foundation resting on either a visco-elastic half-space or a visco-elastic layered infinite foundation are carried out in this section.

6.1.1 Dynamic Response of a Square Plate on a Visco-elastic Half-Space under Harmonic Loading

Although the dynamic behaviour of massless, frictionless rectangular foundations on a homogeneous, isotropic and visco-elastic half-space has been studied extensively over the past years, a detailed report on the following two aspects is very limited: (1) the effects of different proportions of radiation damping and material damping with respect to the total damping of an infinite medium and (2) the effects of material damping on the distribution of wave motion in the near field of the infinite medium. To investigate these effects in this section, the dynamic response of a square plate on a visco-elastic half-space is simulated using the coupled computational model of three-dimensional finite (plate) elements and dynamic infinite elements. Owing to the symmetrical nature of the problem, only a quarter of the plate-foundation system needs to be simulated in the corresponding computational model.

Figure 6.1 shows the computational model of a square massless plate resting on a homogeneous, isotropic and visco-elastic half-space, in which a quarter of both the plate and the half-space is simulated using three-dimensional finite and dynamic infinite elements. The symmetrical boundary condition is applied to the xz (i.e. $y = 0$) and yz (i.e. $x = 0$) planes when vertical vibration of the square massless plate is considered, while the symmetrical boundary condition is applied to the xz (i.e. $y = 0$) plane and the anti-symmetrical boundary condition is applied to the yz (i.e. $x = 0$) plane when horizontal vibration of the square massless plate is considered. The following parameters are used in the coupled computational model of three-dimensional finite and dynamic infinite elements: the elastic modulus of the rock foundation (E_r) is 24×10^9Pa; Poisson's ratio of the rock foundation (ν_r) is 1/3; the density of the rock foundation (ρ_r) is 2400 kg m^{-3}; the elastic modulus of the rigid plate (E_p) is 24×10^{12}Pa so that the plate is "relatively rigid" to the underlying rock; the half-width of the plate (B) is 10 m; the thickness of the plate is $B/10$. According to these parameters, the decay factor (α) used in the three-dimensional dynamic infinite elements is assumed to be 0.028, while the P-wave, S-wave and R-wave velocities, which can be determined from elastic wave theory (Graff 1975), are 3872, 1936 and 1804 m s^{-1} in the rock foundation, respectively. Either a horizontal harmonic load or a vertical harmonic load (P_0) with an amplitude of 22.5×10^9 N is applied at the central point (X = 0, Y = 0, Z = 0) of the plate.

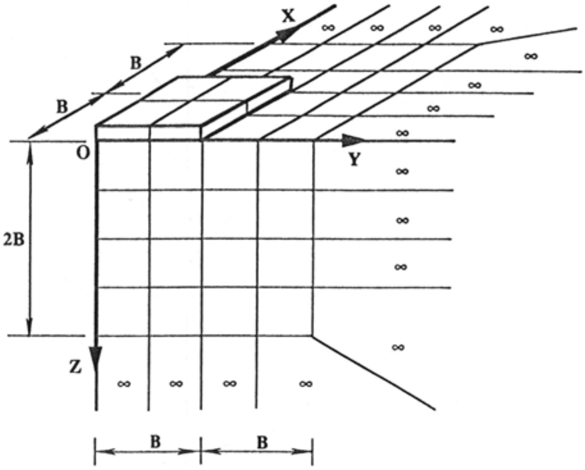

Fig. 6.1 Computational model of a plate foundation overlying on a visco-elastic half-space: the near field is simulated using plate and solid finite elements, while the far field is simulated using dynamic infinite elements

To examine the effect of material damping on the vibration of the plate, three different hysteretic coefficients of the rock material, namely $\eta_d = 0$, 0.1 and 0.25, are used in the corresponding computation models. When $\eta_d = 0$, only the radiation damping of the rock foundation is considered, while for either $\eta_d = 0.1$ or 0.25, both the radiation damping and the material damping of the rock foundation are included in the corresponding computation models. By comparing the numerical results obtained when $\eta_d = 0$ with those obtained when either $\eta_d = 0.1$ or 0.25, different proportions of radiation damping and material damping with respect to the total damping of the rock foundation can be determined.

6.1.1.1 Effects of Material Damping on the Complex Compliance of the Plate

Under a harmonic loading condition, the dimensionless complex compliance of a plate can be expressed as

$$C_{HH}(a_0) = \frac{GB\Delta_1}{P_0}, \tag{6.1}$$

$$C_{VV}(a_0) = \frac{GB\Delta_3}{P_0}, \tag{6.2}$$

where C_{HH} and C_{VV} are the dimensionless complex compliances of the plate due to the concentrated dynamic load (P_0) applied at the plate centre in the x and z directions, respectively; Δ_1 and Δ_3 are the corresponding complex displacements of the plate in the x and z directions; G is the shear modulus of the rock foundation; and a_0 is a dimensionless frequency with the definition:

$$a_0 = \frac{\omega B}{C_S}, \tag{6.3}$$

where ω is the circular frequency of the excitation load; C_S is the S-wave velocity in the rock foundation.

Figure 6.2 shows the effects of material damping on the dimensionless complex compliances of the plate. In this figure, Re is the real part of the dimensionless complex compliances of the plate, while Im is the imaginary part of the dimensionless complex compliances of the plate. The numerical results clearly indicate that with an increase of material damping (η_d), the real parts of the dimensionless complex compliance of the plate, Re(C_{HH}) and Re(C_{VV}), decrease. With $a_0 = 0.5$ taken as an example and for $\eta_d = 0$, Re(C_{HH}) and Re(C_{VV}) are equal to 0.163 and 0.132, while for $\eta_d = 0.1$ and $\eta_d = 0.25$, the pair of (Re(C_{HH}), Re(C_{VV})) is equal to (0.142, 0.117) and (0.122, 0.096), respectively. Thus, compared with the numerical results obtained when $\eta_d = 0$, there is a reduction of 13% and 11% for Re(C_{HH}) and Re(C_{VV}) when $\eta_d = 0.1$, and a reduction of 25% and 27% for $\eta_d = 0.25$. This indicates that material damping has a considerable influence on the dimensionless complex compliance of the plate. Note that as η_d increases, the negative values of the imaginary parts of the dimensionless complex compliance, –Im(C_{HH})

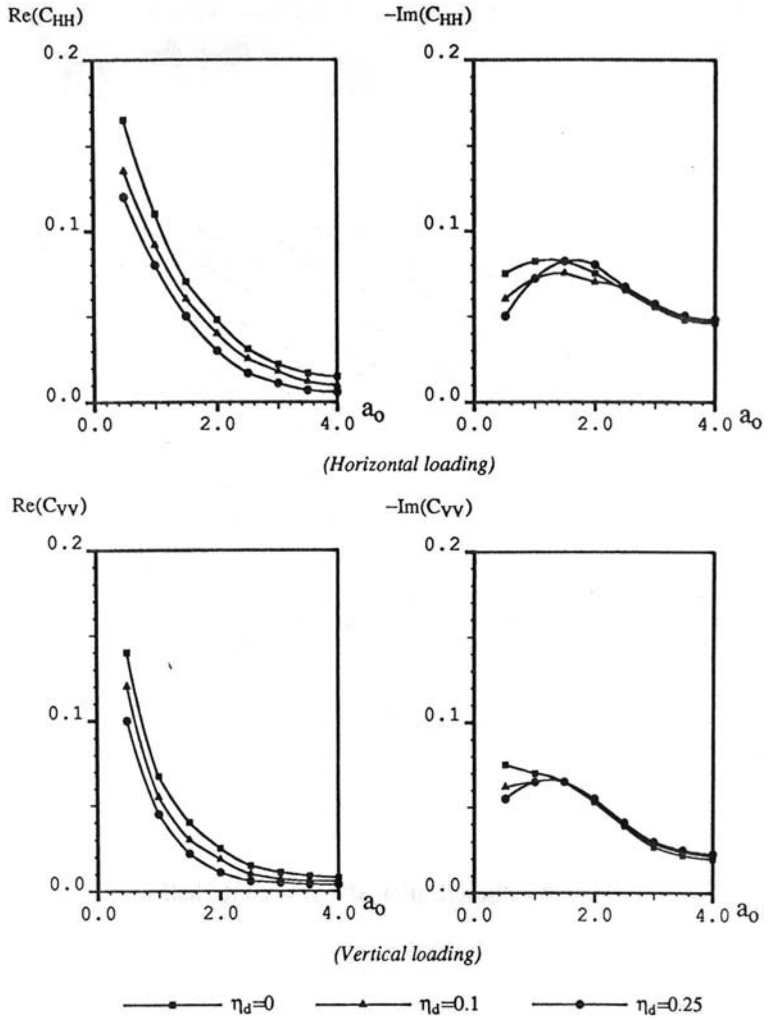

Fig. 6.2 Effects of material damping on the dynamic compliance of the rigid plate

and –Im(C_{VV}), increase slightly in the lower frequency range, implying that the effect of material damping on the imaginary parts is not as great as it is on the real parts of the dimensionless complex compliance of the plate. Generally, both the real and imaginary parts of the dimensionless complex compliance of the plate strongly depend on the excitation frequency of the harmonic load.

To investigate the relative proportions of radiation damping and material damping in the rock foundation, the reciprocal of the compliance amplitude of the plate for $\eta_d = 0$ can be used to express approximately the radiation damping of the rock foundation, whereas the different reciprocals of the compliance amplitudes of the plate corresponding to different values of material damping can be used to express approximately the total damping of the rock foundation with these different values of material damping. For this purpose, the amplitudes of the dimensionless complex compliances of the plate can be defined as follows:

$$A_U\left(a_0, \eta_d\right) = \sqrt{\left\{\operatorname{Re}\left[C_{HH}\left(a_0, \eta_d\right)\right]\right\}^2 + \left\{\operatorname{Im}\left[C_{HH}\left(a_0, \eta_d\right)\right]\right\}^2}, \tag{6.4}$$

$$A_W\left(a_0, \eta_d\right) = \sqrt{\left\{\operatorname{Re}\left[C_{VV}\left(a_0, \eta_d\right)\right]\right\}^2 + \left\{\operatorname{Im}\left[C_{VV}\left(a_0, \eta_d\right)\right]\right\}^2}, \tag{6.5}$$

where $A_U\left(a_0, \eta_d\right)$ is the amplitude of the dimensionless complex compliance, $C_{HH}\left(a_0, \eta_d\right)$, of the plate in the horizontal direction due to a horizontal harmonic loading; $A_W\left(a_0, \eta_d\right)$ is the amplitude of the dimensionless complex compliance, $C_{VV}\left(a_0, \eta_d\right)$, of the plate in the vertical direction due to a vertical harmonic loading.

Using Eqs. (6.4) and (6.5), the ratios of radiation damping to the total damping due to horizontal and vertical loadings can be defined as

$$\psi_H(a_0, \eta_d) = \frac{\frac{1}{A_U(a_0, 0)}}{\frac{1}{A_U(a_0, \eta_d)}} = \frac{A_U\left(a_0, \eta_d\right)}{A_U\left(a_0, 0\right)}, \tag{6.6}$$

$$\psi_V(a_0, \eta_d) = \frac{\frac{1}{A_W(a_0, 0)}}{\frac{1}{A_W(a_0, \eta_d)}} = \frac{A_W\left(a_0, \eta_d\right)}{A_W\left(a_0, 0\right)}, \tag{6.7}$$

where ψ_H and ψ_V are the ratios of radiation damping to the total damping in the horizontal and vertical directions due to horizontal and vertical loadings, respectively.

If the total damping, which is the sum of the damping and material damping of the rock foundation, is defined as 100%, then $1 - \psi_H$ and $1 - \psi_V$ can be used to represent the ratios of the material damping to the total damping for the different values of the material damping of the rock foundation. In this section, ψ_{H1} and ψ_{V1} are used to represent the ratios of the radiation damping to the total damping for $\eta_d = 0.1$, while ψ_{H2} and ψ_{V2} are used to represent the ratios of the radiation damping to the total damping of the rock foundation for $\eta_d = 0.25$.

Table 6.1 shows the proportions of the radiation damping and material damping for the two different values of the material damping, namely $\eta_d = 0.1$ and 0.25, in the rock foundation. These numerical results clearly indicate that the radiation damping plays a dominant role in the total damping of the rock foundation, but the material damping is a relatively small proportion of the total damping of the rock foundation. With $a_0 = 0.5$ taken as an example and for $\eta_d = 0.1$, the ratios of the radiation damping to the total damping are 89.5% and 93% in the horizontal and vertical directions due to horizontal and vertical harmonic loadings, whereas the ratios of the material damping to the total damping are 10.5% and 7%, respectively. When $\eta_d = 0.25$, the ratios of the radiation damping to the total damping are 83.1%

Table 6.1 Proportions of the radiation damping and material damping (Total damping = 100%)

	$\eta_d = 0.1$				$\eta_d = 0.25$			
a_0	$\psi_{H1}(\%)$	$1-\psi_{H1}(\%)$	$\psi_{V1}(\%)$	$1-\psi_{V1}(\%)$	$\psi_{H2}(\%)$	$1-\psi_{H2}(\%)$	$\psi_{V2}(\%)$	$1-\psi_{V2}(\%)$
0.5	89.5	10.5	93.0	7.0	83.1	16.9	84.5	15.5
1.0	92.5	7.5	94.5	5.5	87.5	12.5	89.2	10.8
1.5	93.7	6.3	96.2	3.8	89.3	10.7	89.9	10.1
2.0	94.6	5.4	96.7	3.3	89.9	10.1	91.2	8.8
2.5	95.0	5.0	97.1	2.9	92.2	7.8	92.8	7.2
3.0	96.2	3.8	97.5	2.5	92.9	7.1	96.1	3.9
3.5	99.3	0.7	98.9	1.1	94.8	5.2	98.8	1.2
4.0	99.5	0.5	99.6	0.4	97.2	2.8	99.4	0.6

and 84.5% in the horizontal and vertical directions due to horizontal and vertical harmonic loadings, whereas the corresponding ratios of the material damping to the total damping are 16.9% and 15.5%. This indicates that the higher the material damping of a rock foundation is, the greater will be the ratio of the material damping to the total damping of the rock foundation.

For a given frequency, a_0, the ratio of the material damping to the total damping increases gradually as the material damping of the rock foundation increases. With $a_0 = 0.5$ taken as an example and for $\eta_d = 0.1$, the ratio of the material damping to the total damping of the rock foundation is equal to 10.5%; while for $\eta_d = 0.25$, this ratio is increased to 16.9%. Although the absolute value of the material damping increases as the excitation frequency increases, the ratio of the material damping to the total damping gradually decreases. Since the ratios of the material damping to the total damping of the rock foundation are relatively small for higher-frequency excitations, it can be concluded that the material damping of a rock foundation is negligible for simulating plate vibration problems due to higher-frequency excitations. For instance, when $a_0 = 0.5$, the ratio of the material damping to the total damping is 10.5%, but when $a_0 = 3.5$, this ratio is reduced to 0.7%. This conclusion implies that for the dynamic analysis of a structure–foundation interaction problem, the radiation damping of the infinite rock foundation plays a dominant role in controlling the dynamic behaviour of the structure and therefore, it must be appropriately considered in a computational model. From this point of view, the coupled computational method of three-dimensional finite and dynamic infinite elements provides a useful tool for simulating dynamic structure–foundation interaction problems in infinite foundations.

6.1.1.2 Effects of Material Damping on the Distribution of Wave Motion in the near Field

From a structural foundation design point of view, not only can the dynamic response of a plate foundation play an important role, but also the distribution of wave motion in the near field of the underlying infinite medium can affect the design of the plate foundation, because large displacements in the near field of the underlying infinite medium may result in the failure of the plate foundation. For this reason, studies of the effects of material damping on the distribution of wave motion in the near field of the underlying infinite medium are certainly of engineering significance. Numerical results obtained from such studies can cast new light on how the displacement field distributes in the vicinity of the plate foundation. Since the nodal displacements of both the plate foundation and the underlying infinite medium are used as fundamental variables for the coupled computational model of three-dimensional finite and dynamic infinite elements, it is convenient to use the coupled computational model to obtain the nodal displacement distribution in the near field of the underlying infinite medium. This is one of the major advantages of the coupled computational method of three-dimensional finite and dynamic infinite elements over the previous analytical and semi-analytical methods. In the coupled computational method of three-dimensional finite and dynamic infinite elements, both the plate foundation and the underlying infinite medium are considered as an entire system, while in the analytical and semi-analytical methods, the main focus is on the plate foundation so that the displacement field of the underlying infinite medium is usually not available.

Figures 6.3 and 6.4 show the distributions of displacement amplitudes along the Z axis (i.e. $X = Y = 0$) and X axis (i.e. $Y = Z = 0$) in the near field of the underlying infinite medium. The related numerical results indicate that for both cases, $a_0 = 0.5$ and 1.5, the displacement amplitudes along the depth of the underlying infinite medium decrease as the distance from the plate foundation increases. When the plate foundation is subjected to a harmonic load, it becomes a vibration source and the resulting vibration energy propagates from the plate foundation into the underlying infinite medium as different waves. Owing to the divergence of the three-dimensional geometry and the material damping of the underlying infinite medium, the energy density of the propagating wave, which is defined as the flow of wave energy through a unit area, gradually decreases in the homogeneous and visco-elastic half-space with an increase in the distance from the plate foundation. For both frequencies, $a_0 = 0.5$ and 1.5, the distribution pattern of the wave motion in the near field of the underlying infinite medium is exactly the same, indicating that the variation of an excitation frequency has little effect on the distribution pattern of the wave motion in the near field of the underlying homogeneous and visco-elastic half-space, even though displacement amplitudes may be different for different excitation frequencies of the plate foundation. Since the material damping of an underlying infinite medium has a certain influence on the dynamic response of the whole system for a lower excitation frequency, it can affect the dynamic displacement response in the near field. Generally, the greater the material damping of an underlying infinite medium is, the smaller will be the dynamic displacement amplitude in the near field of the underlying infinite medium. On the interface between the plate foundation and the underlying infinite medium, both horizontal and vertical displacement amplitudes are constant over the width of the plate foundation, as expected, because of the rigidity of the plate foundation.

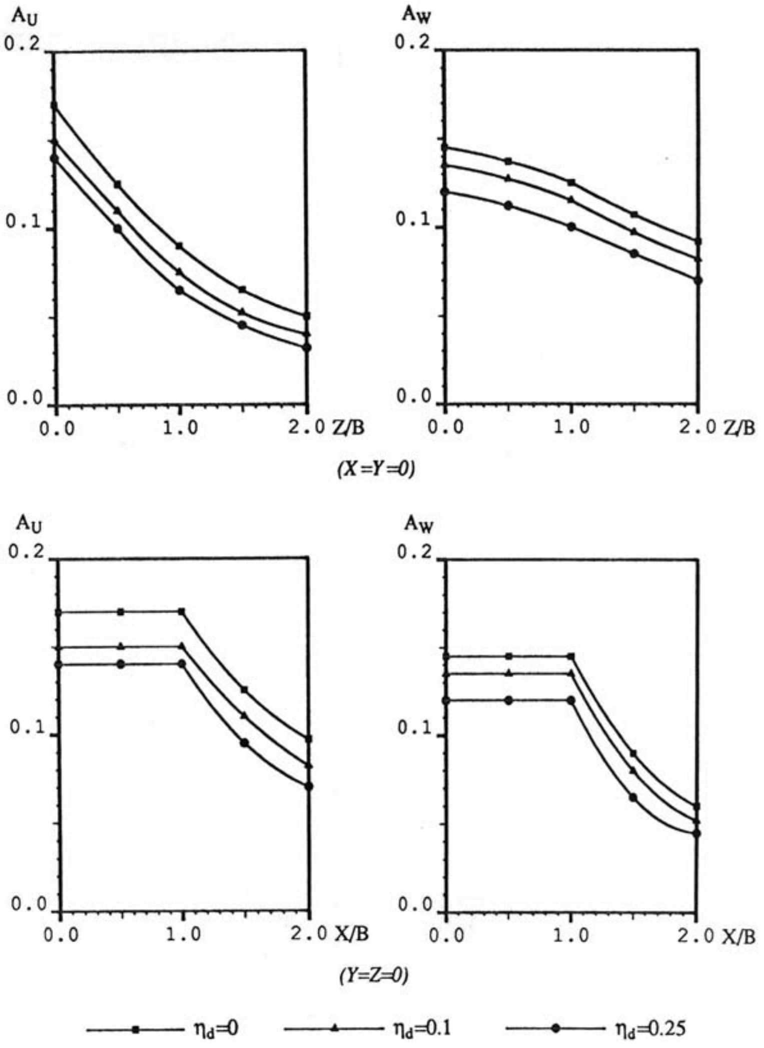

Fig. 6.3 Distributions of displacement amplitudes within the underlying rock foundation ($a_0 = 0.5$)

6.1.2 Dynamic Response of a Square Plate on a Layered Visco-elastic Half-Space under Harmonic Loading

In most previous studies (Luco 1974, 1976; Luco and Aspel 1983; Chow 1987), an overlying layer was assumed to be fixed on a rigid half-space so that the bottom of the overlying layer can be treated as a fixed boundary. However, natural layered media are usually located on flexible media. In this subsection, the dynamic response of a square plate on a layered medium overlying a flexible half-space is

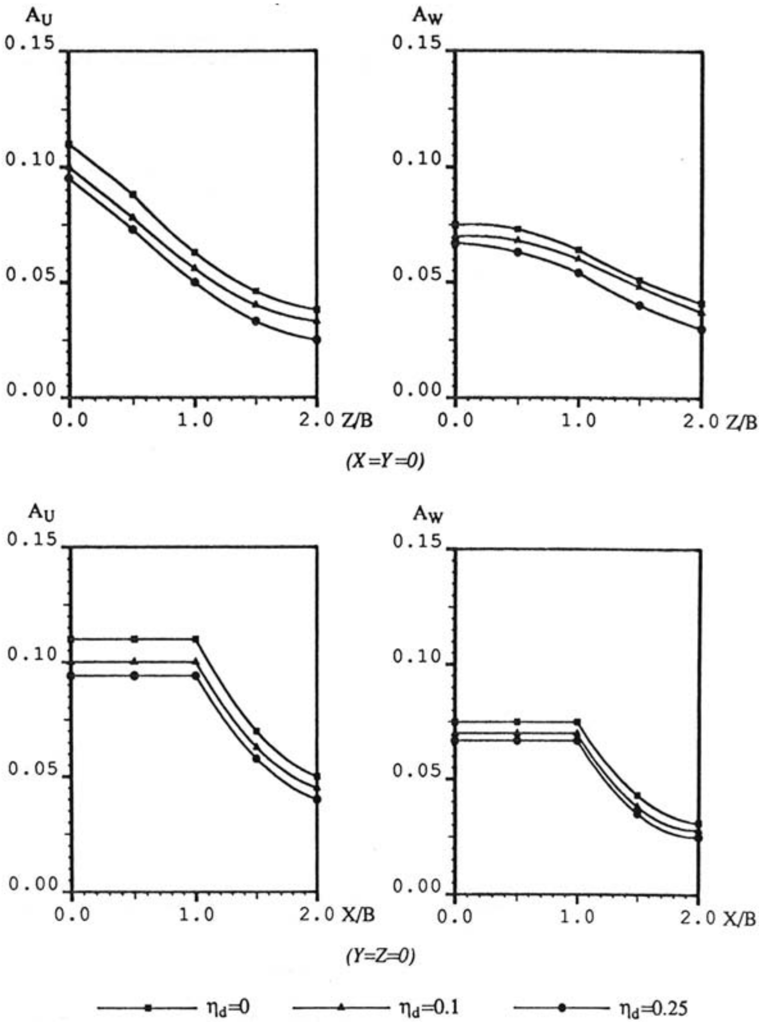

Fig. 6.4 Distributions of displacement amplitudes within the underlying rock foundation ($a_0 = 1.5$)

considered to investigate both the effect of the varying stiffness ratio of the layer to the underlying half-space and the effect of thickness of the layer immediately underlying the square plate.

Figure 6.5 shows the computational model of a plate-layered medium-underlying half-space system, where only a quarter of the whole system is considered due to the symmetrical nature of the problem. In this figure, E_1 and E_2 are the elastic moduli of the layered medium and the underlying rock; H is the thickness of the layered medium; B is the half-width of the square plate. The parameters for the underlying rock are as follows: the elastic modulus (E_2) is 24×10^9 Pa; Poisson's

Fig. 6.5 Conceptual model of a plate foundation overlying on a visco-elastic layered half-space

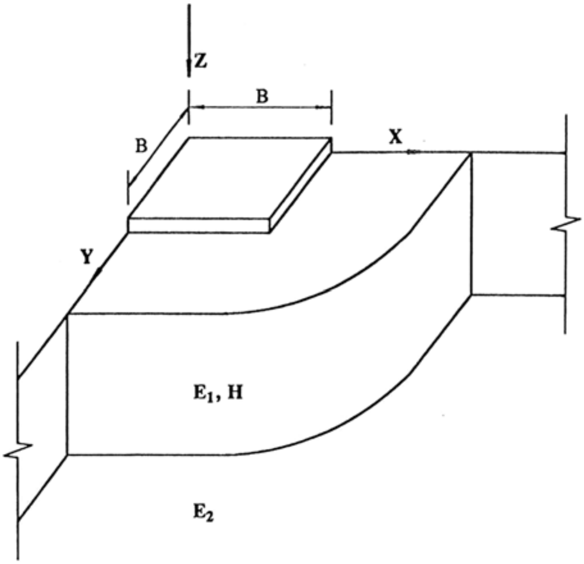

ratio (ν) is 1/3; the rock density (ρ) is 2400 kg m^{-3}; the hysteretic coefficient of the rock material (η_d) is 0.1. For the layered medium, the value of Poisson's ratio, the density and the hysteretic coefficient are assumed to be exactly the same as those used for the underlying rock. Three different ratios of the layer thickness to the plate half-width, namely $H/B = 0.5$, 1.0 and 1.5, are considered to investigate the effects of the layer thickness on the dynamic response of the square plate. For the purpose of examining the effects of the layer stiffness on the dynamic response of the square plate, five different ratios of the elastic modulus of the underlying rock to that of the layered medium, namely $E_2/E_1 = 1$, 10, 15, 50 and 100, are considered in the coupled computational model of three-dimensional finite elements and dynamic infinite elements. Note that $E_2/E_1 = 1$ means that the square plate rests on a homogeneous half-space.

Figures 6.6 and 6.7 show the effects of the elastic modular ratios of the underlying rock to the layered medium on the complex displacement amplitudes of the square plate for a given ratio of the layer thickness to the plate half-width, $H/B = 1.5$. For a square plate overlying a homogeneous visco-elastic half-space (i.e. $E_2/E_1 = 1$), no resonant peak appears in the dynamic response curve of the square plate for either horizontal harmonic loading (in Fig. 6.6) or vertical harmonic loading (in Fig. 6.7). However, in the layered medium cases, the system resonance takes place and some resonant peaks appear in the dynamic response curve of the square plate due to wave reflection and refraction within the layered medium. Generally, both the resonant frequency and the complex displacement amplitude of the square plate depend on the elastic modular ratios of the underlying rock to the layered medium. For a given elastic modulus of the underlying rock, E_2, a greater value of E_2/E_1 means a smaller value of E_1 and a softer layered medium. Obviously, a softer layered medium results in a greater dynamic displacement response of the square plate and a lower resonant frequency of the whole plate-layered medium-underlying rock system.

For both horizontal and vertical loadings, three resonant frequencies of the whole system appear for each value of E_2/E_1 and the largest displacement response of the square plate takes place when E_2/E_1 is equal to 100 for the parameters used in the coupled computational model. If the excitation frequency of the square plate is higher, the radiation damping of the layered infinite foundation becomes greater so that no obvious peak appears in the displacement amplitude response curve of the square plate. The corresponding excitation frequency, above which the system resonance no longer takes place, is defined as the upper limit of the excitation frequency of the whole system. This upper limit depends on the ratio of the elastic moduli of the underlying rock to the layered medium. The related numerical results shown in Figs. 6.6 and 6.7 indicate that the smaller the value of this ratio of the underlying rock to the layered medium (E_2/E_1), the higher the upper limit of the excitation frequency of the whole plate-layered medium-underlying rock system. The dynamic displacement response of the square plate for horizontal loading is different from that for vertical loading, indicating that the dynamic response of a plate also depends on how the plate is loaded.

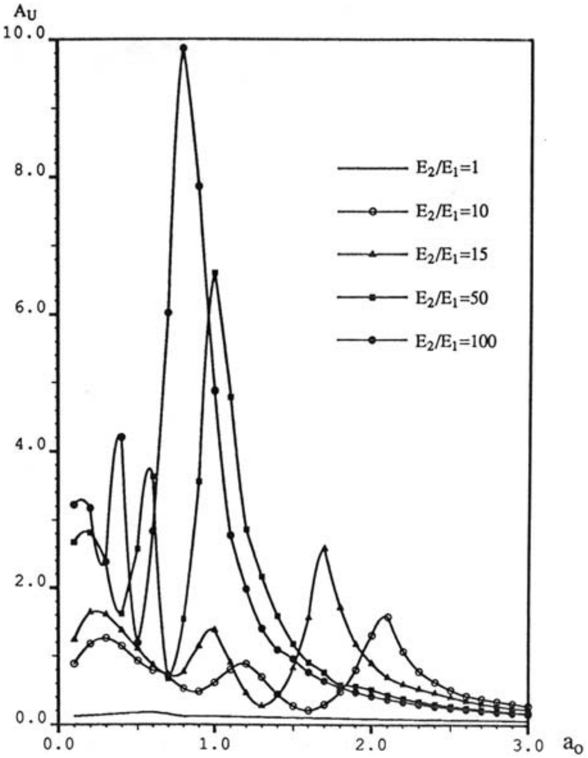

Fig. 6.6 Effects of the ratios of the elastic moduli on the horizontal displacement amplitudes of the plate foundation (*H/B* = 1.5)

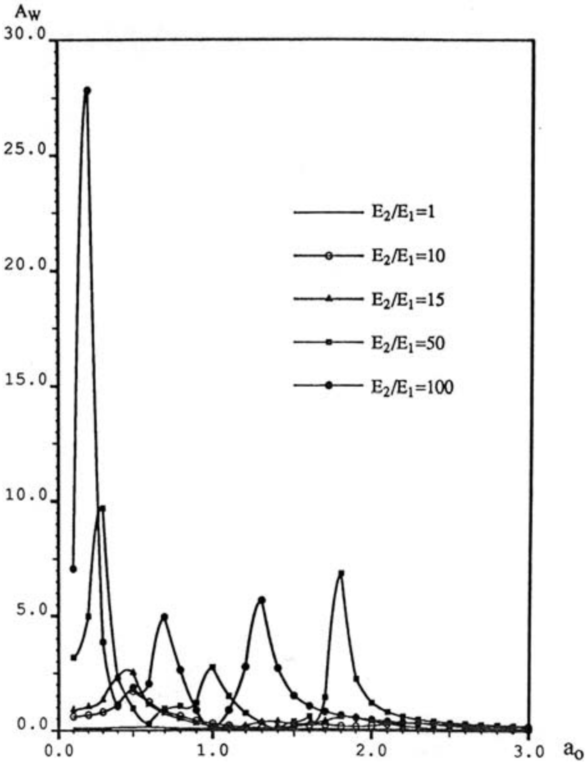

Fig. 6.7 Effects of the ratios of the elastic moduli on the vertical displacement amplitudes of the plate foundation (*H/B* = 1.5)

Figures 6.8, 6.9, 6.10 and 6.11 show the effects of layer thickness on the complex displacement amplitudes of the square plate for $E_2/E_1 = 100$ and $E_2/E_1 = 10$, respectively. Note that the thickness of the layered medium has a significant influence on the dynamic response of a square plate. The overall trend of the influence is that the thicker the layered medium, the lower the resonant frequency of the whole plate-layered medium-underlying rock system. The related numerical results shown in Figs. 6.8, 6.9, 6.10 and 6.11 indicate that the resonant frequency of the whole plate-layered medium-underlying rock system is inversely proportional to the layer thickness for both, horizontal (Figs. 6.8 and 6.10) and vertical vibration (Figs. 6.9 and 6.11) of the square plate. Through comparison of the dynamic response of the square plate for $E_2/E_1 = 100$ with that for $E_2/E_1 = 10$, it can be concluded that the resonant frequency of the whole plate-layered medium-underlying rock system is directly proportional to the elastic modulus of the layered medium for a given elastic modulus of the underlying rock. For instance, when $E_2/E_1 = 10$ (in Fig. 6.11), the dimensionless resonant frequency of the whole plate-layered medium-underlying rock system is about 0.5, 0.9 and 1.95 for the three different values of *H/B* = 1.5, 1.0 and 0.5, respectively, whereas when $E_2/E_1 = 100$ (in Fig. 6.9), the dimensionless resonant frequency of the whole system is about 0.2, 0.35 and 0.7 for *H/B* = 1.5, 1.0 and 0.5, respectively. This indicates that, if the elastic modulus of the underlying

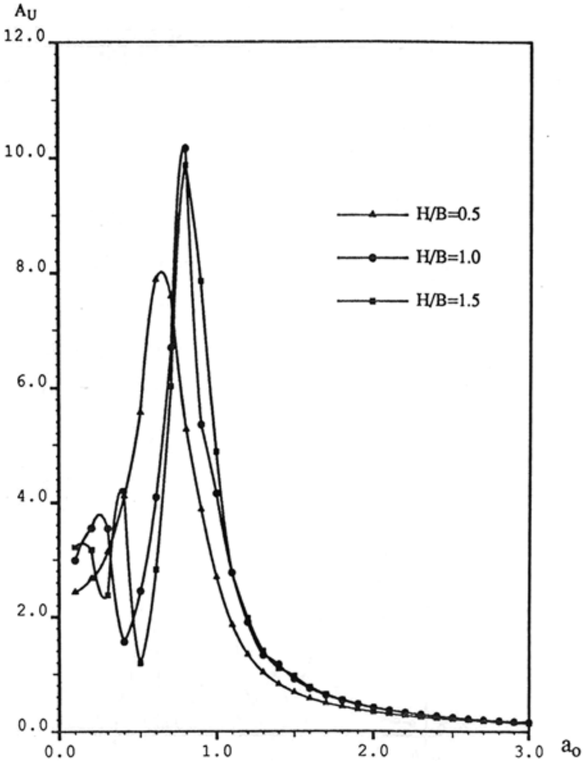

Fig. 6.8 Effects of layer thickness on the horizontal displacement amplitudes of the plate foundation ($E_2/E_1 = 100$)

rock (E_2) is kept constant, a smaller elastic modulus of the layered medium implies a lower resonant frequency of the whole plate-layered medium-underlying rock system. The same phenomenon can be observed from the numerical results obtained in the case of the horizontal vibration of the square plate (in Figs. 6.8 and 6.10). For larger values of the dimensionless layer thickness (*H*/*B*) and ratio of the elastic moduli (E_2/E_1), the distribution curve of the displacement amplitudes of the square plate fluctuates significantly, indicating that a deeper and softer layer may result in not only a greater dynamic response of the plate foundation, but also a complicated distribution pattern of the complex frequency response of the whole plate-layered medium-underlying rock system. In this situation, it is necessary to strengthen the layered medium so as to avoid the dynamic failure of the plate foundation.

Figures 6.12 and 6.13 show the distributions of the horizontal and vertical displacement amplitudes in the near field of the whole plate-layered medium-underlying rock system due to two different excitation frequencies, respectively. These results can be used to investigate the effects of non-homogeneity, layer thickness and excitation frequency on the dynamic response of the whole plate-layered medium-underlying rock system. For example, the effects of medium non-homogeneity, which is represented by the ratio of the elastic moduli of the underlying rock to the layered medium (E_2/E_1), on the dynamic response in the near field of the system are shown in Fig. 6.12 for both a particular dimensionless layer thickness (*H*/*B* $= 1.5$) and a particular dimensionless frequency ($a_0 = 0.5$).

Fig. 6.9 Effects of layer thickness on the vertical displacement amplitudes of the plate foundation ($E_2/E_1 = 100$)

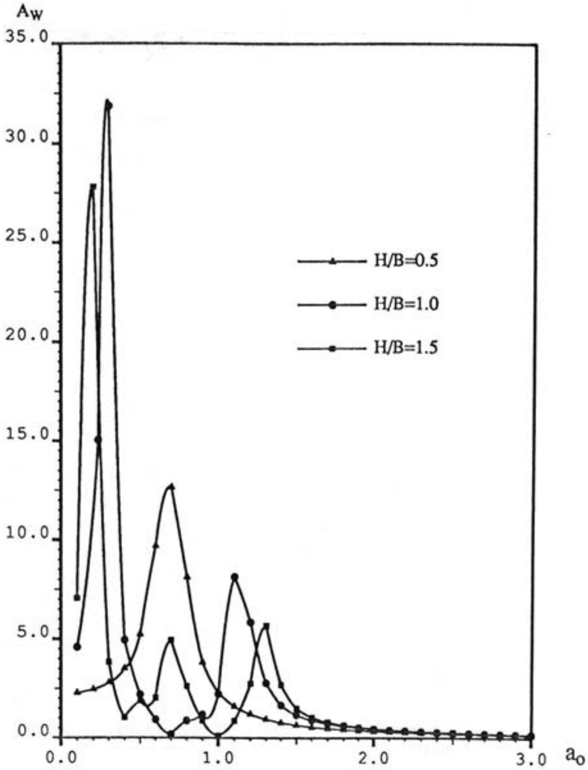

Note that there is no general trend for the distribution pattern of displacement amplitudes in the near field of the system due to the combined complex effect of the three factors mentioned above. Since the dynamic response of a square plate on a layered medium fluctuates significantly with an excitation frequency, which can be seen from Figs. 6.6 and 6.7, it is difficult to draw any general conclusion about how the layer characteristics affect the distribution pattern of displacement amplitudes in the near field of the system. Nevertheless, through this investigation, it is possible to gain some basic recognition about the displacement distribution in the near field of the whole plate-layered medium-underlying rock system.

As shown in Fig. 6.12 for a lower dimensionless frequency ($a_0 = 0.5$), the maximum dynamic response for either horizontal or vertical displacement amplitudes occurs within the layer itself for all the three cases of layer non-homogeneities, namely $E_2/E_1 = 10$, 50 and 100, especially for a higher ratio of the elastic moduli ($E_2/E_1 = 100$). However, for a higher dimensionless frequency ($a_0 = 1.5$), the numerical results shown in Fig. 6.13 indicates that the horizontal displacement amplitude reaches its maximum value within the layer when $E_2/E_1 = 10$, while the vertical displacement amplitude reaches its maximum value within the layer when either $E_2/E_1 = 10$ or $E_2/E_1 = 50$. This indicates that the dynamic response in the near field of a plate-layered medium-underlying rock system is different from that in the near field of a plate-homogeneous half-space system. In the latter case, the

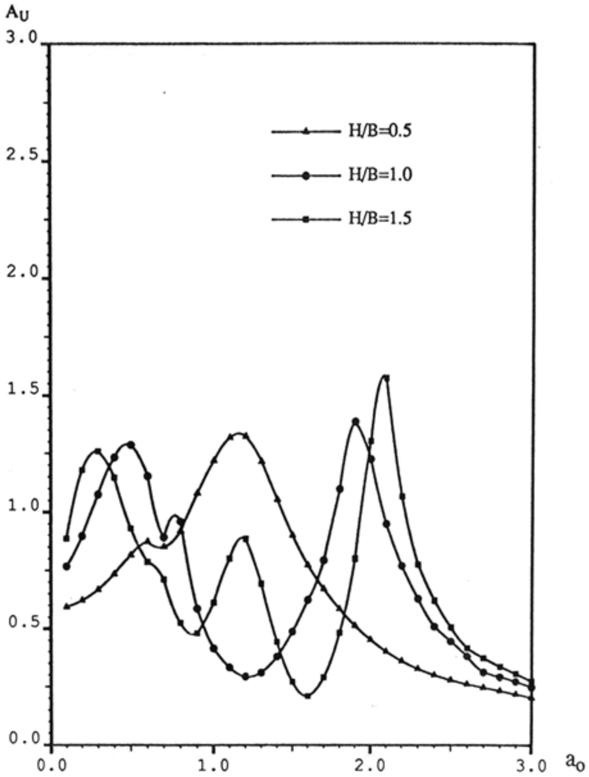

Fig. 6.10 Effects of layer thickness on the horizontal displacement amplitudes of the plate foundation ($E_2/E_1 = 10$)

maximum dynamic response of the system always takes place at the surface of the plate foundation.

The engineering implications of this investigation can be summarized as follows: for a plate overlying a layered infinite medium, if a low-frequency range of excitation is of interest, then it is essential to give proper and careful considerations to the layered medium so as to avoid any first failure within the layered medium, while if a high-frequency range of excitation is of interest, then it is essential to give appropriate considerations to both the plate foundation and the layered medium, because the first failure of the system may take place either in the plate foundation or in the layered medium in this latter case.

6.2 Numerical Simulation of the Dynamic Response of a Framed Structure–Raft Foundation–Underlying Soil/Rock System

As extensive studies have demonstrated, the dynamic response of a structure is affected by the following factors (Warburton and Hutton 1978; Gupta et al. 1982; Riggs and Waas 1985; Chen and Penzien 1986; Wolf 1985, 1988; Zhao and Valliappan 1993e, Zhao and Xu 1994; Zhao et al. 1995): (1) the dynamic

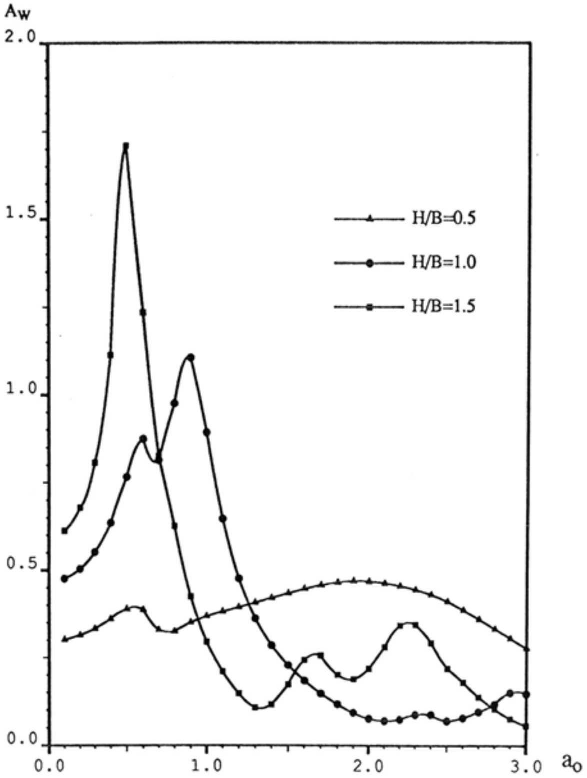

Fig. 6.11 Effects of layer thickness on the vertical displacement amplitudes of the plate foundation ($E_2/E_1 = 10$)

characteristics of the structure itself; (2) the configuration and flexibility of either a raft (shallow) foundation or a pile (deep) foundation; (3) the properties of the underlying soil/rock; and (4) the dynamic load exerted on the structure. Owing to the complexity of a dynamic structure–foundation–underlying rock interaction problem, the above factors are usually considered separately and the dynamic interaction effect is neglected in the previous theoretical analysis, especially for a three-dimensional structure–foundation–underlying rock system. For this reason, computational methods are widely used to deal with dynamic structure–foundation–underlying rock interaction problems (Zhao and Valliappan 1991, 1993c, e; Zhao et al. 1992, 1993, 1995).

For a three-dimensional dynamic structure–foundation–underlying rock interaction problem, the structure and its foundation are of limited size, whereas the underlying rock can be treated as an infinite medium. Thus, the key issue associated with the numerical simulation of a three-dimensional dynamic structure–foundation–underlying rock interaction problem is how to simulate effectively and efficiently the infinite domain of the underlying rock. When the finite element method is used to deal with three-dimensional dynamic structure–foundation–underlying rock interaction problems, the size of the finite elements is controlled by the

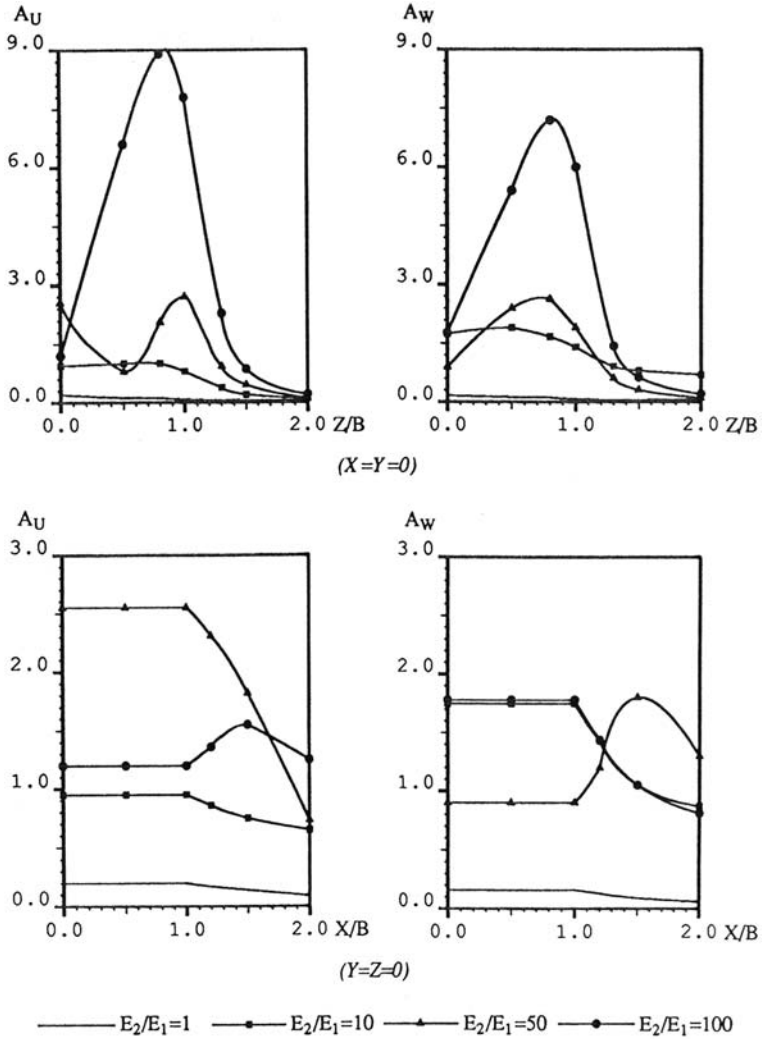

Fig. 6.12 Effects of the ratios of the elastic moduli on displacement amplitude distribution in the near field of the system ($a_0 = 0.5$ and $H/B = 1.5$)

corresponding wave length so that the wave propagation mechanism can be captured within each element in a finite element model. To avoid wave reflection and refraction on the artificially truncated boundary, the extension of a finite element mesh in the infinite direction of the medium must be large enough so as to obtain useful and accurate numerical results. For the purpose of reducing the finite element simulated region of an infinite domain, some special treatments on the artificially truncated boundary have been proposed in the past few decades (Lysmer and Kuhlemyer 1969; White et al. 1977; Chow and Smith 1981; Medina and Taylor 1983; Zhao et al. 1987; Zhao and Valliappan 1991). Because of easy implementation into a finite element

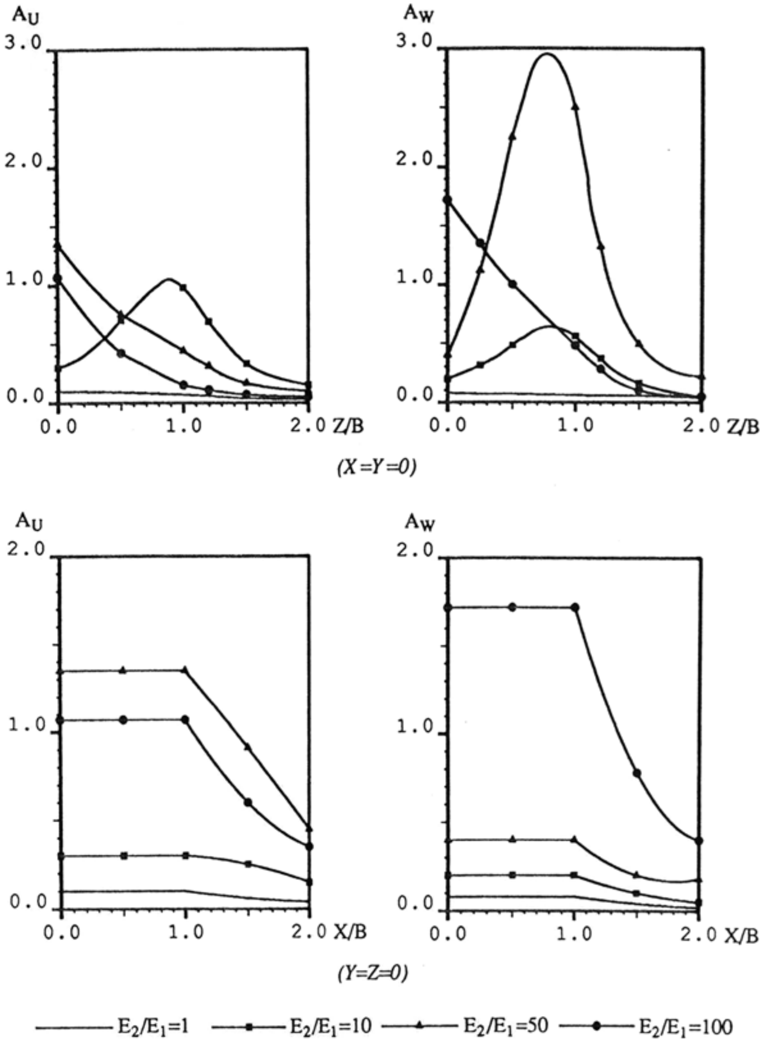

Fig. 6.13 Effects of the ratios of the elastic moduli on displacement amplitude distribution in the near field of the system ($a_0 = 1.5$ and $H/B = 1.5$)

code, the coupled computational model of three-dimensional finite elements and dynamic infinite elements has been successfully used for solving a wide range of three-dimensional dynamic structure–foundation–underlying soil/rock interaction problems (Zhao and Valliappan 1993d, e).

In this section, the coupled computational model of three-dimensional finite elements and dynamic infinite elements is used to simulate the dynamic response of a three-dimensional framed structure–raft foundation–underlying soil/rock interaction system. This system is comprised of the following three substructures. The first is the superstructure that is a three-dimensional framed structure; the second is the raft foundation that is made up of concrete or reinforced concrete; and the third is the underlying soil/rock that is of infinite extent. Since each of these three substructures has different deformation characteristics, it is necessary to use different kinds of elements in the coupled computational model. For this reason, the superstructure is simulated using three-dimensional frame elements (Zienkiewicz 1977), while the raft foundation is simulated using a combination of thick plate elements (Rock and Hinton 1974) and plane stress elements (Zhao and Valliappan 1991). Based on the dynamic condensation technique (Zhao and Valliappan 1993e), the dynamic property matrix of both the superstructure and the raft foundation can be reduced to a small matrix associated with the degree of freedoms on the raft foundation–underlying soil/rock interface. This reduced matrix can be easily assembled into the property matrix of the underlying soil/rock substructure. By solving the dynamic equation of motion of the underlying soil/rock substructure, which includes the interaction effects of both the superstructure and the raft foundation, the dynamic response of the underlying soil/rock substructure can be obtained. As a result, the dynamic response of both the superstructure and the raft foundation can be evaluated using backward computation. The benefit of using the coupled computational method is that both the infinite medium and the wave input mechanism can be simulated more reasonably and realistically (Zhao and Valliappan 1993d, e).

6.2.1 Numerical Simulation of a Three-Dimensional Framed Structure–Raft Foundation–Underlying Soil/Rock System

In the conventional numerical simulation of a three-dimensional dynamic structure–foundation interaction system, a building structure is usually simulated using three-dimensional frame elements, while a raft foundation and its underlying soil/rock are roughly simulated using a fixed boundary or the impedance (or compliance) of the underlying soil/rock. Compared with the use of a fixed boundary, the use of the impedance of the underlying soil/rock is more reasonable. Since the impedance of an infinite medium is a function of the excitation frequency, the frequency-domain-analysis technique needs to be used in the numerical simulation of the three-dimensional dynamic structure–foundation interaction system. Furthermore, the basic idea behind the earthquake input method used in the conventional numerical simulation of a three-dimensional dynamic structure–foundation interaction system is to transform the ground earthquake acceleration into the inertial forces exerted on the masses of the superstructure. Obviously, the earthquake wave propagation mechanism in the underlying soil/rock foundation is neglected in the above-mentioned earthquake input method. To overcome these drawbacks, together with the dynamic condensation technique, the coupled computational method of three-dimensional finite elements and dynamic infinite elements is used to deal with the three-dimensional framed structure–raft foundation–underlying soil/rock interaction problems.

6.2.1.1 Numerical Simulation of a Three-Dimensional Framed Structure

The superstructure in the whole framed structure–raft foundation–underlying soil/rock system is simulated by using three-dimensional frame elements (Zienkiewicz 1977), resulting in the discretized dynamic equation of motion for the three-dimensional framed structure in the frequency domain:

$$\left\{-\omega^2 [M_F] + (1 + i\eta_{dF}) [K_F]\right\} \{\Delta_F\} = \{P_F\}, \tag{6.8}$$

where $[M_F]$ and $[K_F]$ are the global mass and stiffness matrices of the framed structure; η_{dF} is the hysteretic damping coefficient of the structural material; ω is the excitation circular frequency; and $\{\Delta_F\}$ and $\{P_F\}$ are the global displacement vector and dynamic load vector of the framed structure.

6.2.1.2 Numerical Simulation of a Raft Foundation

If a framed structure is located on a raft foundation, a combination of the thick plate element and the plane stress element can be used to simulate the raft foundation for a horizontal earthquake movement propagating from the underlying soil/rock into the framed structure. In this situation, the discretized dynamic equation of motion for the raft foundation can be expressed as

$$\left\{-\omega^2 [M_R] + (1 + i\eta_{dR}) [K_R]\right\} \{\Delta_R\} = \{P_R\}, \tag{6.9}$$

where $[M_R]$ and $[K_R]$ are the global mass and stiffness matrices of the raft foundation; η_{dR} is the hysteretic damping coefficient of the raft foundation material; ω is the excitation circular frequency; $\{\Delta_R\}$ and $\{P_R\}$ are the global displacement vector and dynamic load vector of the raft foundation. These matrices and vectors can be rewritten into the forms:

$$[M_R] = [M_{R1}] + [M_{R2}], \tag{6.10}$$

$$[K_R] = [K_{R1}] + [K_{R2}], \tag{6.11}$$

$$\{\Delta_R\} = \{\Delta_{R1}\} + \{\Delta_{R2}\}, \tag{6.12}$$

$$\{P_R\} = \{P_{R1}\} + \{P_{R2}\}, \tag{6.13}$$

where $[M_{R1}]$, $[K_{R1}]$, $\{\Delta_{R1}\}$ and $\{P_{R1}\}$ express the contributions of the thick plate elements to the corresponding matrices or vectors of the raft foundation, whilst $[M_{R2}]$, $[K_{R2}]$, $\{\Delta_{R2}\}$ and $\{P_{R2}\}$ express the contributions of the plane stress elements to the corresponding matrices or vectors of the raft foundation, respectively.

6.2.1.3 Numerical Simulation of an Infinite Soil/Rock Medium

For the numerical simulation of the wave propagation in an infinite soil/rock medium, the coupled computational method of three-dimensional solid finite elements and dynamic infinite elements (Zhao et al. 1989; Zhao and Valliappan 1991, 1993e) is used in this subsection. The discretized dynamic equation of motion for the infinite soil/rock medium can be expressed as

$$\left\{-\omega^2\left[M_S\right]+\left(1+i\eta_{dS}\right)\left[K_S\right]\right\}\left\{\Delta_S\right\}=\left\{P_S\right\}, \tag{6.14}$$

where $[M_S]$ and $[K_S]$ are the global mass and stiffness matrices of the infinite soil/rock medium; η_{dS} is the hysteretic damping coefficient of the infinite soil/rock medium; ω is the excitation circular frequency; $\{\Delta_S\}$ and $\{P_S\}$ are the global displacement vector and dynamic load vector of the infinite soil/rock medium.

6.2.1.4 Coupling Equation of the Framed Structure–Raft Foundation–Underlying Soil/Rock System

The dynamic equation of motion for each substructure of the whole system is already expressed in Eqs. (6.8), (6.9) and (6.14). Since the nodal degrees-of-freedom for each substructure are not necessarily the same, the global dynamic equation of motion for the whole system cannot be obtained by simply assembling the above three equations. For instance, a three-dimensional frame element has six degrees-of-freedom at each nodal point, namely three translational movements and three rotations, while either a three-dimensional finite element or a three-dimensional dynamic infinite element has only three translational but no rotational degrees-of-freedom at each nodal point. A plate element for simulating the plate flexure has three degrees-of-freedom at each nodal point, namely one out-of-plane translational movement that is normal to the middle plane of the plate and two rotations, while a plane stress element has two in-plane translational degrees-of-freedom at each nodal point. This means that the combination of a plate element and a plane stress element has five degrees-of-freedom at each nodal point.

To obtain the dynamic response of the whole framed structure–raft foundation–underlying soil/rock system, the dynamic condensation technique (Zhao and Valliappan 1993e) is used in this subsection. This means that the framed structure and plate foundation need to be treated as a combined substructure, while the underlying soil/rock is treated as another substructure. The dynamic interaction between these two substructures can be simulated by considering the dynamic force–stiffness relationship on their interface. The benefit of using such a substructure method is that either of these two substructures can be solved separately. If Eqs. (6.8) and (6.9) are arranged appropriately, the dynamic equation of motion for the combined substructure consisting of both the framed structure and the raft foundation can be obtained. The resulting global dynamic stiffness matrix for such a combined substructure will correspond to six degrees-of-freedom at each nodal point. To derive the dynamic force–stiffness relationship, which is cause by the combined substructure consisting of both the framed structure and the raft foundation, on the interface between the plate foundation and the underlying soil/rock, this matrix can be partitioned in the following forms:

$$[S_{11}(\omega)]\{\Delta_1\} + [S_{12}(\omega)]\{\Delta_2\} = \{P_1\}, \tag{6.15}$$

$$[S_{12}(\omega)]^T\{\Delta_1\} + [S_{22}(\omega)]\{\Delta_2\} = \{P_2\}, \tag{6.16}$$

where $\{\Delta_1\}$ is the nodal translational displacement vector associated with nodal points at the interface between the (raft) plate foundation and the underlying soil/rock; $\{\Delta_2\}$ is a displacement vector, which consists of both translational and rotational movements and is associated with nodal points at the remaining part of the framed structure and raft foundation; $[S_{11}(\omega)]$, $[S_{12}(\omega)]$ and $[S_{22}(\omega)]$ are the corresponding dynamic stiffness matrices; $\{P_1\}$ and $\{P_2\}$ are the corresponding dynamic load vectors.

Eliminating $\{\Delta_2\}$ from Eqs. (6.15) and (6.16) yields the contribution of the framed structure and raft foundation to the dynamic stiffness matrix of the underlying soil/rock as follows:

$$\left[S_{11}^*(\omega)\right]\{\Delta_1\} = \left\{P_1^*\right\}, \tag{6.17}$$

where

$$\left[S_{11}^*(\omega)\right] = [S_{11}(\omega)]\ [S_{12}(\omega)]\ [S_{22}(\omega)]^{-1}\ [S_{12}(\omega)]^T, \tag{6.18}$$

$$\left\{P_1^*\right\} = \{P_1\} - [S_{12}(\omega)]\ [S_{22}(\omega)]^{-1}\ \{P_2\}. \tag{6.19}$$

Since the nodal displacement vector of the underlying soil/rock contains the nodal displacement vector on the interface between the raft foundation and the underlying soil/rock, Eq. (6.17) can be straightforwardly assembled into Eq. (6.14), resulting in the global dynamic equation of motion for the underlying soil/rock including the effects of both the framed structure and the raft foundation. Consequently, the nodal displacements of the underlying soil/rock can be obtained by directly solving the global dynamic equation of motion for the underlying soil/rock. By means of the back-substitution technique, the nodal displacements for both the raft foundation and the framed structure can be computed so that the dynamic response of the whole framed structure–raft foundation–underlying soil/rock system can be obtained.

6.2.2 Effects of Raft Foundation Flexibility on the Dynamic Response of a Three-Dimensional Framed Structure

The proposed numerical method in the previous subsection can be used to investigate the effects of raft foundation flexibility on the dynamic response of a three-dimensional framed structure. Figure 6.14 shows the computational model,

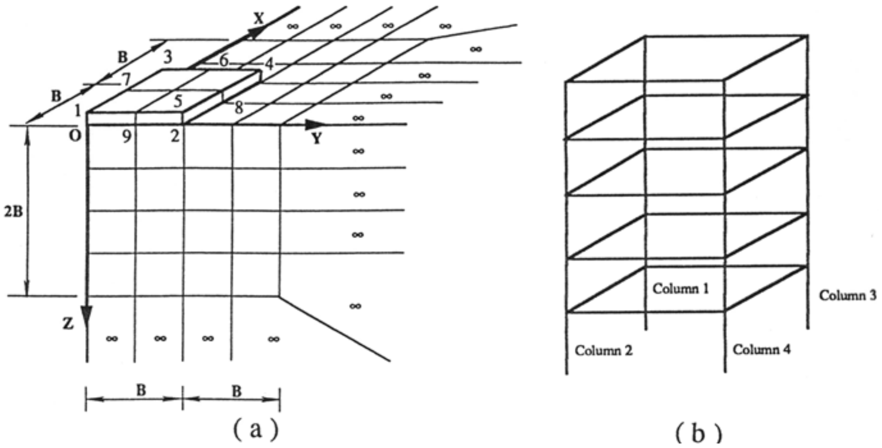

Fig. 6.14 Computational model of a framed structure–raft foundation–underlying soil/rock system: (**a**) raft foundation and underlying soil/rock; (**b**) framed structure

in which only a quarter of the whole framed structure–raft foundation–underlying rock system is simulated due to the geometrically symmetrical nature of the system. To show the raft foundation and the underlying rock more clearly, the framed structure is separately shown in the right part of this figure. Note that column 2 is in coincidence with the Z axis of the coordinate system used in Fig. 6.14, while columns 1, 3 and 4 are directly connected with nodal points 3, 4 and 5 respectively. For the purpose of examining the effects of raft-foundation flexibility on the dynamic response of the three-dimensional framed structure, the raft foundation is considered as either a "relatively rigid" foundation or a flexible foundation by changing the elastic modulus of the raft foundation in the corresponding computational models. Only horizontal harmonic loading is applied at the centre of the plate foundation (i.e. point O in Fig. 6.14).

The following parameters are used in the computational model. For the underlying rock, the elastic modulus (E_r) is 24×10^9 Pa; the value of Poisson's ratio (ν_r) is 1/3; the rock density (ρ_r) is 2400 kg m^{-3}. For the raft foundation, the elastic modulus (E_R) is 24×10^{12} Pa so that the raft (plate) is "relatively rigid" to the underlying rock; the half-width of the plate (B) is 10 m; the thickness of the plate is $B/10$. For the flexible raft foundation, the elastic modulus, the value of Poisson's ratio and the material density are exactly the same as those for the underlying rock. For the framed structure, the cross-sectional areas of both the columns and the beams are $0.4 \times 0.4\,\text{m}^2$; the elastic modulus ($E_F$) is 24×10^9 Pa; the value of Poisson's ratio (ν_F) is 0.16; the material density (ρ_F) is $2400\,\text{kg m}^{-3}$.

Dimensionless quantities are useful for expressing the dynamic behaviour of a class of systems, rather than an individual system. A specific dimensionless quantity is defined by considering the related parameters that can be used to represent the fundamental characteristics of the system. For investigating the horizontal and vertical vibration of a rigid plate on an elastic, homogeneous and isotropic half-space, dimensionless compliances and bending moments were defined to display the dynamic response of the plate (Luco 1974, 1976; Luco and Aspel 1983; Chow 1987). Since both the plate foundation and the underlying rock play an important role in controlling the dynamic response of the entire framed structure–plate foundation–underlying soil/rock system, the dimensionless compliances and bending moments defined for plate vibration problems can be used to display the dynamic response of the framed structure. For this reason, the numerical results obtained from the framed structure are expressed using the following dimensionless compliance and bending moment:

$$C_{HH}\left(a_0\right) = \frac{GB\Delta_1}{P_0}, \tag{6.20}$$

$$\overline{M}_y\left(a_0\right) = \frac{M_y}{GB^3}, \tag{6.21}$$

where C_{HH} is the dimensionless complex compliance of the framed structure due to the concentrated dynamic load (P_0) applied at the centre of the raft foundation in the X direction; Δ_1 is the corresponding complex displacement of the framed structure in the X direction; G is the shear modulus of the underlying rock; B is the half-width of the raft foundation; M_y is the bending moment of the framed structure with respect to the Y axis; $\overline{M}_y$ is the corresponding dimensionless bending moment of the framed structure; a_0 is a dimensionless frequency defined as

$$a_0 = \frac{\omega B}{C_S}, \tag{6.22}$$

where ω is the circular frequency of the concentrated dynamic load; C_S is the S-wave velocity in the underlying rock.

Figure 6.15 shows the dimensionless horizontal displacement of the framed structure (C_{HH}) in the X direction. In this figure, H is the height of the framed structure; *Re* and *Im* are the real part and imaginary part of the dimensionless horizontal displacement; solid triangles, solid dots and solid squares are used to represent the numerical results for columns 1, 2 and 3 when the raft foundation is flexible. Note that instead of the relative displacement, the absolute displacement of the framed structure is obtained using the proposed computational method in this section. When the framed structure is subjected to a horizontal ground motion induced by the dynamic load applied at the centre of the raft foundation, the maximum value of displacement differences within each story of the framed structure takes place in the ground story for both the “relatively rigid” and the flexible raft foundation cases. This indicates that the safety of the columns in the ground story of a framed structure is an important issue for the seismic design of the framed structure due to a sudden change in the mass and stiffness along the columns. Such a sudden change is often caused by the mass and stiffness of the beams in each floor of the framed structure. From the wave motion point of view, repeated wave reflection takes place within the columns between the ground floor and the first floor of the framed structure so that

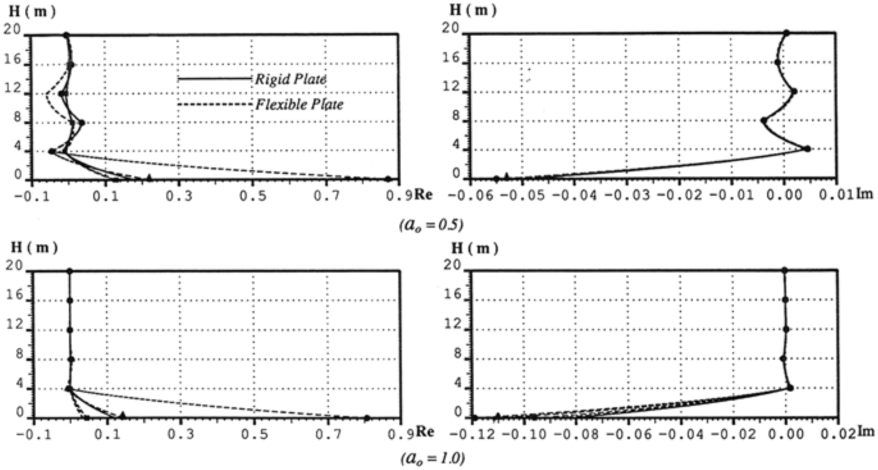

Fig. 6.15 Dimensionless horizontal displacement distributions of the framed structure

wave energy is trapped in the related columns, resulting in the maximum value of displacement differences within the columns of the ground story.

The flexibility of the raft foundation has a significant effect on the dynamic displacement response of the ground story of a framed structure. With $a_0 = 0.5$ taken as an example, in the case of a flexible-raft foundation, maximum values for the real part of dimensionless displacement differences in the ground floor of the framed structure are 0.225, 0.875 and 0.13 for columns 1, 2 and 3 respectively, while the corresponding maximum value is 0.178 when the raft foundation is relatively rigid. The numerical results shown in Fig. 6.15 indicate that the displacement difference between a “relatively rigid” raft foundation and a flexible raft foundation is too large to be ignored, especially for the real part of the dynamic compliance of the framed structure.

Figure 6.16 shows the distribution of the dimensionless bending moment $\overline{M}_y$ (with respect to the Y axis) of the framed structure. In this figure, H is the height of the framed structure; *Re* and *Im* are the real part and imaginary part of the dimensionless bending moment; solid triangles, solid dots and solid squares are used to represent the numerical results for columns 1, 2 and 3 when the raft foundation is flexible. Note that the dimensionless bending moment ($\overline{M}_y$) with respect to the Y axis is expressed on the basis of the sign convention adopted in structural mechanics. The maximum value of the dimensionless bending moment occurs within the columns on the ground floor when the raft foundation is either “relatively rigid” or flexible. Compared with the numerical results obtained from the framed structure with a “relatively rigid” raft foundation, the maximum dynamic response of the dimensionless bending moment is much greater when the framed structure is attached on a flexible raft foundation. Since the flexibility of a raft foundation results in an uneven displacement distribution within the raft foundation, the resulting displacement difference can cause a larger dynamic response of the dimensionless bending moment within the framed structure.

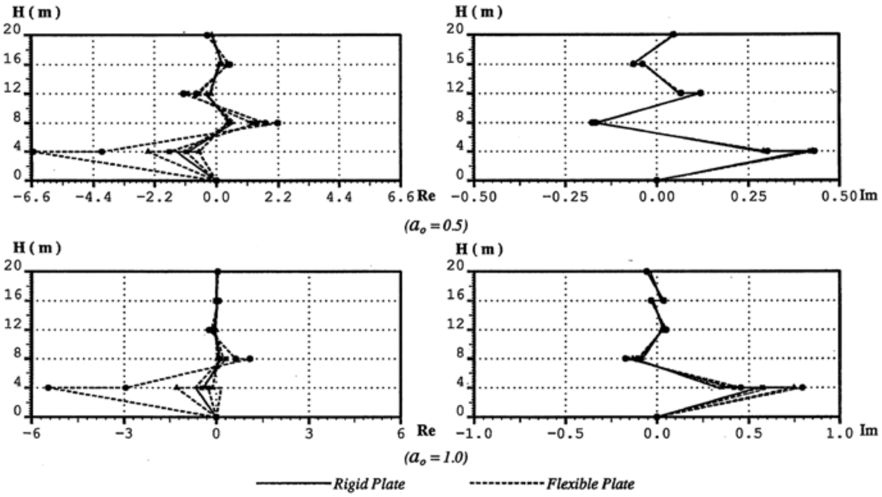

Fig. 6.16 Dimensionless bending moment distributions of the framed structure

Owing to the assumption that columns and the raft foundation are connected by joints at the bottoms of the columns on the ground floor, the maximum dimensionless bending moment ($\overline{M}_y$) occurs at the top ends of the columns on the ground floor of the framed structure. This assumption is based on the fact that when a column and a raft foundation are rigidly connected, the first plastic joint always occurs at the bottom of the column on the ground floor of a framed structure during strong earthquakes. The detailed study on the sequence of plastic joint appearance and the resulting internal force redistribution within the framed structure is needed in future research. Although the flexibility of a raft foundation has a significant effect on the real part of the dimensionless bending moment, it has little influence on the imaginary part of the dimensionless bending moment within the framed structure. This implies that the flexibility of a raft foundation has negligible effects on the damping of the full system, even though it has indeed a significant effect on its dynamic stiffness. For this reason, the flexibility of a raft foundation needs to be considered in the dynamic response of a three-dimensional framed structure so as to obtain realistic numerical solutions.

6.2.3 Effects of Underlying Soil/Rock on the Dynamic Response of a Three-Dimensional Framed Structure

In this subsection, the computational simulation of a three-dimensional multi-story framed structure with a square-raft foundation overlying a layered half-space is carried out to investigate the effects of the properties of the layered material on the dynamic response of the framed structure. The computational model for this problem is the same as that used in Sect. 6.2.2, except that the underlying soil/rock is a layered half-space, instead of a homogeneous half-space. This means that the homogeneous half-space used in Fig. 6.14 needs to be replaced by the layered half-space shown in Fig. 6.5. To describe the characteristics of the layered material, two parameters, namely the ratio of the elastic moduli of the underlying rock to the layered material (E_2/E_1) and the dimensionless thickness of the layer (H_L/B), are used in this subsection.

The following parameters are used in the computational model. For the underlying rock, the elastic modulus (E_2) is 24×10^9 Pa; the value of Poisson's ratio (ν) is 1/3; the rock density (ρ) is 2400 kg m^{-3}; the hysteretic coefficient of the rock material (η_d) is 0.1. For the layered medium, the value of Poisson's ratio, the density and the hysteretic coefficient are assumed to be exactly the same as for the underlying rock. Three different dimensionless layer thickness, namely $H_L/B = 0.5$, 1.0 and 1.5, are considered, to investigate the effects of the layer thickness on the dynamic response of the framed structure. For the purpose of examining the effects of the layer stiffness on the dynamic response of the framed structure, three different ratios of the elastic moduli of the underlying rock to the layered medium, namely $E_2/E_1 = 1$, 10 and 100, are considered in the coupled computational model of the three-dimensional framed structure–raft foundation–underlying soil/rock system. Note that $E_2/E_1 = 1$ means that the raft foundation of the framed structure is on a homogeneous half-space.

Figures 6.17 and 6.18 show the effects of the layer compressibility on the dimensionless horizontal displacement (C_{HH}) and bending moment ($\overline{M}_y$) distributions along the column of the framed structure. Since the raft foundation is assumed to be "relatively rigid" in this subsection, the four columns in Fig. 6.14 have identical horizontal displacement distributions. As the layer compressibility is directly proportional to the ratio of the elastic moduli of the underlying rock to the layered material, the numerical results clearly indicate that the layer compressibility has a significant effect on the dynamic response of the framed structure, resulting in a remarkable change in both the magnitude and distribution pattern of the dimensionless horizontal displacement and bending moment along the columns of the framed structure. Generally, a softer layer can cause a greater dynamic response of the framed structure. With $a_0 = 0.5$ taken as an example, the maximum values of dimensionless horizontal displacement amplitudes of the framed structure are 0.185, 1.07 and 1.09 for $E_2/E_1 = 1$, 10 and 100, respectively.

The dynamic responses of the framed structure are different when different excitation frequencies of the horizontal load are considered in the computational model. The layer compressibility has only a significant effect on the dynamic response at the lower part of the framed structure for the higher-frequency excitation (i.e. $a_0 = 1.0$), while it has a significant influence on the dynamic response over the entire framed structure for the lower-frequency excitation (i.e. $a_0 = 0.5$). This indicates that when a framed structure is located on a soft layer, the whole framed structure must be considered appropriately in the seismic analysis because the predominant frequency of an earthquake is usually in the lower-frequency range. However, when a framed structure is located on a stiff homogeneous half-space, it may be sufficient to concentrate attention on the lower part of the framed structure in the seismic design.

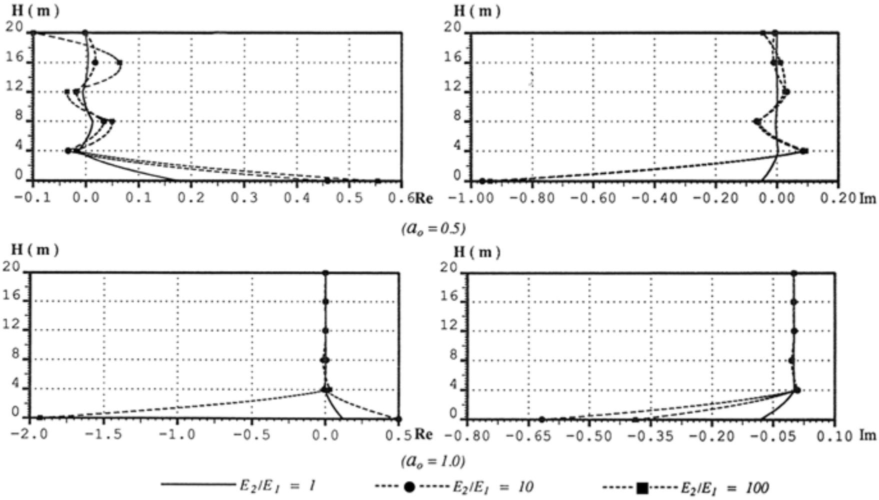

Fig. 6.17 Effects of layer compressibility on dimensionless horizontal displacement distributions of the framed structure

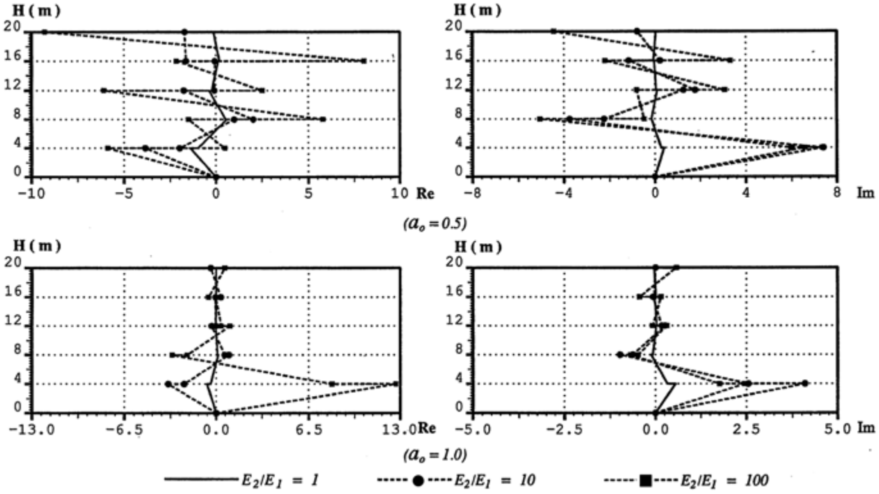

Fig. 6.18 Effects of layer compressibility on dimensionless bending moment distributions of the framed structure

Figures 6.19 and 6.20 show the effects of three dimensionless layer thicknesses on the distributions of the dimensionless horizontal displacement (C_{HH}) and bending moment ($\overline{M}_y$) along the column of the framed structure when $E_2/E_1 = 10$, while Figs. 6.21 and 6.22 show the corresponding numerical results when $E_2/E_1 = 100$. Clearly, the layer thickness has a significant effect on the dynamic response of the framed structure. Since a change in the layer thickness can result in a remarkable change in the dynamic characteristics of the layered medium (Zhao and Valliappan

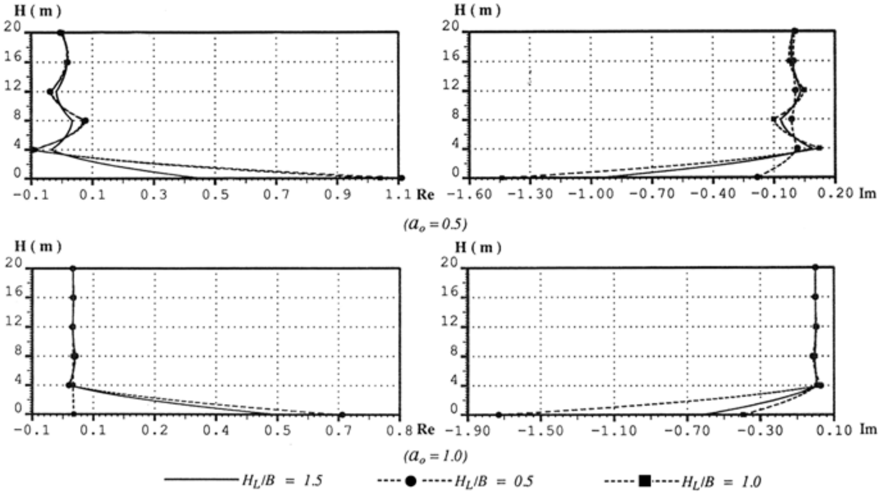

Fig. 6.19 Effects of layer thickness on dimensionless horizontal displacement distributions of the framed structure ($E_2/E_1 = 10$)

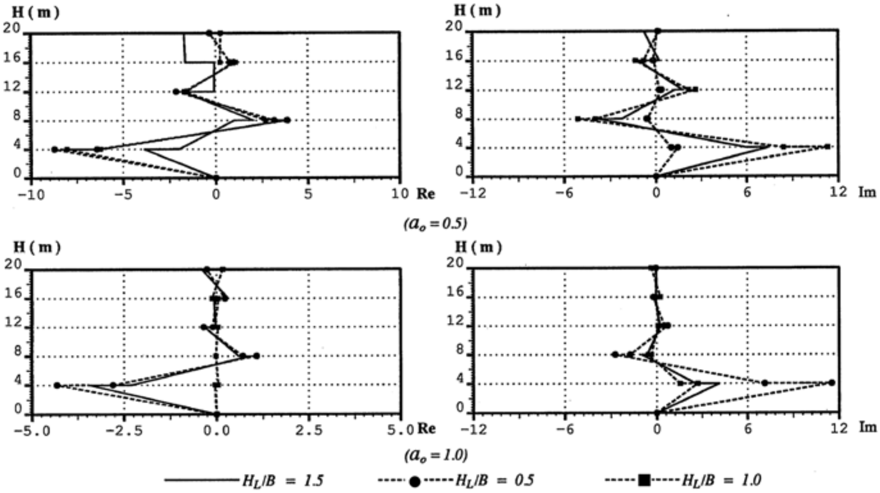

Fig. 6.20 Effects of layer thickness on dimensionless bending moment distributions of the framed structure ($E_2/E_1 = 10$)

1991, 1993e), the dynamic response of a framed structure on the layered medium will be changed accordingly because it depends on the dynamic characteristics of the layered medium. As the same parameters for the layered medium and underlying rock as those used in Sect. 6.1.2 are employed in this subsection, some previous numerical results obtained in Sect. 6.1.2 can be used to interpret the current numerical results.

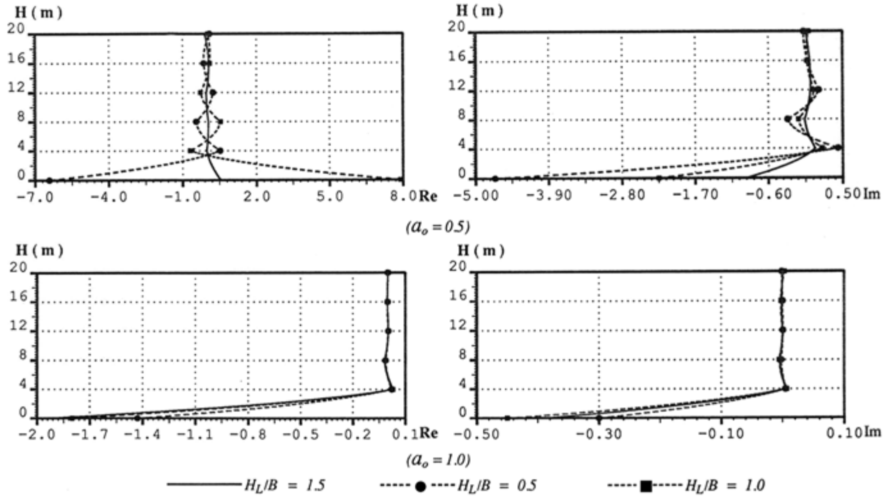

Fig. 6.21 Effects of layer thickness on dimensionless horizontal displacement distributions of the framed structure ($E_2/E_1 = 100$)

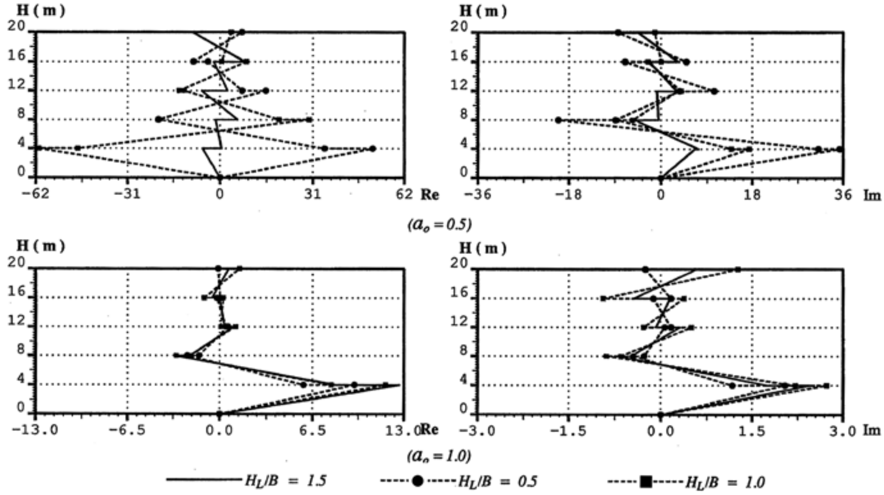

Fig. 6.22 Effects of layer thickness on dimensionless bending moment distributions of the framed structure ($E_2/E_1 = 100$)

When $E_2/E_1 = 10$ and $a_0 = 0.5$, the dimensionless horizontal displacement amplitudes of the "relatively rigid" raft foundation without the framed structure are 0.81, 1.3 and 0.93 for $H_L/B = 0.5$, 1.0 and 1.5, respectively. When the three-dimensional framed structure is included in the computational simulation, the corresponding maximum values of the dimensionless horizontal displacement amplitudes of the framed structure are 1.12, 1.78 and 1.07 for $H_L/B = 0.5$, 1.0 and 1.5. This indicates that when a three-dimensional framed structure is founded on a stiffer-layered medium, the dynamic response of the framed structure is mainly dominated by the dynamic behaviour of the layered medium so that it is very difficult to draw any general conclusions about the extent of how the layered medium affects the dynamic response of the framed structure. Nevertheless, the effect of the layer thickness on the dynamic response at the upper part of a framed structure is smaller than that at the lower part, especially for higher-frequency excitation of the framed structure (i.e. $a_0 = 1.0$).

When $E_2/E_1 = 100$ and $a_0 = 0.5$, the dimensionless horizontal displacement amplitudes of the "relatively rigid" raft foundation without the framed structure are 5.58, 2.43 and 1.22 for $H_L/B = 0.5$, 1.0 and 1.5, respectively. Once the three-dimensional framed structure is included in the computational model, the corresponding maximum values of the dimensionless horizontal displacement amplitudes of the framed structure are 7.69, 8.21 and 1.09 for $H_L/B = 0.5$, 1.0 and 1.5. This indicates that the flexibility of the framed structure may affect the dynamic characteristics of the whole framed structure–raft foundation–underlying soil/rock system when the framed structure is founded on a softer layered medium. Although the effect of the layer thickness on the dimensionless horizontal displacement amplitude at the upper part of the framed structure is negligible, the effect of the layer thickness on the displacement distribution pattern is still worth considering because the different displacement distribution patterns of a framed structure can result in different internal force distributions, as can be seen from Fig. 6.22. Since the irregular variation of the dimensionless bending moment along the columns of a framed structure is obtained in the case of a softer layered medium, proper attention should be paid to the internal force distribution pattern of the framed structure in the seismic analysis of three-dimensional framed structures.

In summary, the flexibility of a plate has significant effects on the dynamic response of the three-dimensional framed structure, especially for the ground story of the framed structure. Because of a sudden change in the mass and stiffness along the columns due to the beams of each floor, the repeated wave reflection occurs between the ground floor and the first floor, so that the wave energy is mainly trapped within these particular regions of the framed structure. As a result, the maximum dynamic response of the internal forces of the entire system occurs within the columns of the ground story of the framed structure. Compared with a "relatively rigid" plate, a flexible plate can result in an uneven displacement distribution within the plate. Such displacement differences can further cause a larger dynamic response of the internal forces within the framed structure.

The layer characteristics of soil media underneath a plate can affect the dynamic response of the three-dimensional framed structure significantly. A softer layer causes a larger dynamic response of the framed structure. Generally, the compressibility of the layered material can only have a remarkable influence on the dynamic response at the lower part of the framed structure for higher-frequency excitation, but it has a significant effect on the dynamic response of the entire framed structure for lower-frequency excitation. Although the effect of the layer thickness on the displacement amplitude at the upper part of the framed structure is negligible, it is still worth considering because different displacement-distribution patterns can result in different internal force distributions within the framed structure.

Chapter 7
Theory of Transient Infinite Elements for Simulating Pore-Fluid Flow and Heat Transfer in Porous Media of Infinite Domains

Pore-fluid flow and heat transfer in fluid-saturated porous media of infinite domains are important phenomena in many scientific and engineering fields. For example, in the field of exploration geoscience, pore-fluid flow and heat transfer from the interior of the Earth to the surface of the Earth are two important physical processes to control ore body formation and mineralization within the upper crust of the Earth. Owing to the increasing demand of natural minerals and the possible exhaustion of existing mineral resources in the foreseeable future, there has been an ever-increasing interest in the study of key controlling processes associated with ore body formation and mineralization within the upper crust of the Earth (Phillips 1991; Yeh and Tripathi 1991; Nield and Bejan 1992; Steefel and Lasaga 1994; Raffensperger and Garven 1995; Schafer et al. 1998a, b; Xu et al. 1999; Schaubs and Zhao 2002; Ord et al. 2002; Gow et al. 2002; Zhao et al. 1997–2008). In the field of environmental engineering, carbon dioxide gas sequestration in the deep Earth is becoming a potential way to reduce the greenhouse effect. Even in our daily lives, pore-fluid flow through fluid-saturated porous soils can be encountered almost everywhere. Although pore-fluid flow and heat transfer processes in fluid-saturated porous media are often coupled together, these two processes will be considered separately in this chapter, so as to facilitate the establishment of the fundamental theory of transient infinite elements for simulating pore-fluid flow and heat transfer problems in fluid-saturated porous media of infinite domains.

In numerical simulations of infinite domains, a primitive and most simple method, in which the infinite domain was approximately truncated as a large enough finite domain, was widely used at the early stage of the finite element analysis. The major disadvantages in using this primitive method are as follows: (1) the numerical simulation for a sufficiently large domain leads to computer CPU costs and storage penalties; (2) the boundary conditions of a problem at infinity cannot be rigorously satisfied. For instance, stresses and displacements approaching zero at infinity for a static problem and the wave radiation condition in the far field for a dynamic problem are violated in the numerical analysis; (3) stretching a fixed number of finite elements to model a vast domain can result in a severe loss of solution accuracy for static problems and spurious solutions for dynamic problems due to the element size requirement for appropriately simulating dynamic problems; (4) for transient

C. Zhao, *Dynamic and Transient Infinite Elements*, Advances in Geophysical and Environmental Mechanics and Mathematics, DOI 10.1007/978-3-642-00846-7_7,

pore-fluid flow and heat transfer problems, use of artificially truncated boundaries can cause unexpected numerical reflections back into the near field, where the solutions are usually of great interest to the analyst, of a system.

For the simulation of many pore-fluid flow and heat transfer problems in scientific and engineering fields, their computational domains can be treated as either homogeneous isotropic or homogeneous orthotropic porous media of infinite extent (Bear 1972; Freeze and Cherry 1979; Zhao and Valliappan 1993g, h). From a mathematical point of view, the two mutually alien subjects of transient pore-fluid flow and heat transfer can be treated together in this chapter, because they are described by the analogous boundary value problems. Since either a homogeneous isotropic or a homogeneous orthotropic porous medium has two orthogonal principal axes, it is possible to arrange these two principal axes to coincide with the x and y axes of a Cartesian coordinate system so that the presentation of the mathematics related to the derivation of transient infinite element formulation can be greatly simplified. One of the major advantages of considering either a homogeneous isotropic or a homogeneous orthotropic porous medium is that the property matrices of two-dimensional transient infinite elements can be evaluated either analytically or numerically. In the former case, the corresponding matrices of a transient infinite element can be expressed in closed forms (Zhao and Valliappan 1993g), whereas in the latter case, the corresponding matrices need to be computed using numerical integration (Zhao and Valliappan 1993h). Consequently, from a computational point of view, two different numerical methods are demonstrated in deriving the property matrices of two-dimensional transient infinite elements. As for a porous medium of general anisotropy, from the best knowledge of the author, the formulation of two-dimensional transient infinite elements remains unavailable so that future research is needed in this respect. The main purpose of this chapter is to summarize the fundamental theories of two-dimensional transient infinite elements for simulating transient pore-fluid flow and heat transfer problems in either fluid-saturated homogeneous isotropic or fluid-saturated homogeneous orthotropic porous media consisting of infinite domains.

7.1 Fundamental Theory of Transient Infinite Elements for Simulating Pore-Fluid Flow Problems in Fluid-Saturated Porous Media of Infinite Domains

7.1.1 Derivation of the Hydraulic Head Distribution Functions of Transient Infinite Elements

The key issue of constructing transient infinite elements for simulating pore-fluid flow problems in fluid-saturated porous media of infinite domains is to appropriately propose a hydraulic head distribution function in the infinite direction of the element. A general form of the hydraulic head distribution function for such a transient infinite element can be derived from the analytical solution of a representative problem. For this purpose, a pore-fluid flow problem, which has a unit hydraulic head at the origin of a Cartesian coordinate system in a one-dimensional fluid-saturated porous medium of infinite domain, is considered to derive the general form of the hydraulic head distribution function for such a transient infinite element. The governing equation of this one-dimensional problem in a fluid-saturated porous medium of infinite domain can be written as follows (Freeze and Cherry 1979; Zhao and Valliappan 1993g):

$$K_x \frac{\partial^2 h}{\partial x^2} = S_s \frac{\partial h}{\partial t}, \tag{7.1}$$

where K_x is the hydraulic conductivity in the x direction; h is the hydraulic head that represents energy per unit weight of pore-fluid (i.e. water); S_s is the specific storage of a saturated aquifer (i.e. porous medium) and is defined as the volume of pore-fluid released from a unit volume of the aquifer under a unit decline in hydraulic head. Since a decrease in hydraulic head implies either a decrease in pore-fluid pressure or an increase in effective stress, the pore fluid released from the aquifer under the condition of decreasing hydraulic head is mainly caused by the following two mechanisms. The first mechanism is the compression of the aquifer as a result of increasing effective stress so that it is controlled by the aquifer (i.e. porous medium) compressibility, α, while the second mechanism is the expansion of the pore fluid as a result of decreasing pore-fluid pressure so that it is controlled by the pore-fluid compressibility, β. Thus, the specific storage of a fluid-saturated aquifer can be expressed as follows (Freeze and Cherry 1979):

$$S_s = \rho_f g(\alpha + \phi\beta), \tag{7.2}$$

where ρ_f is the pore-fluid density; g is the acceleration due to gravity; ϕ is the porosity of the porous medium. Note that the specific storage (S_s) has the dimension of L^{-1}.

For constant K_x and S_s, the analytical solution for this one-dimensional pore-fluid flow problem with a unit hydraulic head at the origin of the Cartesian coordinate system can be expressed in the following form (Carslaw and Jaeger 1959; Harr 1962):

$$h(x, t) = \sqrt{\frac{S_s}{4\pi K_x t}} \exp\left(-\frac{S_s x^2}{4K_x t}\right). \tag{7.3}$$

For a typical transient infinite element shown in Fig. 7.1, the global coordinate of node 1 is x_1 and the local coordinate of this node is identical to zero. The hydraulic head at this node for a given time, t, can be expressed as:

$$h(x_1, t) = \sqrt{\frac{S_s}{4\pi K_x t}} \exp\left(-\frac{S_s x_1^2}{4K_x t}\right). \tag{7.4}$$

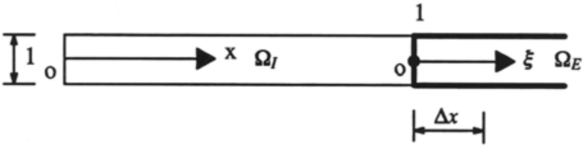

Fig. 7.1 A typical one-dimensional transient infinite element for simulating transient pore-fluid flow problems

For any point within this transient infinite element, taking $x = x_1 + \Delta x$ as an example, the hydraulic head at this point can be directly derived from Eq. (7.4):

$$h(x_1 + \Delta x, t) = h(x_{1,} t) \exp\left[-\frac{S_s(\Delta x^2 + 2x_1 \Delta x)}{4K_x t}\right]. \tag{7.5}$$

Since $\xi = \Delta x$ for this one-dimensional transient infinite element, the hydraulic head distribution function of this element can be expressed as

$$F_{hd}(\xi, t) = \exp\left[-\frac{S_s(\xi^2 + 2x_1 \xi)}{4K_x t}\right]. \tag{7.6}$$

As a result, the hydraulic head field within the one-dimensional transient infinite element can be expressed using the following equation:

$$h(\xi,t) = h_1 F_{hd}(\xi,t) = h_1 N_1, \tag{7.7}$$

where h_1 is the nodal hydraulic head of the one-dimensional transient infinite element; h is the hydraulic head distribution within the infinite element; N_1 is the shape function of the one-dimensional transient infinite element. Note that for one-dimensional transient pore-fluid flow problems, the hydraulic head distribution function is identical to the shape function of the one-dimensional transient infinite element.

$$N_1 = F_{hd}(\xi, t) = \exp\left[-\frac{S_s(\xi^2 + 2x_1 \xi)}{4K_x t}\right]. \tag{7.8}$$

The first derivative of the shape function with respect to ξ is

$$\frac{\partial N_1}{\partial \xi} = -\frac{S_s(\xi + x_1)}{2K_x t} \exp\left[-\frac{S_s(\xi^2 + 2x_1 \xi)}{4K_x t}\right]. \tag{7.9}$$

Using the finite element method (Zienkiewicz 1977; Rao 1989) and the condition of $dx = d\xi$, the property matrices of the one-dimensional transient infinite element can be expressed as

$$G_{11} = \int_0^\infty \left(\frac{K_x}{S_s} \frac{\partial N_1}{\partial \xi} \frac{\partial N_1}{\partial \xi} \right) d\xi, \tag{7.10}$$

$$R_{11} = \int_0^\infty (N_1 N_1)\, d\xi. \tag{7.11}$$

Substituting Eqs. (7.8) and (7.9) into Eqs. (7.10) and (7.11) yields

$$G_{11} = \frac{S_s}{4K_x t^2} \int_0^\infty \left\{ (\xi + x_1)^2 \exp\left[-\frac{S_s(\xi^2 + 2x_1\xi)}{2K_x t} \right] \right\} d\xi, \tag{7.12}$$

$$R_{11} = \int_0^\infty \exp\left[-\frac{S_s(\xi^2 + 2x_1\xi)}{2K_x t} \right] d\xi. \tag{7.13}$$

To evaluate Eqs. (7.12) and (7.13), the following integrals have been encountered:

$$I_1 = \int_0^\infty \exp\left(-x^2\right) dx = \frac{\sqrt{\pi}}{2}, \tag{7.14}$$

$$I_2 = \int_0^\infty x^2 \exp\left(-x^2\right) dx = \frac{\sqrt{\pi}}{4}, \tag{7.15}$$

$$I_3 = \int_a^\infty \exp\left(-x^2\right) dx = \frac{\sqrt{\pi}}{2} - \sum_{n=0}^{\infty} \frac{(-1)^n}{n!} \frac{1}{2n+1} a^{2n+1}, \tag{7.16}$$

$$I_4 = \int_a^\infty x^2 \exp\left(-x^2\right) dx = \frac{\sqrt{\pi}}{4} + \frac{a}{2} e^{-a^2} - \frac{1}{2} \sum_{n=0}^{\infty} \frac{(-1)^n}{n!} \frac{1}{2n+1} a^{2n+1}. \tag{7.17}$$

Note that mathematically, the value of an integral is independent of the symbol of the integration variable used in the integral. Thus, using these integrals expressed in Eqs. (7.14), (7.15), (7.16) and (7.17), Eqs. (7.12) and (7.13), after some mathematical manipulations, can be expressed as

$$R_{11} = \sqrt{\frac{2K_x t}{S_s}} \exp\left(\frac{S_s x_1^2}{2K_x t} \right) \left[\frac{\sqrt{\pi}}{2} - \sum_{n=0}^{\infty} \left(\frac{(-1)^n}{n!} \frac{1}{2n+1} \lambda_1^{2n+1} \right) \right], \tag{7.18}$$

$$\begin{aligned} G_{11} = \sqrt{\frac{K_x}{8S_s t}} \exp\left(\frac{S_s x_1^2}{2K_x t} \right) \Bigg[& \frac{\sqrt{\pi}}{2} + \lambda_1 \exp\left(-\frac{S_s x_1^2}{2K_x t} \right) \\ & - \sum_{n=0}^{\infty} \left(\frac{(-1)^n}{n!} \frac{1}{2n+1} \lambda_1^{2n+1} \right) \Bigg]. \end{aligned} \tag{7.19}$$

$$\lambda_1 = x_1 \sqrt{\frac{S_s}{2K_x t}}. \tag{7.20}$$

Similarly, if the positive direction of the ξ-axis in the local coordinate system is opposite to that of the x-axis in the global coordinate system, the hydraulic head distribution function of the one-dimensional transient infinite element can be expressed as follows:

$$F_{hd}^{*}(\xi, t) = \exp\left[-\frac{S_s(\xi^2 - 2x_1\xi)}{4K_x t}\right]. \tag{7.21}$$

Consequently, the corresponding property matrices of the one-dimensional transient infinite element can be expressed using the following equations:

$$R_{11}^{*} = \sqrt{\frac{2K_x t}{S_s}} \exp\left(\frac{S_s x_1^2}{2K_x t}\right)\left[\frac{\sqrt{\pi}}{2} - \sum_{n=0}^{\infty}\left(\frac{(-1)^n}{n!}\frac{1}{2n+1}\lambda_2^{2n+1}\right)\right], \tag{7.22}$$

$$\begin{aligned} G_{11}^{*} = \sqrt{\frac{K_x}{8S_s t}} \exp\left(\frac{S_s x_1^2}{2K_x t}\right)\Bigg[\frac{\sqrt{\pi}}{2} + \lambda_2 \exp\left(-\frac{S_s x_1^2}{2K_x t}\right) \\ -\sum_{n=0}^{\infty}\left(\frac{(-1)^n}{n!}\frac{1}{2n+1}\lambda_2^{2n+1}\right)\Bigg], \end{aligned} \tag{7.23}$$

$$\lambda_2 = -x_1\sqrt{\frac{S_s}{2K_x t}}. \tag{7.24}$$

After the general form of the hydraulic head distribution function is derived for a one-dimensional transient infinite element, the same procedure can be used to derive the general form of the hydraulic head distribution function for a two-dimensional transient infinite element. If a two-dimensional pore-fluid flow problem, which has a point hydraulic head at the origin of a Cartesian coordinate system in a fluid-saturated homogeneous, orthotropic porous medium of infinite extent, is considered, then the governing equation of this problem (Freeze and Cherry 1979; Zhao and Valliappan 1993g) can be expressed as follows:

$$K_x\frac{\partial^2 h}{\partial x^2} + K_y\frac{\partial^2 h}{\partial y^2} = S_s\frac{\partial h}{\partial t}, \tag{7.25}$$

where K_x and K_y are the hydraulic conductivities in the x and y directions, which are two principal directions of the fluid-saturated homogeneous and orthotropic porous medium; h is the hydraulic head in the fluid-saturated porous medium of the infinite domain.

For constant K_x, K_y and S_s, the analytical solution for the hydraulic head of this problem (Larder and Song 1991) can be expressed as

$$h(x, y, t) = \sqrt{\frac{S_s}{4\pi K_x t}}\sqrt{\frac{S_s}{4\pi K_y t}} h_0 \exp\left(-\frac{S_s x^2}{4K_x t}\right)\exp\left(-\frac{S_s y^2}{4K_y t}\right), \tag{7.26}$$

where h_0 is the point hydraulic head at the origin of the Cartesian coordinate system.

In order to derive the hydraulic head distribution function for a two-dimensional transient infinite element, Eq. (7.21) can be straightforwardly rewritten into the form:

$$h(x, y, t) = h_0 g_1(x, t) g_2(y, t), \tag{7.27}$$

where

$$g_1(x, t) = \sqrt{\frac{S_s}{4\pi K_x t}} \exp\left(-\frac{S_s x^2}{4K_x t}\right), \tag{7.28}$$

$$g_2(y, t) = \sqrt{\frac{S_s}{4\pi K_y t}} \exp\left(-\frac{S_s y^2}{4K_y t}\right). \tag{7.29}$$

Since the orthotropy of the porous medium and the different features of pore-fluid flow are considered in the two principal directions of the porous medium, more shapes of transient infinite elements need to be considered in the course of constructing transient infinite elements for the simulation of two-dimensional transient pore-fluid flow problems in fluid-saturated porous media of infinite domains. As shown in Fig. 7.2, if the positive directions of pore-fluid flow are identical to those of the x- and y-axes, then eight categories of transient infinite elements should

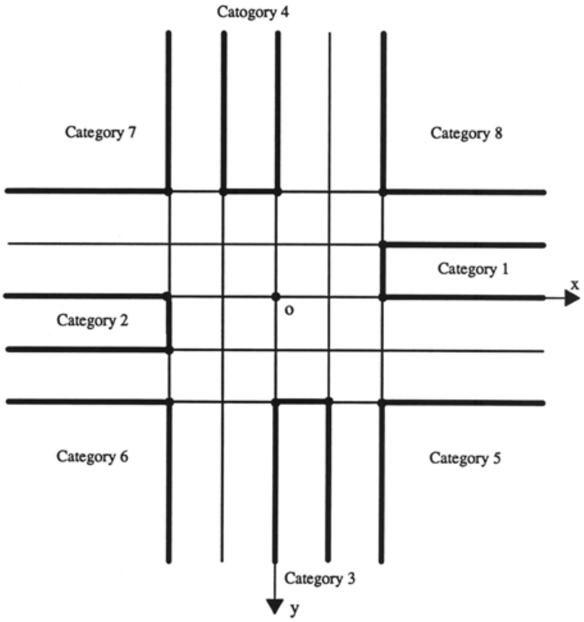

Fig. 7.2 Eight categories of two-dimensional transient infinite elements for simulating transient pore-fluid flow problems

be constructed to simulate two-dimensional transient pore-fluid flow problems in a full infinite plane. According to the feature of infinite extent, the transient infinite elements in categories one to four are called uni-infinite elements, while the transient infinite elements in categories five to eight are called bi-infinite elements. Following the same procedure as that used to derive the hydraulic head distribution function for one-dimensional transient pore-fluid flow problems, the general forms of hydraulic head distribution functions for two-dimensional transient pore-fluid flow problems in fluid-saturated porous media of infinite domains can be derived and expressed as follows:

$$F_{hd}(\xi,t) = \exp\left[-\frac{S_s(\xi^2 + 2x_1\xi)}{4K_x t}\right], \tag{7.30}$$

$$F_{hd}^*(\xi,t) = \exp\left[-\frac{S_s(\xi^2 - 2x_1\xi)}{4K_x t}\right], \tag{7.31}$$

$$F_{hd}(\eta,t) = \exp\left[-\frac{S_s(\eta^2 + 2y_1\eta)}{4K_y t}\right], \tag{7.32}$$

$$F_{hd}^*(\eta,t) = \exp\left[-\frac{S_s(\eta^2 - 2y_1\eta)}{4K_y t}\right], \tag{7.33}$$

where $F_{hd}(\xi,t)$ and $F_{hd}^*(\xi,t)$ are the hydraulic head distribution functions of two-dimensional transient infinite elements when the positive direction of the ξ axis is identical or opposite to that of the x axis; $F_{hd}(\eta,t)$ and $F_{hd}^*(\eta,t)$ are the hydraulic head distribution functions of two-dimensional transient infinite elements when the positive direction of the η axis is identical or opposite to that of the y axis, respectively; x_1 and y_1 are nodal coordinates in the global coordinate system.

7.1.2 Derivation of the Property Matrices of Two-Dimensional Transient Infinite Elements for Simulating Pore-Fluid Flow Problems

Another key issue associated with the construction of two-dimensional transient infinite elements is to derive the property matrices of the transient infinite elements in a mathematical manner. Generally, there are two ways that can be used to derive the property matrices of two-dimensional transient infinite elements. The first way is to use more different kinds of parent infinite elements, which have different shapes, in the process of deriving the property matrices of the transient infinite elements, while the second way is to use only two kinds of mapped parent infinite elements in the process of deriving the property matrices of two-dimensional transient infinite elements. Owing to this significant difference, the property matrices derived using the first way can be expressed in closed forms, but the property matrices derived using the second way need to be evaluated numerically. In this section, the first way is used to derive the property matrices of two-dimensional transient infinite elements that can be employed to simulate two-dimensional transient pore-fluid flow problems in fluid-saturated porous media of infinite domains. To avoid unnecessary repeats, the second way will be adopted in the next section to derive the property matrices of two-dimensional transient infinite elements, which can be used to simulate two-dimensional heat transfer problems in fluid-saturated porous media of infinite domains.

Since the governing equation is of the same mathematical form for both a finite element and a transient infinite element, the conventional finite element method (Zienkiewicz 1997; Rao 1989) can be used to derive the property matrices of transient infinite elements. Using the Galerkin weighted residual method, Eq. (7.25) can be discretized into a set of algebraic equations as follows:

$$[G]\{h\} + [R]\left\{\frac{\partial h}{\partial t}\right\} = \{f\}, \tag{7.34}$$

where $\{h\}$ is the global nodal hydraulic head vector of the system; $\{f\}$ is the global nodal "load" vector of the system; $[G]$ and $[R]$ are the global property matrices of the system and their element property matrices can be expressed as

$$[G_e] = \iint_A \left(\frac{K_x}{S_s}\frac{\partial[N]^T}{\partial x}\frac{\partial[N]}{\partial x} + \frac{K_y}{S_s}\frac{\partial[N]^T}{\partial y}\frac{\partial[N]}{\partial y}\right) dA, \tag{7.35}$$

$$[R_e] = \iint_A \left([N]^T[N]\right) dA, \tag{7.36}$$

where $[N]$ is the (hydraulic head) shape function matrix of either a finite element or a transient infinite element; $[N]^T$ is the transpose of $[N]$; A is the area of the corresponding element.

7.1.2.1 The First Category of Two-Dimensional Transient Infinite Elements

As shown in Fig. 7.3(A), the shape function matrix of this category of two-dimensional transient infinite elements can be written as follows:

$$[N] = [N_1 \quad N_2] \tag{7.37}$$

where N_1 and N_2 are the shape functions for nodes 1 and 2 of the element, respectively.

$$N_1 = F_{hd}(\xi, t)\frac{1-\eta}{2}, \tag{7.38}$$

$$N_2 = F_{hd}(\xi, t)\frac{1+\eta}{2}. \tag{7.39}$$

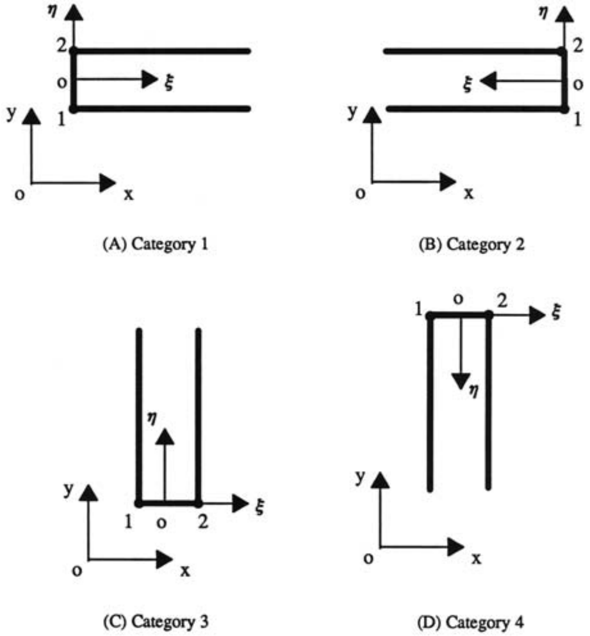

(A) Category 1 (B) Category 2

(C) Category 3 (D) Category 4

Fig. 7.3 Four categories of two-dimensional transient uni-infinite elements

It is noted that for this category of two-dimensional transient infinite elements, the following relationship exists between the local coordinate system and the global one.

$$dx = d\xi, \tag{7.40}$$

$$dy = \frac{1}{2}(y_2 - y_1)d\eta. \tag{7.41}$$

Substituting Eqs. (7.37), (7.38), (7.39), (7.40) and (7.41) into Eqs. (7.35) and (7.36) yields the property matrices of the first category of two-dimensional transient infinite elements as follows:

$$[G_e]_1 = \int_0^\infty \int_{-1}^1 \left(\frac{K_x}{S_s} \frac{\partial [N]^T}{\partial \xi} \frac{\partial [N]}{\partial \xi} + \frac{4K_y}{S_s(y_2 - y_1)^2} \frac{\partial [N]^T}{\partial \eta} \frac{\partial [N]}{\partial \eta} \right) \frac{y_2 - y_1}{2} d\eta d\xi, \tag{7.42}$$

$$[R_e]_1 = \int_0^\infty \int_{-1}^1 \left([N]^T [N] \right) \frac{y_2 - y_1}{2} d\eta d\xi \tag{7.43}$$

After Eqs. (7.42) and (7.43) are integrated analytically, the resulting property matrices of the first category of two-dimensional transient infinite elements can be expressed in the following forms:

$$[G_e]_1 = \frac{K_x(y_2 - y_1)}{3S_s} G_{11}(x_1, t) \begin{bmatrix} 1 & 0.5 \\ 0.5 & 1 \end{bmatrix} + \frac{K_y}{S_s(y_2 - y_1)} R_{11}(x_1, t) \begin{bmatrix} 1 & -1 \\ -1 & 1 \end{bmatrix}, \tag{7.44}$$

$$[R_e]_1 = \frac{y_2 - y_1}{3} R_{11}(x_1, t) \begin{bmatrix} 1 & 0.5 \\ 0.5 & 1 \end{bmatrix}, \tag{7.45}$$

where $R_{11}(x_1, t)$ and $G_{11}(x_1, t)$ are defined below:

$$R_{11}(x_1, t) = \sqrt{\frac{2K_x t}{S_s}} \exp\left(\lambda_1^2\right) \left[\frac{\sqrt{\pi}}{2} - \sum_{n=0}^{\infty} \left(\frac{(-1)^n}{n!} \frac{1}{2n+1} \lambda_1^{2n+1} \right) \right], \tag{7.46}$$

$$\begin{aligned} G_{11}(x_1, t) = \sqrt{\frac{S_s}{8K_x t}} \exp\left(\lambda_1^2\right) \Bigg[& \frac{\sqrt{\pi}}{2} + \lambda_1 \exp\left(-\lambda_1^2\right) \\ & - \sum_{n=0}^{\infty} \left(\frac{(-1)^n}{n!} \frac{1}{2n+1} \lambda_1^{2n+1} \right) \Bigg], \end{aligned} \tag{7.47}$$

where

$$\lambda_1 = x_1 \sqrt{\frac{S_s}{2K_x t}}. \tag{7.48}$$

7.1.2.2 The Second Category of Two-Dimensional Transient Infinite Elements

Figure 7.3(B) shows the second category of two-dimensional transient infinite elements, the main characteristic of which is that the positive direction of the x axis is opposite to that of the ξ axis. The shape function matrix of this category of two-dimensional transient infinite elements can be expressed as follows:

$$[N] = [N_1 \quad N_2], \tag{7.49}$$

where N_1 and N_2 are the shape functions for nodes 1 and 2 of the element, respectively.

$$N_1 = F_{hd}^*(\xi, t) \frac{1 - \eta}{2}, \tag{7.50}$$

$$N_2 = F_{hd}^*(\xi, t) \frac{1 + \eta}{2}. \tag{7.51}$$

Following the similar procedure to that used above, the property matrices of the second category of two-dimensional transient infinite elements can be derived as follows:

$$[G_e]_2 = \frac{K_x(y_2 - y_1)}{3S_s} G_{11}^*(x_1,t) \begin{bmatrix} 1 & 0.5 \\ 0.5 & 1 \end{bmatrix} + \frac{K_y}{S_s(y_2 - y_1)} R_{11}^*(x_1,t) \begin{bmatrix} 1 & -1 \\ -1 & 1 \end{bmatrix}, \tag{7.52}$$

$$[R_e]_2 = \frac{y_2 - y_1}{3} R_{11}^*(x_1,t) \begin{bmatrix} 1 & 0.5 \\ 0.5 & 1 \end{bmatrix}, \tag{7.53}$$

where $R_{11}^*(x_1,t)$ and $G_{11}^*(x_1,t)$ are defined below:

$$R_{11}^*(x_1,t) = \sqrt{\frac{2K_x t}{S_s}} \exp\left(\lambda_2^2\right) \left[\frac{\sqrt{\pi}}{2} - \sum_{n=0}^{\infty} \left(\frac{(-1)^n}{n!} \frac{1}{2n+1} \lambda_2^{2n+1} \right) \right], \tag{7.54}$$

$$\begin{aligned} G_{11}^*(x_1,t) = \sqrt{\frac{S_s}{8K_x t}} \exp\left(\lambda_2^2\right) \Bigg[& \frac{\sqrt{\pi}}{2} + \lambda_2 \exp\left(-\lambda_2^2\right) \\ & - \sum_{n=0}^{\infty} \left(\frac{(-1)^n}{n!} \right) \frac{1}{2n+1} \lambda_2^{2n+1} \Bigg], \end{aligned} \tag{7.55}$$

where

$$\lambda_2 = -x_1 \sqrt{\frac{S_s}{2K_x t}} \tag{7.56}$$

7.1.2.3 The Third Category of Two-Dimensional Transient Infinite Elements

The fundamental characteristic of the third category of two-dimensional transient infinite elements is that their sizes extend to infinity in the η direction, instead of the ξ direction. In order to simulate the vertical component of the pore-fluid flow, it is assumed that the η axis is parallel to the y axis. As shown in Fig. 7.3(C), the shape function matrix of this category of two-dimensional transient infinite elements can be written as follows:

$$[N] = [N_1 \quad N_2], \tag{7.57}$$

where N_1 and N_2 are the shape functions for nodes 1 and 2 of the infinite element, respectively.

$$N_1 = F_{hd}(\eta,t) \frac{1-\xi}{2}, \tag{7.58}$$

$$N_2 = F_{hd}(\eta,t) \frac{1+\xi}{2}. \tag{7.59}$$

Using the similar procedure to that used above, the property matrices of the third category of two-dimensional transient infinite elements can be derived as follows:

$$[G_e]_3 = \frac{K_x}{S_s(x_2 - x_1)} R_{11}(y_1, t) \begin{bmatrix} 1 & -1 \\ -1 & 1 \end{bmatrix} + \frac{K_y(x_2 - x_1)}{3S_s} G_{11}(y_1, t) \begin{bmatrix} 1 & 0.5 \\ 0.5 & 1 \end{bmatrix}, \tag{7.60}$$

$$[R_e]_3 = \frac{x_2 - x_1}{3} R_{11}(y_1, t) \begin{bmatrix} 1 & 0.5 \\ 0.5 & 1 \end{bmatrix}, \tag{7.61}$$

where $R_{11}(y_1, t)$ and $G_{11}(y_1, t)$ are defined below:

$$R_{11}(y_1, t) = \sqrt{\frac{2K_y t}{S_s}} \exp\left(\lambda_3^2\right) \left[\frac{\sqrt{\pi}}{2} - \sum_{n=0}^{\infty} \left(\frac{(-1)^n}{n!} \frac{1}{2n+1} \lambda_3^{2n+1} \right) \right], \tag{7.62}$$

$$\begin{aligned} G_{11}(y_1, t) = \sqrt{\frac{S_s}{8K_y t}} \exp\left(\lambda_3^2\right) \Bigg[& \frac{\sqrt{\pi}}{2} + \lambda_3 \exp\left(-\lambda_3^2\right) \\ & - \sum_{n=0}^{\infty} \left(\frac{(-1)^n}{n!} \frac{1}{2n+1} \lambda_3^{2n+1} \right) \Bigg], \end{aligned} \tag{7.63}$$

where

$$\lambda_3 = y_1 \sqrt{\frac{S_s}{2K_y t}}. \tag{7.64}$$

7.1.2.4 The Fourth Category of Two-Dimensional Transient Infinite Elements

The basic characteristic of the fourth category of two-dimensional transient infinite elements is that the positive direction of the η direction is opposite to that of the y-axis. As shown in Fig. 7.3(D), the shape function matrix of this category of two-dimensional transient infinite elements can be expressed as follows:

$$[N] = [N_1 \quad N_2], \tag{7.65}$$

where N_1 and N_2 are the shape functions for nodes 1 and 2 of the infinite element, respectively:

$$N_1 = F_{hd}^*(\eta, t) \frac{1 - \xi}{2}, \tag{7.66}$$

$$N_2 = F_{hd}^*(\eta, t) \frac{1 + \xi}{2}. \tag{7.67}$$

Similarly, the property matrices of the fourth category of two-dimensional transient infinite elements can be derived as follows:

$$[G_e]_4 = \frac{K_x}{S_s(x_2 - x_1)} R^*_{11}(y_1, t) \begin{bmatrix} 1 & -1 \\ -1 & 1 \end{bmatrix} + \frac{K_y(x_2 - x_1)}{3S_s} G^*_{11}(y_1, t) \begin{bmatrix} 1 & 0.5 \\ 0.5 & 1 \end{bmatrix}, \tag{7.68}$$

$$[R_e]_4 = \frac{x_2 - x_1}{3} R^*_{11}(y_1, t) \begin{bmatrix} 1 & 0.5 \\ 0.5 & 1 \end{bmatrix}, \tag{7.69}$$

where $R^*_{11}(y_1, t)$ and $G^*_{11}(y_1, t)$ are defined below:

$$R^*_{11}(y_1, t) = \sqrt{\frac{2K_y t}{S_s}} \exp\left(\lambda_4^2\right) \left[\frac{\sqrt{\pi}}{2} - \sum_{n=0}^{\infty} \left(\frac{(-1)^n}{n!} \frac{1}{2n+1} \lambda_4^{2n+1} \right) \right], \tag{7.70}$$

$$\begin{aligned} G^*_{11}(y_1, t) = \sqrt{\frac{S_s}{8K_y t}} \exp\left(\lambda_4^2\right) \Bigg[& \frac{\sqrt{\pi}}{2} + \lambda_4 \exp\left(-\lambda_4^2\right) \\ & - \sum_{n=0}^{\infty} \left(\frac{(-1)^n}{n!} \frac{1}{2n+1} \lambda_4^{2n+1} \right) \Bigg], \end{aligned} \tag{7.71}$$

where

$$\lambda_4 = -y_1 \sqrt{\frac{S_s}{2K_y t}}. \tag{7.72}$$

7.1.2.5 Two-Dimensional Transient Bi-infinite Elements

The fifth to eighth categories of two-dimensional transient infinite elements are called bi-infinite elements due to their infinite extension in both the ξ and the η directions. Following the same procedures as those used in the previous subsections, the property matrices of two-dimensional transient bi-infinite elements can be derived and expressed below.

For the fifth category of two-dimensional transient infinite elements shown in Fig. 7.4(A), the corresponding property matrices are as follows:

$$[G_e]_5 = \frac{K_x}{S_s} G_{11}(x_1, t) R_{11}(y_1, t) + \frac{K_y}{S_s} R_{11}(x_1, t) G_{11}(y_1, t), \tag{7.73}$$

$$[R_e]_5 = R_{11}(x_1, t) R_{11}(y_1, t). \tag{7.74}$$

For the sixth category of two-dimensional transient infinite elements shown in Fig. 7.4(B), the corresponding property matrices can be expressed as follows:

$$[G_e]_6 = \frac{K_x}{S_s} G^*_{11}(x_1, t) R_{11}(y_1, t) + \frac{K_y}{S_s} R^*_{11}(x_1, t) G_{11}(y_1, t), \tag{7.75}$$

$$[R_e]_6 = R^*_{11}(x_1, t) R_{11}(y_1, t). \tag{7.76}$$

Fig. 7.4 Four categories of two-dimensional transient bi-infinite elements

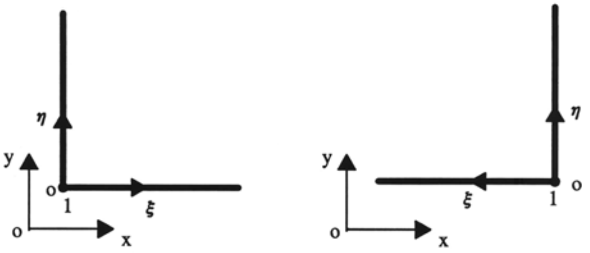

(A) Category 5 (B) Category 6

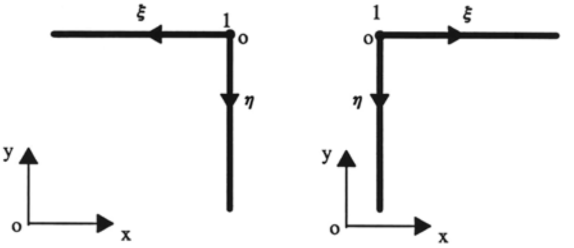

(C) Category 7 (D) Category 8

For the seventh category of two-dimensional transient infinite elements shown in Fig. 7.4(C), the corresponding property matrices can be written as follows:

$$[G_e]_7 = \frac{K_x}{S_s} G_{11}^*(x_1, t) R_{11}^*(y_1, t) + \frac{K_y}{S_s} R_{11}^*(x_1, t) G_{11}^*(y_1, t), \tag{7.77}$$

$$[R_e]_7 = R_{11}^*(x_1, t) R_{11}^*(y_1, t). \tag{7.78}$$

Finally, for the eighth category of two-dimensional transient infinite elements shown in Fig. 7.4(D), the corresponding property matrices can be expressed as follows:

$$[G_e]_8 = \frac{K_x}{S_s} G_{11}(x_1, t) R_{11}^*(y_1, t) + \frac{K_y}{S_s} R_{11}(x_1, t) G_{11}^*(y_1, t), \tag{7.79}$$

$$[R_e]_8 = R_{11}(x_1, t) R_{11}^*(y_1, t). \tag{7.80}$$

Up to now, closed-form solutions have been derived for all property matrices of two-dimensional transient infinite elements, which can be used to simulate the far fields of transient pore-fluid flow problems in two-dimensional fluid-saturated porous media of infinite domains. Since the series involved in the property matrices of two-dimensional transient infinite elements converges for all real numbers, the computation of these property matrices can be easily carried out using any computers. This is the main advantage in deriving closed-form solutions for all property matrices of two-dimensional transient infinite elements of eight different shapes.

7.2 Fundamental Theory of Transient Infinite Elements for Simulating Heat Transfer Problems in Fluid-Saturated Porous Media of Infinite Domains

7.2.1 Derivation of the Heat Transfer Functions of Transient Infinite Elements

Like constructing transient infinite elements for simulating pore-fluid flow problems, the key issue of constructing transient infinite elements for simulating heat transfer problems in fluid-saturated porous media of infinite domains is to appropriately choose a heat transfer function in the infinite direction of the element. The general form of the heat transfer function for such a transient infinite element can be derived from the analytical solution of a representative one-dimensional heat transfer problem in an infinite domain. For this particular purpose, a heat advection–conduction problem, which has a given temperature at the origin of a Cartesian coordinate system in a one-dimensional fluid-saturated porous medium of an infinite domain, is considered to derive the general form of the heat transfer function. If heat equilibrium is attained between the pore fluid and the solid matrix, the governing equation of this one-dimensional heat transfer problem in a fluid-saturated porous medium of an infinite domain (Nield and Bejan 1992) can be written as follows:

$$[\phi c_{pf}\rho_f + (1-\phi)c_{ps}\rho_s]\frac{\partial T}{\partial t} + c_{pf}\rho_f V_x\frac{\partial T}{\partial x} = [\phi\lambda_{xf} + (1-\phi)\lambda_{xs}]\frac{\partial^2 T}{\partial x^2}, \tag{7.81}$$

where c_{pf} and c_{ps} are the specific heats for the pore-fluid and solid matrix; ρ_f and ρ_s are the densities of the pore-fluid and solid matrix; λ_{xf} and λ_{xs} are the thermal conductivities of the pore-fluid and solid matrix, respectively; ϕ is the porosity of the porous medium; V_x is the Darcy velocity in the x direction; T is the temperature of the porous medium.

It is obvious that Eq. (7.81) can be rewritten into the following form:

$$(c_p\rho)_m\frac{\partial T}{\partial t} + \alpha(c_p\rho)_m V_x\frac{\partial T}{\partial x} = \lambda_x^m\frac{\partial^2 T}{\partial x^2}, \tag{7.82}$$

where

$$\lambda_x^m = \phi\lambda_{xf} + (1-\phi)\lambda_{xs}, \tag{7.83}$$

$$(c_p\rho)_m = \phi c_{pf}\rho_f + (1-\phi)c_{ps}\rho_s, \tag{7.84}$$

$$\alpha = \frac{c_{pf}\rho_f}{\phi c_{pf}\rho_f + (1-\phi)c_{ps}\rho_s}. \tag{7.85}$$

If the coefficients in front of the derivatives of Eq. (7.82) are constant, the analytical solution for this partial differential equation with a unit constant temperature at the origin of the global coordinate system can be expressed as follows (Carslaw and Jaeger 1959):

$$T(x,t) = \sqrt{\frac{(c_p\rho)_m}{4\pi\lambda_x^m t}} \exp\left[-\frac{(c_p\rho)_m(x-\alpha V_x t)^2}{4\lambda_x^m t}\right]. \tag{7.86}$$

For a transient infinite element shown in Fig. 7.5, the global coordinate of node 1 is x_1, while the local coordinate of this node is zero. To express the relationship between the positive direction of the x axis and that of the ξ axis, node 2 is defined for this transient infinite element. It is assumed that the global coordinate of node 2 is x_2 and that the local coordinate is 1. The temperature of node 1 at a given time, t, can be expressed as follows:

$$T(x_1,t) = \sqrt{\frac{(c_p\rho)_m}{4\pi\lambda_x^m t}} \exp\left[-\frac{(c_p\rho)_m(x_1-\alpha V_x t)^2}{4\lambda_x^m t}\right]. \tag{7.87}$$

For any point within this transient infinite element, taking $x = x_1 + \Delta x$ as an example, the corresponding temperature at this point can be written below:

$$T(x_1+\Delta x,t) = T(x_1,t)\exp\left\{-\frac{(c_p\rho)_m[\Delta x^2 + 2\Delta x(x_1-\alpha V_x t)]}{4\lambda_x^m t}\right\}. \tag{7.88}$$

Because $\xi = \Delta x$ for this one-dimensional transient infinite element, the heat transfer function of this transient infinite element can be expressed as follows:

$$F_{ht}(\xi,t) = \exp\left\{-\frac{(c_p\rho)_m[\xi^2 + 2\xi(x_1-\alpha V_x t)]}{4\lambda_x^m t}\right\}. \tag{7.89}$$

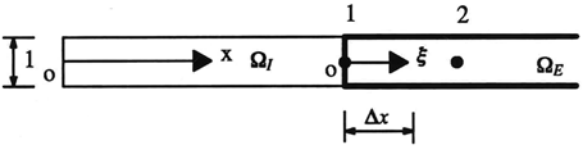

Fig. 7.5 A one-dimensional mapped transient infinite element for simulating transient heat transfer problems

7.2.2 Derivation of the Property Matrices of Two-Dimensional Transient Infinite Elements for Simulating Heat Transfer Problems

Following the same procedures as those used in the previous section, the property matrices of the transient two-dimensional infinite elements for simulating heat transfer problems can be derived in a mathematical manner. Supposing the principal heat conduction directions of an orthotropic porous medium are parallel to the x and y axes in a global Cartesian coordinate system, the governing equation of a heat transfer problem in a uniform pore-fluid flow field (Nield and Bejan 1992; Zhao and Valliappan 1993h) can be expressed as follows:

$$(c_p\rho)_m\frac{\partial T}{\partial t}+\alpha(c_p\rho)_m V_x\frac{\partial T}{\partial x}+\alpha(c_p\rho)_m V_y\frac{\partial T}{\partial y}=\lambda_x^m\frac{\partial^2 T}{\partial x^2}+\lambda_y^m\frac{\partial^2 T}{\partial y^2}, \tag{7.90}$$

where

$$\lambda_x^m=\phi\lambda_{xf}+(1-\phi)\lambda_{xs}, \tag{7.91}$$

$$\lambda_y^m=\phi\lambda_{yf}+(1-\phi)\lambda_{ys}, \tag{7.92}$$

$$(c_p\rho)_m=\phi c_{pf}\rho_f+(1-\phi)c_{ps}\rho_s, \tag{7.93}$$

$$\alpha=\frac{c_{pf}\rho_f}{\phi c_{pf}\rho_f+(1-\phi)c_{ps}\rho_s}, \tag{7.94}$$

where c_{pf} and c_{ps} are the specific heats for the pore-fluid and solid matrix; ρ_f and ρ_s are the densities of the pore-fluid and solid matrix; λ_{xf} and λ_{xs} are the thermal conductivities of the pore-fluid and solid matrix in the x direction; λ_{yf} and λ_{ys} are the thermal conductivities of the pore-fluid and solid matrix in the y direction, respectively; ϕ is the porosity of the porous medium; V_x and V_y are the Darcy velocities in the x and y directions; T is the temperature of the porous medium.

Using the Galerkin weighted residual method (Zienkiewicz 1977; Rao 1989), Eq. (7.90) can be discretized into a set of algebraic equations as follows:

$$[\hat{G}]\{T\}+[\hat{H}]\{T\}+[\hat{R}]\left\{\frac{\partial T}{\partial t}\right\}=\left\{\hat{f}\right\}, \tag{7.95}$$

where $\{T\}$ is the global nodal temperature vector of the system; $\left\{\hat{f}\right\}$ is the global nodal "load" vector of the system; $[\hat{G}]$, $[\hat{H}]$ and $[\hat{R}]$ are the global property matrices of the system. These global property matrices can be formed by assembling the following element property matrices:

$$[\hat{G}_e]_1 = \iint_A \left(\frac{\lambda_x^m}{(c_p\rho)_m} \frac{\partial[\hat{N}]^T}{\partial x} \frac{\partial[\hat{N}]}{\partial x} + \frac{\lambda_y^m}{(c_p\rho)_m} \frac{\partial[\hat{N}]^T}{\partial y} \frac{\partial[\hat{N}]}{\partial y} \right) dA, \tag{7.96}$$

$$[\hat{H}_e]_1 = \iint_A \left(\alpha V_x [\hat{N}]^T \frac{\partial[\hat{N}]}{\partial x} + \alpha V_y [\hat{N}]^T \frac{\partial[\hat{N}]}{\partial y} \right) dA, \tag{7.97}$$

$$[\hat{R}_e]_1 = \iint_A \left([\hat{N}]^T [\hat{N}] \right) dA, \tag{7.98}$$

where $[\hat{N}]$ is the temperature shape function of the element; $[\hat{N}]^T$ is the transpose of $[\hat{N}]$; A is the area of the element. It needs to be pointed out that Eqs. (7.96), (7.97) and (7.98) hold for both finite elements and transient infinite elements for simulating heat transfer problems in fluid-saturated porous media.

Using the heat transfer functions of transient infinite elements, the temperature shape function matrix of a two-dimensional transient infinite element can be derived. Figure 7.6 shows a two-dimensional four-node transient infinite element, for which the mapping relationship between the global coordinate system and the local one can be expressed as follows:

$$x = \sum_{i=1}^{4} M_i x_i, \tag{7.99}$$

$$y = \sum_{i=1}^{4} M_i y_i, \tag{7.100}$$

where M_i is the mapping function at each node of the element.

$$M_1 = \frac{1}{2}(1-\xi)(1-\eta), \tag{7.101}$$

$$M_2 = \frac{1}{2}(1-\xi)(1+\eta), \tag{7.102}$$

$$M_3 = \frac{1}{2}\xi(1+\eta), \tag{7.103}$$

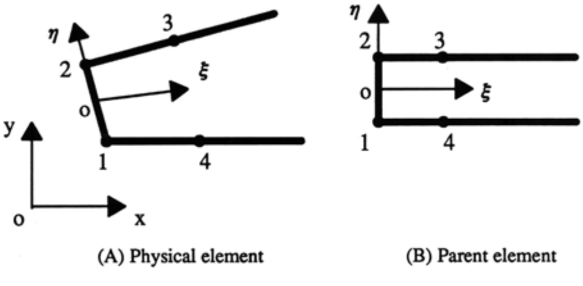

Fig. 7.6 Two-dimensional mapped transient uni-infinite elements

$$M_4 = \frac{1}{2}\xi(1-\eta). \tag{7.104}$$

The temperature field within the two-dimensional transient infinite element shown in Fig. 7.6 can be defined as follows:

$$T = \sum_{i=1}^{2} \hat{N}_i T_i = [\hat{N}] \begin{Bmatrix} T_1 \\ T_2 \end{Bmatrix}, \tag{7.105}$$

where $\hat{N}_1$ and $\hat{N}_2$ are the shape functions of nodes 1 and 2, respectively.

$$\hat{N}_1 = \frac{1}{2}F_{ht}(\xi, t)(1-\eta), \tag{7.106}$$

$$\hat{N}_2 = \frac{1}{2}F_{ht}(\xi, t)(1+\eta). \tag{7.107}$$

Since the number of nodes used for defining the shape of the two-dimensional transient infinite element is greater than that used for defining the temperature field of the two-dimensional transient infinite element, the corresponding parent transient infinite element is a superparametric element.

Substituting Eqs. (7.99), (7.100), (7.101) and (7.102) into Eqs. (7.96), (7.97) and (7.98) yields the property matrices of this two-dimensional transient infinite element as follows:

$$[\hat{G}_e]_1 = \int_0^\infty \int_{-1}^1 \left(\frac{\lambda_x^m}{(c_p\rho)_m} \frac{\partial [\hat{N}]^T}{\partial x} \frac{\partial [\hat{N}]}{\partial x} + \frac{\lambda_y^m}{(c_p\rho)_m} \frac{\partial [\hat{N}]^T}{\partial y} \frac{\partial [\hat{N}]}{\partial y} \right) |J| \, d\eta d\xi, \tag{7.108}$$

$$[\hat{H}_e]_1 = \int_0^\infty \int_{-1}^1 \left(\alpha V_x [\hat{N}]^T \frac{\partial [\hat{N}]}{\partial x} + \alpha V_y [\hat{N}]^T \frac{\partial [\hat{N}]}{\partial y} \right) |J| \, d\eta d\xi, \tag{7.109}$$

$$[\hat{R}_e]_1 = \int_0^\infty \int_{-1}^1 \left([\hat{N}]^T [\hat{N}] \right) |J| \, d\eta d\xi, \tag{7.110}$$

where $|J|$ is the Jacobian determinant of the two-dimensional transient infinite element.

By using the variable substitution technique and letting $\xi = (1+\beta)/(1-\beta)$, Eqs. (7.108), (7.109) and (7.110) can be rewritten into the following forms:

$$[\hat{G}_e]_1 = \int_{-1}^1 \int_{-1}^1 \left(\frac{\lambda_x^m}{(c_p\rho)_m} \frac{\partial [\hat{N}]^T}{\partial x} \frac{\partial [\hat{N}]}{\partial x} + \frac{\lambda_y^m}{(c_p\rho)_m} \frac{\partial [\hat{N}]^T}{\partial y} \frac{\partial [\hat{N}]}{\partial y} \right) \frac{2}{(\beta-1)^2} |J| \, d\eta d\beta, \tag{7.111}$$

$$[\hat{H}_e]_1 = \int_{-1}^1 \int_{-1}^1 \left(\alpha V_x [\hat{N}]^T \frac{\partial [\hat{N}]}{\partial x} + \alpha V_y [\hat{N}]^T \frac{\partial [\hat{N}]}{\partial y} \right) \frac{2}{(\beta-1)^2} |J| \, d\eta d\beta, \tag{7.112}$$

$$[\hat{R}_e]_1 = \int_{-1}^{1}\int_{-1}^{1}\left([\hat{N}]^T[\hat{N}]\right)\frac{2}{(\beta-1)^2}\,|J|\,d\eta d\beta. \tag{7.113}$$

Equations (7.111), (7.112) and (7.113) indicate that the property matrices of the two-dimensional transient infinite element can be evaluated using the Gauss–Legendre integration scheme.

It is noted that under certain situations, a two-dimensional three-node transient bi-infinite element, as shown in Fig. 7.7, can be useful for the numerical analysis. Similarly, the mapping relationship of this two-dimensional three-node transient bi-infinite element can be defined as follows:

$$x = \sum_{i=1}^{3} M_i x_i, \tag{7.114}$$

$$y = \sum_{i=1}^{3} M_i y_i, \tag{7.115}$$

where M_i is the mapping function at each node of the two-dimensional three-node transient bi-infinite element.

$$M_1 = (1-\xi)(1-\eta), \tag{7.116}$$

$$M_2 = \frac{1}{2}\xi(1+\eta), \tag{7.117}$$

$$M_3 = \frac{1}{2}(1+\xi)\eta. \tag{7.118}$$

The temperature shape function for this two-dimensional three-node transient bi-infinite element can be expressed as follows:

$$[\hat{N}] = [\hat{N}_1] = [F_{ht}(\xi,t)F_{ht}(\eta,t)]. \tag{7.119}$$

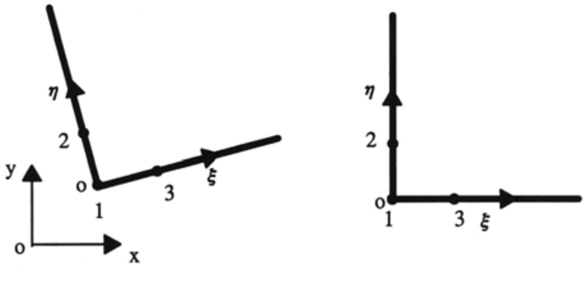

(A) Physical element

(B) Parent element

Fig. 7.7 Two-dimensional mapped transient bi-infinite elements

Finally, the property matrices of the two-dimensional three-node transient bi-infinite element can be derived.

$$[\hat{G}_e]_2 = \int_{-1}^{1}\int_{-1}^{1}\left(\frac{\lambda_x^m}{(c_p\rho)_m}\frac{\partial[\hat{N}]^T}{\partial x}\frac{\partial[\hat{N}]}{\partial x}+\frac{\lambda_y^m}{(c_p\rho)_m}\frac{\partial[\hat{N}]^T}{\partial y}\frac{\partial[\hat{N}]}{\partial y}\right) \times \frac{4}{(\beta-1)^2(\gamma-1)^2}\,|J|\,d\gamma d\beta, \tag{7.120}$$

$$[\hat{H}_e]_2 = \int_{-1}^{1}\int_{-1}^{1}\left(\alpha V_x[\hat{N}]^T\frac{\partial[\hat{N}]}{\partial x}+\alpha V_y[\hat{N}]^T\frac{\partial[\hat{N}]}{\partial y}\right)\frac{4}{(\beta-1)^2(\gamma-1)^2}\,|J|\,d\gamma d\beta, \tag{7.121}$$

$$[\hat{R}_e]_2 = \int_{-1}^{1}\int_{-1}^{1}\left([\hat{N}]^T[\hat{N}]\right)\frac{2}{(\beta-1)^2(\gamma-1)^2}\,|J|\,d\gamma d\beta, \tag{7.122}$$

7.3 Verification of Transient Infinite Elements for Simulating Pore-Fluid Flow and Heat Transfer Problems in Fluid-Saturated Porous Media of Infinite Domains

7.3.1 Verification of Transient Infinite Elements for Simulating a Pore-Fluid Flow Problem in the Fluid-Saturated Porous Medium of an Infinite Domain

The correctness and usefulness of the proposed transient infinite element theory can be verified by some simple but critical problems, for which the exact analytical solutions are already available. To examine the two-dimensional behaviour of the proposed transient infinite element theory, a fundamental problem with a given hydraulic head at the centre of a horizontal infinite plane is considered in this subsection. Figure 7.8 shows the discretized model of this problem, where the origin of the global coordinate system is subjected to a given point hydraulic head with the value of 10 m (i.e. $h_0 = 10\,\text{m}$) at $t = 0$. The near field of the system, which is chosen as $80 \times 80\,\text{m}$, has been simulated by two-dimensional four-node square finite elements, while the far field is simulated by eight categories of two-dimensional transient infinite elements as proposed in Sect. 7.1. The following parameters are used in the numerical analysis: the specific storage of the porous medium is $10^{-6}(1/\text{m})$; the hydraulic conductivities are $2 \times 10^{-6}\text{m/day}$ in the x and y directions; the time step used in the computation is 10 days.

Figure 7.9 shows the comparison between the current numerical solutions and the analytical ones (Lardner and Song 1991). In this figure, the dimensionless hydraulic head distributions in the near field of the first quadrant of the global coordinate system, namely in the region of $40\,\text{m} \geq x \geq 0$ and $40\,\text{m} \geq y \geq 0$, have been

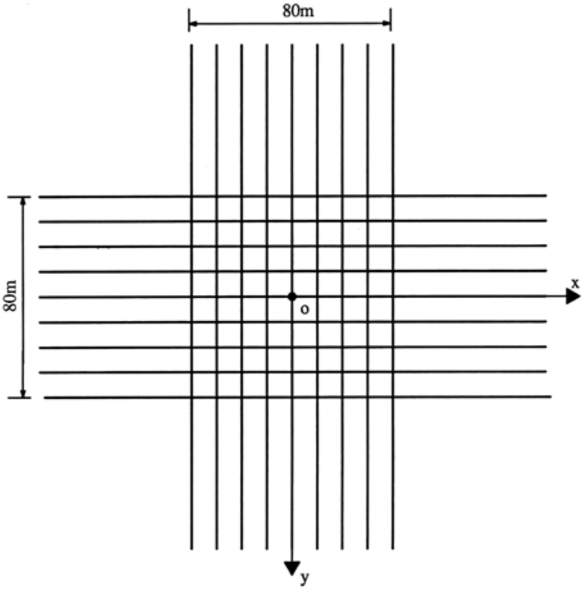

Fig. 7.8 Computational model for simulating a transient pore-fluid flow problem in the fluid-saturated porous medium of an infinite domain: the near field is simulated using 64 finite elements, while the far field is simulated using 36 transient infinite elements.

displayed at three different time instants. From the numerical solutions shown in Fig. 7.9, it can be observed that excellent coincidence exists between the current numerical results with the analytical solutions, even though the near field simulated by finite elements is very small. This demonstrates that the proposed transient infinite element theory is very useful for the numerical simulation of transient pore-fluid flow problems in fluid-saturated porous media of infinite domains.

7.3.2 *Verification of Transient Infinite Elements for Simulating a Heat Transfer Problem in the Fluid-Saturated Porous Medium of an Infinite Domain*

In this case, a fundamental problem with a given point temperature at the centre of a horizontal infinite plane is considered. As shown in Fig. 7.10, the origin of the global coordinate system is subjected to a unit point temperature, $T_0 = \delta(t)\delta(x)\delta(y)$. The computation domain is divided into an interior domain that is referred to as the near field of the system and an exterior domain that is considered as the far field of the system. The region of the near field is chosen as $80 \times 80\,\text{m}$ and simulated by 64 two-dimensional finite elements, while the far field is simulated by 32 two-dimensional transient infinite elements and 4 two-dimensional transient bi-infinite elements as proposed in Sect. 7.2. Supposing the porous medium is made of clay, the following parameters are used in the numerical analysis: the equivalent product of specific heat and density (i.e. $(c_p\rho)_m$) of the porous medium is $396\,\text{kcal}/(\text{m}^3\cdot℃)$; the

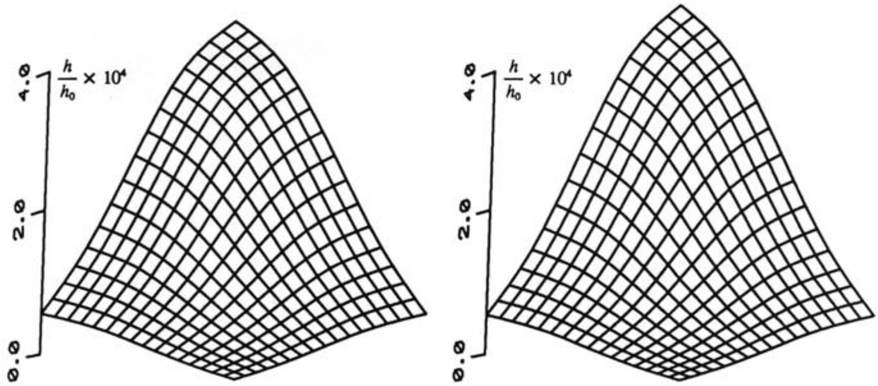

(Numerical solution) (Analytical solution)

(t=100days)

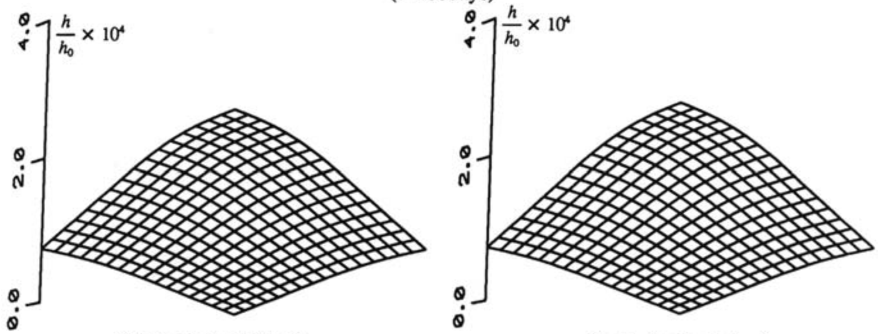

(Numerical solution) (Analytical solution)

(t=200days)

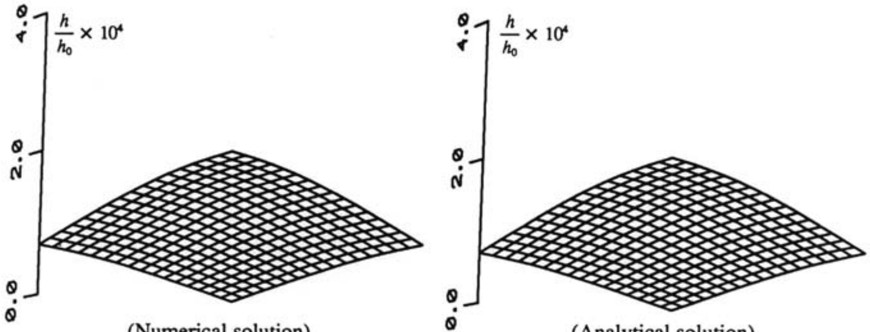

(Numerical solution) (Analytical solution)

(t=300days)

Fig. 7.9 Comparisons of numerical simulation results with analytical solutions for the transient pore-fluid flow problem

thermal conductivity coefficients of the porous medium are 25.92 kcal/(m · day ·° C) in both the x and y directions. It is assumed that no pore-fluid flow occurs in the porous medium so that $V_x = 0$ and $V_y = 0$. The time step used in the computation is 300 days.

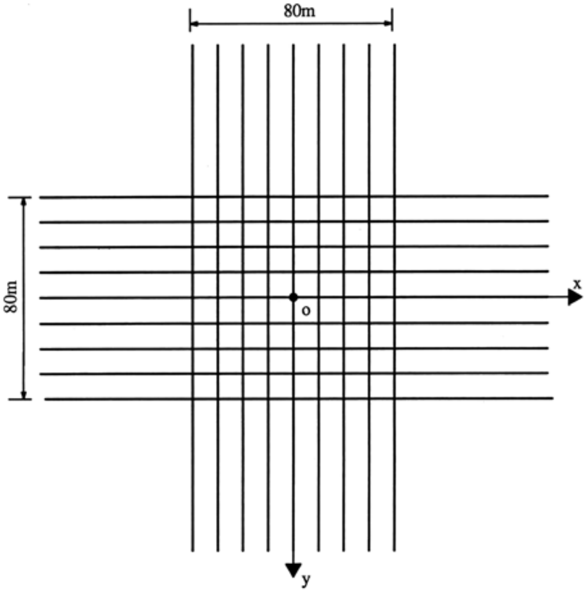

Fig. 7.10 The verification example for simulating a transient heat transfer problem in the fluid-saturated porous medium of an infinite domain: the near field is simulated using 64 finite elements, while the far field is simulated using 36 transient infinite elements

Figure 7.11 shows the comparison between the current numerical solutions and the previous analytical ones (Lardner and Song 1991). It is clear from these results that although the maximum time to be considered in the numerical analysis is 15000 days, there is no evidence that the temperature at any point is approaching a constant value. This indicates that the time-dependent effect is important for most transient heat transfer problems in fluid-saturated porous media. As expected, the symmetrical distribution of the temperature has been obtained at symmetrical locations of the system. For example, three locations, namely $x = 20$ m, $y = 0$ and $x = 0$, $y = 20$ m as well as $x =- 20$ m, $y = 0$, have the same temperature due to their symmetrical characteristics. It is also observed that even though the near field simulated by finite elements is very small, there exists excellent agreement between the current numerical results and the previous analytical solutions, except for a little oscillation at an early time. This oscillation is due to the rapid variation of temperature within a very short time and can be eliminated using a smaller time step in the computation. Therefore, it has demonstrated that the proposed transient infinite element theory is very useful for the numerical simulation of transient heat transfer problems in fluid-saturated porous media of infinite domains.

In summary, transient infinite element theory has been presented for simulating transient pore-fluid flow and heat transfer problems in fluid-saturated orthotropic porous media of infinite domains. Two different ways are used to derive the property matrices of transient infinite elements. In the first way, more different kinds of parent infinite elements with different shapes are used in the process of deriving the property matrices of transient infinite elements. In contrast, in the second way, only

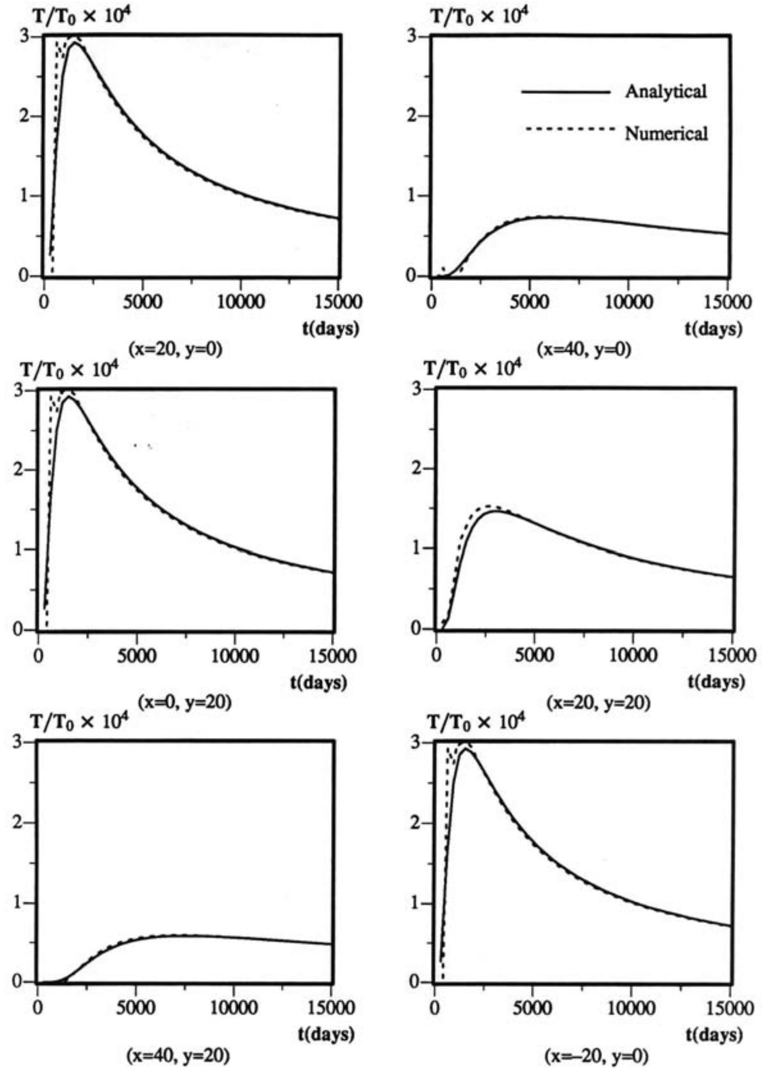

Fig. 7.11 Comparisons of numerical simulation results with analytical solutions for the transient heat transfer problem

two kinds of mapped parent infinite elements are used to derive the property matrices of transient infinite elements. Owing to this significant difference, the property matrices derived using the first way can be expressed in closed forms, but the property matrices derived using the second way need to be evaluated numerically. To demonstrate how to use these two different ways, the first way is used to derive the property matrices of two-dimensional transient infinite elements that can be employed to simulate transient pore-fluid flow problems in fluid-saturated orthotropic porous media of infinite domains, while the second way is employed to derive the property matrices of two-dimensional transient infinite elements, which can be used for simulating transient heat transfer problems in fluid-saturated orthotropic porous media of infinite domains.

Although the transient infinite element theory is presented on the basis of two-dimensional problems, it can be straightforwardly extended to the simulation of three-dimensional transient pore-fluid flow and heat transfer problems in fluid-saturated orthotropic porous media of infinite domains. In addition, the present transient infinite element theory can also be extended to the simulation of coupled problems of transient pore-fluid flow, mass transport and heat transfer in fluid-saturated orthotropic porous media of infinite extent. However, for a porous medium of general anisotropy, the formulation of two- and three-dimensional transient infinite elements remains unavailable so that future research is needed in this respect.

Chapter 8

Theory and Application of Transient Infinite Elements for Simulating Contaminant Transport Problems in Fractured Porous Media of Infinite Domains

Numerical simulation of contaminant transport in fractured porous media of infinite domains is a complex problem in various aspects. The solution for this kind of problem becomes more difficult once practical considerations, such as the infinite extension of the problem domain, the leakage effect between the porous medium and the fissured network, the characterization of the fissured network and other physical and chemical parameters, are appropriately included in the analysis (Rowe and Booker 1989, 1990a, 1991). On the other hand, the practical problems involving contaminant transport in fractured porous media have received rapidly increasing attention as a result of the treatment of industrial and agricultural wastes, the evaluation of potential contamination from nuclear power plants and the disposal activities of wastes from our daily lives. For the purpose of a better understanding of contaminant transport processes, it is imperative to develop an efficient and effective numerical method for simulating transient contaminant (i.e. mass in a general term) transport problems in fractured porous media of infinite domains.

Since a naturally fractured system contains various discontinuities, most of the immobile pore-fluid resides in low permeability, disjoint matrix blocks, while most of the mobile pore-fluid resides in the high permeability, interconnected fissured network. When contaminant transport takes place in such a system, both advection and dispersion are dominant processes within the fissured network, while dispersion may be a dominant process in the porous matrix. Generally, advection is due to the bulk movement of pore-fluid, which is caused by a pore-fluid pressure gradient, according to Darcy's law (Phillips 1991; Nield and Bejan 1992; Zhao et al. 1997, 1998, 1999a). Dispersion is due to the irregular movement of pore-fluid in a porous medium (Bear 1972; Bear and Bachmat 1990). On the microscopic scale (i.e. the pore scale), these irregularities are caused by the tortuosity of flow paths, while on the macroscopic scale, they are caused by the presence of zones of different permeabilities. To simulate a naturally fractured system appropriately, the double porosity model (Barenblatt et al. 1960; Duguid and Lee 1977; Valliappan and Naghadah 1990) may be the best choice because it bridges the gap between equivalent porous media and discrete fracture theory. For the double porosity model, the porous block and fissured network are viewed as two overlapping continua. Equations of mass

C. Zhao, *Dynamic and Transient Infinite Elements*, Advances in Geophysical and Environmental Mechanics and Mathematics, DOI 10.1007/978-3-642-00846-7_8,

transport for each continuum can be linked by a leakage term that describes the mass exchange between the two overlapping continua.

In terms of modelling an infinite medium, the coupled computational method of finite elements and infinite elements (Bettess 1977, 1980, 1992; Chow and Smith 1981; Medina and Taylor 1983; Zhao et al. 1987, 1989, 1992, 1995; Zhao and Valliappan 1991, 1993a, b, c, d, e) is more appropriate because of the following two main reasons: (1) both geometrical irregularities and material complexities in the near field of a system can be simulated using finite elements; and (2) the infinite extension of the system can be effectively and efficiently simulated using infinite elements. For simulating static and dynamic problems, both static and dynamic infinite elements have been developed during the past few decades (Beer and Meek 1981; Zhang and Zhao 1987; Valliappan and Zhao 1992; Zhao et al. 1991, 1992). Since the displacement decay function and wave propagation function are independent of time, both static and dynamic infinite elements can be considered as time-independent infinite elements. For simulating transient pore-fluid flow, heat transfer and mass transport in fluid-saturated porous media of infinite domains, Zhao and Valliappan (1993g, h, 1994a) developed transient infinite elements, in which a time variable is explicitly considered.

In this chapter, two-dimensional mapped transient infinite elements are presented for simulating contaminant transport problems in fractured porous media of infinite domains. To investigate the coupling effect between porous blocks and fissured networks, various parameters, such as contaminant transmissive coefficients between porous blocks and fissured networks, porosities, dispersion coefficients and pore-fluid velocities, are considered in the coupled computational model of finite elements and transient infinite elements. Since the mass transport function of the transient infinite element explicitly depends on both time and space variables, transient contaminant transport processes can be rigorously simulated using the coupled computational model of finite elements and transient infinite elements for simulating fractured porous media of infinite domains.

8.1 Coupled Computational Method of Finite Elements and Transient Infinite Elements for Simulating Transient Contaminant Transport Problems in Fractured Porous Media of Infinite Domains

If advection plays a predominant role in a mass transport problem, the conventional Galerkin finite element method fails in solving the problem so that the resulting solution exhibits pronounced oscillatory behaviour and excessive numerical dispersion. Although a drastic refinement of the finite element mesh can be used to avoid such unwanted oscillatory behaviour and numerical dispersion, it is very inefficient, from the computational point of view. To overcome this problem, the upwind finite element scheme is usually used in the finite element analysis of advection-dominated mass transport problems (Heinrich et al. 1977;

Huyakorn 1977; Huyakorn and Nilkuha 1979). This scheme differs from the conventional Galerkin finite element scheme in the following two aspects: (1) spatial discretization is performed through a general weighted residual technique that employs asymmetrical weighting functions and yields an upwind weighting effect for the advection term of a mass transport equation; (2) the time derivative term of the mass transport equation is weighted using the standard trial functions of symmetrical nature. For this reason, the upwind finite element scheme is used to derive the related formulation for simulating contaminant transport problems in fractured porous media of infinite domains.

8.1.1 Upwind Finite Element Formulation of the Problem

Supposing the principal directions of a double porosity medium are parallel to those of the x and y axes in a global coordinate system, the governing equations of a contaminant transport problem in the double porosity medium with a uniform pore-fluid flow field can be expressed as follows (Barenblatt et al. 1960; Duguid and Lee 1977; Valliappan and Naghadah 1990; Zhao and Valliappan 1994b):

$$D_{1x}\frac{\partial^2 C_1}{\partial x^2}+D_{1y}\frac{\partial^2 C_1}{\partial y^2}-\overline{V}_{1x}\frac{\partial C_1}{\partial x}-\overline{V}_{1y}\frac{\partial C_1}{\partial y}=\frac{\partial C_1}{\partial t}+\frac{1}{\phi_1}\Gamma, \tag{8.1}$$

$$D_{2x}\frac{\partial^2 C_2}{\partial x^2}+D_{2y}\frac{\partial^2 C_2}{\partial y^2}-\overline{V}_{2x}\frac{\partial C_2}{\partial x}-\overline{V}_{2y}\frac{\partial C_2}{\partial y}=\frac{\partial C_2}{\partial t}-\frac{1}{\phi_2}\Gamma, \tag{8.2}$$

where D_{1x} and D_{1y} are the dispersion coefficients of contaminant for the porous block in the x and y directions; D_{2x} and D_{2y} are the dispersion coefficients of contaminant for the fissured network in the x and y directions; $\overline{V}_{1x}$ and $\overline{V}_{1y}$ are the average linear velocities, which are averaged by the pore space (Bear 1972), of the pore-fluid flow within the porous block in the x and y directions; $\overline{V}_{2x}$ and $\overline{V}_{2y}$ are the average linear velocities of the pore-fluid flow within the fissured network; C_1 and C_2 are the contaminant concentrations of the porous block and fissured network, respectively; Γ is a leakage term to express mass exchange between the porous block and the fissured network; ϕ_1 and ϕ_2 are the porosities of the porous block and fissured network.

From the mass conservation law, the leakage term, Γ, can be expressed as

$$\Gamma=\chi\left(\phi_1 C_1-\phi_2 C_2\right) sign\left(C_1-C_2\right) sign\left(\phi_1 C_1-\phi_2 C_2\right), \tag{8.3}$$

where χ is a transmissive coefficient expressing the contaminant concentration exchange per unit concentration between the porous block and the fissured network per unit time. It has a dimension of $1/s$. $\chi=0$ means that there is no exchange between the porous block and the fissured network, while $\chi=1$ means that maximum exchange takes place between the porous block and the fissured network.

Note that Eq. (8.3) always expresses the contaminant transmission from a high-concentration to a low-concentration region. For example, if the concentration in the porous block is greater than that in the fissured network, the contaminant will transmit from the porous block to the fissured network and vice versa. This process is guaranteed by the product of *sign* $(C_1 - C_2)$ and *sign* $(\phi_1 C_1 - \phi_2 C_2)$, even though the porosities of both the porous block and the fissured network are involved. To facilitate computation and to express the formulations concisely, the average contaminant concentrations of a finite element, $\overline{C}_1$ and $\overline{C}_2$, are used instead of C_1 and C_2 in Eq. (8.3). This leads to the following equation:

$$G\left(\overline{C}_1, \overline{C}_2, \phi_1, \phi_2\right) = sign\left(\overline{C}_1 - \overline{C}_2\right) sign\left(\phi_1 \overline{C}_1 - \phi_2 \overline{C}_2\right). \tag{8.4}$$

Equation (8.4) indicates that the value of function G is equal to 1, 0 or –1, depending on the values of $\overline{C}_1$, $\overline{C}_2$, ϕ_1 and ϕ_2.

8.1.1.1 Spatial Discretization of the Problem

In the upwind finite element scheme (Heinrich et al. 1977; Huyakorn 1977; Huyakorn and Nilkuha 1979), the dispersion and advection terms of the transient mass transport equations are weighted using asymmetrical weighting functions to avoid oscillatory solutions, while the time derivative term and transmissive term are weighted using conventional shape functions. Based on this idea, Eqs. (8.1) and (8.2) can be rewritten for an element as follows (Zhao and Valliappan 1994b):

$$\begin{aligned} &\iint_A [W]_1^T \left[D_{1x} \frac{\partial^2 C_1}{\partial x^2} + D_{1y} \frac{\partial^2 C_1}{\partial y^2} - \overline{V}_{1x} \frac{\partial C_1}{\partial x} - \overline{V}_{1y} \frac{\partial C_1}{\partial y} \right] dA \\ &\quad - \iint_A [N]^T \left[\frac{\partial C_1}{\partial t} + \frac{G}{\phi_1} \chi \left(\phi_1 C_1 - \phi_2 C_2 \right) \right] dA = 0 \end{aligned}, \tag{8.5}$$

$$\begin{aligned} &\iint_A [W]_2^T \left[D_{2x} \frac{\partial^2 C_2}{\partial x^2} + D_{2y} \frac{\partial^2 C_2}{\partial y^2} - \overline{V}_{2x} \frac{\partial C_2}{\partial x} - \overline{V}_{2y} \frac{\partial C_2}{\partial y} \right] dA \\ &\quad - \iint_A [N]^T \left[\frac{\partial C_2}{\partial t} - \frac{G}{\phi_2} \chi \left(\phi_1 C_1 - \phi_2 C_2 \right) \right] dA = 0 \end{aligned}, \tag{8.6}$$

where A is the area of the element; $[W]_1$ and $[W]_2$ are the non-symmetrical weighting function matrices of the element for the porous block and fissured network, respectively; C_1 and C_2 are the trial functions of the element for the porous block and fissured network. They can be expressed as the functions of nodal concentrations of the element in the finite element sense.

$$C_i = [N]\{C_i\}^e \qquad (i = 1, 2), \tag{8.7}$$

where $[N]$ is the conventional shape-function matrix of the element; $\{C_1\}^e$ and $\{C_2\}^e$ are the nodal concentration vectors of the element for the porous block and fissured network at a given time.

Through integrating by parts and applying Green's theorem to the second-order derivatives, Eqs. (8.5) and (8.6) can be written as follows:

$$\left([E_1]^e + [H_1]^e\right)\{C_1\}^e + \frac{G\chi}{\phi_1}[Q_1]^e\left(\phi_1[C_1]^e - \phi_2[C_2]^e\right) + [R_1]^e\left\{\frac{\partial C_1}{\partial t}\right\}^e = \{f_1\}^e, \tag{8.8}$$

$$\left([E_2]^e + [H_2]^e\right)\{C_2\}^e - \frac{G\chi}{\phi_2}[Q_2]^e\left(\phi_1[C_1]^e - \phi_2[C_2]^e\right) + [R_2]^e\left\{\frac{\partial C_2}{\partial t}\right\}^e = \{f_2\}^e, \tag{8.9}$$

where

$$[E_i]^e = \iint_A \left[D_{ix}\frac{\partial[W]_i^T}{\partial x}\frac{\partial[N]}{\partial x} + D_{iy}\frac{\partial[W]_i^T}{\partial y}\frac{\partial[N]}{\partial y}\right] dA \qquad (i = 1, 2), \tag{8.10}$$

$$[H_i]^e = \iint_A \left[\overline{V}_{ix}[W]_i^T\frac{\partial[N]}{\partial x} + \overline{V}_{iy}[W]_i^T\frac{\partial[N]}{\partial y}\right] dA \qquad (i = 1,2), \tag{8.11}$$

$$[Q_i]^e = \iint_A \left([N]^T[N]\right) dA \qquad (i = 1, 2), \tag{8.12}$$

$$[R_i]^e = \iint_A \left([N]^T[N]\right) dA \qquad (i = 1, 2), \tag{8.13}$$

$$\{f_i\}^e = \int_S [W]_i^T \left(D_{ix}\frac{\partial C_1}{\partial x}n_x + D_{iy}\frac{\partial C_2}{\partial y}n_y\right) dS \qquad (i = 1, 2), \tag{8.14}$$

where A is the area of the element; S is the boundary line of the element; n_x and n_y are the direction cosines of the outward unit normal vector on the boundary of the element.

Since Eqs. (8.10), (8.11), (8.12), (8.13) and (8.14) are equally valid for both finite and transient infinite elements, the corresponding global matrix can be obtained using the standard assembly procedure in the finite element method (Zienkiewicz 1977). As a result, the global matrix equations for the problem can be expressed as follows:

$$[A_1]\{C_1\} - \frac{G\chi\phi_2}{\phi_1}[Q_1]\{C_2\} + [R_1]\left\{\frac{\partial C_1}{\partial t}\right\} = \{f_1\}, \tag{8.15}$$

$$[A_2]\{C_2\} - \frac{G\chi\phi_1}{\phi_2}[Q_2]\{C_1\} + [R_2]\left\{\frac{\partial C_2}{\partial t}\right\} = \{f_2\}, \tag{8.16}$$

where

$$[A_1] = [E_1] + [H_1] + G\chi\,[Q_1], \tag{8.17}$$

$$[A_2] = [E_2] + [H_2] + G\chi\,[Q_2]. \tag{8.18}$$

Since Eqs. (8.15) and (8.16) are coupled by the exchange term, they are better written in the matrix form:

$$[A]\{C\} + [R]\left\{\frac{\partial C}{\partial t}\right\} = \{f\}, \tag{8.19}$$

where

$$[A] = \begin{bmatrix} [A_1] & -\frac{G\chi\phi_2}{\phi_1}[Q_1] \\ -\frac{G\chi\phi_1}{\phi_2}[Q_2] & [A_2] \end{bmatrix}, \tag{8.20}$$

$$[R] = \begin{bmatrix} [R_1] & 0 \\ 0 & [R_2] \end{bmatrix}, \tag{8.21}$$

$$\{C\} = \begin{Bmatrix} \{C_1\} \\ \{C_2\} \end{Bmatrix}, \tag{8.22}$$

$$\{f\} = \begin{Bmatrix} \{f_1\} \\ \{f_2\} \end{Bmatrix}. \tag{8.23}$$

Note that $[A]$ is an asymmetrical matrix due to the consideration of advective pore-fluid flow and the use of asymmetrical weighting functions in formulating the property matrices of the upwind finite element. On the other hand, since $[A]$ and $[R]$ are assembled by both finite elements and transient infinite elements, they are time-dependent matrices and need to be evaluated at any time of interest.

8.1.1.2 Temporal Discretization of the Problem

The solution of Eq. (8.19) in the time domain can be carried out using the finite difference approach for $\{\partial C/\partial t\}$ as follows:

$$\left\{\frac{\partial C}{\partial t}\right\} = \frac{1}{\Delta t}\left(\{C\}^{t+\Delta t} - \{C\}^{t}\right), \tag{8.24}$$

where the superscript represents the time level and Δt is the time step. In the process of solving transient contaminant transport problems using the upwind finite element scheme, both the element size, Δl, and the time step, Δt, need to be selected in such a way that the resulting value of the Courant number ($Cr = V_{\max}\Delta t/\Delta l$) is less than 2.

After the finite difference approach is used for the first derivative of contaminant concentration with respect to time, it is necessary to determine the time level in a time interval between t and $t + \Delta t$, at which the value of the contaminant concentration is evaluated. Generally, the nodal contaminant concentration vector, $\{C\}$, can be approximated anywhere between t and $t + \Delta t$.

$$\{C\} = (1-\alpha)\{C\}^{t} + \alpha\{C\}^{t+\Delta t}, \tag{8.25}$$

where $0 \le \alpha \le 1$. If $\alpha = 1$, the solution scheme is fully implicit, while if $\alpha = 0$, the solution scheme is fully explicit. If $\{C\}$ is approximated at a time, $t + (\Delta t/2)$, Eq. (8.19) can be rewritten as follows:

$$\left(\frac{1}{2}[A] + \frac{1}{\Delta t}[R]\right)\{C\}^{t+\Delta t} = \left(\frac{1}{\Delta t}[R] - \frac{1}{2}[A]\right)\{C\}^{t} + \{f\}^{t+(\Delta t/2)}. \qquad (8.26)$$

8.1.1.3 Weighting and Shape Functions of the Upwind Finite Element

For a two-dimensional four-node finite element shown in Fig. 8.1, the conventional shape function of the element is well known (Zienkiewicz 1977). The asymmetrical weighting functions for each node of the element can be expressed by the following equations (Zhao and Valliappan 1994b; Zhao et al. 1994):

$$\begin{aligned} W_{1i} = \frac{1}{16}&\left[(1+\xi)\left(-3\overline{\alpha}_{2i}\xi + 3\overline{\alpha}_{2i} + 2\right)\right] \\ &\left[(1+\eta)\left(-3\overline{\beta}_{1i}\eta + 3\overline{\beta}_{1i} + 2\right)\right] \qquad (i = 1,2), \end{aligned} \qquad (8.27)$$

$$\begin{aligned} W_{2i} = \frac{1}{16}&\left[(1+\xi)\left(3\overline{\alpha}_{2i}\xi - 3\overline{\alpha}_{2i} - 2\right) + 4\right] \\ &\left[(1+\eta)\left(-3\overline{\beta}_{2i}\eta + 3\overline{\beta}_{2i} + 2\right)\right] \qquad (i = 1,2), \end{aligned} \qquad (8.28)$$

$$\begin{aligned} W_{3i} = \frac{1}{16}&\left[(1+\xi)\left(3\overline{\alpha}_{1i}\xi - 3\overline{\alpha}_{1i} - 2\right) + 4\right] \\ &\left[(1+\eta)\left(3\overline{\beta}_{2i}\eta - 3\overline{\beta}_{2i} - 2\right) + 4\right] \qquad (i = 1,2), \end{aligned} \qquad (8.29)$$

$$\begin{aligned} W_{4i} = \frac{1}{16}&\left[(1+\xi)\left(-3\overline{\alpha}_{1i}\xi + 3\overline{\alpha}_{1i} + 2\right)\right] \\ &\left[(1+\eta)\left(3\overline{\beta}_{1i}\eta - 3\overline{\beta}_{1i} - 2\right) + 4\right] \qquad (i = 1,2), \end{aligned} \qquad (8.30)$$

where W_{11}, W_{21}, W_{31} and W_{41} are the weighting functions of nodes 1, 2, 3 and 4 of the element for the porous block; W_{12}, W_{22}, W_{32} and W_{42} are the weighting functions of nodes 1, 2, 3 and 4 of the element for the fissured network; ξ and η

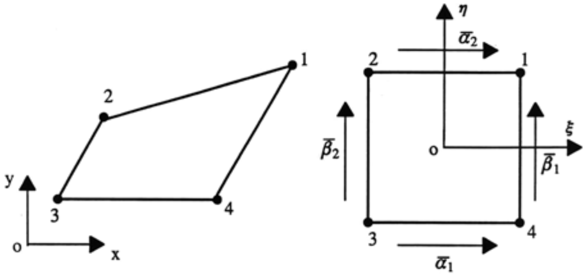

Fig. 8.1 Definition of a four-node upwind finite element

are the local isoparametric coordinates of the element; $\overline{\alpha}_{11}$, $\overline{\beta}_{11}$, $\overline{\alpha}_{21}$ and $\overline{\beta}_{21}$ are the upwind parameters corresponding with sides 3-4, 4-1, 2-1 and 3-2 of the element for the porous block; $\overline{\alpha}_{12}$, $\overline{\beta}_{12}$, $\overline{\alpha}_{22}$ and $\overline{\beta}_{22}$ are the upwind parameters corresponding with sides 3-4, 4-1, 2-1 and 3-2 of the element for the fissured network.

For the upwind finite element scheme, the signs of these upwind parameters depend on the signs of the average pore-fluid flow velocities of the element sides, representing the advective flow direction associated with the contaminant transport process in the fractured porous medium. For this reason, these upwind parameters are expressed as

$$\overline{\alpha}_{ij} = \alpha_{ij}^{opt} sign\left(\overline{V}_j\right) \qquad (i = 1, 2; j = 1, 2), \tag{8.31}$$

$$\overline{\beta}_{ij} = \beta_{ij}^{opt} sign\left(\overline{V}_j\right) \qquad (i = 1, 2; j = 1, 2), \tag{8.32}$$

where α_{ij}^{opt} and β_{ij}^{opt} $(i = 1, 2; j = 1, 2)$ are the optimal values of the upwind parameters for the related element sides; $\overline{V}_1$ is the corresponding average speed of pore-fluid flow along the element side for the porous block; $\overline{V}_2$ is the corresponding average speed of pore-fluid flow along the element side for the fissured network; $\overline{V}_1$ and $\overline{V}_2$ can be determined using the following formulas:

$$\overline{V}_1 = \frac{1}{2}\left(\vec{V}_{1p} + \vec{V}_{1q}\right) \bullet \vec{I}_{pq}, \tag{8.33}$$

$$\overline{V}_2 = \frac{1}{2}\left(\vec{V}_{2p} + \vec{V}_{2q}\right) \bullet \vec{I}_{pq}, \tag{8.34}$$

where p and q are the node numbers of an element side; $\vec{V}_{1p}$ and $\vec{V}_{1q}$ are the velocity vectors of nodes p and q of the element for the porous block; $\vec{V}_{2p}$ and $\vec{V}_{2q}$ are the velocity vectors of nodes p and q of the element for the fissured network; $\vec{I}_{pq}$ is the direction vector of the element side in the local coordinate system with the same positive direction as that of the local coordinate system of the element.

The optimal values of upwind parameters depend on the Courant number of the element side and can be determined using the following equations (Huyakorn and Nilkuha 1979; Zhao et al. 1994):

$$\alpha_{ij}^{opt} = \coth\left(\frac{\left|\overline{V}_j\right| \Delta l}{2D_{ix}}\right) - \frac{2D_{ix}}{\left|\overline{V}_j\right| \Delta l} \qquad (i = 1, 2; j = 1, 2), \tag{8.35}$$

$$\beta_{ij}^{opt} = \coth\left(\frac{\left|\overline{V}_j\right| \Delta l}{2D_{iy}}\right) - \frac{2D_{iy}}{\left|\overline{V}_j\right| \Delta l} \qquad (i = 1, 2; j = 1, 2), \tag{8.36}$$

where coth stands for the hyperbolic cotangent function; Δl is the characteristic length of the element.

To obtain satisfactory solutions, the derivatives, $\partial W_{ij} \big/ \partial \xi$ and $\partial W_{ij} \big/ \partial \eta$ $(i = 1, 2, 3, 4; j = 1, 2)$, of the element need to be evaluated in such a way that when differentiation is taken with respect to one particular coordinate variable, the values of the upwind parameters along the remaining coordinate variables must be set to zero. Thus, the derivatives of the upwind weighting functions of the element can be expressed as follows:

$$\frac{\partial W_{1i}}{\partial \xi} = -\frac{1}{4}(1+\eta)\,(3\overline{\alpha}_{2i}\xi - 1) \qquad (i = 1,2), \tag{8.37}$$

$$\frac{\partial W_{2i}}{\partial \xi} = \frac{1}{4}(1+\eta)\,(3\overline{\alpha}_{2i}\xi - 1) \qquad (i = 1,2), \tag{8.38}$$

$$\frac{\partial W_{3i}}{\partial \xi} = \frac{1}{4}(1-\eta)\,(3\overline{\alpha}_{1i}\xi - 1) \qquad (i = 1,2), \tag{8.39}$$

$$\frac{\partial W_{4i}}{\partial \xi} = -\frac{1}{4}(1-\eta)\,(3\overline{\alpha}_{1i}\xi - 1) \qquad (i = 1,2), \tag{8.40}$$

$$\frac{\partial W_{1i}}{\partial \eta} = -\frac{1}{4}(1+\xi)\left(3\overline{\beta}_{1i}\eta - 1\right) \qquad (i = 1,2), \tag{8.41}$$

$$\frac{\partial W_{2i}}{\partial \eta} = -\frac{1}{4}(1-\xi)\left(3\overline{\beta}_{2i}\eta - 1\right) \qquad (i = 1,2), \tag{8.42}$$

$$\frac{\partial W_{3i}}{\partial \eta} = \frac{1}{4}(1-\xi)\left(3\overline{\beta}_{2i}\eta - 1\right) \qquad (i = 1,2), \tag{8.43}$$

$$\frac{\partial W_{4i}}{\partial \eta} = \frac{1}{4}(1+\xi)\left(3\overline{\beta}_{1i}\eta - 1\right) \qquad (i = 1,2). \tag{8.44}$$

If the conventional mapping technique for isoparametric elements is used, substituting the asymmetrical upwind weighting functions and conventional shape functions of the element into Eqs. (8.10), (8.11), (8.12) and (8.13) yields the following property matrices of the proposed upwind finite element for simulating transient contaminant transport problems in double porosity media:

$$[E_i]^e = \int_{-1}^{1}\int_{-1}^{1}\left(D_{ix}\frac{\partial\,[W]_i^T}{\partial x}\frac{\partial\,[N]}{\partial x} + D_{iy}\frac{\partial\,[W]_i^T}{\partial y}\frac{\partial\,[N]}{\partial y}\right)|J|\,d\xi d\eta \;\; (i = 1,2), \tag{8.45}$$

$$[H_i]^e = \int_{-1}^{1}\int_{-1}^{1}\left(\overline{V}_{ix}\,[W]_i^T\,\frac{\partial\,[N]}{\partial x} + \overline{V}_{iy}\,[W]_i^T\,\frac{\partial\,[N]}{\partial y}\right)|J|\,d\xi d\eta \;\; (i = 1,2), \tag{8.46}$$

$$[Q_i]^e = \int_{-1}^{1}\int_{-1}^{1}\left([N]^T\,[N]\right)|J|\,d\xi d\eta \qquad (i = 1,2), \tag{8.47}$$

$$[R_i]^e = \int_{-1}^{1}\int_{-1}^{1}\left([N]^T\,[N]\right)|J|\,d\xi d\eta \qquad (i = 1,2), \tag{8.48}$$

where $|J|$ is the Jacobian determinant of the upwind finite element.

8.1.2 Fundamental Formulas of Mapped Transient Infinite Elements for Simulating Transient Contaminant Transport Problems

To illustrate the fundamental concept of transient infinite elements, a one-dimensional contaminant transport problem in a fluid-saturated porous medium of an infinite domain is considered in this subsection. Supposing that a unit point contaminant concentraction exists at $x = 0$ and a unidirectional pore-fluid flow is along the positive direction of the x axis, both advection and dispersion will take place from the origin of the x axis ($x = 0$) to the far field of the system. The governing equation for the resulting one-dimensional transient contaminant transport problem in a fluid-saturated porous medium can be expressed as

$$\frac{\partial C}{\partial t} = D_x \frac{\partial^2 C}{\partial x^2} - \overline{V}_x \frac{\partial C}{\partial x}, \tag{8.49}$$

where D_x is the dispersion coefficient of contaminant in the x direction; $\overline{V}_x$ is the average linear velocity of the unidirectional pore-fluid flow; C is the contaminant concentration in the fluid-saturated porous medium.

Since Eq. (8.49) is one-dimensional in space, the analytical solution for this equation with D_x and $\overline{V}_x$ constant and a given initial contaminant concentration at the origin of the global coordinate system is available (Ogata and Banks 1961).

$$C(x, t) = \frac{C_0}{\sqrt{4\pi D_x t}} \exp\left[-\frac{(x - \overline{V}_x t)^2}{4 D_x t}\right], \tag{8.50}$$

where C_0 is the concentration of the point contaminant source at the origin of the global coordinate system.

For a typical one-dimensional transient infinite element shown in Fig. 8.2, the global coordinate of node 1 is x_1 and the local coordinate of this node is identical to zero. The contaminant concentration at this node for a given time, t, can be expressed as follows:

$$C(x_1, t) = \frac{C_0}{\sqrt{4\pi D_x t}} \exp\left[-\frac{(x_1 - \overline{V}_x t)^2}{4 D_x t}\right]. \tag{8.51}$$

For any point within this one-dimensional transient infinite element, taking $x = x_1 + \Delta x$ as an example, the contaminant concentration of this point can be derived from Eq. (8.51).

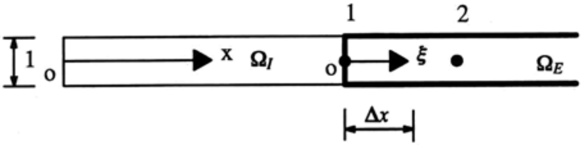

Fig. 8.2 One-dimensional mapped transient infinite elements

$$C(x_1 + \Delta x, t) = C(x_{1,} t) \exp \left[-\frac{\Delta x^2 + 2\Delta x(x_1 - \overline{V}_x t)}{4D_x t} \right]. \tag{8.52}$$

Considering the fact that $\xi = \Delta x$ for this one-dimensional transient infinite element, the mass transport function of this element can be expressed as

$$F_{mt}(\xi, t) = \exp \left[-\frac{\xi^2 + 2(x_1 - \overline{V}_x t)\xi}{4D_x t} \right]. \tag{8.52}$$

As a result, the contaminant concentration field within the one-dimensional transient infinite element can be expressed in the form:

$$C\,(\xi,t) = C_1 F_{mt}\,(\xi,t) = C_1 N_1, \tag{8.54}$$

where C_1 is the nodal contaminant concentration of the one-dimensional transient infinite element; C is the contaminant concentration within the one-dimensional transient infinite element; N_1 is the shape function of the one-dimensional transient infinite element. Note that the mass transport function of the transient infinite element is identical to the shape function for simulating one-dimensional transient contaminant transport problems.

Figures 8.3 and 8.4 show the distributions of the mass transport function for several cases. In these figures, $\overline{V}_x = 0$ and $\overline{V}_x = 0.1\,\mathrm{m\,d^{-1}}$ are considered to illustrate the effects of the pore-fluid flow velocity on the distribution of the mass transport function. Not only can both the dispersion coefficient and the pore-fluid flow velocity have considerable influences on the distribution of the mass transport function, but also the time in the analysis can have a significant effect on the distribution of the mass transport function of the transient infinite element. It is the explicit consideration of the effect of a time variable that determines the characteristic of the proposed transient infinite element. On the other hand, since the mass transport function of the transient infinite element explicitly depends on time, it can be concluded that the time effect should be considered in the process of constructing transient infinite elements for simulating various transient problems. Otherwise, errors in the corresponding numerical simulation will inevitably occur.

The above procedure, associated with the one-dimensional transient infinite element, can be extended to the construction of two-dimensional transient infinite elements for simulating transient contaminant transport problems in fractured porous media of infinite domains (Zhao and Valliappan 1994b). If the near field of an infinite domain system is appropriately chosen, the leakage effect between the porous block and the fissured network in the far field of the system may become negligible as a result of the term, $\phi_1 C_1 - \phi_2 C_2$ in Eq. (8.3), approaching zero. In this case, the mass transport functions of a transient infinite element can be expressed as

$$F_{1mt}(\xi,t) = \exp \left[-\frac{\xi^2 + 2(x_1 - \overline{V}_{1\xi} t)\xi}{4D_{1\xi} t} \right], \tag{8.55}$$

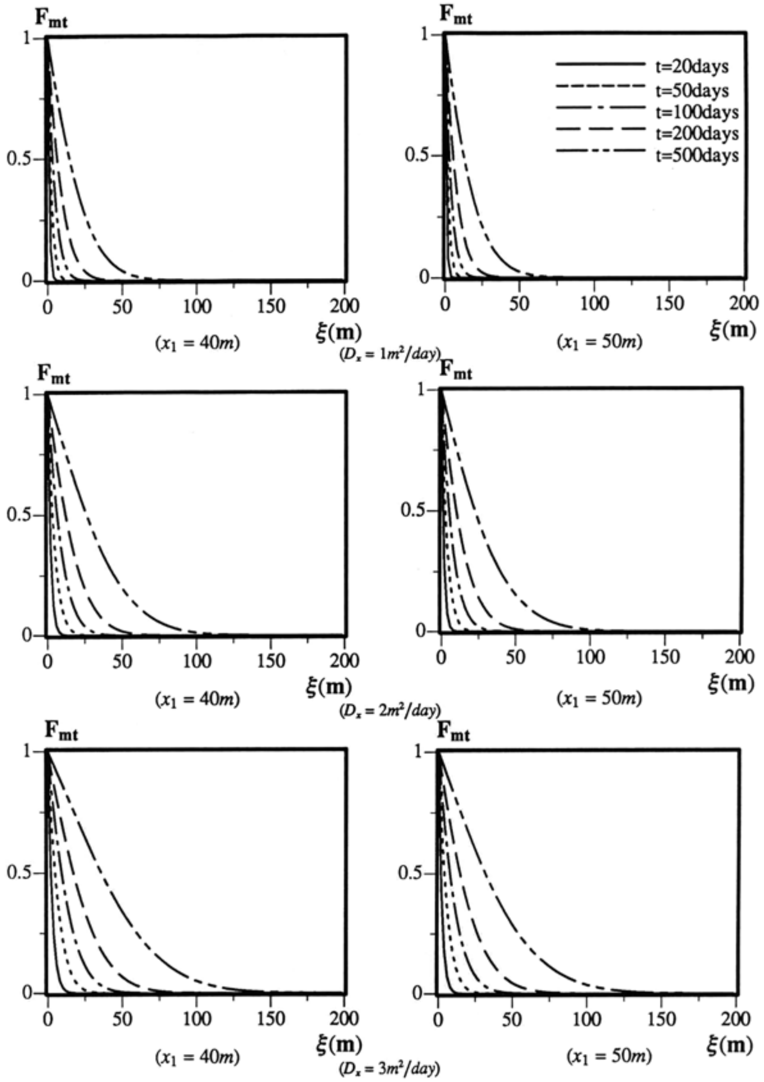

Fig. 8.3 Distributions of mass transport functions of the transient infinite element ($\overline{V}_x = 0$)

$$F_{2mt}(\xi,t) = \exp\left[-\frac{\xi^2 + 2(x_1 - \overline{V}_{2\xi}t)\xi}{4D_{2\xi}t}\right], \tag{8.56}$$

where F_{1mt} and F_{2mt} are the mass transport functions of the transient infinite element for the porous block and fissured network, respectively; $\overline{V}_{1\xi}$ and $\overline{V}_{2\xi}$ are the average linear pore-fluid flow velocities in the ξ direction of the local coordinate system; $D_{1\xi}$ and $D_{2\xi}$ are the dispersion coefficients in the ξ direction of the local coordinate system.

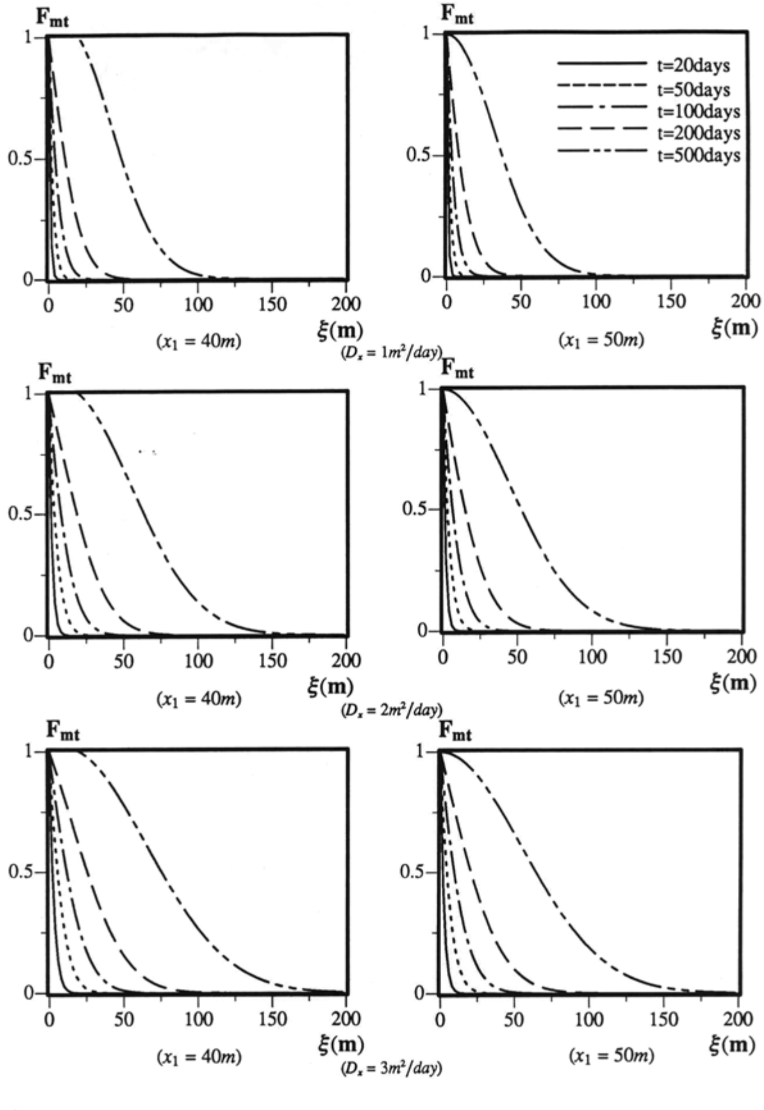

Fig. 8.4 Distributions of mass transport functions of the transient infinite element ($\overline{V}_x = 0.1\,\mathrm{m\,d^{-1}}$)

Based on the mass transport functions of transient infinite elements, the contaminant concentration shape function matrix of a two-dimensional transient infinite element can be derived (Zhao and Valliappan 1994b). Figure 8.5 shows a two-dimensional four-node transient infinite element, for which the mapping relationship between the global and local coordinate systems can be expressed as

$$x = \sum_{i=1}^{4} M_i x_i, \tag{8.57}$$

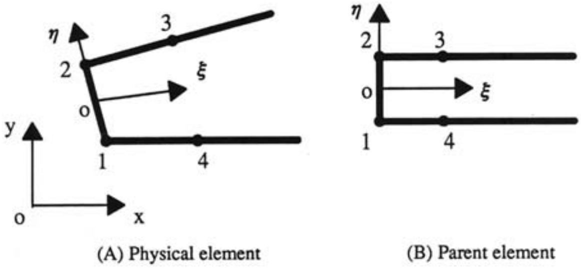

(A) Physical element

(B) Parent element

Fig. 8.5 Two-dimensional mapped transient infinite elements

$$y = \sum_{i=1}^{4} M_i y_i, \tag{8.58}$$

where M_i is the mapping function at each node of the element, viz.,

$$M_1 = \frac{1}{2}(1-\xi)(1-\eta), \tag{8.59}$$

$$M_2 = \frac{1}{2}(1-\xi)(1+\eta), \tag{8.60}$$

$$M_3 = \frac{1}{2}\xi(1+\eta), \tag{8.61}$$

$$M_4 = \frac{1}{2}\xi(1-\eta). \tag{8.62}$$

The contaminant concentration field within the two-dimensional transient infinite element shown in Fig. 8.5 can be defined as

$$C_i = \sum_{j=1}^{2} \hat{N}_{ji} C_{ji} = [\hat{N}]_i \begin{Bmatrix} C_{1i} \\ C_{2i} \end{Bmatrix} \qquad (i = 1, 2), \tag{8.63}$$

where C_1 and C_2 are the contaminant concentrations for the porous block and fissured network; $\left[\hat{N}\right]_1$ and $\left[\hat{N}\right]_2$ are the shape function matrices of the two-dimensional transient infinite element for the porous block and fissured network; $\hat{N}_{1i}$ and $\hat{N}_{2i}$ ($i = 1, 2$) are the shape functions of nodes 1 and 2 for the porous block and fissured network, respectively.

$$\hat{N}_{1i} = \frac{1}{2}F_{imt}(\xi, t)(1-\eta) \qquad (i = 1, 2), \tag{8.64}$$

$$\hat{N}_{2i} = \frac{1}{2}F_{imt}(\xi, t)(1+\eta) \qquad (i = 1, 2). \tag{8.65}$$

Since the number of nodes used for the definition of the shape of the two-dimensional transient infinite element is greater than that used for defining the contaminant concentration field of the two-dimensional transient infinite element, the corresponding two-dimensional parent transient infinite element is a superparametric element.

Based on the same procedures as those used in the conventional finite element method (Zienkiewicz 1977; Zhao and Valliappan 1994b), the property matrices of this two-dimensional transient infinite element can be expressed as

$$[\hat{E}_i]^e = \int_0^\infty \int_{-1}^1 \left(D_{ix} \frac{\partial [\hat{W}]_i^T}{\partial x} \frac{\partial [\hat{N}]_i}{\partial x} + D_{iy} \frac{\partial [\hat{W}]_i^T}{\partial y} \frac{\partial [\hat{N}]_i}{\partial y} \right) |J|\, d\eta d\xi \qquad (i = 1, 2), \tag{8.66}$$

$$[\hat{H}_i]^e = \int_0^\infty \int_{-1}^1 \left(\overline{V}_{ix} [\hat{W}]_i^T \frac{\partial [\hat{N}]_i}{\partial x} + \overline{V}_{iy} [\hat{W}]_i^T \frac{\partial [\hat{N}]_i}{\partial y} \right) |J|\, d\eta d\xi \qquad (i = 1, 2), \tag{8.67}$$

$$[\hat{Q}_i]^e = [\hat{R}_i]^e = \int_0^\infty \int_{-1}^1 \left([\hat{N}]_i^T [\hat{N}]_i \right) |J|\, d\eta d\xi \qquad (i = 1, 2), \tag{8.68}$$

$$\left[\hat{N}\right]_i = \left[\hat{N}_{1i} \quad \hat{N}_{2i}\right], \qquad (i = 1, 2), \tag{8.69}$$

$$\left[\hat{W}\right]_i = \left[\hat{W}_{1i} \quad \hat{W}_{2i}\right], \qquad (i = 1, 2), \tag{8.70}$$

where $|J|$ is the Jacobian determinant of the two-dimensional transient infinite element.

To reflect the upwind effect for the two-dimensional transient infinite element, the following asymmetric weighting functions are used in evaluating the property matrices of the two-dimensional transient infinite elements:

$$\left[\hat{W}\,(\xi, \eta, t)\right]_i = \left[\hat{N}\,(\xi, \eta, t - \Delta t)\right]_i, \qquad (i = 1, 2), \tag{8.71}$$

By using the variable substitution technique and letting $\xi = (1 + \beta)\big/(1 - \beta)$, Eqs. (8.66), (8.67) and (8.68) can be rewritten as

$$[\hat{E}_i]_1^e = \int_{-1}^1 \int_{-1}^1 \left(D_{ix} \frac{\partial [\hat{W}]_i^T}{\partial x} \frac{\partial [\hat{N}]_i}{\partial x} + D_{iy} \frac{\partial [\hat{W}]_i^T}{\partial y} \frac{\partial [\hat{N}]_i}{\partial y} \right) \frac{2}{(\beta - 1)^2} |J|\, d\eta d\beta \ (i = 1, 2), \tag{8.72}$$

$$[\hat{H}_i]_1^e = \int_{-1}^1 \int_{-1}^1 \left(\overline{V}_{ix} [\hat{W}]_i^T \frac{\partial [\hat{N}]_i}{\partial x} + \overline{V}_{iy} [\hat{W}]_i^T \frac{\partial [\hat{N}]_i}{\partial y} \right) \frac{2}{(\beta - 1)^2} |J|\, d\eta d\beta \ (i = 1, 2), \tag{8.73}$$

$$[\hat{Q}_i]_1^e = [\hat{R}_i]_1^e = \int_{-1}^1 \int_{-1}^1 \left([\hat{N}]_i^T [\hat{N}]_i \right) \frac{2}{(\beta - 1)^2} |J|\, d\eta d\beta \qquad (i = 1, 2). \tag{8.74}$$

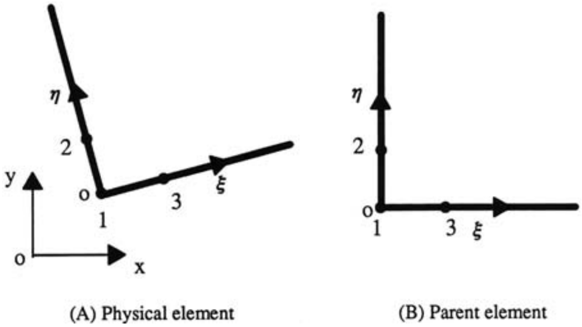

Fig. 8.6 Two-dimensional mapped transient bi-infinite elements

Equations (8.72), (8.73) and (8.74) indicate that the property matrices of the two-dimensional transient infinite element can be evaluated using the Gauss–Legendre integration scheme.

It is noted that under certain situations, a two-dimensional three-node transient bi-infinite element, as shown in Fig. 8.6, can be useful for the numerical analysis. Similarly, the mapping relationship of this two-dimensional three-node transient bi-infinite element can be defined as follows:

$$x = \sum_{i=1}^{3} M_i x_i, \tag{8.75}$$

$$y = \sum_{i=1}^{3} M_i y_i, \tag{8.76}$$

where M_i is the mapping function at each node of the two-dimensional three-node transient bi-infinite element

$$M_1 = (1-\xi)(1-\eta), \tag{8.77}$$

$$M_2 = \frac{1}{2}\xi(1+\eta), \tag{8.78}$$

$$M_3 = \frac{1}{2}(1+\xi)\eta. \tag{8.79}$$

The contaminant concentration shape function of this two-dimensional three-node transient bi-infinite element can be expressed as

$$[\hat{N}]_i = [\hat{N}_1]_i = [F_{imt}(\xi,t)F_{imt}(\eta,t)] \qquad (i=1,2), \tag{8.80}$$

where

$$F_{imt}(\xi,t) = \exp\left[-\frac{\xi^2 + 2(x_1 - \overline{V}_{i\xi}t)\xi}{4D_{i\xi}t}\right] \qquad (i=1,2), \tag{8.81}$$

$$F_{imt}(\eta, t) = \exp\left[-\frac{\eta^2 + 2(y_1 - \overline{V}_{i\eta}t)\eta}{4D_{i\eta}t}\right] \qquad (i = 1, 2). \tag{8.82}$$

Finally, the property matrices of the two-dimensional three-node transient bi-infinite element can be derived (Zhao and Valliappan 1994b).

$$[\hat{E}_i]_2^e = \int_{-1}^{1}\int_{-1}^{1}\left(D_{ix}\frac{\partial[\hat{W}]_i^T}{\partial x}\frac{\partial[\hat{N}]_i}{\partial x} + D_{iy}\frac{\partial[\hat{W}]_i^T}{\partial y}\frac{\partial[\hat{N}]_i}{\partial y}\right)$$
$$\frac{4}{(\beta-1)^2(\gamma-1)^2}\,|J|\,d\gamma d\beta \qquad (i = 1, 2), \tag{8.83}$$

$$[\hat{H}_i]_2^e = \int_{-1}^{1}\int_{-1}^{1}\left(\overline{V}_{ix}[\hat{W}]_i^T\frac{\partial[\hat{N}]_i}{\partial x} + \overline{V}_{iy}[\overline{W}]_i^T\frac{\partial[\hat{N}]_i}{\partial y}\right)$$
$$\frac{4}{(\beta-1)^2(\gamma-1)^2}\,|J|\,d\gamma d\beta \qquad (i = 1, 2), \tag{8.84}$$

$$[\hat{Q}_i]_2^e = [\hat{R}_i]_2^e = \int_{-1}^{1}\int_{-1}^{1}\left([\overline{W}]_i^T[\hat{N}]_i\right)\frac{2}{(\beta-1)^2(\gamma-1)^2}\,|J|\,d\gamma d\beta \qquad (i = 1, 2), \tag{8.85}$$

$$\left[\hat{W}(\xi,\eta,t)\right]_i = \left[\hat{N}(\xi,\eta,t-\Delta t)\right]_i, \qquad (i = 1, 2). \tag{8.86}$$

After the property matrices of both upwind finite elements and transient infinite elements are obtained, the coupled computational method of upwind finite elements and transient infinite elements can be used to solve transient contaminant transport problems in fractured porous media of infinite domains. As the present transient infinite element explicitly depends on time, the corresponding property matrices need to be evaluated at each time step in the computation so that the accuracy of numerical results can be ensured for any time of interest.

8.1.3 Verification of the Coupled Computational Method of Upwind Finite Elements and Transient Infinite Elements

The correctness and usefulness of the coupled computational method of upwind finite elements and transient infinite elements can be verified by some simple but critical problems, for which the exact analytical solutions are already available. To examine the two-dimensional behaviour of the proposed transient infinite elements, a fundamental problem with a given contaminant concentration at the centre of a single porosity medium in a horizontal infinite plane is considered in this subsection. This can be carried out by simply setting the exchange term in a double porosity medium to zero so that the double porosity medium can be treated as two overlapping independent media of single porosity. Figure 8.7 shows the discretized

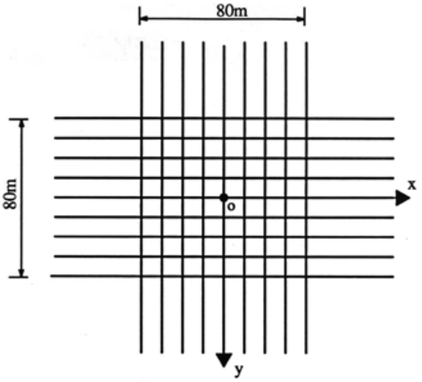

(a) Squared finite element mesh

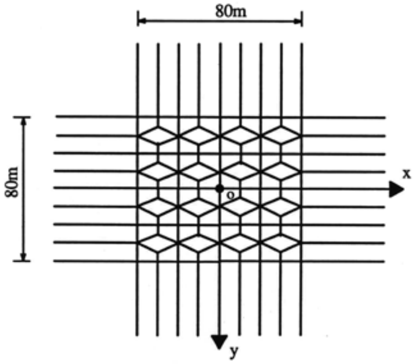

(b) Inclined finite element mesh

Fig. 8.7 Coupled computational model of a verification problem: (**a**) squared finite element mesh; (**b**) inclined finite element mesh

model of this problem, where the origin of the global coordinate system is subjected to a point contaminant source with the concentration of 100 mg cm^{-3} (i.e. $C_0 = 100$ mg cm^{-3}) at $t = 0$. For the purpose of investigating the effect of the finite element mesh on the numerical results, the near field of the system, which is chosen as 80×80 m, has been simulated by squared regular finite elements (see Fig. 8.7(a)) and by inclined irregular finite elements (see Fig. 8.7(b)). The far field is simulated by two-dimensional transient mapped infinite elements as proposed in this chapter. The following parameters are used in the numerical analysis: the average linear velocities of pore-fluid flow are 0.05 m d^{-1} in the x and y directions; the diffusion/dispersion coefficients are 0.5 m^2 d^{-1} in the x and y directions; the time step used in the computation is 10 days.

Figure 8.8 shows the comparison between the current numerical and the analytical solutions (Lardner and Song 1991). In this figure, the dimensionless concentration distributions of the contaminant in the near field of the first quadrant of the global coordinate system, namely in the region of $40\,\text{m} \geq x \geq 0$ and $40\,\text{m} \geq y \geq 0$, have been displayed at three different time instants. It is noted that, in terms of the numerical solutions shown in Fig. 8.8, the solid lines represent the numerical results obtained by using the mesh of squared regular finite elements, while the

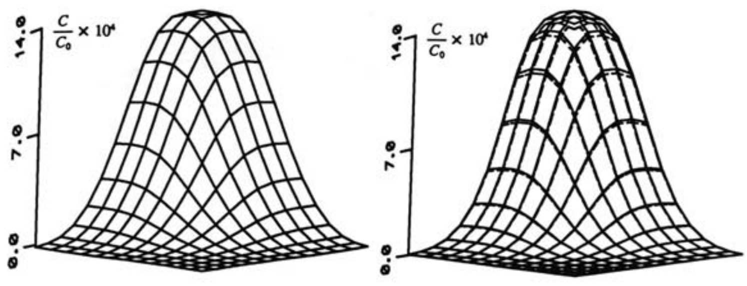

(Analytical solution) (Numerical solution)

(t=100days)

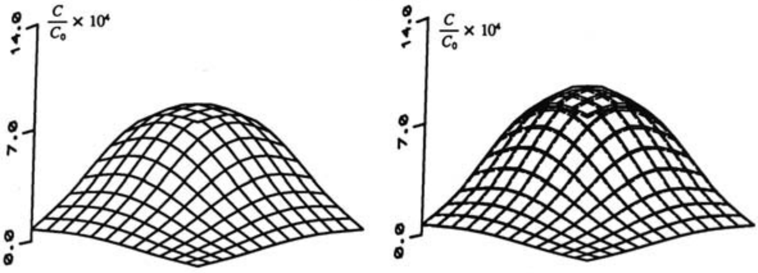

(Analytical solution) (Numerical solution)

(t=200days)

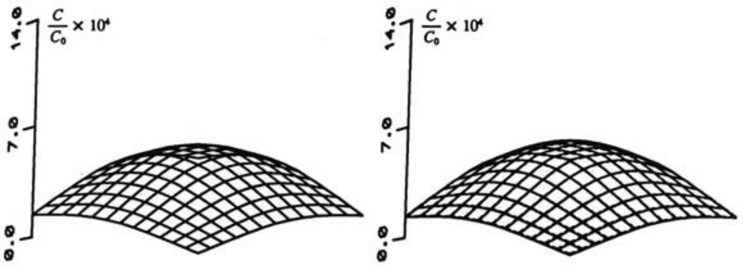

(Analytical solution) (Numerical solution)

(t=300days)

Fig. 8.8 Comparison of numerical results with analytical solutions

dashed lines express the numerical results from using the mesh of inclined irregular finite elements. From this figure, it can be observed that excellent coincidence exists between the current numerical results and the analytical solutions, even though the near field simulated by finite elements is very small. This demonstrates that the coupled computational method of upwind finite elements and transient infinite elements is very useful for the numerical simulation of transient contaminant transport problems in fluid-saturated porous media of infinite domains. In addition, it is clear that the numerical results obtained by using the mesh of the squared regular finite elements yield good agreement with those using the mesh of the inclined irregular finite elements. This illustrates that the coupled method of upwind finite elements and transient infinite elements can be used to solve transient contaminant transport problems with irregular meshes in the near field of the system.

8.2 Parametric Study of Transient Contaminant Transport Problems in Fractured Porous Media of Infinite Domains

Although the quantitative application of a numerical model to a contaminant transport problem in natural environments is limited by difficulties in determining the values of distributions of appropriate field parameters, a sophisticated numerical model can play a useful role in demonstrating the sensitivity of a contaminant transport process to each of the parameters involved. The resulting information from this kind of study may provide an improved understanding of the effect of each parameter on the contaminant transport process. In this regard, the sophisticated numerical model can lead to greater efficiency and insight in the process of collecting field data. This is the main reason for conducting a parametric study on contaminant transport processes in fractured porous media of infinite domains in this section.

Regarding the determination of material parameters involved in the governing equations of transient contaminant transport problems in fractured porous media, Rowe et al. (1988) proposed some laboratory techniques for assessing the effective matrix porosity so that a reduction in the total porosity obtained by normal geotechnical procedures is considered as a result of the dead-end pores and pores too small to permit contaminant transport. On the other hand, if a fissured network is comprised of three orthogonally intersecting sets of equally spaced, parallel fractures, Rowe and Booker (1989, 1990a, b, 1991) presented the relationships between the fissure spacing and related parameters. The general form of such relationships can be expressed in the x direction as follows:

$$v_{ax} = v_{1x}^{f}\frac{h_1}{H_1} + v_{2x}^{f}\frac{h_2}{H_2}, \tag{8.87}$$

$$D_{ax} = D_{1x}^{f}\frac{h_1}{H_1} + D_{2x}^{f}\frac{h_2}{H_2}, \tag{8.88}$$

$$\phi_f = \frac{h_1}{H_1} + \frac{h_2}{H_2} + \frac{h_3}{H_3}, \tag{8.89}$$

where v_{1x}^{f} and v_{2x}^{f} are the average linear pore-fluid velocities in sets one and two of fissures, the normal of whose surfaces are perpendicular to the x axis; D_{1x}^{f} and D_{2x}^{f} are the corresponding dispersion coefficients of these two sets of fissures; v_{ax} is the Darcy velocity in the x direction; D_{ax} is the apparent dispersion coefficient of the fissured network in the x direction; ϕ_f is the porosity of the fissured network; h_1 and h_2 are the widths of these two sets of fissures under consideration; H_1 and H_2 are the corresponding fissure spacing for these two sets of fissures; h_3 and H_3 are the width and spacing of the third set of fissures, of which the normal surface is parallel to the x axis.

For a two- or three-dimensional contaminant transport problem, similar formulas to those expressed in Eqs. (8.87) and (8.88) can be employed to determine the values of the Darcy velocity and apparent dispersion coefficient of the fissured network in the y and z directions. Since the fissure characteristics of a fissured network can be represented by the parameters such as v_{ax}, D_{ax} and ϕ_f, instead of using the fissure spacing and width directly, average linear pore-fluid velocities, dispersion coefficients and the porosity of the fissured network are used to investigate the effects of the fissured network on transient contaminant transport processes in fractured porous media.

8.2.1 Effects of the Leakage between a Porous Block and a Fissured Network on Contaminant Concentration Distributions in the Fractured Porous Medium

In this subsection, the effects of leakages between porous blocks and fissured networks on contaminant transport processes in fractured porous media of infinite domains are considered using the coupled method of upwind finite elements and transient infinite elements. Such leakage effects reflect the interactions between porous blocks and fissured networks in fractured porous media. From a mathematical point of view, since a distributed contaminant source can be decomposed into a sum of several point contaminant sources, the use of a point contaminant source may be the best choice for investigating the general contaminant transport mechanism in fractured porous media of infinite domains. For this reason, a fundamental mass transport problem with an initial point contaminant source of a given concentration at the centre of a horizontal infinite plane is considered in this subsection.

As shown in Fig. 8.9, the origin of the coordinate system is subjected to a point contaminant source with a concentration of $1\,\mathrm{kg\,m^{-3}}$ at $t = 0$. This means that the initial boundary condition of the problem is $C(x, y, t) = \delta(x)\delta(y)\delta(t)\,\mathrm{kgm^{-3}}$, where δ is the Kronecker delta with a value of either one or zero. The whole problem domain is divided into a near field ($|x|<100\,\mathrm{m}$, $|y|<100\,\mathrm{m}$) and a far field ($|x|>100\,\mathrm{m}$, $|y|> 100\,\mathrm{m}$), so that the interface between the near field and the far field is presented by the four lines expressed by $x = \pm 100\,\mathrm{m}$ ($|y|\leq 100\,\mathrm{m}$) and $y = \pm 100\,\mathrm{m}$ ($|x|\leq 100\,\mathrm{m}$) in the computational model. The near field of the problem domain is simulated using upwind finite elements, while the far field of the problem domain is simulated using transient infinite elements. To investigate the effect of advective pore-fluid flow on the contaminant transport process in a fractured porous medium, it is assumed that the positive direction of the pore-fluid flow is in coincidence with that of the x axis.

The following parameters are used in the coupled computational model of upwind finite elements and transient infinite elements. For the porous continuum, the average linear velocities of pore-fluid flow are $0.1\,\mathrm{m\,d^{-1}}$ and $0\,\mathrm{m\,d^{-1}}$ in the x and y directions, respectively; the dispersion coefficients are $1\,\mathrm{m^2d^{-1}}$ and $0.1\,\mathrm{m^2d^{-1}}$ in the x and y directions. For the fissured continuum, both the average linear veloc-

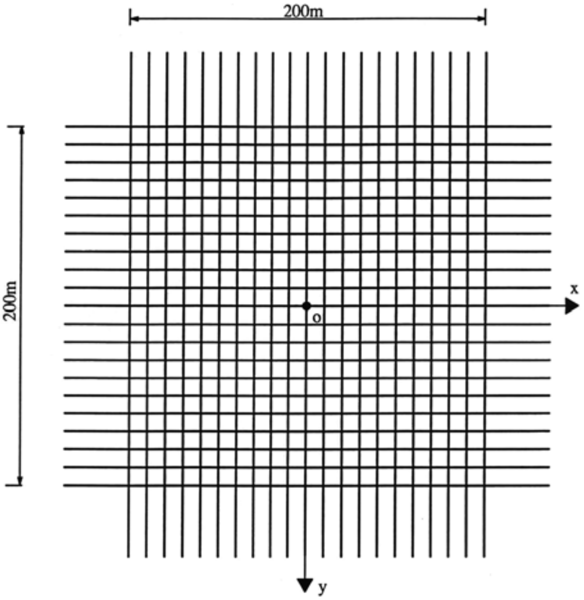

Fig. 8.9 Computational model of contaminant transport in a fractured porous medium: the near field is simulated using finite elements, while the far field is simulated using transient infinite elements

ities of pore-fluid flow and the dispersion coefficients in the x and y directions are exactly the same as those used for the porous continuum. Since only the porosity ratio between the fissured continuum (representing the fissured network) and the porous continuum (representing the porous block) is involved in the governing equations of contaminant transport problems in fractured porous media, which are treated as double porosity continua, the porosity ratio of the fissured continuum to the porous continuum, ϕ_2/ϕ_1, is assumed to be 4, while the porosity of the continuum (i.e. ϕ_1) is 0.05 in the computational model of the overlapping double porosity continua. Regarding the discretization of time, the central difference scheme (Zhao and Valliappan 1994b, c) is used with a time step of $\Delta t = 10$ days. Since the leakage due to the solute diffusion between the porous block and the fissured network can be considered by a transmissive coefficient in the computational model, six different transmissive coefficients between the porous and fissured continua, namely χ =0, 0.001, 0.005, 0.01, 0.1 and 1.0 per unit time, are used to investigate the effects of leakages between the porous block and the fissured network on the contaminant concentration distributions in the fractured porous medium.

Figures 8.10 and 8.11 show the dimensionless concentration distribution of contaminant in the near field of the first quadrant of the fractured porous medium at $t = 100$ and 400 days, respectively. Note that the dimensionless contaminant concentration is defined as $(C/C_0) \times 10^3$. In these figures, Tr is used to represent the transmissive coefficient between the porous and fissured continua so that Tr $= \chi$ in this subsection. The numerical results shown in the left columns are obtained from the porous continuum, which is used to represent the porous block, while the numerical results shown in the right columns are obtained from the fissured

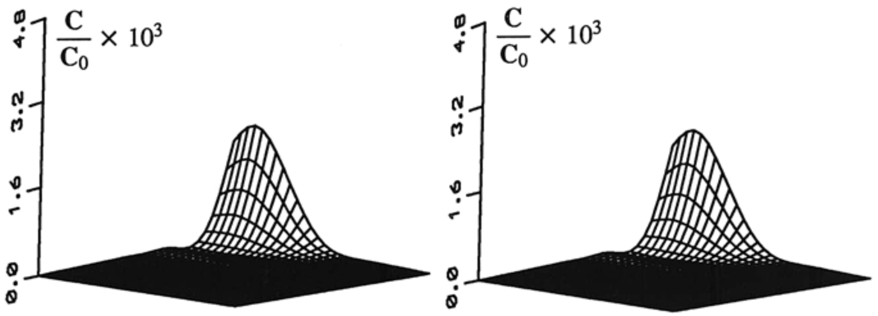

(Porous medium) *(Fissured network)*

(Tr=0.0)

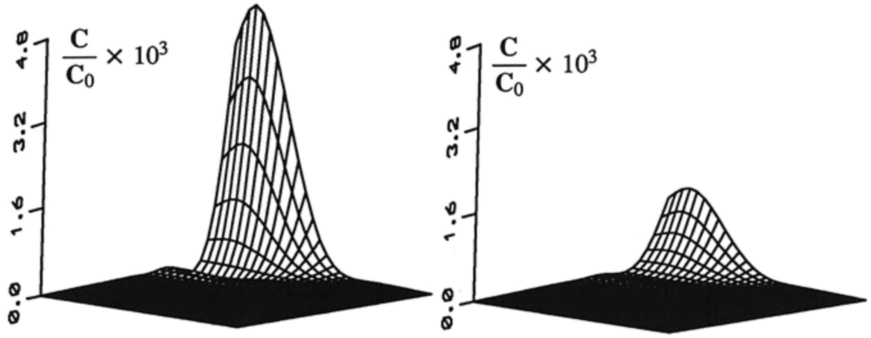

(Porous medium) *(Fissured network)*

(Tr=0.01)

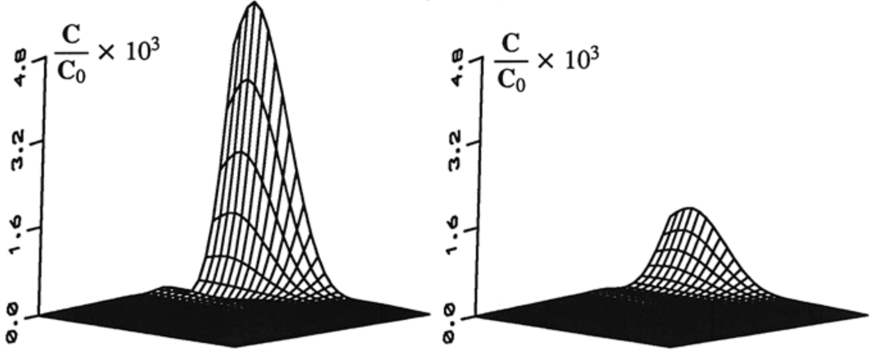

(Porous medium) *(Fissured network)*

(Tr=0.1)

Fig. 8.10 Effects of leakages on dimensionless contaminant distributions in the fractured porous medium (t = 100 days)

continuum, which is used to represent the fissured network of the fractured porous medium. As the strength of the leakage between the porous block and the fissured network can be represented by the value of the transmissive coefficient, the related numerical results indicate that the strength of the leakage has a significant effect on

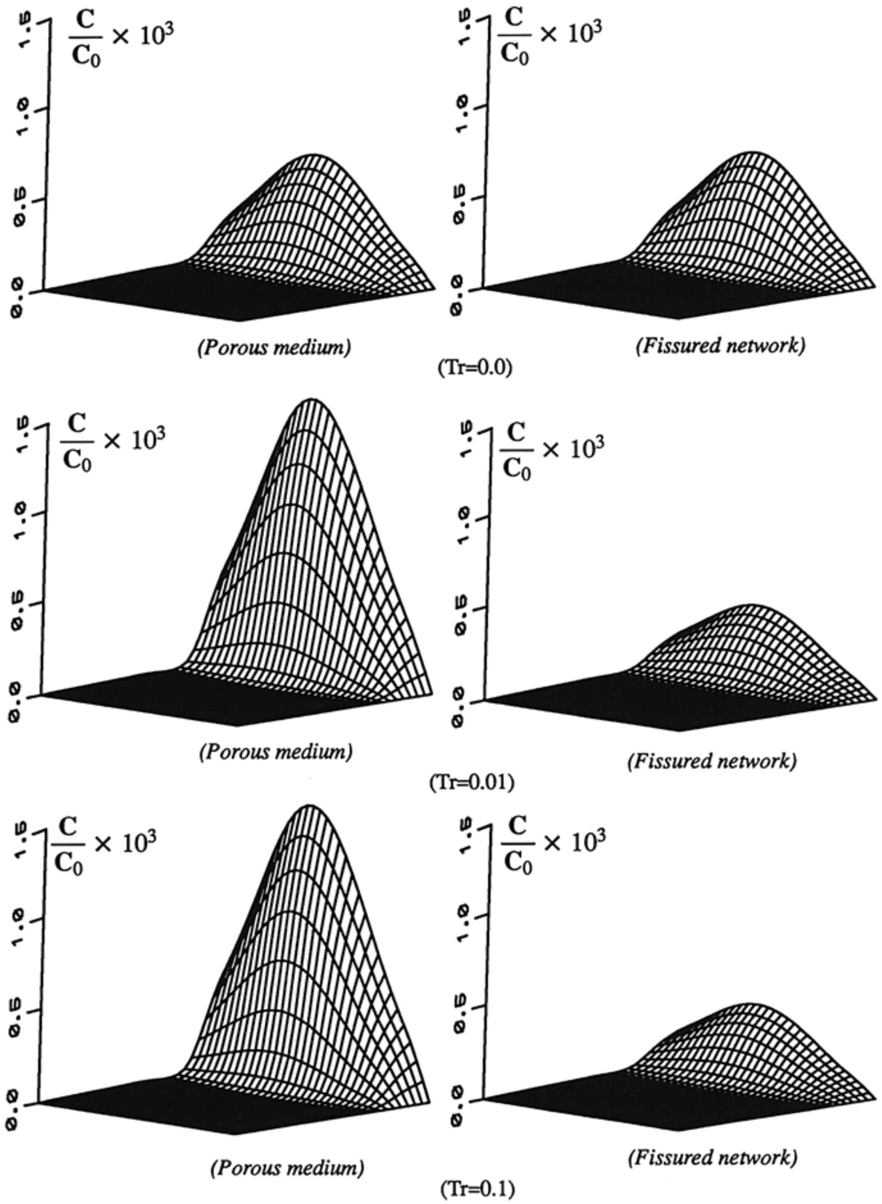

Fig. 8.11 Effects of leakages on dimensionless contaminant distributions in the fractured porous medium (t = 400 days)

the dimensionless concentration distribution of contaminant in the fractured porous medium. With an increase in the value of the transmissive coefficient, Tr, the maximum value of the dimensionless contaminant concentration increases in the porous block, but decreases in the fissured network. With $t = 100$ days taken as an example, the maximum values of the dimensionless contaminant concentration in the case of no leakage (i.e. Tr = 0) between the two continua are 1.86 for both the porous block and the fissured network. However, the corresponding maximum values for Tr = 0.01(1/s) are 4.29 and 1.26 for the porous block and the fissured network, respectively. This indicates that a higher concentration may appear in the porous block because the porosity of the porous block is smaller than that of the fissured network in the computational model. Since advective pore-fluid flow is considered in the x direction only, both advection and dispersion take place in this direction, so that the contaminant transport speed in the x direction is much faster than that in the y direction.

With the increase of time, the maximum values of the dimensionless contaminant concentration in both the porous block and the fissured network decrease because the contaminant spreads over a broad area due to the development of solute advection and dispersion in the fractured porous medium. For instance, when Tr = 0.01(1/s), the maximum values of the dimensionless contaminant concentration are 4.29 and 1.26 at $t = 100$ days for the porous block and the fissured network, respectively, while they are 1.41 and 0.35 at $t = 400$ days for the porous block and the fissured network. The numerical results also indicate that the proposed coupled model of upwind finite elements and transient infinite elements reflects the mass conservation law very well during contaminant transport in the fractured porous medium. Since the contaminant has reached the right boundary of the upwind finite elements (at $x = 100$ m) in the x direction but only reached about one-third of the near field (at $y = 30$ m) in the y direction when $t = 400$ days, it can be concluded that pore-fluid flow advection plays an important role in the contaminant transport processes in fractured porous media of infinite domains. Although the transmissive coefficient between the porous block and the fissured network has a significant influence on the contaminant concentration distribution in the fractured porous medium, it has little effect on the contaminant transport speed in the coupled computational model of upwind finite elements and transient infinite elements.

Figures 8.12 and 8.13 show the dimensionless contaminant concentration versus time at six observation points in the computational model of the fractured porous medium. In these figures, the unit of time is day. Similarly, the results shown in the left columns are obtained for the porous continuum, while the results shown in the right columns are obtained for the fissured continuum. These results clearly indicate that the contaminant arrives at different observation points with different times. For example, the first arrival time of the contaminant at the observation point of $x = 20$ m and $y = 0$ m is about 20 days, while the corresponding arrival times at the other two observation points, namely ($x = 60$ m, $y = 0$ m) and ($x = -20$ m, $y = 0$ m), are about 100 and 35 days, respectively. Since the three observation points are located on the x axis and the contaminant source is located at the origin of the coordinate system when t = 0, both advection and dispersion take place at the three observation points in the fractured porous medium. Owing to the effect of a dispersion process, the contaminant arrives at the upstream observation point of $x = -20$ m and $y = 0$ m after it arrives at the downstream observation point of $x = 20$ m and $y = 0$ m. Through comparing the arrival time of the contaminant at an

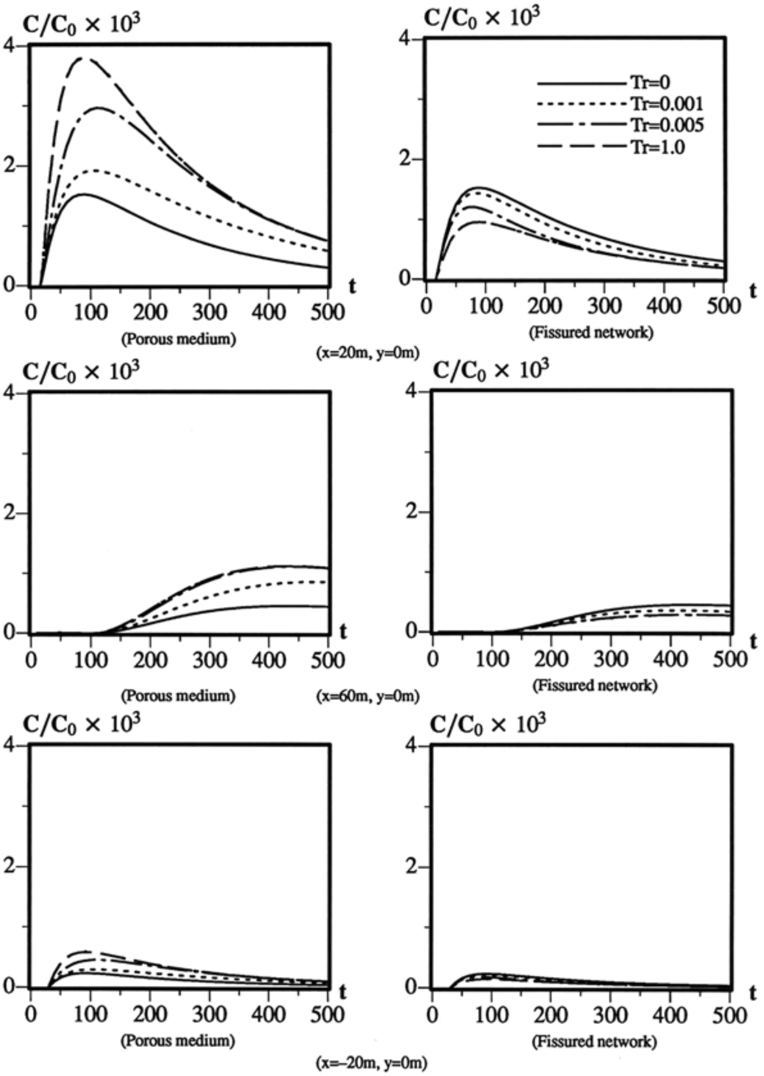

Fig. 8.12 Time-history distributions of dimensionless contaminant concentration due to different transmissive coefficients

observation point in the *x* axis with that at similar observation point, which is of the same distance from the origin of the coordinate system but is located in the *y* axis, it has been found that the contaminant travels much faster in the *x* direction than in the *y* direction. The first arrival time of the contaminant is 20 days for the observation point of $x = 20$ m and $y = 0$ m, while it is 200 days for the observation point of $x = 0$ m and $y = 20$ m. Since only dispersion takes place in the *y* direction, the first arrival time of the contaminant is identical for the three observation points shown

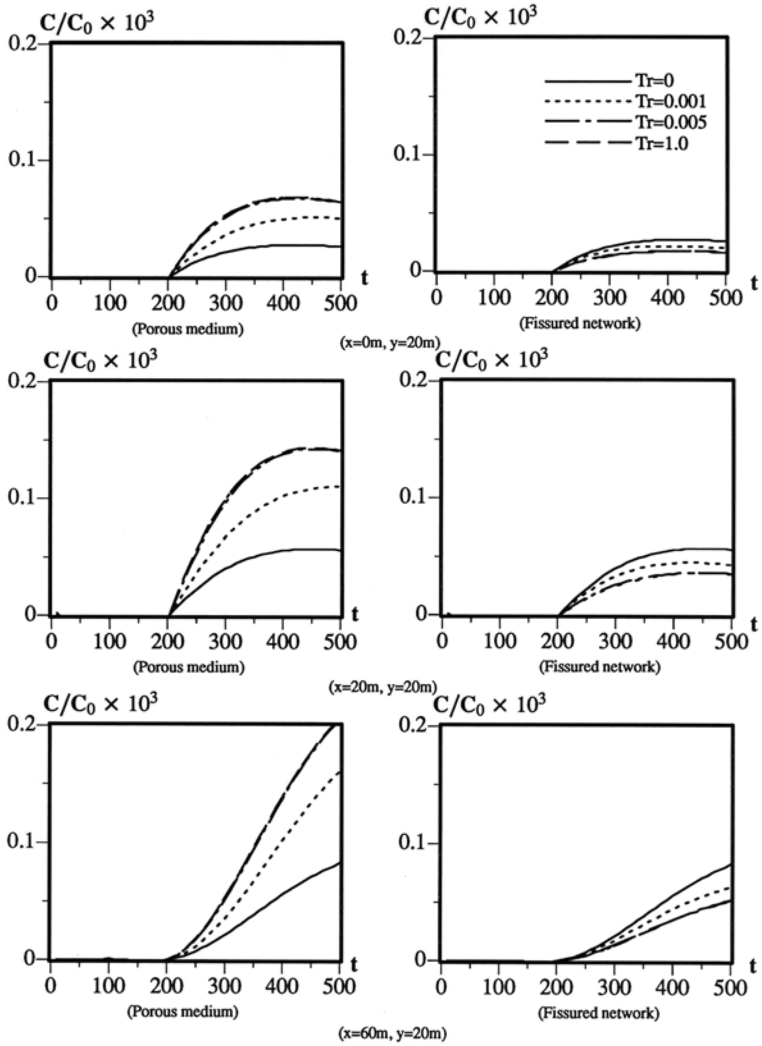

Fig. 8.13 Time-history distributions of dimensionless contaminant concentration due to different transmissive coefficients

in Fig. 8.13. These three observation points have the same *y* coordinates (i.e. $y = 20$ m) but different *x* coordinates (i.e. $x = 0$, 20 and 60 m, respectively). Owing to the advection effect, the first arrival time of the contaminant is different for a pair of symmetric observation points at the *x* axis, as can be seen from the two observation points at $x = 20$ m and $x = -20$ m at the *x* axis of the coordinate system.

In terms of the leakage effect between the porous block and the fissured network on the contaminant transport process in the fractured porous medium, it has been recognized that when the transmissive coefficient, Tr, is within a range between 0 and 0.005 s^{-1}, any small change in its value can have a profound influence on the dimensionless contaminant concentration distribution in the fractured porous medium. However, when the transmissive coefficient becomes greater, an increase in its value has only some effects on the dimensionless contaminant concentration distribution in a limited adjacent region around the input contaminant source during the early period of time. This means that if the leakage effect between the porous block and the fissured network is weak, great caution should be taken for determining the value of the transmissive coefficient because it is very sensitive to the contaminant concentration distribution in both the near field and the far field of the system. On the other hand, if the leakage effect between the porous block and the fissured network is strong, any variation in the value of the transmissive coefficient has only a short-term effect on the contaminant concentration distribution in the near field of the system.

8.2.2 Effects of Medium Porosities on Contaminant Concentration Distributions in the Porous Block and Fissured Network

To investigate the effects of the porosities of the medium in both the porous block and the fissured network on contaminant transport processes in fractured porous media of infinite domains, the same fundamental problem as considered in Sect. 8.2.1 is simulated by the coupled computational model of upwind finite elements and transient infinite elements in this subsection. The following parameters are used in the coupled computational model. For the porous continuum, both the average linear velocities of pore-fluid flow and the dispersion coefficients in the x and y directions are exactly the same as those used in Sect. 8.2.1. For the fissured continuum, the average linear velocities of pore-fluid flow and the dispersion coefficients in the x and y directions are assumed to be the same as those used for the porous continuum. The transmissive coefficient between the porous and fissured continua is 0.01 (1/s). The porosity of the porous continuum (i.e. ϕ_1) is 0.05. Five different porosity ratios of the fissured continuum to the porous continuum, namely ϕ_2/ϕ_1=1, 2, 4, 6 and 10, are considered to investigate the effects of medium porosities on the contaminant concentration distribution in the fractured porous medium.

Figures 8.14 and 8.15 show the dimensionless concentration distribution of the contaminant in the near field of the first quadrant of the fractured porous medium at two different time instants. In these figures, n_2, is used to represent the porosity ratio of the fissured medium to the porous medium, ϕ_2/ϕ_1, so that $n_2 = \phi_2/\phi_1$ in this subsection. Clearly, the porosity ratio of the fissured medium to the porous medium has a significant influence on the dimensionless concentration distribution of the contaminant in the computational model of the fractured porous medium. The greater the porosity ratio of the fissured medium to the porous medium, the greater the dimensionless contaminant concentration in the near field of the porous medium is. Owing to the mass conservation of the contaminant, the greater the porosity ratio, the smaller the dimensionless contaminant concentration in the fissured medium is.

With an increase in the porosity ratio of the fissured medium to the porous medium, the maximum value of the dimensionless contaminant concentration

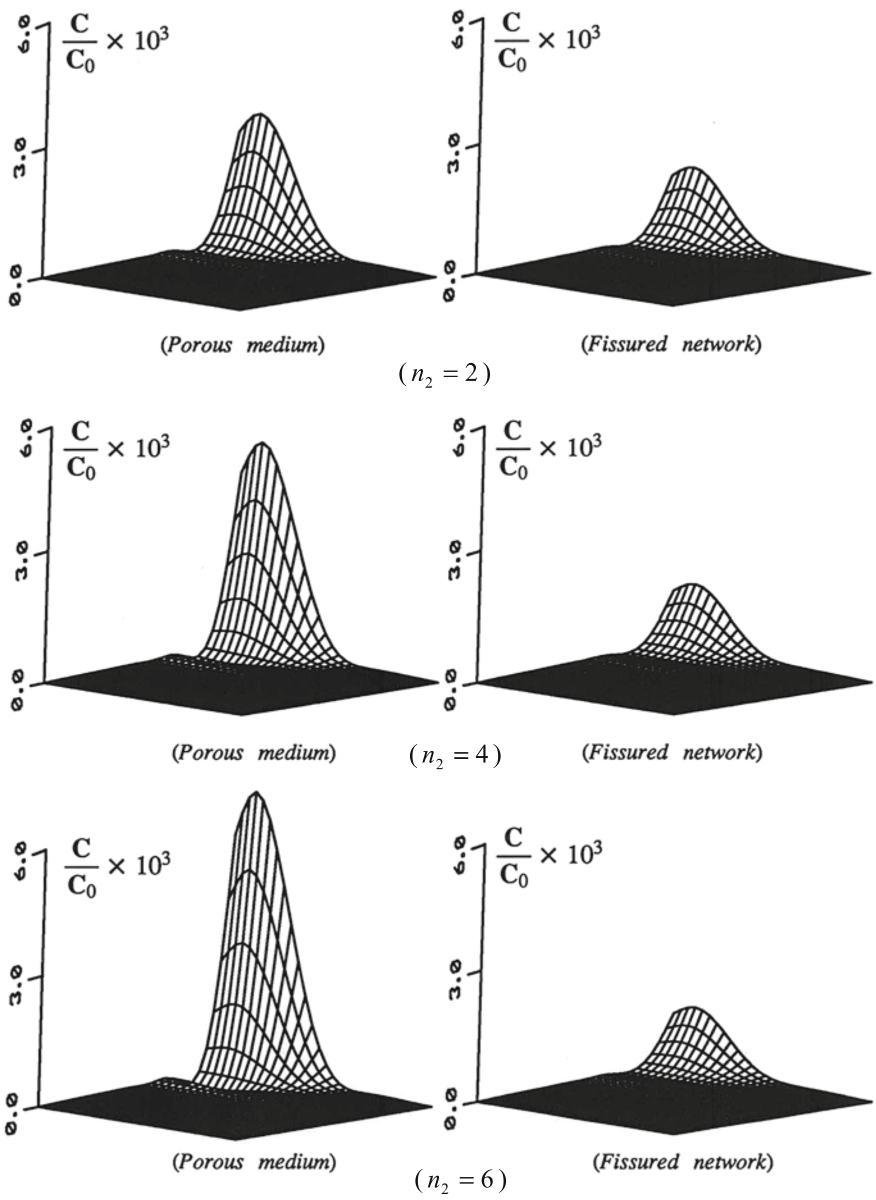

Fig. 8.14 Effects of porosity ratios on dimensionless contaminant distributions in the fractured porous medium (t = 100 days)

increases in the porous block but decreases in the fissured network. For example, the maximum values of the dimensionless contaminant concentration in the case of $n_2 = \phi_2/\phi_1 = 2$ are 1.575 and 0.795 for the porous block and the fissured network,

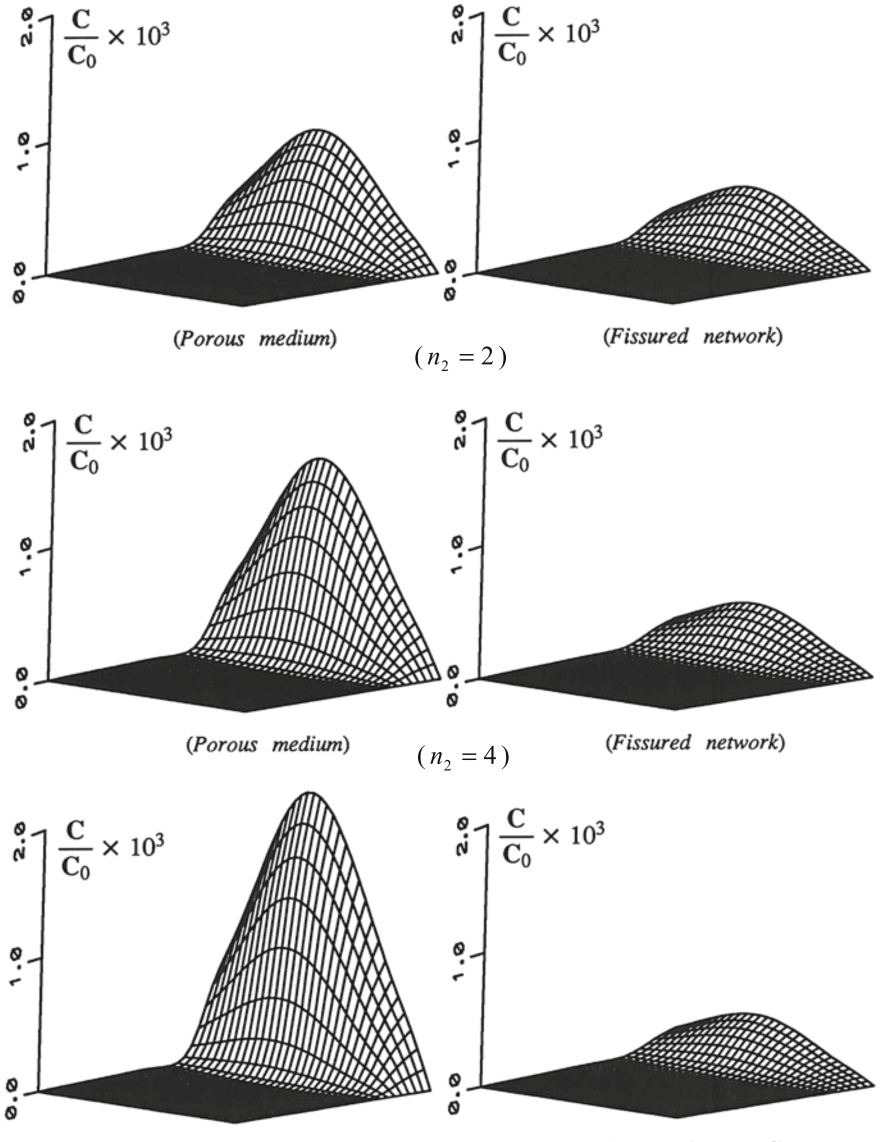

(Porous medium) (Fissured network)

$(n_2 = 2)$

(Porous medium) (Fissured network)

$(n_2 = 4)$

(Porous medium) (Fissured network)

$(n_2 = 6)$

Fig. 8.15 Effects of porosity ratios on dimensionless contaminant distributions in the fractured porous medium (t = 400 days) respectively, while the corresponding maximum values in the case of $n_2 = 6$ are 3.469 and 0.624, indicating that more contaminant may reside in the porous block when the porosity of the porous block is smaller than that of the fissured network. Since pore-fluid flow is considered in the x direction only, both advection and dispersion takes place in this direction, so that the contaminant transport speed in the x direction is faster than that in the y direction of the computational model. With the increase of time, the maximum value of the dimensionless contaminant concentration for both the porous medium and the fissured medium decreases as a result of the wide spread of the contaminant. Since the average linear velocity of the pore-fluid flow in the x direction is constant in the computational model, a change in the porosity ratio of the fissured medium to the porous medium has little effect on the contaminant transport speed in the computational model, even though it has a significant influence on the contaminant concentration distribution in the fractured porous medium.

Figures 8.16 and 8.17 show the dimensionless contaminant concentration versus time at several observation points of the computational model. Due to the consideration of a point contaminant source acting at the origin of the coordinate system at $t = 0$, the contaminant arrives at different observation points with different times, indicating that the contaminant concentration distribution is dependent on both space and time. Since the porosity ratio of the fissured medium to the porous medium and the transmissive coefficient between the porous medium and the fissured medium play similar roles in the contaminant transport process for the double porosity model of a fractured porous medium, the same conclusions as those obtained in Sect. 8.2.1 can be made on the first arrival time of the contaminant at a given observation point in the coupled computational model of upwind finite elements and transient infinite elements.

Regarding the effects of the porosity ratio of the fissured medium to the porous medium on the contaminant concentration distribution in the fractured porous medium, the related numerical results (in Figs. 8.16 and 8.17) indicate that within the parameter range studied, a slight change in the value of the porosity ratio can have a significant effect on both the short-term and the long-term contaminant concentration distributions in the fractured porous medium of infinite domain. For example, in the case of $x = 20$ m and $y = 0$ m, the dimensionless contaminant concentrations of the porous block at $t = 100$ days are 1.51, 2.16, 3.47, 4.77 and 7.38 for $n_2 = \phi_2/\phi_1 = 1, 2, 4, 6$ and 10, respectively, while the corresponding dimensionless contaminant concentrations at $t = 500$ days are 0.30, 0.45, 0.74, 1.04 and 1.63 for $n_2 = \phi_2/\phi_1 = 1, 2, 4, 6$ and 10. Although the dimensionless contaminant concentrations in both the porous block and the fissured network at each observation point vary as time goes on, their change rates are considerably different for different porosity ratios of the fissured medium to the porous medium in the fractured porous medium. This indicates that great caution should be taken for determining the value of the porosity ratio of the fissured network to the porous block because it can significantly affect the contaminant concentration distribution in both the near field and the far field of a fractured porous medium.

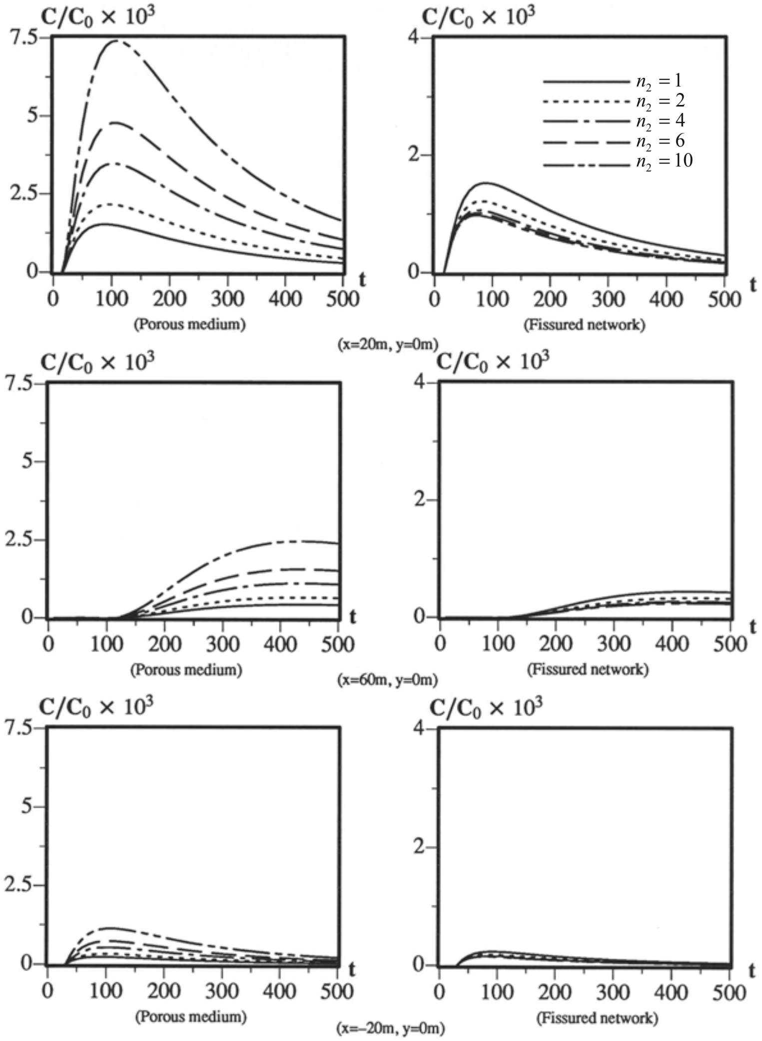

Fig. 8.16 Time-history distributions of dimensionless contaminant concentration due to different porosity ratios

8.2.3 Effects of Pore-Fluid Advection on Contaminant Concentration Distributions in the Porous Block and Fissured Network

The main purpose of this subsection is to investigate the effects of pore-fluid advection on contaminant concentration distributions in the porous block and fissured network of a fractured porous medium. For this purpose, a fundamental mass transport problem with an initial point contaminant source at the centre of a horizontal infinite plane consisting of a fractured porous medium is simulated using the coupled

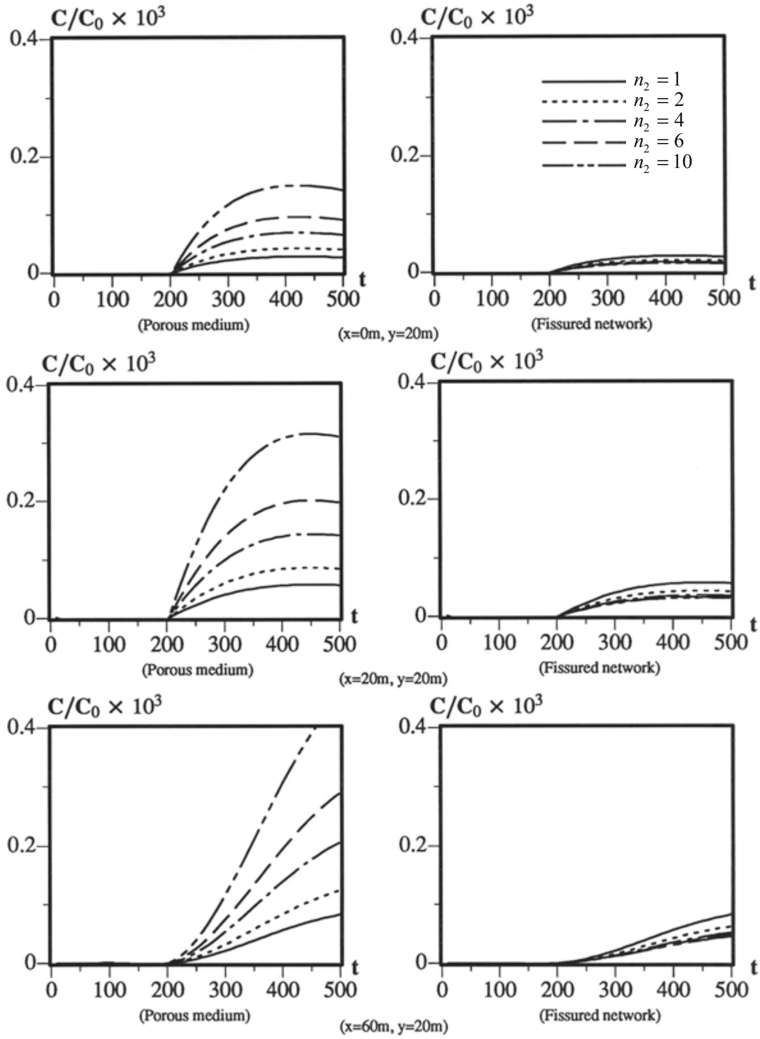

Fig. 8.17 Time-history distributions of dimensionless contaminant concentration due to different porosity ratios

computational method of upwind finite elements and transient infinite elements. With the porosity ratio, the dispersion coefficient and the transmissive coefficient kept constant, several different average linear velocities of pore-fluid flow are considered to examine the effects of pore-fluid advection on contaminant concentration distributions in the porous block and fissured network of a fractured porous medium.

The following parameters are used in the coupled computational model of the fractured porous medium. For the porous continuum, the dispersion coefficients are $1\,\text{m}^2\text{d}^{-1}$ and $0.1\,\text{m}^2\text{d}^{-1}$ in the x and y directions, respectively; the average linear velocity of the pore-fluid flow in the x direction (i.e. $\overline{V}_{1x}$) is 0.05 m d^{-1} when the average linear velocity of the pore-fluid flow in the y direction (i.e. $\overline{V}_{1y}$) is equal to either 0 or 0.05 m d^{-1}. For the fissured continuum, the dispersion coefficients are 1 m^{2}d^{-1} and 0.1 m^{2}d^{-1} in the x and y directions, respectively; four different average linear velocities of the pore-fluid flow in the x direction, namely $\overline{V}_{2x}$=0.05, 0.1, 0.2 and 0.5 m d^{-1}, are considered in the case of $\overline{V}_{2y}$=0 m d^{-1}, while the average linear velocity of the pore-fluid flow in the x direction is 0.1 m d^{-1} in the case of $\overline{V}_{2y}$=0.1 m d^{-1}; the porosity ratio of the fissured continuum to the porous continuum is 4; the porosity of the continuum (i.e. ϕ_1) is 0.05; the transmissive coefficient between the porous block and the fissured network is 0.01 s^{-1}.

Figure 8.18 shows the effects of pore-fluid advection on the dimensionless concentration distribution of the contaminant in the near field of the first quadrant of the fractured porous medium at $t = 100$ days. In this figure, the numerical results associated with $\overline{V}_{2x}$= 0.05, 0.1 and 0.5 are obtained when the average linear velocities in the x and y directions are 0.05 m d^{-1} and 0 m d^{-1} in the porous continuum, but the average linear velocity in the y direction is 0 m d^{-1} in the fissured continuum. These results indicate that for three different values of the average linear velocity in the x direction within the fissured network, the distribution patterns of the dimensionless contaminant concentration are significantly different, implying that the average linear velocity of the pore-fluid flow has a remarkable influence on the dimensionless concentration distribution of the contaminant in the coupled computational model of the fractured porous medium.

Figures 8.19 and 8.20 show the dimensionless contaminant concentration distribution versus time at several observation points of the computational model. In these two figures, the numerical results marked by $\overline{V}_{2x}$= 0.05, 0.1, 0.2 and 0.5 are obtained when the average linear velocities in the x and the y directions are 0.05 m d^{-1} and 0 m d^{-1} in the porous continuum, but the average linear velocity in the y direction is 0 m d^{-1} in the fissured continuum. In contrast, the numerical results marked by $\overline{V}_{2x}$= 0.1 and $\overline{V}_{2y}$= 0.1 are obtained when the average linear velocities in both the x and the y directions are 0.05 m d^{-1} in the porous continuum. Obviously, the pore-fluid advection, which is represented by a different set of pore-fluid velocities, has a profound effect on the contaminant transport speed in the computational model of the fractured porous medium. The greater the average liner velocity of pore-fluid flow, the greater the contaminant transport speed in the fractured porous medium is.

For a given observation point, the average linear velocity of the pore-fluid flow affects not only the time-history distribution pattern, but also the maximum value of the dimensionless contaminant concentration in the fractured porous medium. With the three observation points (in Fig. 8.19) at the x axis taken as an example, the maximum value of the dimensionless contaminant concentration in the case of $\overline{V}_{1x} = \overline{V}_{1y}$=0.05 m d^{-1} and $\overline{V}_{2x} = \overline{V}_{2y}$=0.1 m d^{-1} is smaller than that in the other four cases. However, for the three observation points beyond the x axis (in Fig. 8.20), the maximum value of the dimensionless contaminant concentration in the case of $\overline{V}_{1x} = \overline{V}_{1y}$= 0.05 m d^{-1} and $\overline{V}_{2x} = \overline{V}_{2y}$=0.1 m d^{-1} is greater than that in the other four cases. This phenomenon is due to the fact that the contaminant can spread a broader area when advection takes place in both the x and y directions, compared

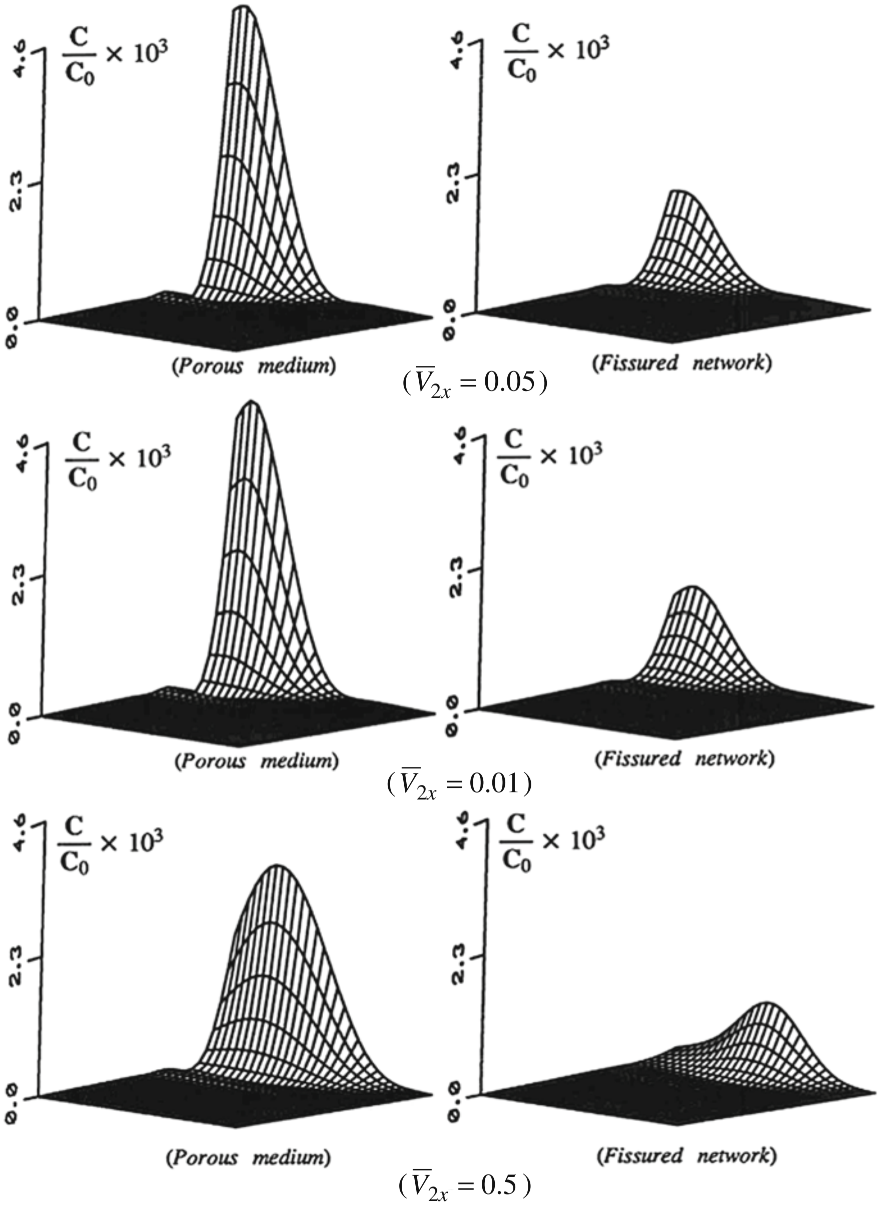

$(\overline{V}_{2x} = 0.05)$

$(\overline{V}_{2x} = 0.01)$

$(\overline{V}_{2x} = 0.5)$

Fig. 8.18 Effects of pore-fluid advection on dimensionless contaminant distributions in the fractured porous medium (t = 100 days)

with when it takes place in the *x* direction only. Since the average linear velocity of pore-fluid flow affects both the contaminant transport speed and the maximum value of the contaminant concentration in a fractured porous medium, it should

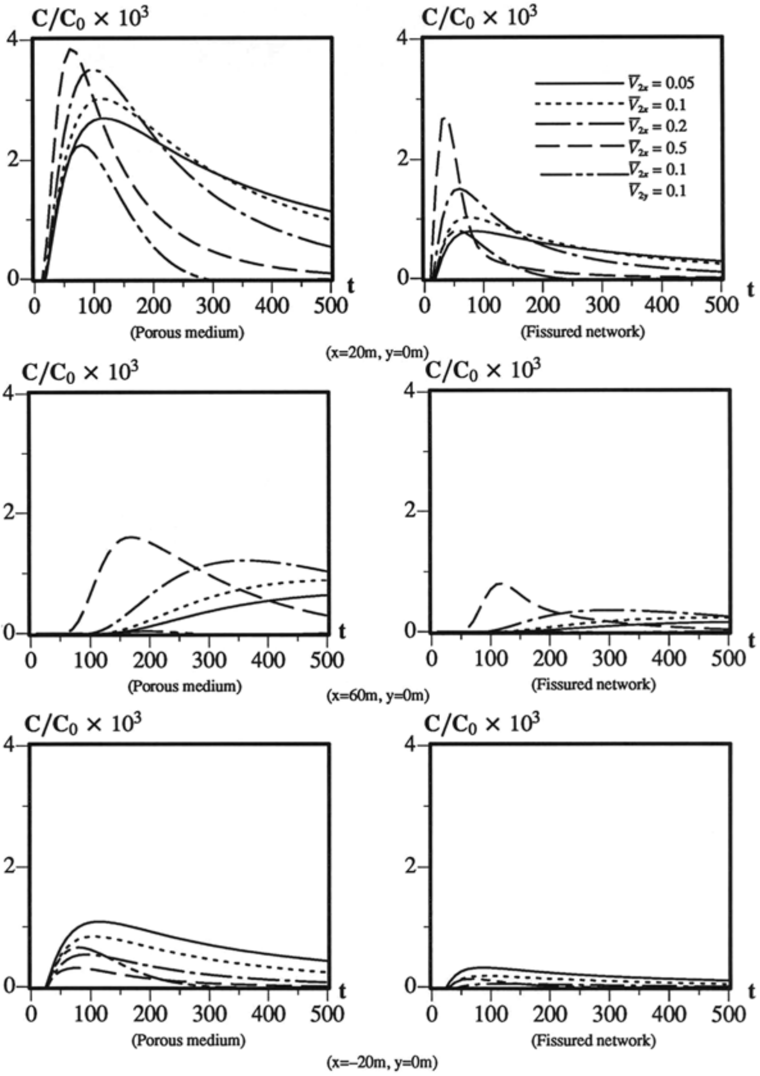

Fig. 8.19 Time-history distributions of dimensionless contaminant concentration due to different pore-fluid flow velocities

be determined carefully for the computational simulation of transient contaminant transport problems in fractured porous media of infinite domains.

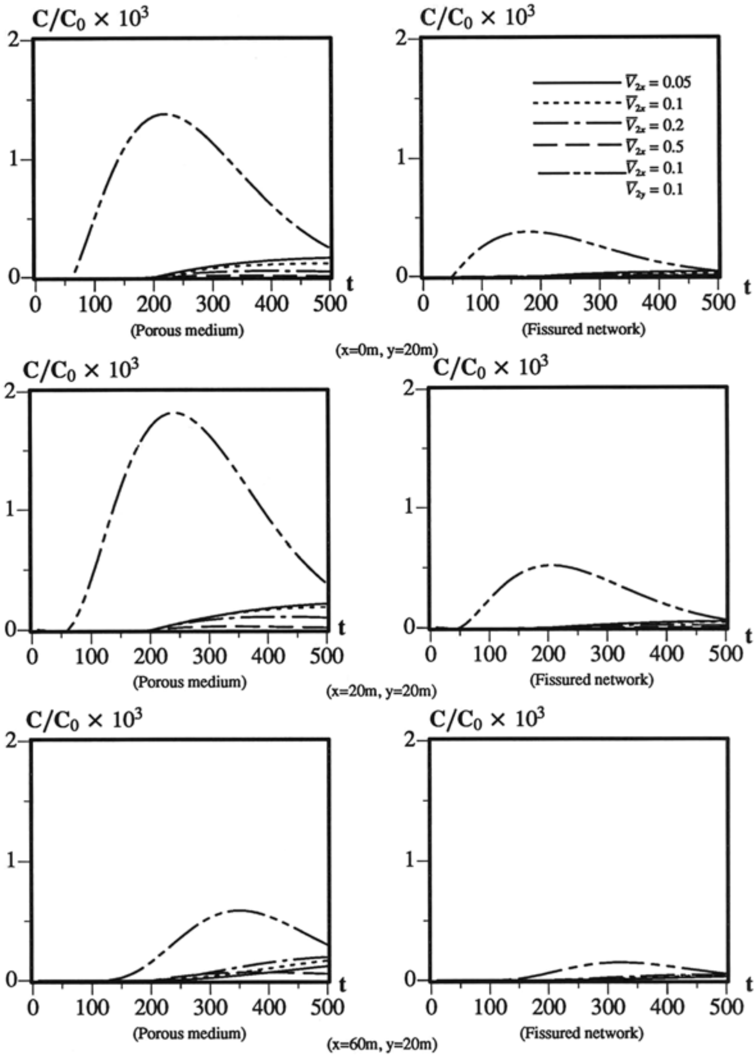

Fig. 8.20 Time-history distributions of dimensionless contaminant concentration due to different pore-fluid flow velocities

8.2.4 *Effects of Solute Dispersion on Contaminant Concentration Distributions in the Porous Block and Fissured Network*

To investigate the effects of solute dispersion in both the porous block and the fissured network on contaminant transport processes in fractured porous media of infinite domains, the same fundamental mass transport problem as that considered in the previous subsections is simulated by the coupled computational model of upwind finite elements and transient infinite elements in this subsection. Through keeping the porosity ratio, the average linear velocity of pore-fluid flow and the transmissive coefficient constant, several different dispersion coefficients are considered to examine the effects of solute dispersion in both the porous block and the fissured network on contaminant transport processes in fractured porous media of infinite domains.

The following parameters are used in the coupled computational model. For the porous continuum, the average linear velocity of pore-fluid flow is 0.1 m d^{-1} in the x direction and zero in the y direction; the dispersion coefficient in the x direction (i.e. D_{1x}) is 1 m^2 d^{-1} when the dispersion coefficient in the y direction (i.e. D_{1y}) is equal to either 0.1 m^2 d^{-1} or 0.05 m^2 d^{-1}. For the fissured continuum, the average linear velocity of pore-fluid flow is 0.1 m d^{-1} in the x direction and zero in the y direction; four different dispersion coefficients in the x direction, namely D_{2x}= 0.2, 0.5, 0.7 and 1.0 m^{2}d^{-1}, are considered when the dispersion coefficient in the y direction (i.e. D_{2y}) is equal to 0.1 m^2 d^{-1}; while only the dispersion coefficient of 0.2 m^2 d^{-1} in the x direction is considered when the dispersion coefficient in the y direction is equal to 0.2 m^2 d^{-1}; the porosity ratio of the fissured continuum to the porous continuum is 4; the porosity of the porous continuum (i.e. ϕ_1) is 0.05; the transmissive coefficient between the porous block and the fissured network is 0.01 s^{-1}.

Figure 8.21 shows the effects of solute dispersion on the dimensionless concentration distribution of the contaminant in the near field of the first quadrant of the fractured porous medium at $t = 100$ days. In this figure, the numerical results associated with D_{2x}= 0.2, 0.5 and 1.0 are obtained when the dispersion coefficient of the porous continuum are 1.0 and 0.1 m^2 d^{-1} in the x and y directions, respectively, while the dispersion coefficient of the fissured continuum (i.e. D_{2y}) is 0.1 m^2 d^{-1} in the y direction. These results indicate that for the three different dispersion coefficients of the fissured network in the x direction, the distribution patterns of the dimensionless contaminant concentration are significantly different, implying that the solute dispersion has a remarkable influence on the dimensionless concentration distribution of the contaminant in the coupled computational model of the fractured porous medium.

Figures 8.22 and 8.23 show the dimensionless contaminant concentration distribution versus time at several observation points of the computational model. In these two figures, the numerical results marked with D_{2x}= 0.2, 0.5, 0.7 and 1.0 are obtained when the dispersion coefficients of the porous continuum are 1.0 and 0.1 m^2 d^{-1} in the x and y directions, while the dispersion coefficients of the fissured continuum is 0.1 m^2 d^{-1} in the y direction. On the other hand, the numerical results marked with D_{2x}= 0.2 and D_{2y}= 0.2 are obtained when the dispersion coefficients of the porous continuum are equal to 1.0 m^2 d^{-1} in both the x and y directions. Clearly, the solute dispersion, which is represented by a different set of dispersion coefficients in this study, has a profound effect on the contaminant transport speed in the computational model of the fractured porous medium. The greater the dispersion coefficient, the greater the contaminant transport speed in the fractured porous medium is.

Similarly, for a given observation point, the solute advection affects not only the time-history distribution pattern, but also the maximum value of the dimensionless contaminant concentration in the fractured porous medium. For the three observa-

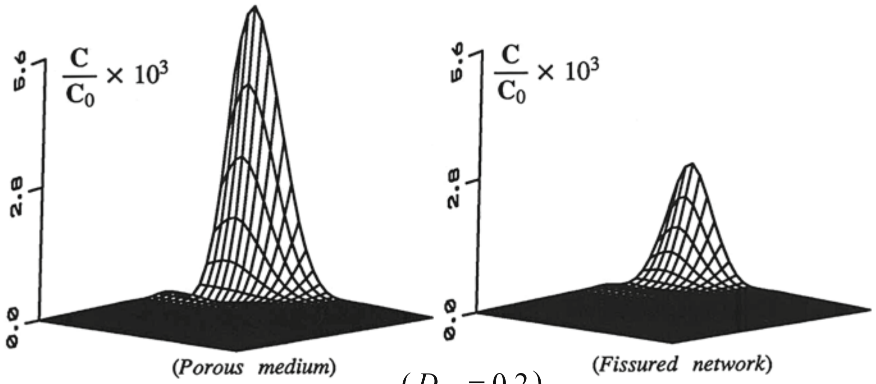

$(D_{2x} = 0.2)$

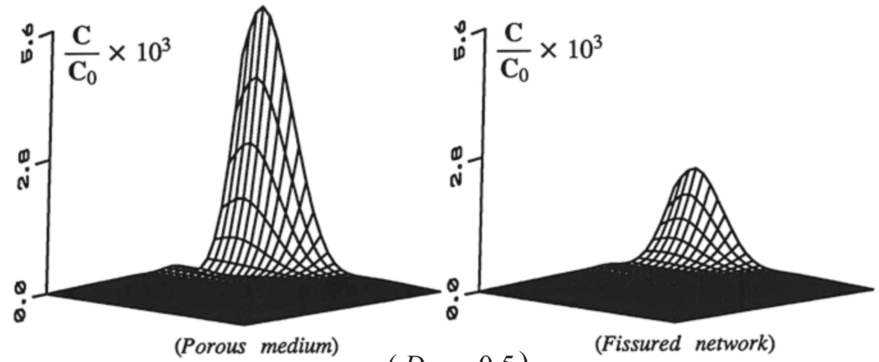

$(D_{2x} = 0.5)$

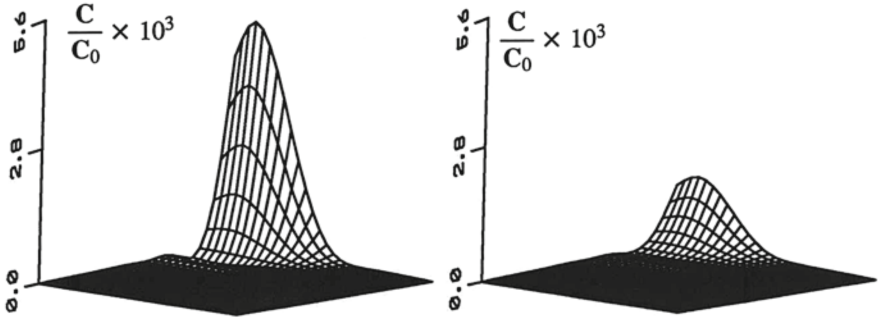

(Porous medium) $(D_{2x} = 1.0)$ (Fissured network)

Fig. 8.21 Effects of solute dispersion on dimensionless contaminant distributions in the fractured porous medium (t = 100 days)

tion points (in Fig. 8.22) at the x axis, the maximum value of the dimensionless contaminant concentration in the case of $D_{1x} = D_{1y}$=1.0 m^2 d^{-1} and $D_{2x} = D_{2y}$= 0.2 m^2 d^{-1} is smaller than that in the other four cases. However, for the three observation points beyond the x axis (in Fig. 8.23), the maximum value of the dimen-

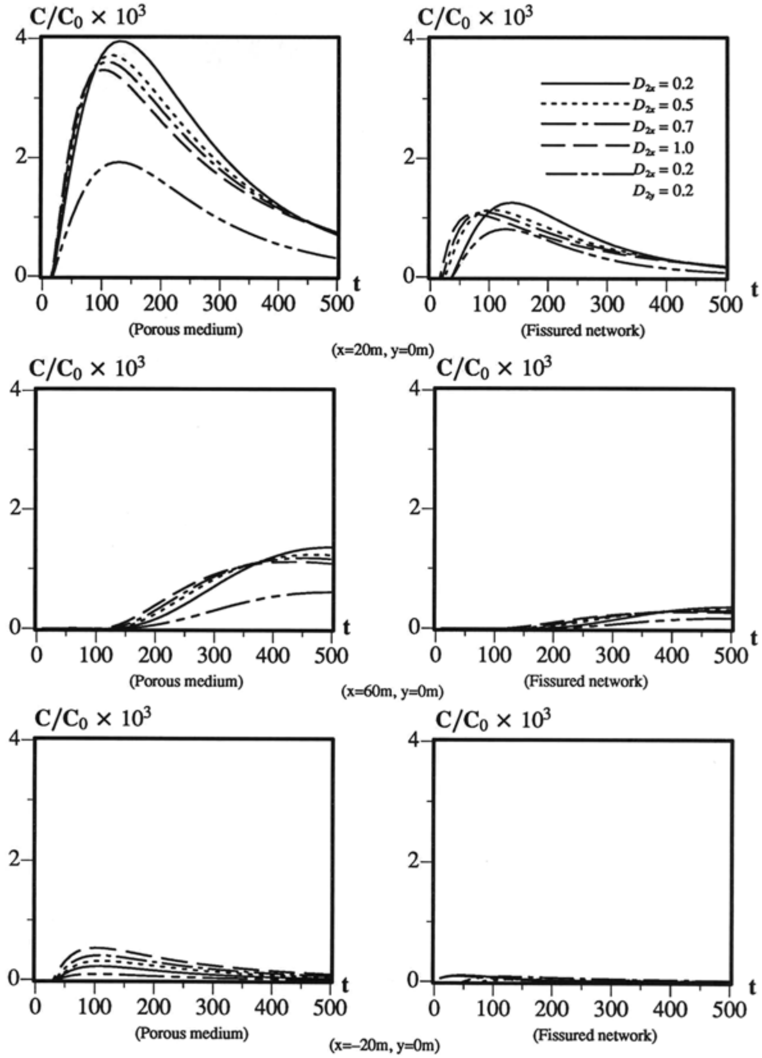

Fig. 8.22 Time-history distributions of dimensionless contaminant concentration due to different dispersion coefficients

sionless contaminant concentration in the case of $D_{1x} = D_{1y}$=1.0 m^2 d^{-1} and $D_{2x} = D_{2y}$=0.2 m^2 d^{-1} is greater than that in the other four cases. Since dispersion coefficients can affect both the contaminant transport speed and the maximum value of the contaminant concentration in a fractured porous medium, they should be determined carefully in the coupled computational model of upwind finite elements and transient infinite elements for simulating transient contaminant transport problems in fractured porous media of infinite domains.

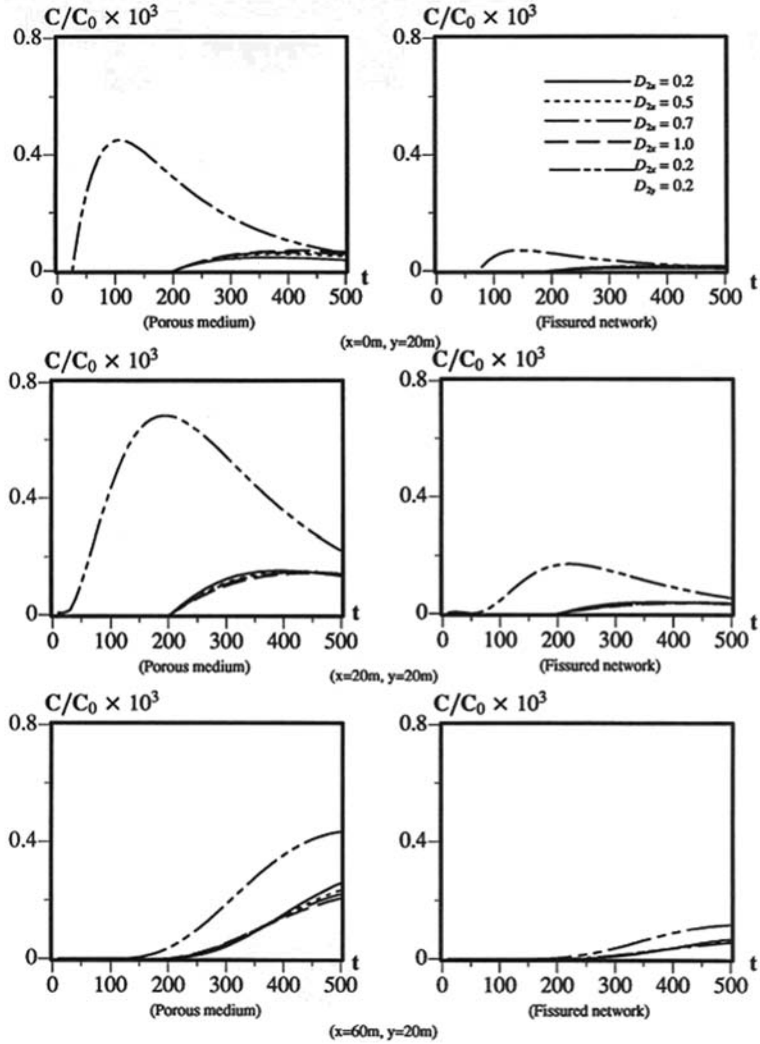

Fig. 8.23 Time-history distributions of dimensionless contaminant concentration due to different dispersion coefficients

In summary, the leakage between the porous block and the fissured network has a significant influence on the distributions of the contaminant concentration in fractured porous media. Generally, the maximum value of the contamination concentration increases in the porous block, but it decreases in the fissured network as a result of the leakage between the porous block and the fissured network. This indicates that more contaminant resides in the porous block. With the increase of time, the maximum values of the contaminant concentration in both the porous block and the fissured network decrease as the contaminant spreads over a broad area.

The transmissive coefficient between the porous block and the fissured network has little effect on the transport speed of the contaminant, even though it has a significant influence on the values of the contaminant concentration in a fractured porous medium.

Considering the effect of the porosities of the fractured porous medium, a larger porosity of the fissured network results in a greater value of the contaminant concentration in the near field of the porous block, whereas it results in a smaller value in the near field of the fissured network. With an increase in the porosity of the fissured network, the maximum value of the contaminant concentration increases in the porous block but decreases in the fissured network.

The average linear velocity (representing the advection) of pore-fluid flow has a significant influence on both the concentration distribution pattern and the transport speed of the contaminant in the fractured porous medium. The larger the average linear velocity of the pore-fluid flow is, the greater will be the transport speed of the contaminant in both the porous block and the fissured network. The same conclusion can be made when the effect of the dispersion is considered in the fractured porous medium.

Summary Statements

In this monograph, the coupled computational method of finite elements and dynamic/transient infinite elements has been presented for dealing with geophysical, geotechnical and geoenvironmental engineering problems in infinite domains. For a given wave propagation problem, the near field of the problem is simulated using finite elements so that complicated geometries and complex material properties can be considered in the coupled computational method. The far field of the problem is simulated using dynamic infinite elements so that waves can be propagated from the near field to the far field without causing spurious reflection and refraction at the interface between finite elements and dynamic infinite elements in the coupled computational model. By taking advantages of both finite elements and dynamic infinite elements, the coupled computational method of finite elements and dynamic infinite elements provides a powerful simulation tool for dealing with a wide range of practical problems, such as the distributions of the free-field motion during earthquakes, the seismic responses of dam–reservoir water–sediment–foundation systems and the dynamic analyses of civil structure–foundation interactions. To simulate transient pore-fluid flow, heat transfer and mass transport problems in fluid-saturated porous media of infinite domains, the coupled computational method of finite elements and transient infinite elements is also presented. As an application example, this coupled method has been used to investigate the effects of several key factors on contaminant transport processes in fractured porous media of infinite domains. The following inferences have been drawn from the related theoretical and numerical results.

(1) Owing to the characteristics of propagating waves from the near field to the far field of a system, the wave propagation function of a dynamic infinite element plays a key role in the formulation of the element. Since the wave propagation function explicitly depends on frequency, the coupled computational method of finite elements and dynamic infinite elements can be directly used to solve linear wave propagation problems in the frequency domain, while it can be only used to deal with nonlinear wave propagation problems in the hybrid frequency–time domain.

(2) For a two-dimensional dynamic infinite element, the corresponding wave propagation function has two independent wavenumbers so that it can be used to simulate explicitly both P-wave and SV-wave propagation in the far field of a system. Similarly, for a three-dimensional dynamic infinite element, the corresponding wave propagation function has three independent wavenumbers so that it is capable

C. Zhao, *Dynamic and Transient Infinite Elements*, Advances in Geophysical and Environmental Mechanics and Mathematics, DOI 10.1007/978-3-642-00846-7_BM2,

of simulating simultaneously P-wave, SV-wave and R-wave propagation in the far field of a system. Based on the wave propagation concept, the detailed formulations associated with both two-and three-dimensional dynamic infinite elements are presented. Since a common side is shared at the interface between a finite element and a dynamic infinite element, the mass and stiffness matrices of a dynamic infinite element can be straightforwardly assembled into the global mass and stiffness matrices of the system.

(3) The coupled computational method of finite elements and dynamic infinite elements can be used to solve both wave scattering and wave radiation problems in infinite domains. When dealing with wave scattering problems, a wave input procedure, which can be easily applied to the coupled computational model of finite elements and dynamic infinite elements, is presented to transform an incident wave into equivalent nodal loads at a wave input boundary located within the coupled computational model. The related numerical results from several benchmark problems have demonstrated the correctness and usefulness of both the coupled computational method and the wave input procedure.

(4) For the application of dynamic infinite elements to dam engineering problems, the coupled computational method of two-dimensional finite elements and dynamic infinite elements is used to simulate the dynamic responses of both a gravity dam–water–sediment–foundation system and an embankment dam–water–sediment–foundation system. For a gravity dam, the related numerical results have indicated that the reservoir bottom sediment has a remarkable effect on the dynamic response of the dam, while for an embankment dam, the corresponding results have demonstrated that both the type and the location of impervious members within the dam have significant influences on the dynamic response of the embankment dam.

(5) As an application, the coupled computational method of two-dimensional finite elements and dynamic infinite elements is used to investigate the effects of canyon topographical and geological conditions on the distributions of the free-field motion during an earthquake. The related numerical results have demonstrated that both topographical and geological conditions have significant influences on seismic acceleration distributions along the surface of a canyon, implying that structures located on softer soils may be subjected to stronger seismic loads than those located on stiffer rocks.

(6) The coupled computational model of three-dimensional finite elements and dynamic infinite elements is used to solve dynamic framed structure–raft foundation–underlying medium interaction problems. The related numerical results have demonstrated that, since the radiation damping of an underlying medium plays a predominant role in determining the total damping of the underlying medium, the dynamic response of a three-dimensional framed structure on a layered medium is much stronger than that on a homogeneous medium, as a result of wave reflection and refraction within the soft layer.

(7) To construct transient infinite elements for simulating pore-fluid flow and heat transfer problems in fluid-saturated orthotropic porous media of infinite domains, both the hydraulic head distribution function and the heat transfer function are presented for deriving the corresponding formulations of the transient infinite elements.

Since these functions explicitly depend on time, the coupled computational method of finite elements and transient infinite elements can be straightforwardly used for solving transient pore-fluid flow and heat transfer problems in the time domain.

(8) Based on the mass transport function concept, the formulations of transient infinite elements are derived for simulating the far fields of mass transport problems in fractured porous media of infinite domains. With the use of the double porosity continuum approach, the porous block and fissured network in a fractured porous medium are treated as an equivalent medium consisting of two overlapping continua. This enables the coupled computational method of finite elements and transient infinite elements to be used for investigating the effects of various key factors on contaminant transport processes in fractured porous media of infinite domains. The related numerical results have demonstrated that the leakage between the porous block and the fissure network, the porosity ratio of the fissured network to the porous block, pore-fluid advection and solute dispersion have significant effects on contaminant concentration distributions in fractured porous media of infinite domains.

(9) One of the important values of this monograph is to provide an effective and efficient way for simulating the far field of an infinite domain so that computational resources can be focused not only on the simulation of complicated geometries and complex material distributions in the near field of a problem, but also on the simulation of multiple-process and multiple-scale aspects of the problem. As boundary conditions may have a conspicuous effect on the solution of a set of partial differential equations, the far field of a geoscience problem needs to be appropriately simulated so as to obtain meaningful numerical solutions. Because of the effective and efficient simulation of the far field, the coupled computational method of finite elements and dynamic (or transient) infinite elements provides a powerful tool for solving not only a wide range of engineering problems, but a broad range of geoscience problems as well. From this point of view, dynamic and transient infinite elements may play an important role in the further development of the emerging computational geoscience discipline.

(10) Although transient infinite elements have been systematically presented in this monograph, there is much work to be done in future. For instance, the present theory of the transient infinite element needs to be extended to (i) the simulation of three-dimensional pore-fluid flow, heat transfer and mass transport problems in fluid-saturated porous media of infinite domains; (ii) the consideration of fluid-saturated and unsaturated porous media of general anisotropy; and (iii) the simulation of coupled problems involving pore-fluid flow, heat transfer and mass transport processes.

References

Adeli, H., Hejazi, M. S., Keer, L. M. and Nemat-Nasser, S., 1981. Dynamic response of foundations with arbitrary geometries, *Journal of Engineering Mechanics, ASCE*, **107**, 953–967.

Aki, K. and Larner, K. L., 1970. Surface motion in a layered medium having an irregular interface due to incident plane SH-waves, *Journal of Geophysical Research*, **75**, 933–954.

Asano, S., 1966. Reflection and refraction of elastic waves at a corrugated surface, *Bulletin of Seismology Society of American*, **56**, 201–222.

Astley, R. J., 1996. Transient wave-envelope elements for wave problems, *Journal of Sound and Vibration*, **192**, 245–261.

Astley, R. J., 1998. Transient spheroidal elements for unbounded wave problems, *Computer Methods in Applied Mechanics and Engineering*, **164**, 3–15.

Barenblatt, G. I., Zheltov, I. P. and Kochina, I. N., 1960. Basic concepts in the theory of seepage of homogeneous liquids in fissured rocks, *Journal of Applied Mathematics and Mechanics*, **24**, 852–864.

Bard, P. Y., 1982. Diffracted waves and displacement field over two-dimensional elevated topographies, *Geophysical Journal of Royal Astronaut Society*, **71**, 731–760.

Bear, J., 1972. *Dynamics of Fluids in Porous Media*, American Elsevier Publishing Company, New York.

Bear, J. and Bachmat, Y., 1990. *Introduction to Modelling of Transport Phenomena in Porous Fractured Media*, Kluwer Academic Press, New York.

Beer, G. and Meek, J. L., 1981. Infinite domain element, *International Journal for Numerical Methods in Engineering*, **17**, 43–52.

Bettess, P., 1977. Infinite elements, *International Journal for Numerical Methods in Engineering*, **11**, 53–64.

Bettess, P., 1980. More on infinite element, *International Journal for Numerical Methods in Engineering*, **15**, 1613–1626.

Bettess, P., 1992. *Infinite Elements*, Penshaw Press, Sunderland.

Booker, J. R. and Small, J. C., 1981. Finite element analysis of problems with infinitely distant boundaries, *International Journal for Numerical and Analytical Methods in Geomechanics*, **5**, 345–368.

Boor, D. M., 1972. A note on the effect of simple topography on seismic SH-waves, *Bulletin of Seismology Society of American*, **62**, 275–284.

Bouchon, M., 1973. Effect of topography on surface motion, *Bulletin of Seismology Society of American*, **63**, 615–632.

Brebbia, C. A., 1978. *The Boundary Element Method for Engineers*, Pentech Press, Plymouth.

Carslaw, H. S. and Jaeger, J. C., 1959. *Conduction of Heat in Solids*, Clarendon Press, Oxford.

Chakarbarti, P. and Chopra, A. K., 1974. Hydrodynamic effects in earthquake response of brevity dams, *Journal of Engineering Mechanics*, *ASCE*, **100**, 1211–1224.

Chen, C. H. and Penzien, J., 1986. Dynamic modeling of axisymmetric foundations, *Earthquake Engineering and Structural Dynamics*, **14**, 823–840.

Cheng, A. H. D., 1986. Effect of sediment on earthquake-induced reservoir hydrodynamic responses, *Journal of Engineering Mechanics, ASCE*, **112**, 654–665.

Cheung, Y. K., 1976. *Finite Strip Method in Structural Analysis*, Pergamon, Oxford.

Chopra, A. K., 1968. Earthquake behaviour of reservoir dam system, *Journal of Engineering Mechanics, ASCE*, **94**, 1475–1500.

Chopra, A. K. and Gupta, S., 1982. Hydrodynamic and foundation interaction effects in frequency response function for concrete gravity dams, *Earthquake Engineering and Structural Dynamics*, **10**, 89–106.

Chow, Y. K. and Smith, I. M., 1981. Static and periodic infinite solid elements, *International Journal for Numerical Methods in Engineering*, **17**, 503–526.

Chow, Y. K., 1986. Simplified analysis of dynamic response of rigid foundations with arbitrary geometries, *Earthquake Engineering and Structural Dynamics*, **14**, 643–653.

Chow, Y. K., 1987. Vertical vibration of three-dimensional rigid foundation on layered media, *Earthquake Engineering and Structural Dynamics*, **15**, 585–594.

Clough, R. W., Chang, K. T., Chen, H. Q. and Ghanaat, Y., 1985. *Dynamic Interaction Effects in Arch Dams*, University of California, Berkeley, CA.

Clough, R. W. and Penzien, J., 1975. *Dynamics of Structures*, McGraw-Hill, New York.

Cundall, P. A., Kunar, R. R., Carpenter, P. C. and Marti, J., 1978. Solution of infinite dynamic problems by finite modeling in the time domain, *Conference on Applied Numerical Modeling*, Madrid, Spain.

Datta, S. K. and El-Akily, N., 1978. Diffraction of elastic waves by cylindrical cavity in half-space. *Journal of Acoustical Society of American*, **64**, 1692–1699.

Dominquez, J. and Roesset, J. M., 1978. Dynamic stiffness of rectangular foundations, *Research Report R78-20*, Massachusetts Institute of Technology, Boston, MA.

Dravinski, M., 1983. Scattering of plane harmonic SH waves by dipping layers of arbitrary shape, *Bulletin of Seismology Society of American*, **73**, 1303–1319.

Duguid, J. O. and Lee, P. C. Y., 1977. Flow in fractured porous media, *Water Resources Research*, **13**, 558–566.

Elorduy, J., Nieto, J. A. and Szekely, E. M., 1967. Dynamic response of basis of arbitrary shape subjected to periodic vertical loading, *Proceedings of International Symposium on Wave Propagation and Dynamic Properties of Earth Materials*, University of New Mexico, Albuquerque.

Eshraghi, H. and Dravinski, M., 1989a. Scattering of elastic waves by nonaxisymmetric three-dimensional dipping layer, *Numerical Methods for Partial Differential Equations*, **5**, 327–345.

Eshraghi, H. and Dravinski, M., 1989b. Scattering of plane harmonic SH, SV, P and Rayleigh waves by non-axisymmetric three-dimensional canyons: a wave function approach, *Earthquake Engineering and Structural Dynamics*, **18**, 983–998.

Fenves, G. and Chopra, A. K., 1983. Effects of reservoir bottom absorption on earthquake response of concrete gravity dams, *Earthquake Engineering and Structural Dynamics*, **11**, 809–829.

Fenves, G. and Chopra, A. K., 1984. Earthquake analysis of concrete gravity dams including reservoir bottom absorption and dam–water–foundation rock interaction, *Earthquake Engineering and Structural Dynamics*, **12**, 663–680.

Fenves, G. and Chopra, A. K., 1985. Effects of reservoir bottom absorption and dam-water-foundation rock interaction on frequency response functions for concrete gravity dams, *Earthquake Engineering and Structural Dynamics*, **13**, 13–31.

Freeze, R. A. and Cherry, J. A., 1979. *Groundwater*, Prentice-Hall, Englewood Cliffs, New Jersey.

Gazetas, G. and Roesset, J. M., 1979. Vertical vibration of machine foundations, *Journal of Geotechnical Engineering, ASCE*, **105**, 1435–1454.

Geli, L., Bard, P. Y. and Jullien, B., 1988. The effect of topography on earthquake ground motion: a review and new results, *Bulletin of Seismology Society of American*, **78**, 42–63.

Gow, P., Upton, P., Zhao, C. and Hill, K., 2002. Copper-Gold mineralization in the New Guinea: Numerical modeling of collision, fluid flow and intrusion-related hydrothermal systems, *Australian Journal of Earth Sciences*, **49**, 753–771.

Graff, K. F., 1975. *Wave Motion in Elastic Solids*, Clarendon Press, Oxford.

Gupta, S., Pensien, J., Lin, T. W. and Yeh, C. S., 1982. Three-dimensional hybrid modeling of soil–structure interaction, *Earthquake Engineering and Structural Dynamics*, **10**, 69–87.

Gutierrez, J. A. and Chopra, A. K., 1978. A substructure method for earthquake analysis of structures including structure–soil interaction, *Earthquake Engineering and Structural Dynamics*, **6**, 51–69.

Hall, J. F. and Chopra, A. K., 1982. Two-dimensional analysis of concrete gravity and embankment dams including hydrodynamic effects, *Earthquake Engineering and Structural Dynamics*, **10**, 305–332.

Hamidzadeh-Eraghi, H. R. and Grootenhuis, P., 1981. The dynamics of a rigid foundation on the surface of an elastic half-space, *Earthquake Engineering and Structural Dynamics*, **9**, 505–515.

Harr, M. E., 1962. *Groundwater and Seepage*, McGraw-Hill, New York.

Heinrich, J. C., Huyakorn, P. S., Zienkiewicz, O. C. and Mitchell, A. R., 1977. An upwind finite element scheme for two dimensional convection transport equation, *International Journal for Numerical Methods in Engineering*, **11**, 131–143.

Huyakorn, P. S., 1977. Solution of steady state, convective transport equation using an upwind finite element scheme, *Applied Mathematics Modelling*, **1**, 187–195.

Huyakorn, P. S. and Nilkuha, K., 1979. Solution of steady state, convective transport equation using an upwind finite element scheme, *Applied Mathematics Modelling*, **3**, 7–17.

Karabalis, D. I. and Beskos, D. E., 1984. Dynamic response of 3D rigid surface foundations by time boundary element method, *Earthquake Engineering and Structural Dynamics*, **12**, 73–93.

Kausel, E., 1974. Forced vibrations of circular foundations in layered media, *MIT Research Report*, **R74-11**, MIT, USA.

Kawase, H., 1988. Time-domain response of a semi-circular canyon for incident SV, P and Rayleigh waves calculated by the discrete wavenumber boundary element method, *Bulletin of Seismology Society of American*, **78**, 1415–1437.

Khair, K. R., Datta, S. K. and Shah, A. H., 1989. Amplification of obliquely incident seismic waves by cylindrical alluvial valleys of arbitrary cross-sectional shapes. Part I: Incident P and SV waves, *Bulletin of Seismology Society of American*, **79**, 610–630.

Khalili, N., Yazdchi, M. and Valliappan, S., 1999a. Wave propagation analysis of two-phase saturated porous media using coupled finite-infinite element method, *Soil Dynamics and Earthquake Engineering*, **18**, 533–553.

Khalili, N., Valliappan, S. and Yazdchi, M., 1999b. An axi-symmetric infinite element for transient radial flow problems, *International Journal for Numerical and Analytical Methods in Geomechanics*, **23**, 801–813.

Kitamura, Y. and Sakurai, S., 1979. Dynamic stiffness for rectangular rigid foundations on a semi-infinite elastic medium, *International Journal for Numerical and Analytical Methods in Geomechanics*, **3**, 159–171.

Lai, Y. M., Liu, S. Y., Wu, Y. P. and Konrad, J. M., 2002. Numerical simulation for the coupled problem of temperature and seepage fields in cold region dams, *Journal of Hydraulic Research*, **40**, 631–635.

Lardner, R. W. and Song, Y., 1991. An algorithm for three-dimensional convection and diffusion with very different horizontal and vertical length scales, *International Journal for Numerical Methods in Engineering*, **32**, 1303–1319.

Lee, V. W., 1984. Three-dimensional diffraction of plane P, SV and SH waves by a hemispherical alluvial valley, *Soil Dynamics and Earthquake Engineering*, **3**, 133–144.

Liam-Finn, W. D. and Varoglu, E., 1972a. Dynamics of a gravity dam–reservoir system, *Computers and Structures*, **3**, 913–925.

Liam-Finn, W. D. and Varoglu, E., 1972b. Dynamics of a gravity dam–reservoir system on a flexible layer foundation, *Proceedings of Special Conference on FEM in Civil Engineering*, Montreal, Canada.

Liam-Finn, W. D. and Varoglu, E., 1975. A study of dynamic interaction in a plate–reservoir system, *Proceedings of 5th European Conference on Earthquake Engineering*, Istanbul, Turkey.

Liam-Finn, W. D., Varoglu, E. and Cherry, S., 1977. Seismic water pressures against concrete dams, *Structural and Geotechnical Materials*, New Jersey, 420–442.

Liao, Z. P., Wong, H. L., Yang, B. P. and Yuan, Y. F., 1984. A transmitting boundary for transient wave analysis, *Scientia Sinica*, **27**, 1063–1073.

Lotfi, V., Roesset, J. M. and Tassoulas, J. L., 1987. A technique for the analysis of the response of dams to earthquakes, *Earthquake Engineering and Structural Dynamics*, **15**, 463–490.

Luco, J. E., 1974. Impedance functions for a rigid surface on a layered medium, *Nuclear Engineering Design*, **31**, 204–217.

Luco, J. E., 1976. Vibrations of a rigid disc on a layered viscoelastic medium, *Nuclear Engineering Design*, **36**, 325–340.

Luco, J. E., 1986. On the relation between radiation and scattering problems for foundations embedded in an elastic half-space, *Soil Dynamics and Earthquake Engineering*, **5**, 97–101.

Luco, J. E. and Aspel, R. J., 1983. On the Green's function for a layered half-space, parts I and II, *Bulletin of Seismology Society of American*, **73**, 909–951.

Lysmer, J. and Kuhlemyer, R. L., 1969. Finite dynamic model for infinite media, *Journal of Engineering Mechanics, ASCE*, **95**, 859–877.

McEvilly, T. V., Bakun, W. H. and Casaday, K. B., 1967. The Parkfield, California, earthquake of 1966, *Bulletin of Seismology Society of American*, **57**, 1221–1244.

McIvor, I. K., 1969. Two-dimensional scattering of plane compressional wave by surface imperfections, *Bulletin of Seismology Society of American*, **59**, 1349–1364.

Medina, F. and Taylor, R. L., 1983. Finite element techniques for problems of unbounded domains, *International Journal for Numerical Methods in Engineering*, **19**, 699–709.

Medina, F., Dominguez, J. and Tassoulas, J. L., 1990. Response of dams to earthquakes including effects of sediments, *Journal of Structural Engineering, ASCE*, **116**, 3108–3121.

Mita, A. and Takanashi, W., 1983. Dynamic soil-structure interaction by hybrid method, in Brebbia, C. A. et al. (eds), *Boundary Elements*, Springer-Verlag, Berlin.

Nield, D. A. and Bejan, A., 1992. *Convection in Porous Media*, Springer-Verlag, New York.

Ogata, A. and Banks, R. B., 1961. A solution of the differential equation of longitudinal dispersion in porous media, *US Geological Survey Professional Paper-411A*, 1–7.

Ohtsuki, A. and Harumi, K., 1984. Effect of topography and subsurface inhomogeneities on seismic SV waves, *Earthquake Engineering and Structural Dynamics*, **12**, 37–58.

Ord, A., Hobbs, B. E., Zhang, Y., Broadbent, G. C., Brown, M., Willetts, G., Sorjonen-Ward, P., Walshe, J. and Zhao, C., 2002. Geodynamic modelling of the Century deposit, Mt Isa Province, Queensland, *Australian Journal of Earth Sciences*, **49**, 1011–1039.

Phillips, O. M., 1991. *Flow and Reactions in Permeable Rocks*, Cambridge University Press, Cambridge.

Raffensperger, J. P. and Garven, G., 1995. The formation of unconformity-type uranium ore deposits: Coupled hydrochemical modelling, *American Journal of Science*, **295**, 639–696.

Rao, S. S., 1989. *The Finite Element Method in Engineering*, Pergamon Press, Oxford.

Reimer, R. B., Clough, R. W. and Rapheal, J. M., 1974. Seismic response of Pacoima dam in the San Fernando earthquake, *Proceedings of 5th World Conference on Earthquake Engineering (Rome)*, **2**, 2328–2337.

Riggs, H. R. and Waas, G., 1985. Influence of foundation flexibility on soil-structure interaction, *Earthquake Engineering and Structural Dynamics*, **13**, 597–615.

Rock, T. and Hinton, E., 1974. Free vibration and transient response of thick and thin plates using the finite element method, *Earthquake Engineering and Structural Dynamics*, **3**, 51–63.

Rogers, A. M., Katz, L. J. and Benett, T. J., 1974. Topographic effect on ground motion for incident P-waves: a model study, *Bulletin of Seismology Society of American*, **64**, 437–456.

Rowe, R. K., Caers, C. J. and Barone, F., 1988. Laboratory determination of diffusion and distribution coefficients of contaminants using undisturbed clayey soil, *Canadian Geotechnical Journal,* **25**, 108–118.

Rowe, R. K. and Booker, J. R., 1989. A semi-analytical model for contaminant migration in a regular two or three dimensional fractured network: Conservative contaminant, *International Journal for Numerical and Analytical Methods in Geomechanics*, **13**, 531–550.

Rowe, R. K. and Booker, J. R., 1990a. Contaminant migration in a regular two or three dimensional fractured network: Reactive contaminant, *International Journal for Numerical and Analytical Methods in Geomechanics*, **14**, 401–425.

Rowe, R. K. and Booker, J. R., 1990b. Contaminant migration through fractured till into an underling aquifer, *Canadian Geotechnical Journal*, **27**, 484–495.

Rowe, R. K. and Booker, J. R., 1991. Modelling of two dimensional contaminant migration in a layered and fractured zone beneath landfills, *Canadian Geotechnical Journal*, **28**, 338–352.

Saini, S. S., Bettess, P. and Zienkiewicz, O. C., 1978. Coupled hydro-dynamic response of concrete gravity dams using finite and infinite elements, *Earthquake Engineering and Structural Dynamics*, **6**, 363–374.

Sanchez-Sesma, F. J., 1983. Diffraction of elastic waves by three-dimensional surface irregularities, *Bulletin of Seismology Society of American*, **73**, 1621–1636.

Sanchez-Sesma, F. J., Bravo, M. A. and Herrera, I., 1985. Surface motion of topographical irregularities, *Bulletin of Seismology Society of American*, **75**, 263–269.

Schafer, D., Schafer, W. and Kinzelbach, W., 1998a. Simulation of reactive processes related to biodegradation in aquifers: 1. Structure of the three-dimensional reactive transport model, *Journal of Contaminant Hydrology*, **31**, 167–186.

Schafer, D., Schafer, W. and Kinzelbach, W., 1998b. Simulation of reactive processes related to biodegradation in aquifers: 2. Model application to a column study on organic carbon degradation, *Journal of Contaminant Hydrology*, **31**, 187–209.

Schaubs, P. and Zhao, C., 2002. Numerical modelling of gold-deposit formation in the Bendigo-Ballarat zone, Victoria, *Australian Journal of Earth Sciences*, **49**, 1077–1096.

Shah, A. H., Wong, K. C. and Datta, S. K., 1982. Diffraction of plane SH waves in a half-space, *Earthquake Engineering and Structural Dynamics*, **10**, 519–528.

Shah, A. H., Wong, K. C. and Datta, S. K., 1983. Single and multiple scattering of elastic waves in two dimensions, *Journal of Acoustical Society of American*, **74**, 1033–1043.

Smith, W. D., 1975. The application of finite element analysis to body wave propagation problems, *Geophysical Journal of Royal Astronaut Society*, **42**, 747–768.

Steefel, C. I. and Lasaga, A. C., 1994. A coupled model for transport of multiple chemical species and kinetic precipitation/dissolution reactions with application to reactive flow in single phase hydrothermal systems, *American Journal of Science*, **294**, 529–592.

Toki, K. and Sato, T., 1983. Seismic response analysis of ground with irregular profiles by the boundary element method, in Brebbia, C. A. et al. (eds), *Boundary Elements*, Springer-Verlag, Berlin.

Trifunac, M. D., 1973. Scattering of plane SH-waves by a semi-cylindrical canyon, *Earthquake Engineering and Structural Dynamics*, **1**, 267–281.

Trifunac, M. D. and Udwadia, F. E., 1974. Parfield, California, earthquake of June 27, 1966: A three-dimensional moving dislocation, *Bulletin of Seismology Society of American*, **64**, 511–533.

Ungless, R. F., 1973. An infinite finite element, *M. A. SC. Thesis*, University of British Columbia, Vancouver.

Valliappan, S. and Naghadah, N. K., 1990. Flow through fissured porous media with deformable matrix, *International Journal for Numerical Methods in Engineering*, **29**, 1079–1094.

Valliappan, S. and Zhao, C., 1992. Dynamic response of concrete gravity dams including dam-water-foundation interaction, *International Journal for Numerical and Analytical Methods in Geomechanics*, **16**, 79–99.

Wang, G. C., Chen, L. Z. and Song, C. Y., 2006. Finite-infinite element for dynamic analysis of axisymmetrically saturated composite foundations, *International Journal for Numerical Methods in Engineering*, **67**, 916–932.

Warburton, G. B. and Hutton, S. G., 1978. Dynamic interaction for idealized off-shore structure, *Earthquake Engineering and Structural Dynamics*, **6**, 557–567.

White, W., Valliappan, S. and Lee, I. K., 1977. Unified boundary for finite dynamic model, *Journal of Engineering Mechanics, ASCE*, **103**, 949–964.

Wolf, J. P., 1985. *Dynamic Soil-Structure Interaction*, Prentice-Hall, Englewood Cliffs, New Jersey.

Wolf, J. P., 1988. *Soil-Structure-Interaction Analysis in Time Domain*, Prentice-Hall, Englewood Cliffs, New Jersey.

Wong, H. L., 1982. Effect of surface topography on the diffraction of P, SV and Rayleigh waves, *Bulletin of Seismology Society of American*, **72**, 1167–1183.

Wong, H. L. and Jennings, P. C., 1975. Effect of topography on strong ground motion, *Bulletin of Seismology Society of American*, **65**, 1239–1257.

Wong, H. L. and Luco, J. E., 1976. Dynamic response of rigid foundations of arbitrary shape, *Earthquake Engineering and Structural Dynamics*, **4**, 579–587.

Wong, H. L. and Trifunac, M. D., 1974. Scattering of plane SH-waves by a semi-elliptical canyon, *Earthquake Engineering and Structural Dynamics*, **3**, 157–169.

Wong, K. C., Shah, A. H. and Datta, S. K., 1985. Diffraction of elastic waves in a half-space, *Bulletin of Seismology Society of American*, **75**, 69–92.

Xu, T. F., Samper, J. Ayora, C., Manzano, M. and Custodio, E., 1999. Modelling of non-isothermal multi-component reactive transport in field scale porous media flow systems, *Journal of Hydrology*, **214**, 144–164.

Yang, Y. B., Kuo, S. R. and Huang, H. H., 1996. Frequency-independent infinite elements for analysing semi-infinite problems, *International Journal for Numerical Methods in Engineering*, **39**, 3553–3569.

Yang, Y. B. and Huang, H. H., 2001. A 2.5D finite/infinite element approach for visco-elastic bodies subjected to moving loads, *International Journal for Numerical Methods in Engineering*, **51**, 1317–1336.

Yeh, G. T. and Tripathi, V. S., 1991. A model for simulating transport of reactive multispecies components: Model development and demonstration, *Water Resources Research*, **27**, 3075–3094.

Yun, C. B., Kim, D. K. and Kim, J. M., 2000. Analytical frequency-dependent infinite elements for soil-structure interaction analysis in two-dimensional medium, *Engineering Structures*, **22**, 258–271.

Yun, C. B., Chang, S. H., Seo, C. G. and Kim, J. M., 2007. Dynamic infinite elements for soil-structure interaction analysis in a layered soil medium, *International Journal of Structural stability and Dynamics*, **7**, 693–713.

Zahradnik, J. and Urban, L., 1984. Effect of a simple mountain range on underground seismic motion, *Geophysical Journal of Royal Astronaut Society*, **79**, 167–183.

Zhang, C. and Zhao, C., 1987. A coupling method of finite and infinite elements for strip foundation wave problems, *Earthquake Engineering and Structural Dynamics*, **15**, 839–851.

Zhang, C. and Zhao, C., 1988. Effects of canyon topography and geological conditions on strong ground motion, *Earthquake Engineering and Structural Dynamics*, **16**, 81–97.

Zhang, X. F., Xiao, J. Z., Zhang, Y. N. and Xiao, S. X., 2007. Study of the function of the insulation layer for treating leakage in permafrost tunnels, *Applied Thermal Engineering*, **27**, 637–645.

Zhao, C., Zhang, C. and Zhang, G., 1986. Simulation of semi-infinite plane elastic foundation using infinite elements, (in Chinese), *Journal of Tsinghua University*, **26**, 51–63.

Zhao, C., 1987. A simulation of infinite domain for arch dam foundation and seismic input procedures, (in Chinese), *Ph. D. Thesis*, Tsinghua University, Beijing.

Zhao, C., Zhang, C. and Zhang, G., 1987. Study on the characteristics of mapping dynamic infinite elements, (in Chinese), *Earthquake Engineering and Engineering Vibration*, **7**, 1–15.

Zhao, C., Zhang, C. and Zhang, G., 1989. Analysis of 3-D foundation wave problems by mapped dynamic infinite elements, *Science in China Series A*, **32**, 469–491.

Zhao, C. and Valliappan, S., 1991. Vibration of three-dimensional rigid raft foundation on viscoelastic medium, *Earthquake Engineering and Structural Dynamics*, **20**, 1159–1177.

Zhao, C., Valliappan, S. and Wang, Y. C., 1991. An approximate method for simulating infinite media, *Computers and Structures*, **41**, 1041–1049.

Zhao, C., Valliappan, S. and Wang, Y. C., 1992. A numerical model for wave scattering problems in infinite media due to P- and SV-wave incidences, *International Journal for Numerical Methods in Engineering*, **33**, 1661–1682.

Zhao, C. and Valliappan, S., 1993a. Seismic wave scattering effects under different canyon topographic and geological conditions, *Soil Dynamics and Earthquake Engineering*, **12**, 129–143.

Zhao, C. and Valliappan, S., 1993b. Incident P and SV wave scattering effects under different canyon topographic and geological conditions, *International Journal for Numerical and Analytical Methods in Geomechanics*, **17**, 73–94.

Zhao, C. and Valliappan, S., 1993c. Dynamic analysis of a reinforced retaining wall using finite and infinite element coupled method, *Computers and Structures*, **47**, 239–244.

Zhao, C. and Valliappan, S., 1993d. A dynamic infinite element for 3D infinite domain wave problems, *International Journal for Numerical Methods in Engineering*, **36**, 2567–2580.

Zhao, C. and Valliappan, S., 1993e. Effect of raft flexibility and soil media on the dynamic response of a framed structure, *Computers and Structures*, **48**, 227–239.

Zhao, C. and Valliappan, S., 1993f. An efficient wave input procedure for infinite media, *Communications in Numerical Methods in Engineering*, **9**, 407–415.

Zhao, C. and Valliappan, S., 1993g. Transient infinite elements for seepage problems in infinite media, *International Journal for Numerical and Analytical Methods in Geomechanics*, **17**, 323–341.

Zhao, C. and Valliappan, S., 1993h. Mapped transient infinite elements for heat transfer problems in infinite media, *Computer Methods in Applied Mechanics and Engineering*, **108**, 119–131.

Zhao, C., Valliappan, S. and Tabatabaie, J., 1993, Effect of impervious members and reservoir bottom sediment on dynamic response of embankment dams, *Soil Dynamics and Earthquake Engineering*, **12**, 199–208.

Zhao, C., 1994. Effects of reservoir bottom sediments on hydrodynamic pressure of gravity dams, *Computers and Structures*, **52**, 297–307.

Zhao, C. and Valliappan, S., 1994a. Transient infinite element for contaminant transport problems, *International Journal for Numerical Methods in Engineering*, **37**, 1143–1158.

Zhao, C. and Valliappan, S., 1994b. Numerical modelling of transient contaminant migration problems in infinite porous fractured media using finite/infinite element technique: theory, *International Journal for Numerical and Analytical Methods in Geomechanics*, **18**, 523–541.

Zhao, C. and Valliappan, S., 1994c. Numerical modelling of transient contaminant migration problems in infinite porous fractured media using finite/infinite element technique: Parametric study, *International Journal for Numerical and Analytical Methods in Geomechanics*, **18**, 543–564.

Zhao, C. and Xu, T. P., 1994. Effects of backfill soils and incident wave types on seismic response of a reinforced retaining wall, *Computers and Structures*, **53**, 105–117.

Zhao, C., Xu, T. P. and Valliappan, S., 1994. Numerical modelling of mass transport problems in porous media: A review, *Computers and Structures*, **53**, 849–860.

Zhao, C., Xu, T. P. and Valliappan, S., 1995. Seismic response of concrete gravity dams including water-dam-sediment-foundation interaction, *Computers and Structures*, **54**, 705–715.

Zhao, C., Mühlhaus, H. B. and Hobbs, B. E., 1997. Finite element analysis of steady-state natural convection problems in fluid-saturated porous media heated from below, *International Journal for Numerical and Analytical Methods in Geomechanics*, **21**, 863–881.

Zhao, C., Hobbs, B. E. and Mühlhaus, H. B., 1998. Finite element modelling of temperature gradient driven rock alteration and mineralization in porous rock masses, *Computer Methods in Applied Mechanics and Engineering*, **165**, 175–187.

Zhao, C., Hobbs, B. E., Baxter, K., Mühlhaus, H. B. and Ord, A., 1999a. A numerical study of pore-fluid, thermal and mass flow in fluid-saturated porous rock basins, *Engineering Computations*, **16**, 202–214.

Zhao, C., Hobbs, B. E., Mühlhaus, H. B. and Ord, A., 1999b. A consistent point-searching algorithm for solution interpolation in unstructured meshes consisting of 4-node bilinear quadrilateral elements, *International Journal for Numerical Methods in Engineering*, **45**, 1509–1526.

Zhao, C., Hobbs, B. E., Mühlhaus, H. B., Ord, A. and Lin, G., 2000. Numerical modelling of double diffusion driven reactive flow transport in deformable fluid-saturated porous media with particular consideration of temperature-dependent chemical reaction rates, *Engineering Computations*, **17**, 367–385.

Zhao, C., Hobbs, B. E., Walshe, J. L., Mühlhaus, H. B. and Ord, A., 2001. Finite element modelling of fluid-rock interaction problems in pore-fluid saturated hydrothermal/sedimentary basins, *Computer Methods in Applied Mechanics and Engineering*, **190**, 2277–2293.

Zhao, C., Lin, G., Hobbs, B. E., Wang, Y., Mühlhaus, H. B. and Ord, A., 2002. Finite element modelling of reactive fluids mixing and mineralization in pore-fluid saturated hydrothermal/sedimentary basins, *Engineering Computations*, **19**, 364–387.

Zhao, C. and Liu, T., 2002. Nonreflecting artificial boundaries for modelling scalar wave propagation problems in two-dimensional half space, *Computer Methods in Applied Mechanics and Engineering*, **191**, 3137–3152.

Zhao, C., Lin, G., Hobbs, B. E., Ord, A., Wang, Y. and Mühlhaus, H. B., 2003. Effects of hot intrusions on pore-fluid flow and heat transfer in fluid-saturated rocks, *Computer Methods in Applied Mechanics and Engineering*, **192**, 2007–2030.

Zhao, C. and Liu, T., 2003. Nonreflecting artificial boundaries for transient scalar wave propagation in a two-dimensional infinite homogeneous layer, *International Journal for Numerical Methods in Engineering*, **58**, 1435–1456.

Zhao, C., Hobbs, B. E., Ord, A., Peng, S., Mühlhaus, H. B. and Liu, L., 2004. Theoretical investigation of convective instability in inclined and fluid-saturated three-dimensional fault zones, *Tectonophysics*, **387**, 47–64.

Zhao, C., Hobbs, B. E., Ord, A., Peng, S., Mühlhaus, H. B. and Liu, L., 2005. Numerical modelling of chemical effects of magma solidification problems in porous rocks, *International Journal for Numerical Methods in Engineering*, **64**, 709–728.

Zhao, C., Hobbs, B. E., Ord, A., Kuhn, M., Mühlhaus, H. B. and Peng, S., 2006. Numerical simulation of double-diffusion driven convective flow and rock alteration in three-dimensional fluid-saturated geological fault zones, *Computer Methods in Applied Mechanics and Engineering*, **195**, 2816–2840.

Zhao, C., Hobbs, B. E., Ord, A., Hornby, P., Peng, S. and Liu, L., 2007. Mineral precipitation associated with vertical fault zones: The interaction of solute advection, diffusion and chemical kinetics, *Geofluids*, **7**, 3–18.

Zhao, C., Hobbs, B. E., Ord, A., Hornby, P., Mühlhaus, H. B. and Peng, S., 2008. Theoretical and numerical analyses of pore-fluid-flow focused heat transfer around geological faults and large cracks, *Computers and Geotechnics*, **35**, 357–371.

Zienkiewicz, O. C., 1977. *The Finite Element Method*, McGraw-Hill, London.

Zienkiewicz, O. C. and Bettess, P., 1975. Infinite element in the study of fluid-structure interaction problems, *Proceedings of 2nd International Symposium on Computer Methods in Applied Science and Engineering*, Versailles, France.

Index